UNIVERSITY OF SOUTHAMPTON

DEPARTMENT OF ELECTRONICS AND COMPUTER SCIENCE

CHARACTERISATION TECHNIQUES FOR SPECIAL OPTICAL FIBRES

by

MARTIN EMANUEL FERMANN

A thesis submitted for the degree of
Doctor of Philosophy
September 1988

UNIVERSITY OF SOUTHAMPTON

ABSTRACT

FACULTY OF ENGINEERING
ELECTRONICS AND COMPUTER SCIENCE

DOCTOR of PHILOSOPHY

CHARACTERISATION TECHNIQUES FOR SPECIAL OPTICAL FIBRES

by Martin Emanuel Fermann

Special optical fibres are introduced with the emphasis on rare-earth-doped fibres and fibres with crystal-like properties. Characterisation techniques for these types of fibre are discussed and several applications are described. In particular, optical time-domain reflectometry is used to demonstrate a distributed temperature sensor based on the temperature dependence of the absorption in rare-earth-doped fibres. Further, energy transfer between ytterbium and erbium is characterised and an erbium fibre laser sensitised with ytterbium is demonstrated. Finally, techniques for the creation of crystal-like properties in optical fibres are developed and second-order nonlinear phenomena in these fibres are analysed both experimentally and theoretically.

Acknowledgements

I am indebted to Dr. D.N. Payne and Professor W.A. Gambling for their guidance and technical advice given throughout this research programme. Special thanks are also due to all other members of the Optical Fibre Group who have willingly given their time and aided the realisation of my research projects. In particular, I would like to acknowledge Dr. S.B. Poole and Miss J.E. Townsend for fabricating most of the fibres characterised by myself. Further, the enthusiastic collaboration of Dr. M.C. Farries, L. Li and Mrs. L.J. Poyntz-Wright in various major experiments is deeply appreciated. Dr. P.St.J. Russell provided a constant source of encouragement and a never ending source of challenging ideas. Valuable assistance was given by Dr. A.H. Hartog from York Technology plc, Dr. E.J. Tarbox from Pirelli General plc and Dr. P. Sumi from the Physics Department at Southampton University.

Professor W.A. Gambling, Dr. P.St.J. Russell, P.R. Morkel and R.I. Laming proof-read the manuscript and contributed with a lot of useful discussions to its completion. Thanks are also due to J.C. Nash, who provided many of the drawings. Finally, I would like to acknowledge our secretaries Miss N.J. Pink and Miss H. Krause for organising me.

CONTENTS

Chapter 1: Introduction

1.1 Fibres as Passive Light-Guides

Since the early development of optical fibres, first as light-guides for medical endoscopes[1], and later for long-distance telecommunications as originally proposed by Kao and Hockam[2], the principal aim was to manufacture low-loss, and low-dispersion, high-quality waveguides to optimise their performance as passive light transmitters. Only in recent years has it been realised that optical fibres also have an attractive potential as active devices.

1.2 Optical Fibre Sensors

The first step into employing fibres as active devices was made by developing fibre sensors. Over the years a large variety of fibre sensors were produced. Early versions were based on simple interferometric designs copied from bulk-optics; in later stages the transmission characteristics of optical fibres were made sensitive to environmental conditions[3]. More recently, advanced systems based on the propagation of polarised light in single-mode fibres have been developed[4]. There is also a strong interest in exploiting other fundamental physical properties of fibres, or modified special fibres, for sensing applications, e.g. third-order nonlinear phenomena[5], black-body radiation[6] and fluorescence[7]. Distributed sensors, which give a read-out of environmental conditions along the whole length of fibres have also been developed[8,9].

1.3 Special Fibres

Active fibres have been made possible by the development of what is now commonly known as special fibres, in which the Optical Fibre Group led by Gambling and Payne has played a leading role. Special fibres may be categorised into five sections, i.e 1) special birefringent fibres,

2) fibres with optional evanescent field access, 3) non-glass fibres, 4) rare-earth-ion-doped fibres and 5) fibres with crystal-like properties.

1.3.1 Special Birefringent Fibres

Special birefringent fibres are single-moded and aimed at transmitting the polarisation state of light in a well defined manner. One may distinguish high-birefringence fibres having a linear birefringence of 10^{-4}-10^{-3}, which preserve polarisation even in the presence of external perturbations[10]. Further, low-birefringence fibres with a linear birefringence of less than 10^{-8}, and circularly birefringent fibres, have also been developed[10]. Such fibres are important for coherent communications and may be used in many different sensor applications by manipulating the polarisation state of the transmitted light inside the fibres[11].

1.3.2 Fibres with Optional Evanescent Field Access

Fibres with optional evanescent field access of fibre are very versatile since they comprise a large range of different fibre designs, which may be exploited. One may list polished fibres[12], D-shaped fibres[13], multi-core fibres[14] and fibres with holes[15]. In all cases an interaction with the evanescent field of the fibre core produces the required performance. In particular, fibre holes alongside a fibre core may be filled with a gas, liquid or metal to produce chemical sensors, temperature sensors or polarisers[15] by evanescent field access. There are some applications, where the interactions are of long range. In this case direct evanescent field access is not required, but the above mentioned fibre design still proves to be useful. For example two holes alongside a fibre core may be filled with metal to allow electro-optic modulation via the application of a strong electric field across the fibre core[16].

1.3.3 Non-Glass Optical Fibres

These are fibres in which either the fibre core or the whole fibre has been replaced by a non-glass substance to obtain properties not achievable in glass fibres on their own. One may list liquid-core fibre[8], single crystal[17] and plastic fibres[18]. The potential of these types of fibre as non-linear optical devices, lasers and sensors, is very large. However, the applications are still very limited due to inadequate fibre quality and difficulty in handling or manufacture.

1.3.4 Rare-Earth-Ion-Doped Fibres

Rare-earth-ion-doped fibres were developed initially with the aim of making single-transverse mode glass lasers in fibre form[19,20]. In particular, optical Nd^{3+} and Er^{3+}-doped fibre lasers emit both in the 2nd and 3rd window of telecommunications and are thus potentially attractive as optical sources for telecommunications applications. Further, rare-earth-ion doped fibres may be operated as superfluorescent sources[21], low-noise optical amplifiers[22] and sensors[23].

1.3.5 Fibres with Crystal-Like Properties

The interest in second-order nonlinear phenomena in fibres started in 1986 with the observation of efficient second-harmonic generation in ordinary telecommunications fibres[24]. Second-order nonlinear phenomena in glass are caused by defect centres giving rise to crystal-like properties[25]. This has renewed the interest in defect centres in glass and their exploitation. Although, this field is still in its infancy, interesting applications of such fibres as frequency converters[26] and electro-optic modulators[27] have already been demonstrated.

1.3.6 Other Special Fibres

Other fibre designs are sometimes also included under the heading of special fibres. In particular, one may mention dispersion-shifted or flattened fibres[28], fibres designed for transmitting either far infra-red[29] or ultra-violet light[30] and radiation hardened fibres[31]. I have not included these fibre designs here, since their main objective is still to passively transmit light with as little loss or dispersion as possible, which is also the objective of standard telecommunications fibres.

1.4 Optical Fibre System Integration

The eventual aim of developing special fibres lies in the integration of optical fibre technology. It is hoped that any bulk-optical parts of an optical fibre applications system may be replaced by fibre optic components. For example rare-earth-doped fibres may be used as optical light sources and amplifiers. Fibre polarisers and electro-optic modulators may replace bulk crystals. Bulk optical frequency converters may be substituted by fibres with crystal-like properties. The integration of optical fibre technology has made fast progress since 1985, because the development of rare-earth-doped fibres and fibres with crystal-like properties has been of major significance.

1.5 The Author's Contribution

The author has made significant contributions to both the development and characterisation of rare-earth-ion-doped fibres and fibres having crystal-like properties. Single-mode rare-earth-doped fibres were developed by Poole et al[19] in 1985 and have since become a major research topic in fibre optics. The author's research was initially aimed at testing the quality of these fibres.

Based on what may be called a zero-order characterisation of rare-earth-doped fibres, i.e. measurements of absorption and fluorescence spectra and fluorescence decay times, a distributed temperature sensor was developed[23,32]. The performance of this sensor is discussed in chapter 3.

Later a more sophisticated higher-order characterisation of fibre properties, i.e measurements of rare-earth-ion interactions, was carried out. This led eventually to the design of co-doped fibres for fibre laser applications. In particular, an efficient Er^{3+}-fibre laser operating around 1.55μm, in the third window of telecommunications, was demonstrated using an optical pumping scheme based on ion/ion interactions (energy-transfer) between Yb^{3+} and Er^{3+}[33]. This work is discussed in chapter 4.

Finally, the author has been involved in the characterisation of second-order nonlinear phenomena in optical fibres. The results of this work are presented in chapter 5 and form the major part of this thesis. A series of novel experiments were carried out in the course of this research, which led to the first explanation of why efficient second-harmonic generation in fibres is possible[34]. A large variety of specially-designed fibres were then used both to optimise the performance of optical fibre harmonic generators and to improve the understanding of this novel effect[26,35]. The work resulted in the development of a simple technique (optical fibre poling[25]) for the creation of large second-order nonlinearities in glass and enabled the first demonstration of the Pockels effect[27] in glasses.

References

1) H.H. Hopkins and N.S. Kapany: "A Flexible Fibrescope Using Static Scanning", Nature, **173**, 1954, pp. 54

2) K.C. Kao and G.A. Hockam: "Dielectric Fibre Surface Waveguides for Optical Frequencies", Proc. IEEE, **113**, 1966, pp. 1151-1158

3) G.D. Pitt et al: "Optical Fibre Sensors", IEE Proc., **132**, 1985, pp. 214-215

4) S.C. Rashleigh: "Origins and Control of Polarisation Effects in Single-Mode Fibres", J. Light. Tech., **LT-1**, 1983, pp. 312-331

5) C. Lin: "Nonlinear Optics in Fibres for Measurements", J. Light. Tech., **LT-4**, 1986, pp. 1103-1115

6) M. Gottlieb and G.B. Brandt: "Fibre-Optic Temperature Sensor Based on Internally Generated Thermal Radiation", Appl. Opt., **20**, 1981, pp. 3408-3415

7) J.P. Dakin and D.J. Pratt: "Fibre-Optic Distributed Temperature Measurement—a Comparative Study of Techniques", IEE Colloquium on Distributed Optical Fibre Sensors, London, 1986, paper 10

8) A.H. Hartog: "A Distributed Temperature Sensor Based on Liquid Core Optical Fibres", J. Light. Tech., **LT-1**, 1983, pp. 498-509

9) A.H. Hartog, A.P. Leach and M.P. Gold: "Distributed Temperature Sensing in Solid Core Fibres", Electron. Lett., **21**, 1985, pp. 1061-1062

10) D.N. Payne, A.J. Barlow and J.J. Ramskov Hansen: "Development of Low and High Birefringence Optical Fibres", IEEE J. Quantum Electronics, **QE-18**, 1982, pp. 477-488

11) L. Li, J.R. Qian and D.N. Payne: "Current Sensors Using Highly Birefringent Bow-Tie Fibres", Electron. Lett., **22**, 1986, pp. 1142-1144

12) C.D. Hussey and J.D. Minelly: "Optical Fibre Polishing with a Motor Driven Polishing Wheel", Electron. Lett., **24**, 1988, pp. 805-807

13) A.C. Boucouvalais, M.P. Greaves and N.S. Rayit: "Special Shaped Fibres for Distributed Sensors", IEE Colloquium on Distributed Temperature Sensors, London, 1983, paper 8

14) G. Schiffner, H. Schneider and G. Schoner: "Double-Core Single-Mode Optical Fibre as Directional Coupler", Appl. Phys., **13**, 1980, pp. 41-45

15) L. Li, G. Wylangowski, D.N. Payne and R.D. Birch: "Broadband Metal/Glass Single-Mode Fibre Polarisers", Electron. Lett., **22**, 1986, pp. 1020-1022

16) L. Li, R.D. Birch and D.N. Payne: "An all Fibre Electro-Optic Kerr Modulator", IEE Colloquium on Advanced Fibre Waveguide Devices, London, 1986

17) M.J.F Digonnet, C.J. Gaeta and H.J. Shaw: "1.064- and 1.32-μm Nd:YAG Single Crystal Fibre Lasers", J. Light. Tech., **LT-4**, 1986, pp. 454-460

18) T. Kaino, K. Jingui and S. Nara: "Low Loss Poly (Methylmethacrylate-d8) Core Optical Fibres", Appl. Phys. Lett., **42**, 1983, pp. 567-569

19) S.B. Poole, D.N. Payne and M.E. Fermann: "Fabrication of Low-Loss Optical Fibres Containing Rare-Earth Ions", Electron. Lett., **21**, 1985, pp. 737-738

20) L. Reekie, R.J. Mears, S.B. Poole and D.N. Payne: "Tunable Single Mode Fibre Lasers", J. Light. Tech., **LT-4**, 1986, pp. 956-960

21) M.J.F. Digonnet: "Theory of Superfluorescent Fibre Lasers", J. Light. Tech., **LT-4**, 1986, pp. 1631-1639

22) R.I. Laming, P.R. Morkel, D.N. Payne and L. Reekie: "Noise in Erbium-Doped Fibre Amplifiers", 14th European Conf. on Optical Communication, ECOC, Brighton, 1988

23) M.C. Farries, M.E. Fermann, R.I. Laming, S.B. Poole, D.N. Payne and A. Leach: "Distributed Temperature Sensor Using Nd^{3+}-Doped Optical Fibre", Electron. Lett., **22**, 1986, pp. 418-419

24) U. Österberg and W. Margulis: "Efficient Second-Harmonic Generation in an Optical Fibre", 14th Int. Quantum Electronics Conference, IQEC, San Fransisco, 1986, paper, WBB2

25) M.V. Bergot, M.C. Farries, M.E. Fermann, L. Li, L.J. Poyntz-Wright, P.St.J. Russell and A. Smithson: "Generation of Permanent Optically-Induced Second-Order Nonlinearities in Optical Fibres by Poling", Opt. Lett., **13**, 1988, pp. 592-594

26) M.E. Fermann, M.C. Farries, P.St.J. Russell and L.J. Poyntz-Wright: "Tunable-Holographic Second-Harmonic Generators in High-Birefringence Optical Fibres", Opt. Lett., **13**, 1988, pp. 282-284

27) L. Li: in preparation

28) M.Monerie: "Propagation in Doubly Clad Single-Mode Fibres", IEEE J. Quantum Electronics, **QE-18**, 1982, pp. 535-542

29) T. Miyashita and T. Manabe: "Infrared Optical Fibres", IEEE Trans. Microwave Theory Tech., 1982, **MTT-30**, pp. 1420-1427

30) U. Kubo and K. Okada: "OH Ion Doped UV Optical Fibre", Technical Paper of the Inst. of Electronics and Communications Engineers of Japan, **86**, 1986, pp. 93-97

31) K. Nagasawa, Y.Oshi and Y. Ohki: "Improvement of Radiation Resistance of Pure Silica Core Fibres by Hydrogen Treatment", Jap. J. Appl. Phys., **24**, 1985, pp. 1224-1228

32) M.C. Farries, M.E. Fermann, S.B. Poole and J.E. Townsend: "Distributed Temperature Sensor Using Holmium Doped Optical Fibre", IOOC/OFC, Reno, 1987, pp. 170

33) M.E. Fermann, D.C. Hanna, D.P. Shepherd, P.J. Sumi and J.E. Townsend: "Efficient Operation of an Yb Sensitised Er Fibre Laser at 1.56μm", Electron. Lett., **24**, 1988, pp.

34) M.C. Farries, P.St.J. Russell, M.E. Fermann and D.N. Payne: "Second-Harmonic Generation in an Optical Fibre by Self-Written $\chi^{(2)}$-Grating", Electron. Lett., **23**, 1987, pp. 322-324

35) M.E. Fermann, L. Li, M.C. Farries and D.N. Payne: "Frequency-Doubling by Modal Phase-Matching in Poled Optical Fibres", Electron. Lett., **24**, 1988, pp. 894-895

Chapter 2: Introduction to and Comments on Chapters 3-5

2.1 Summary of Chapter 3

The development and characterisation of a distributed temperature sensor in rare-earth-doped fibres is described. The sensor is based on the variation of the absorption of rare-earth-doped fibres with temperature. An optical time-domain reflectometry technique is employed to provide the read-out of temperature. Initially, the theory and the design of the sensor are discussed. The results obtained with an experimental sensor are then compared to other types of distributed sensor. It is shown that this sensor may compete with conventional distributed temperature sensors based on Raman scattering in optical fibres in low temperature, and high-spatial-resolution, applications.

2.2 Summary of Chapter 4

A detailed characterisation of energy-transfer in Yb^{3+}/Er^{3+}-doped fibres is presented and the development of an Yb^{3+}/Er^{3+}-fibre laser is described. In this, J.E. Townsend manufactured a range of Yb^{3+}/Er^{3+}-doped fibres following the author's specifications. A discussion of the Yb^{3+}/Er^{3+} system and the relevant ion/ion interactions leading to energy-transfer between the two dopant ions is given. The effects of donor excitation diffusion and back-transfer on transfer efficiency are analysed. These results lead to an explanation of acceptor saturation in fibre lasers and amplifiers. It is further shown, both experimentally and theoretically, that diode-laser-pumped Yb^{3+}/Er^{3+}-doped fibres are feasible at dopant ion concentrations of only 1-2%. By choosing an appropriate pump-wavelength for the excitation of Yb^{3+} it is possible to avoid excited-state absorption of the pump radiation in Er^{3+} and to obtain a high slope efficiency for Er^{3+} fibre lasers. Chapter 4 concludes with a comparison of Er^{3+} fibre lasers and Yb^{3+} sensitised Er^{3+} fibre lasers.

2.3 Summary of Chapter 5

A detailed investigation of second-harmonic generation and other second-order nonlinear phenomena in optical fibres is presented. Initially, a review of the present research in this area is given. In the main part of Chapter 5 the theory of nonlinear propagation in optical fibres is developed and applied to explain the main observations related to second-order nonlinear effects. In particular, second-harmonic generation, relevant phase-matching techniques and limiting mechanisms are discussed. Further, a discussion of the Pockels effect and optical rectification is given. Whenever available, relevant experiments are described to support the theories presented and to elucidate short-comings. The majority of the special fibres described in Chapter 5 have been manufactured to the author's or M.C. Farries' specifications by Dr. S.B. Poole and L.J. Poyntz-Wright. The majority of the experimental results described in section 5.10.2.1 on the formation of $\chi^{(2)}$-gratings from noise and by seeding were performed by M.C. Farries. In particular, the results presented in Fig. 5.4 and 5.10 were obtained by him and are included here for completeness. Further, the Pockels effect in glasses described in section 5.10.3.3 was first discovered by L. Li and the experimental results presented in that section were obtained in collaboration with him.

As in most major articles on nonlinear optics esu units have been adopted in the presentation of the theory. Experimental results are quoted in si units for convenience. A table converting esu to si units is presented in Appendix (5.I).

The definition of nonlinear coefficients follows the standards set out by Shen in his discussion of nonlinear optical phenomena[1]. Since a different definition has been adopted by Stolen and Tom[2] in their important paper describing the principal processes behind second-harmonic generation in optical fibres, a brief comparison of their definition and the definition of nonlinear coefficients as used in this thesis is presented in Appendix (5.II).

References

1) Y.R. Shen: "The Principles of Nonlinear Optics", 1984, John Wiley and Sons

2) R.H. Stolen and H.W.K. Tom: "Self-Organised Phase-Matched Second-Harmonic Generation in Optical Fibres", Opt. Lett., 12, 1987, pp. 585-587

CHAPTER 3: Distributed Temperature Sensing Using Rare-Earth-Doped Fibres

3.1 Introduction

During the last two years an increasing interest has been observed in special, rare-earth-doped fibres[1]. Lasing action in these fibres at several tunable wavelength regions with different dopants has already been demonstrated[2]. It is thought that the fibres may be developed into commercial devices, which may potentially be used as high-power tunable laser light sources for optical fibres at wavelengths ranging from 650nm to 2000nm. Applications in telecommunications, non-linear optics, and sensors are also possible.

To ensure a constant quality of these fibres the doping levels have to be predictable and the distribution of the dopants along the fibre should be constant. Since the absorption of these fibres is proportional to the doping level, a technique based on optical time domain reflectometry (OTDR), which measures the local attenuation in fibres, was developed to probe the homogeneity of the distribution of the dopants. Due to the temperature dependence of the absorption[3], this measurement technique was adopted to demonstrate a completely new type of distributed temperature sensor[4]. Subsequent optimisation of the design of this sensor has produced a device that is competitive with other types of distributed temperature sensor.

3.2 Review of Distributed Sensors

There are essentially three types of distributed sensor, which may be distinguished by the detection technique applied. The first type is based on OTDR, where the change of either the backscatter capture fraction[5], the Rayleigh[5], Brillouin or Raman scatter coefficients[6,7], or the absorption[4,8], fluorescence, or polarisation[9], is measured to provide information

about the temperature. The second type uses coherent detection techniques such as homodyne or heterodyne time-division multiplexing[10] and FMCW[11]. The third type is based on nonlinear interactions between counter propagating waves in fibres[12]. The coherent detection technique suffers from many complications. The sensor has to be made of a number of partially-reflecting splices or couplers, which are expensive to manufacture. The resolution and range of the system are limited by thermal instabilities and finite coherence time, or fly-back time, of the laser frequency. The nonlinear measurement technique is not feasible at the present state of the art, since high input powers, of the order of watts, are necessary to produce nonlinear effects which are only weakly dependent on temperature in silica-based fibres. However, the advent of single-mode fibre lasers has opened the possibility of having sufficient power in the fibre and with the production of fibre materials having lower nonlinear thresholds this technique may grow in importance.

The distributed sensors based on OTDR have been so far the only ones with potential practical applications and the most accurate are those relying on Raman scattering[6,7] in solid-core and Rayleigh scattering in liquid-core fibres[5]. However, the latter sensor is thought to be impractical outside the laboratory environment and suffers from stability problems of the liquid. Thus, the former sensor is preferred, despite the fact that the Raman scatter coefficient is about 30dB smaller than the Rayleigh scatter coefficient. The new OTDR sensor utilising the temperature dependence of the absorption in rare-earth-doped fibres combines the advantages of a large signal, comparable to that in the liquid-core sensor, with that of being able to use a solid fibre as in the Raman measurement technique.

3.3 Theory and Design of a Distributed Temperature Sensor Based on the Temperature Dependence of Absorption

Distributed temperature sensors based on the thermal variation of the absorption in special fibres utilise the ability of OTDR to measure local attenuation along the whole length of the fibre[13]. Either single-mode, or multi-mode, fibres may be used as the sensors. Multi-mode fibres may be preferred, since they offer higher source launching efficiency and better backscatter capture fraction. In addition coherence and polarisation noise are reduced. However, single-mode fibres are free of modal noise and may produce the best ultimate sensitivity.

The local attenuation coefficient as measured by OTDR may be written as

$$\alpha(x) = 0.5d[\ln P(x)]/dx, \qquad (3.1)$$

where $P(x)$ is the backscattered power returning to the launch end from a position x along the fibre. The accuracy to which temperature may be measured at a point x may be written as

$$T = 1/[K_t \Delta x (S/N)_x), \qquad (3.2)$$

where Δx is the sampling interval length, $(S/N)_x$ is the signal/noise ratio at the point x and $K_t = d\alpha/dT$ is the temperature sensitivity of the absorption. Using a multi-mode fibre as the sensor, the design of the measurement system will be similar to that of a liquid-core fibre system and has been discussed elsewhere[5]. Typically, the dominant noise mechanism for a 5m spatial resolution system is signal shot noise and a (S/N)-ratio >100 may be achieved on a single waveform. Assuming a signal averaging time of about 1 second and about n=10000 averages, the (S/N)-ratio may be improved to $(S/N)(n)^{1/2}>10000$.

For a two-way OTDR the local attenuation is given by

$$\alpha(x) = \frac{1}{4}\frac{d}{dx}\left(\frac{\ln P_1(x)}{\ln P_2(x)}\right), \qquad (3.3)$$

where $P_1(x), P_2(x)$ are the backscattered powers originating from a point x and arriving at the two launch ends of the fibre. Assuming the performance of the detection system is limited by signal shot noise, it may be shown that the temperature resolution is given by

$$\delta T(x) = \frac{\exp\left[\int_0^x \alpha(x)dx\right] + \exp\left[\int_0^L \alpha(x)dx\right]}{2K_t \Delta x (S/N)_0} \qquad (3.4)$$

where L is the length of the fibre, $(S/N)_0$ is the (S/N)-ratio at the launch ends of the fibre. Coherence, polarisation, and modal noise effects have been neglected. Assuming that the laser pulse width, sampling distance and impulse response of the amplifier are of similar magnitude, the spatial resolution of the system will be twice the sampling distance, since two points are needed for differentiation. To reduce effects of non-linear responses of the detector amplifier system, the two-way loss in the fibre should not exceed 20 dB, unless exact temperature resolution is not important and emphasis is put on hot-spot detection. In Fig. 3.1 the temperature resolution achievable for different values of $\gamma = K_t \Delta x (S/N)_0$ for a two-way OTDR is shown.

3.4 Experiment

The measurements carried out initially were limited to probing the distribution of dopants in rare-earth doped fibres by measuring the local attenuation in the fibre with an OTDR technique. A wavelength-tunable OTDR system involving a dye laser was applied to measurements at the edge of the absorption bands of the dopants. The spatial

resolution achievable was about 3.5m and a measurement wavelength was chosen at which the fibre loss was 50 dB/km, so that the absorption could be measured at 30 points in a 100m section of fibre. Due to the lack of an exact theory that can predict the thermal behaviour of rare-earth ions in a glass environment, the emphasis has to be put on acquiring empirical data to find dopants with a high temperature sensitivity. With the aid of a fibre attenuation measurement system the temperature dependence of the absorption of the doped fibres with wavelength was studied to identify the regions with the highest sensitivity. Due to the large change of attenuation, typically up to several $dBm^{-1}nm^{-1}$, that occurs when the wavelength is scanned through an absorption band a large dynamic range and a high wavelength resolution are required. Furthermore, temperature cycling of high wavelength resolution, attenuation measurements takes several hours, in which drifts in source power and fibre alignment may occur. These drifts may be monitored by relating the attenuation data to a reference wavelength outside the absorption bands, where the attenuation is independent of temperature. Subsequently, the temperature dependence of the absorption was measured with the OTDR system.

Neodymium and holmium were found to be the most interesting dopants and subsequently distributed temperature measurements were carried out on the wavelength tunable backscatter system. The practicability of such a DTS was demonstrated[4] with a diode laser emitting at 904nm as the source together with a fast signal acquisition system provided by Dr.A.H. Hartog. The laser was pulsed at a repetition rate of 4KHz with a pulse width of 40ns. The acquisition system consisted of a Si-APD detector followed by a 20 megasample/ multichannel A/D converter with a sample spacing of 5m and a resolution limited by the analogue bandwidth, of 7.5m. So far only a Nd-doped fibre has been measured with this system and satisfactory results have been achieved. The performance may be improved with a Ho-doped fibre,

since the absorption in Ho-doped fibres is more temperature sensitive than in Nd-doped fibres, as shown in sections (3.6) and (3.7).

3.5 Distribution of Dopants in Temperature Sensitive Fibres

The uniformity of the distribution of rare-earth dopants along the fibres was tested prior to the application of these fibres to DTS. A two-way OTDR technique was employed and the local absorption, as measured by this technique, is given by equation (3.3).

The measurements were made on the dye laser backscatter system at the wavelength λ=620nm at the edge of a Nd^{3+} absorption band. The results for a single-mode fibre are shown in Fig. 3.2, where the local attenuation variations of a Nd^{3+}-doped and an ordinary undoped single-mode fibre are compared. The absorption has mean values of about 48dB/km and 9dB/km in the Nd^{3+}-doped and undoped fibres. However, the apparent attenuation varies by ±8dB/km and ±4dB/km, respectively. These fluctuations are mainly due to variations in the backscatter factor and limit the measurement of true attenuation as explained in the following.

Fig. 3.3 shows the variations in local attenuation of the undoped fibre as derived from a two-way backscatter measurement by using (3.1). The two traces correspond to launching from each end of the fibre ends in turn. The apparent local attenuation varies by ±20dB/km, and a strong anticorrelation between the upper and lower traces is observed. The reproducibility of these fluctuations is indicated in Fig. 3.4, which shows the difference in apparent local attenuation of two independent measurements, using different lengths of optical delay line in front of the detector. The fluctuations may be related to small variations in the backscatter factor of the fibre in the following way. Assuming a length-

dependent backscatter factor $\eta(x)$, the apparent local attenuation may be written as

$$\alpha = \frac{d}{dx} \log[P(x)] + \frac{1}{\eta} \frac{d}{dx} \eta(x).$$

Thus when differentiating a backscatter trace, apparent loss modulations

$$\Delta\alpha = \frac{1}{\eta} \frac{d\eta}{dx} \approx \frac{1}{\eta} \frac{\Delta\eta}{\Delta x}$$

where $\Delta\eta$ is the difference in backscatter factor between two points separated by Δx, appear on top of the true attenuation α. Variations of α of 20dB/km over a length of 3m thus correspond to variations in η of only 1.5%. By using a two-way OTDR, the variations of η may be separated from variations of α, provided the two traces are processed exactly according to (3.3). In practice, the backscatter traces are obtained by sampling the voltage generated in a detector by signals arriving from the fibre at discrete times corresponding to discrete points along the fibre. For a two-way OTDR, the sampling points for the measurements from either end of the fibre have to be at the same position to ensure that the ratio $\ln[P_1(x)]/\ln[P_2(x)]$ in (3.3) is exact. However, the exact positioning of the sampling points is difficult in practice, since small variations occur in the time base of the digitising oscilloscope wich acquires the backscatter traces. Thus the variations of η may not be totally cancelled out on a true absorption curve and small fluctuations of the true absorption, as observed in Fig. 3.2, may occur. An indication that this is the case was found by changing the correlation of two OTDR data, i.e. by shifting one OTDR waveform by fractions of the sampling distance with respect to the other. It was found that the variations observed in the true absorption coefficient can be eliminated for short lengths of the total waveform.

In the case of a Nd^{3+}-doped multi-mode fibre, some true variations of the attenuation were found, as shown in Fig. 3.5. Here, no large variations in the backscatter factor could be observed and the variations are therefore assumed to be real. Thus the sensitivity of multi-mode fibres to temperature will vary according to the local doping level. However, it is possible to scale the sensitivity to the absorption to obtain a constant reading of temperature along the length of the fibre.

3.6 Distributed Temperature Sensing in a Nd^{3+}-Doped Fibre

The absorption of Nd^{3+}-doped fibres shows some temperature sensitivity due to the thermal population of the upper Stark levels of the ground state[14]. The exact fine structure of these levels is difficult to account for. However, in general the population of upper states increases with a rise in temperature, leading to a red-shift and a broadening of the absorption bands[3]. In addition, a change in oscillator strength with temperature causes a change in the peak absorption[14].

The measurements were performed with a multi-mode fibre having a 50μm core, and a 160μm outer, diameter doped with 5ppm Nd^{3+}. The doping level was tailored to produce an attenuation of 50dB/km at the sensing wavelength λ_s=904nm. The attenuation as a function of wavelength at room temperature, i.e. 22°C, is shown in Fig. 3.6. The absorption was found to be most sensitive to temperature at the edges of the absorption bands. In particular, a useful temperature sensitivity occurs at λ=904nm, a wavelength suitable for semiconductor lasers. The spatial variation of the attenuation at this wavelength is shown in Fig. 3.5. The distributed temperature sensitivity measurements were obtained by keeping the two ends of the fibre at a constant temperature of 22°C and changing the temperature in the middle section and are shown in Fig. 3.7.

From results obtained on a standard attenuation measurement system, the temperature dependence of the absorption may be written as

$$\alpha_{ND}(T_1-T_2) = \alpha(T_1)\left[1+0.0033\frac{\alpha(T_0)}{\alpha(T_1)}(T_2-T_1)\right], \qquad (3.6)$$

where the temperatures are given in Kelvin and $\alpha(T_0)$ is the absorption of the sensor fibre at T_0=77K. The relative temperature sensitivity of the absorption $S_t=(1/\alpha)d\alpha/dT$ is about S_t=0.002/°C at room temperature, or with an absorption of 50 dB/km, K_t=0.1dB/km. Using (3.2) and the signal/noise ratio (S/N)=10000 achieved on the backscatter trace it may be calculated that the temperature resolution is about 20°C. Lengths of about 10m at both ends of the fibre are not usable for temperature measurements due to saturation of the detector from front face reflections. However, these could be eliminated by using an acousto-optic modulator at the launch end of the fibre. The overall sensitivity of the fibre is not constant and varies with the doping level in the fibre. A higher doping level will increase the temperature resolution, but also shorten the useful fibre measurement length.

3.7 Distributed Temperature Sensing in a Ho^{3+}-Doped Fibre

As in the case of neodymium, the temperature dependence of the absorption in Ho^{3+}-doped fibres is due to satellite bands close to the ground state that become thermally populated at elevated temperatures[15]. The temperature sensitivity with holmium is one order of magnitude greater than for neodymium and is the highest for the rare-earths that have so far been investigated. The best doping levels, found by trial and error, for DTS-applications are in the range 100ppm to 500ppm, because the red and blue edges of the absorption bands exhibit a large temperature sensitivity and the

attenuation in these bands has to be at least 10dB/km for successful temperature probing by OTDR. The temperature sensitivity in the centre of the absorption bands was measured in a fibre with a low doping level and was found to be of similar magnitude to that in neodymium. Doping levels greater than 1000ppm have produced a non-uniform distribution of dopants and a large number of scattering centres in the fibre. However, it is assumed that the manufacturing process may be improved to allow a uniform dopant distribution even for such high doping levels.

For the measurements a fibre doped with 300ppm Ho^{3+} was fabricated. The attenuation of the fibre as a function of wavelength at temperatures of -196°C and 200°C is shown in Fig. 3.8. Large differences in the fibre attenuation are visible at 555nm, 670nm, and 910nm. Measurements of the temperature dependence of the attenuation have been carried out between 679nm and 690nm. The temperature sensitivity was $d\alpha/dT=0.3dB/^{o}C$ for all these wavelengths. At $\lambda=683nm$ the attenuation was measured on a 200m length of multi-mode fibre, where the first 70m was kept at -196°C, the next 5m at room temperature, and a 35m length was in an oven, the temperature of which was set successively as -60, -10, 40 and 90°C. The remainder of the fibre was held again at -196°C. The results are shown in Fig. 3.9. The change in absorption in the parts of the fibre kept at different temperatures is clearly visible, despite the relatively low (S/N)-ratio of less than 1000 obtained for the backscatter measurements. Also, a very good uniformity of the absorption in the regions of constant temperature is observable. From the distributed temperature measurements, the temperature dependence of the absorption may be written approximately as

$$\alpha(T_2-T_1) = \alpha(T_1)\left[1+0.033\frac{\alpha(T_0)}{\alpha(T_1)}(T_2-T_1)\right], \qquad (3.6)$$

where the same notation as in (3.5) is used. The absolute temperature sensitivity is 0.4dB/°C, and accordingly the relative temperature sensitivity varies between 3.3% at T=77K and 0.4% at T=293K. Thus a significant improvement in temperature sensitive absorption is achieved in Ho^{3+}-doped fibres as compared to Nd^{3+}-doped fibres, especially for temperatures below 300K.

3.8 Discussion

The magnitude of the absorption temperature sensitivities in the rare-earth doped fibres investigated may be explained by a very simple model. The ground, and excited, states are approximated by single levels, in which the thermal populations follow Boltzmann statistics. The effects of varying oscillator strength and thermal broadening of the absorption bands are neglected and it is assumed that the absorption is proportional to the population of the excited states. Then the absolute temperature sensitivity may be written as

$$K_t = (\alpha_0 h\nu_0 / kT^2) \exp[-h\nu_0 / (kT - kT_0)], \qquad (3.7)$$

where α_0 is the absorption at $T_0 = h\nu_0/k$, h is Planck`s constant, k is Boltzmann`s constant, and ν_0 is the transition frequency from the ground, to the excited, state. The relative temperature sensitivity may be written in terms of the half transition temperature $T_h = T_0/2$ at which the absolute sensitivity is maximum, as

$$S_t = 2T_h / T^2. \qquad (3.8)$$

Thus, the relative absorption temperature sensitivity always decreases with increasing temperature. For a sensor requiring a relative sensitivity at T=300K better than 1%, it must hold $T_0 > 900K$, which is equivalent to $\nu_0 > 625cm^{-1}$. A Eu^{3+}-doped fibre will be a possible candidate for sensitive temperature measurements at T=300K due to the bandgap between the ground, and first

excited, state[3], of ν_0=500cm^{-1}. However, very high doping levels are required to get any significant thermally-excited absorption for bandgaps of that order at room temperature.

The real temperature sensitivity of the absorption observed in Nd^{3+}- and Ho^{3+}-doped fibres is more linear than expected from (3.5) and (3.6), which shows an increase in oscillator strength with temperature.

If a DTS based on attenuation is to achieve the same temperature and spatial resolution as a DTS based on Raman scattering, the respective (S/N)-ratios observed on the signal, i.e. $(S/N)_A$ and $(S/N)_R$, must be related as

$$S_{Ta}\Delta x\alpha(S/N)_A = S_{Tr}(S/N)_R, \qquad (3.9)$$

where $S_{Ta;Tr}$ are the relative temperature sensitivities of the absorption and Raman scattering, Δx is the sampling interval for the attenuation based sensor, which is half the interval length of the Raman-scattering-based sensor, and α is the fibre attenuation. In table (3.1) the design specifications of the Nd^{3+}- and Ho^{3+}-based sensors presented in this work, and of a Raman-scattering-based sensor described by Hartog et al[7] designed to give a 5m spatial resolution are shown. In table (3.2) the requirements on the (S/N)-ratio to obtain a 1K temperature resolution at the launch end of the fibre are given, where detector design considerations similar to those for a liquid-core fibre system[5] are assumed. It is seen that the Ho^{3+}-doped fibre shows a better sensing performance only for temperatures below ≈100K. The reason is the rapid reduction in relative attenuation sensitivity with temperature for the Ho^{3+}-doped fibre and the mainly signal shot noise limitation on the performance of the detector, which leads to an increase in (S/N)-ratio proportional to $S^{1/2}$. Thus an advantage of 36dB at 0°C in scattered light power turns out to be only an advantage of 18dB in (S/N)-ratio for the attenuation-based system. However, for shorter

resolutions, the (S/N)-ratio will be increasingly limited by the amplifier noise and the (S/N)-ratio advantage of the holmium based sensor will improve.

Thus, a distributed temperature sensor based on the temperature dependence of absorption produces an improvement in performance over Raman scattering systems when high spatial resolution or operation at low temperatures is required.

Materials that have a higher relative absorption temperature sensitivity than Ho^{3+} at room temperature will produce a competitive DTS even for this temperature region. However, the increase in sensitivity will always pose a problem, since a hot zone in the middle of the fibre will lead to great signal losses and the signal from the far end will be much reduced.

3.9 DTS Based on Fluorescence and the Variation of Capture Fraction in Highly-Birefringent-Fibres

Fluorescence in doped fibres[16] and birefringence in high-birefringence-fibres[17] have been shown to have some temperature dependence and the possibility of applying these effects to DTS will now be analysed.

The fluorescence intensity from the dopant in an optical fibre is proportional to the quantum efficiency of the fluorescence η, the absorption of the dopant α, and is inversely proportional to the decay constant τ. The efficiency is proportional to[18]

$$\eta = K_f/(K_f+K_d),$$

where K_f is the probability of a fluorescent transition and K_d is the probability of non-radiative decay. The decay time is proportional to $1/(K_f+K_d)$. K_f may be expected to have a small temperature dependence, whereas K_d is strongly temperature dependent. Since the fluorescence intensity is proportional to $\eta/\tau=K_f$, only a

small dependence of fluorescence on temperature is expected[18].

In a backscatter measurement the fluorescence signal arriving at the front end of the fibre is

$$Fl(t`) = \text{const.} \int_{-T/2}^{+T/2} \int_{0}^{v_g(t'-t)/2} (\eta\alpha_p/\tau)(x) \exp\{-[\bar{\alpha}_p+\bar{\alpha}_f]x-[(t`-t)-2x/v_g]/\tau\}dxdt, \quad (3.10)$$

where T is the input pulse length, and α_p, α_f are the mean attenuations at the pump, and fluorescence, wavelengths up to the point x, i.e.

$$\bar{\alpha}_{p,f} = (1/x)\int_{0}^{x} \alpha_{p,f}(x)dx. \quad (3.11)$$

For α_p=20dB/Km, α_f=3dB/Km, τ=450μs, which is the fluorescence decay time typical for a Nd-doped fibres, $\alpha_p+\alpha_f >> 2/v_g\tau$. Assuming an input pulse with intensity $I(T)=\delta(T-0)$, we may write

$$\frac{d[Fl(t)]}{dt} = \left[\frac{\eta\alpha_p}{\tau}\right](t)\frac{v_g}{2}\exp[-(\bar{\alpha}_p+\bar{\alpha}_f)t]. \quad (3.12)$$

Thus, the rate of change of the fluorescence signal as it evolves in the fibre may provide the basis for a DTS provided $\eta\alpha_p/\tau$ shows some temperature dependence. However, in a Nd-doped fibre $\eta\alpha_p/\tau$ is only weakly temperature dependent, since the increase of α_p with temperature almost matches the decrease of η/τ with temperature. For short decay times comparable to the input pulse length, we may write

$$Fl(t) = \eta\alpha_p(t)(v_g/2)\exp[-(\bar{\alpha}_p+\bar{\alpha}_f)t]. \quad (3.13)$$

Thus the fluorescence intensity is independent of τ and a strong temperature dependence of the fluorescence intensity is expected. At the moment, Nd^{3+} is the one

practical doping element with the shortest fluorescence decay time giving a spatial resolution of 45km. Transition metal dopants provide decay times of down to 1μs which is equivalent to 100m resolution. However, the fluorescence efficiency of these materials is too low, and the absorption too high. Plastic fibres doped with organic dyes may exhibit decay times of less than 1nsec.. However, the absorption of the plastic matrix, e.g. polymethylmethacrylate, is still very high, about 150dB/Km, but some improvement may be possible in the future and the fluorescence DTS technique may become an alternative to Raman and attenuation DTS.

DTS may also be demonstrated in single-polarization-mode, stress-guiding fibres[19]. The light guidance in these fibres is based on anisotropic stress in the x- and y-directions of the optical fibre, which is chosen in such a way that the index difference between core and cladding along the x-direction is increased and decreased along the y-direction via the elastooptic effect. It may be shown[19] that the equivalent NA as seen by the x-polarized light is then given by

$$NA = (2n_{cl}\Delta n_x)^{1/2},$$

where n_{cl} is the cladding refractive index and n_x is the index difference between core and cladding seen by the x-polarised light. The maximum NA produced by this technique so far reported is NA=0.059 with a temperature sensitivity of Δnx of 0.1%/^{o}C. This corresponds to a 0.1%/^{o}C temperature sensitivity of the backscatter capture fraction at V=2.0. Thus distributed temperature sensing in single-polarization fibres is about five times more sensitive than the change in backscatter capture fraction in normal fibres[5].

3.10 Conclusions

The distribution of rare-earth dopants in fibres manufactured by a new production method has been measured by a backscatter technique and a good uniformity in the distribution found, except for doping levels larger than 1000ppm in a Ho^{3+}-doped fibre. Subsequently, an approximately linear dependence of absorption on temperature in Nd^{3+}-doped fibres was discovered at the edge of the absorption bands. This effect was then used to demonstrate a new type of DTS based on backscatter. The practicability of the sensor was shown by employing a semiconductor laser as the light source. The sensitivity of the DTS was enhanced by incorporating a Ho^{3+}-doped fibre as the sensor. The performance of the attenuation sensor was compared to a Raman scattering sensor and it was found that the former is superior for low temperatures and high spatial resolutions. The requirements on a doping material for further improvement in the sensitivity of this new DTS-technique were then analysed. Finally, two new alternative methods for DTS are described and the sensitivity of these sensors calculated. More research is needed to exploit fully the potential of the latter sensing techniques. In addition, more rare-earth doping materials have to be investigated with a view to developing an attenuation sensor with high absorption temperature sensitivity at room temperature.

References

1) S.B. Poole, D.N. Payne and M.E. Fermann: "Fabrication of Low-Loss Optical Fibres Containing Rare-Earth Ions", Electron. Lett., **21**, 1985, pp. 737-738

2) L. Reekie, R.J. Mears,S.B. Poole and D.N.Payne: "Tunable Single Mode Fibre Lasers", J. Light. Tech., **LT-4**, 1986, pp. 956-960

3) E. Snitzer, W.M. Morey and W.H. Glenn: "Fibre-Optic Rare-Earth Temperature Sensors", Proc. 1st Int. Conf. Opt. Fibre Sensors, OFS, London, 1983, pp.15-18

4) M.C. Farries, M.E. Fermann, R.I. Laming, S.B. Poole, D.N. Payne and A. Leach: "Distributed Temperature Sensor Using Nd^{3+}-Doped Optical Fibre", Electron. Lett., **22**, 1986, pp. 418-419

5) A.H.Hartog: "A Distributed Temperature Sensor Based on Liquid-Core Optical Fibres", J. Light. Tech., **LT-1**, 1984, pp. 498-509

6) J.P. Dakin and D.J. Pratt: "Temperature Distribution Measurement Using Raman Ratio Thermometry", Proc. SPIE 29th Annual Technical Symposium, San Diego, 1985, Vol. 566, pp. 249-256

7) A.H. Hartog, A.P. Leach and M.P. Gold: "Distributed Temperature Sensing in Solid-Core Fibres", Electron. Lett., **21**, 1985, pp. 1061-1062

8) E. Theocharous: "Differential Absorption Distributed Thermometer", Proc. 1st Int. Conf. Opt. Fibre Sensors, OFS, London, 1983, pp.10-12

9) A.J. Rogers: "Polarisation-Optical Time Domain Reflectometry: A Technique for the Measurement of Field Distributions", Appl. Opt., **20**, 1981, pp. 1060-1074

10) J.P. Dakin, C.A. Wade, and M.L. Hemming: "Novel Optical Fibre Hydrophone Array Using a Single Laser Source and Detector", Electron. Lett., **20**, 1984, pp. 53-54

11) D. Uttam, I.P. Giles, B. Culshaw, and D.E.N. Davies: "Coherent Optical-Fibre Sensors with Modulated Laser Sources", Proc. 1st Int. Conf. Opt. Fibre Sensors, OFS, London, 1983, pp.182-184

12) A.J. Rogers and M.C. Farries: "Distributed Sensing Using Stimulated Raman Interaction in a Mono-Mode Optical Fibre", Proc. 2nd Int. Conf. Opt. Fibre Sensors, OFS, Stuttgart, 1984, pp.121-132

13) A.H. Hartog and M.P. Gold: "On the Theory of Backscattering in Single-Mode Optical Fibres", J. Light. Tech., **LT-2**, 1984, pp. 76-82

14) N.B. Rachkovskaya and Przhevuskii: "Effect of Temperature on the Spectral-Luminescence Characteristics of Laser Neodymium Glass", Zhurnal Prikladnoi Spektroskopii, **36**, 1982, pp. 126-133

15) S.J. Collocott and K.N.R. Taylor: "Magneto-Optical Properties of Praesodymium- and Holmium- Doped Soda Glass", J. Phys. C: Solid State Phys., **12**, 1979, pp. 1767-1775

16) S.B. Poole, D.N. Payne, R.J. Mears, M.E. Fermann and R.I. Laming: "Fabrication and Characterisation of Low-Loss Optical Fibres Containing Rare-Earth Ions", J. Light. Tech., **LT-4**, 1986, pp. 870-876

17) A. Ourmazd, M.P. Varnham, R.D. Birch and D.N. Payne: "Thermal Properties of Highly Birefringent Optical Fibres and Preforms", Appl. Opt., **22**, 1983, pp. 2374-2379

18) F.A. Kroeger et al: "The Influence of Temperature Quenching on the Decay of Fluorescence", Physica, 1948, **14**, pp.81-96

19) M.P. Varnham: "A Study of Highly-Birefringent Optical Fibres", PhD-Thesis, Southampton Univ., 1984, pp. 84-117

	Nd,Ho	Raman	units
Power launched	0.35	0.35	W
Pulse length	25	50	ns
Wavelength	904	904	nm
Absorption	20	3	dB/km
Scatter loss	1.3	0.0013	dB/km
Backscatter factor	450	0.14	W/J
NA	0.3	0.3	-
Responsivity	0.7	0.7	A/W
Excess noise factor	0.3	0.3	-

Table 3.1)

Design parameters of distributed temperature sensors based on i) the temperature dependence of absorption in Nd^{3+} and Ho^{3+} doped fibres and ii) Raman scattering.

(S/N) for 1°C T-Resolution			T	Signal-Ratio	(S/N)-Ratio	Advantage Ho over Ra.
Nd	Ho	Ram.	°C	Ho/Ram.	Ho/Ram.	dB
44	34	34	-196	43	24	24
45	38	21	-150	43	23	6
45	40	19	-100	41	21	0
46	42	19	- 50	38	19	-4
46	43	20	0	36	18	-5
47	43	21	20	35	17	-5
47	44	21	50	34	16	-7
47	44	22	100	33	16	-6

Table 3.2)

Comparison of DTS based on the temperature dependence of absorption in Nd^{3+} and Ho^{3+} doped fibres with DTS based on Raman scattering. Column 4 is the temperature of operation. Columns 1-3 are the (S/N)-ratios (in dB) required on the backscatter traces to obtain a temperature readout accurate to within 1°C for a Nd, Ho, and Raman-DTS. Column 5 is the advantage in backscattered power (in dB) arriving at the detector of a Ho-DTS over a Raman DTS. Column 6 is the advantage in (S/N)-ratio observed in the output of the detector of a Ho-DTS over a Raman-DTS. Column 7 is the difference:

[column 6-{column 3-column 2}],

which is the summed advantage of a Ho-DTS over a Raman-DTS.

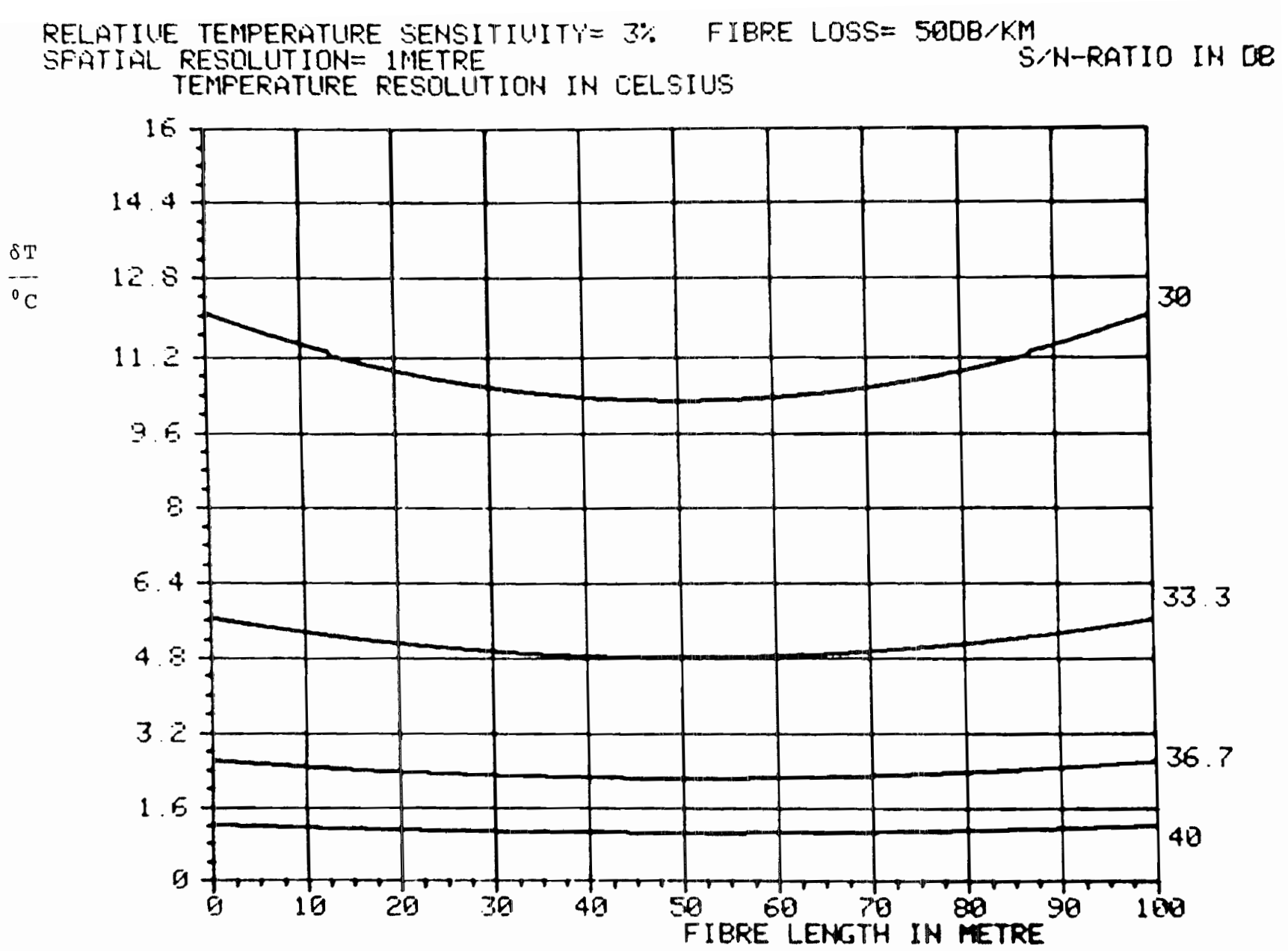

Figure 3.1 δT=Temperature resolution of attenuation based DTS. with different (S/N)-ratios for a 1m spatial resolution system.

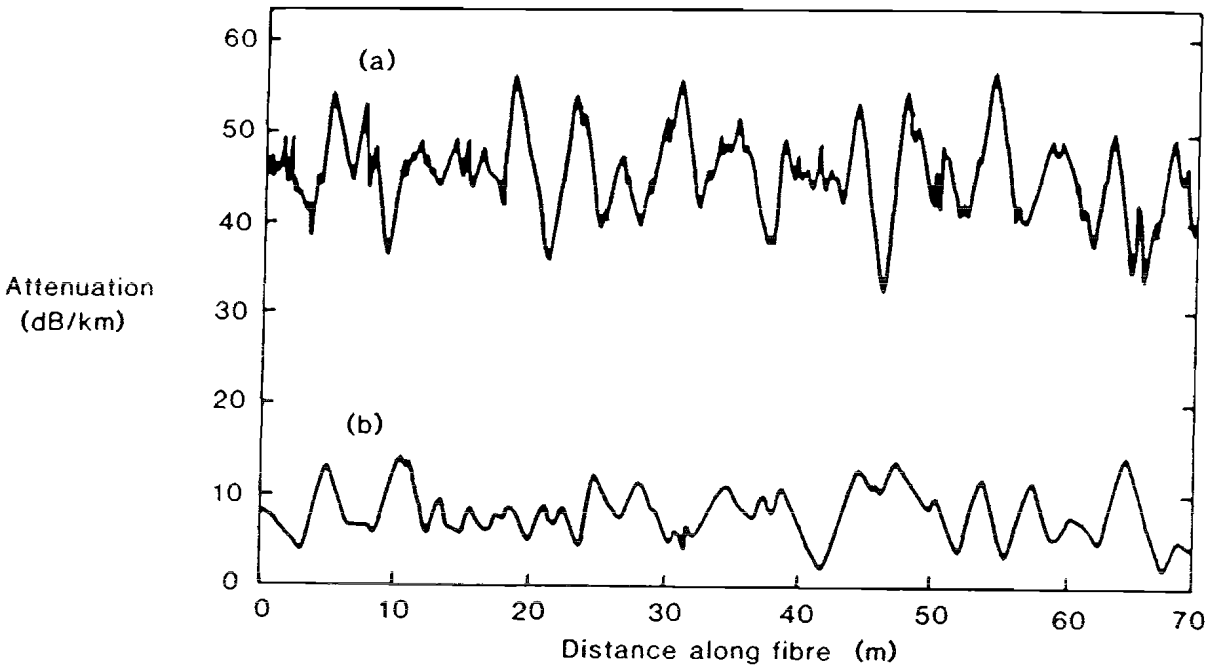

Figure 3.2 The uniformity of the attenuation of a) Nd^{3+}-doped, and b) undoped, fibres as measured by a two way OTDR technique at 620nm.

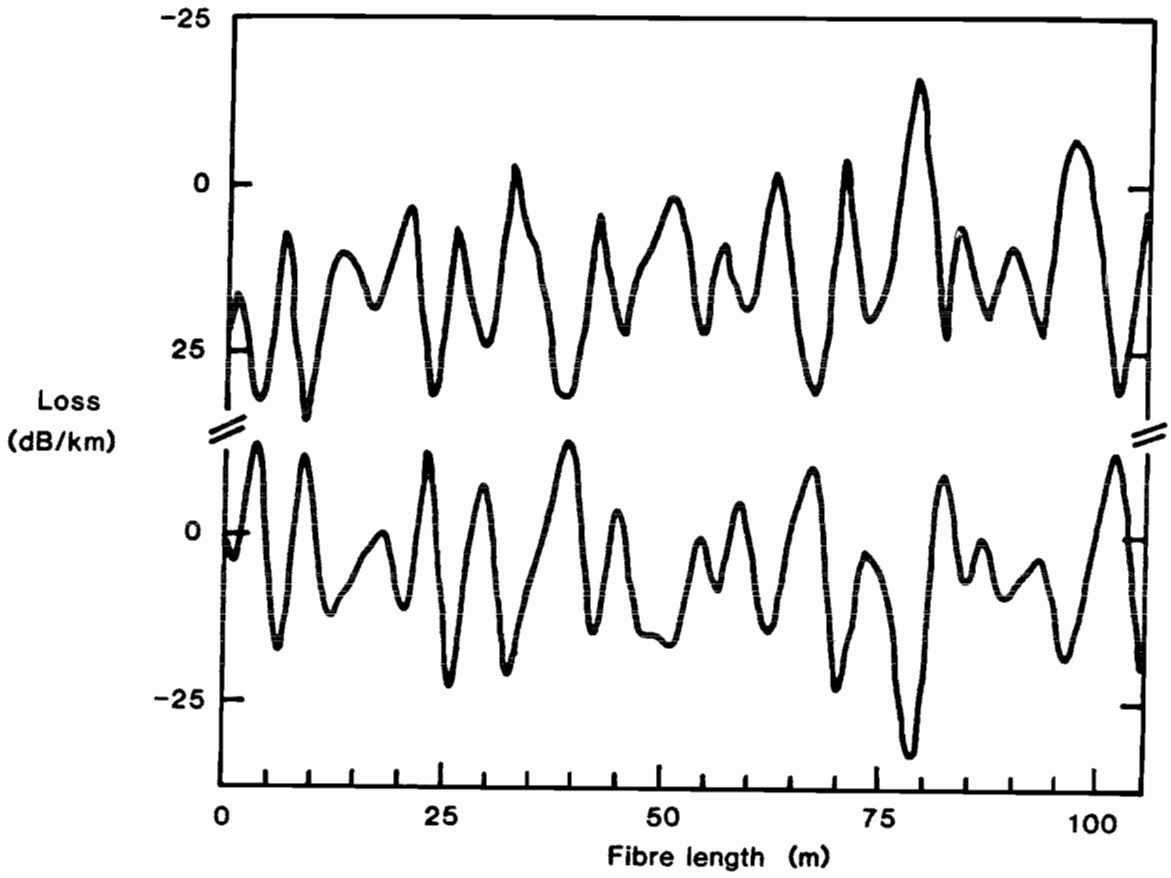

Figure 3.3 The anticorrelation of local attenuation plots obtained from backscatter measurements from each end of a single-mode fibre

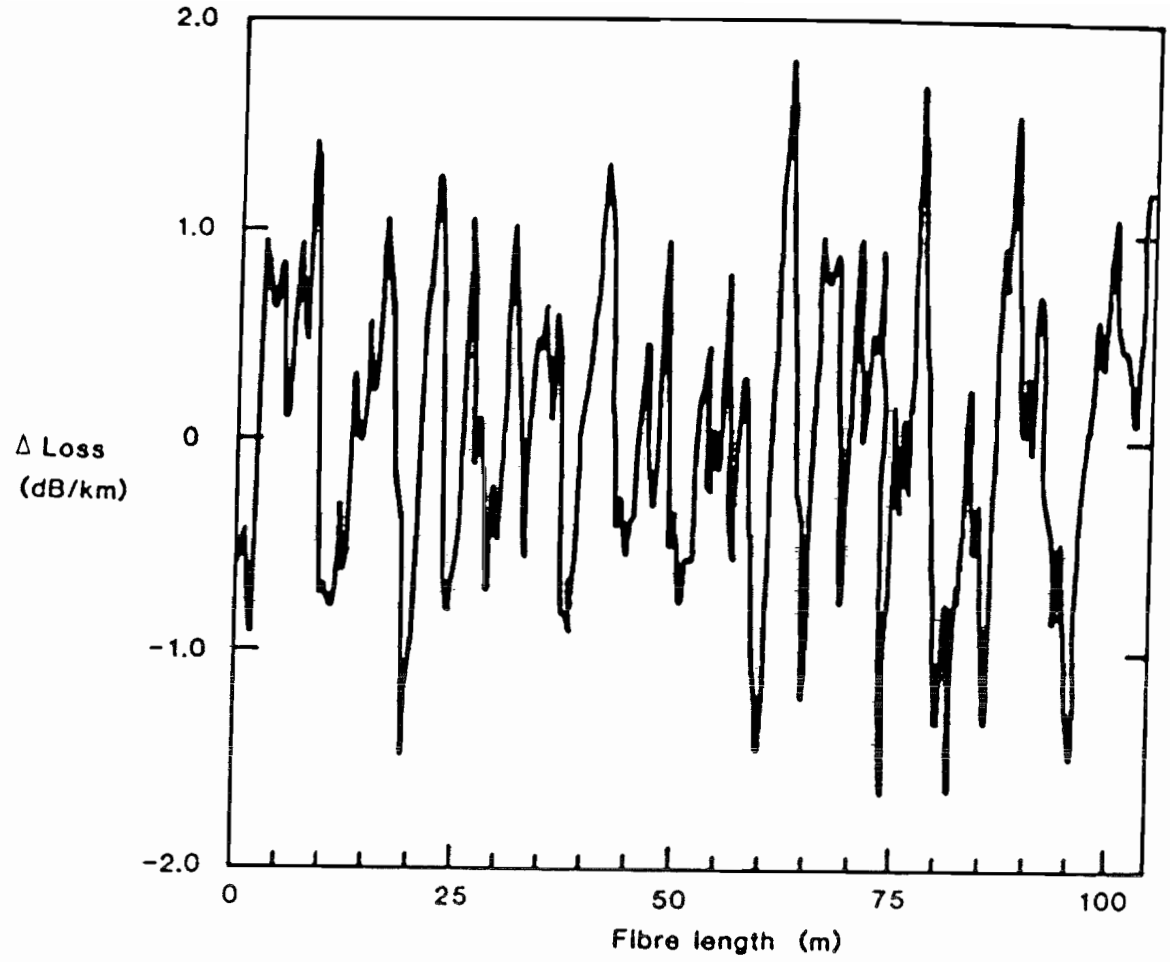

Figure 3.4 Reproducability of the variation in local attenuation. Loss is the difference in local attenuation of two independent measurements.

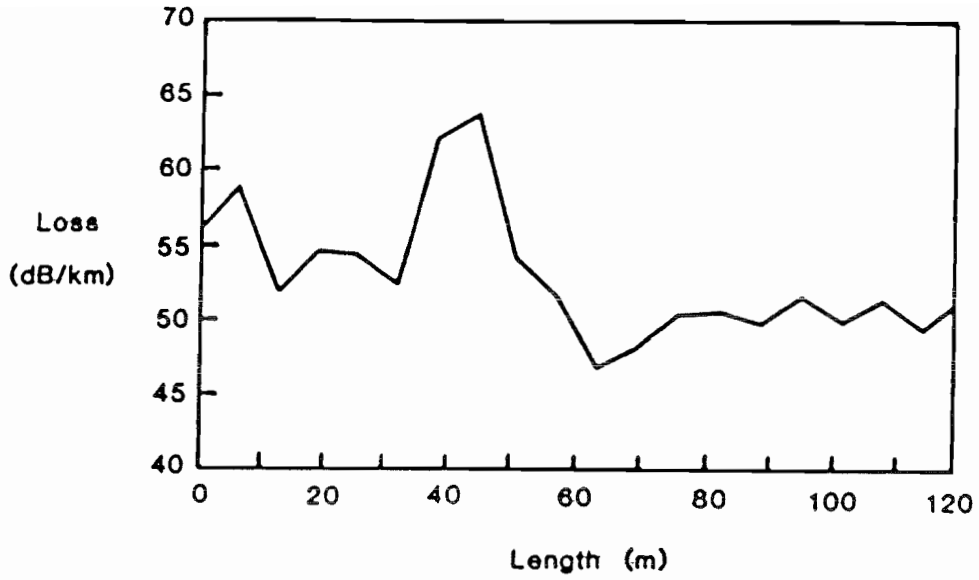

Figure 3.5 Variation in attenuation of a multi-mode fibre doped with 5ppm Nd^{3+} and measured at 904nm.

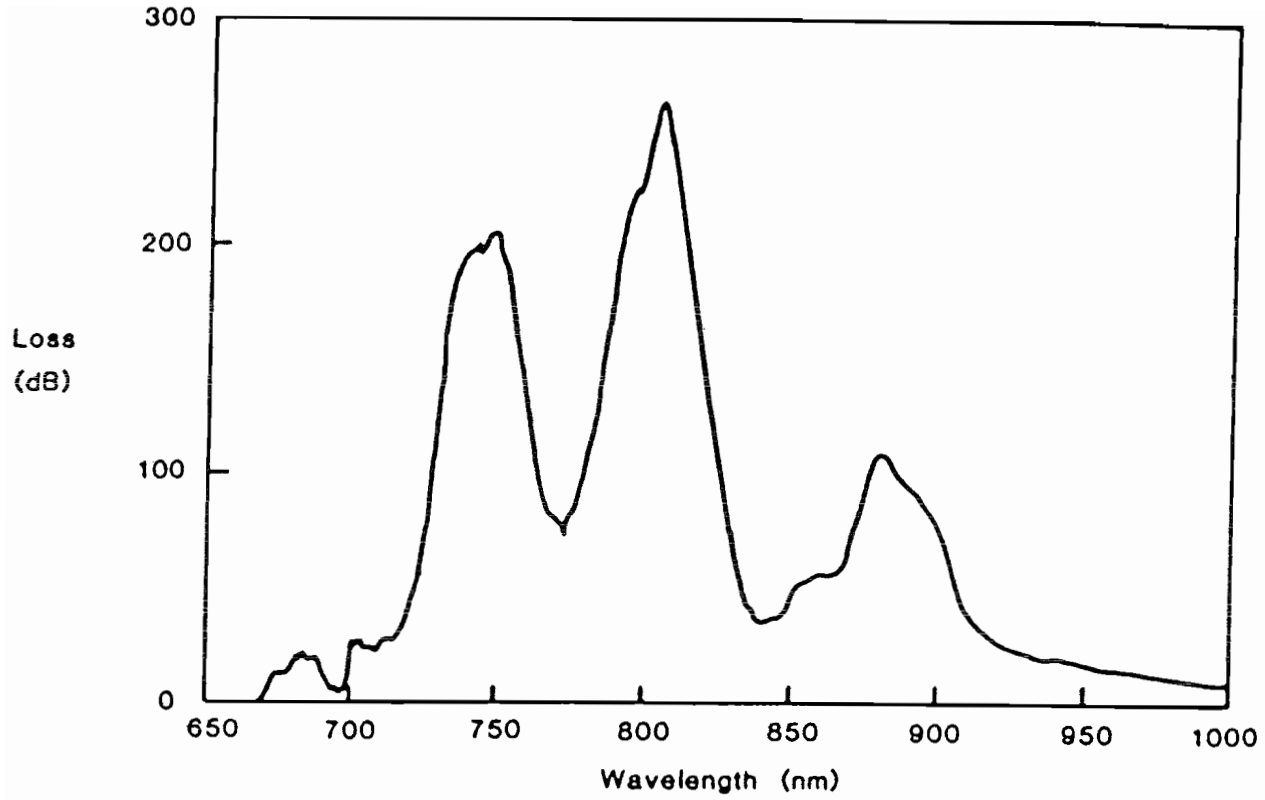

Figure 3.6 Spectral attenuation measured at room temperature for a multi-mode fibre doped with 5ppm Nd^{3+}.

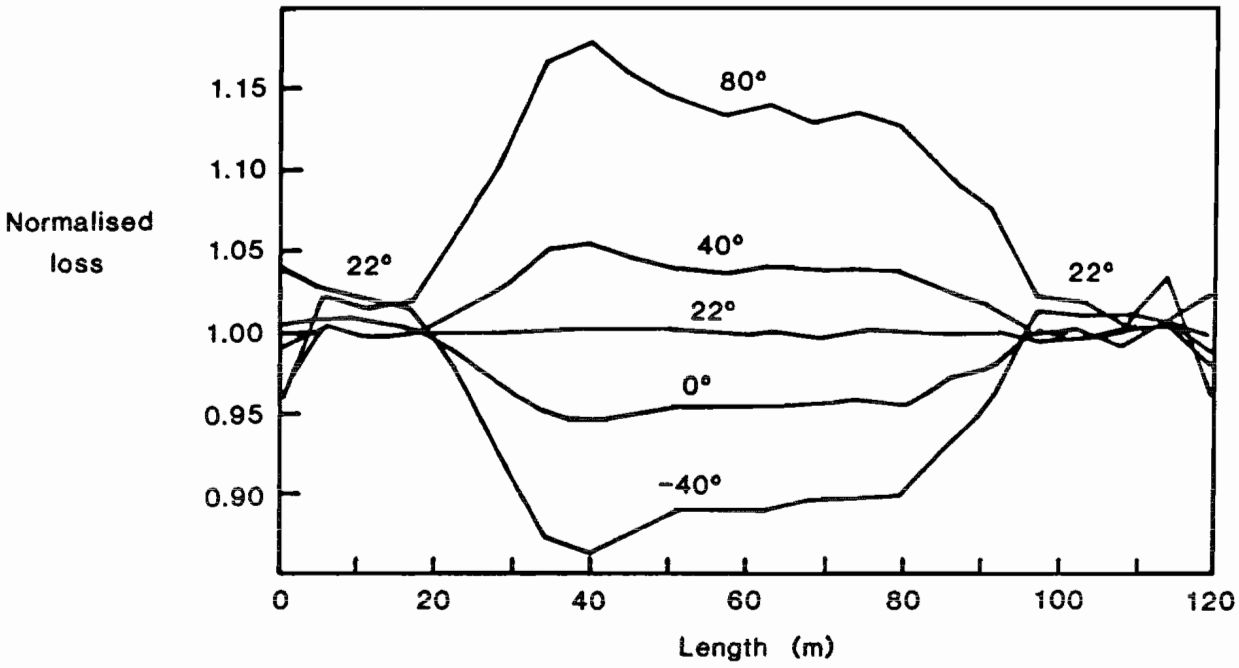

Figure 3.7 Temperature dependence of the absorption in a Nd^{3+}-doped fibre measured at 904nm. The normalised loss is defined as:

Normalised loss=absorption at $T=22^{0}C$/absorption at T

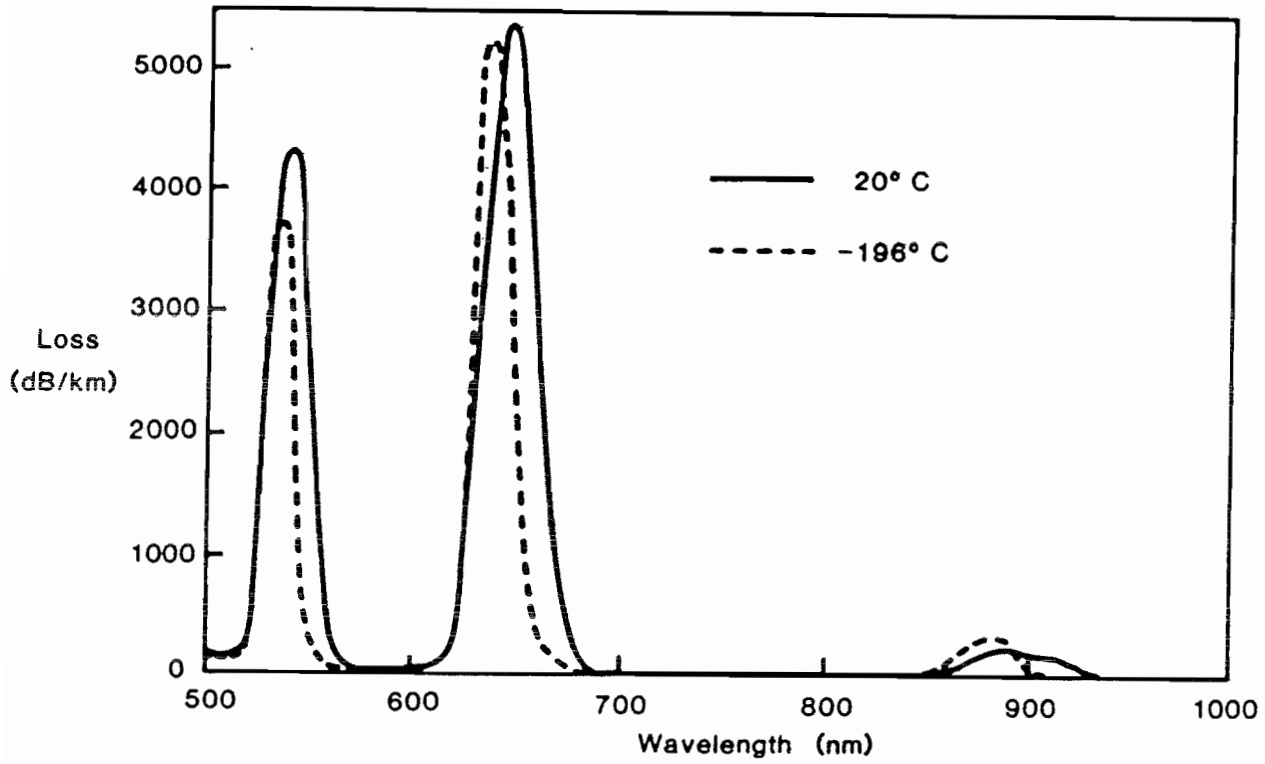

Figure 3.8 Spectral attenuation measured at $T=20^{0}C$ and at $T=-196^{0}C$ of a fibre doped with 300ppm Ho^{3+}.

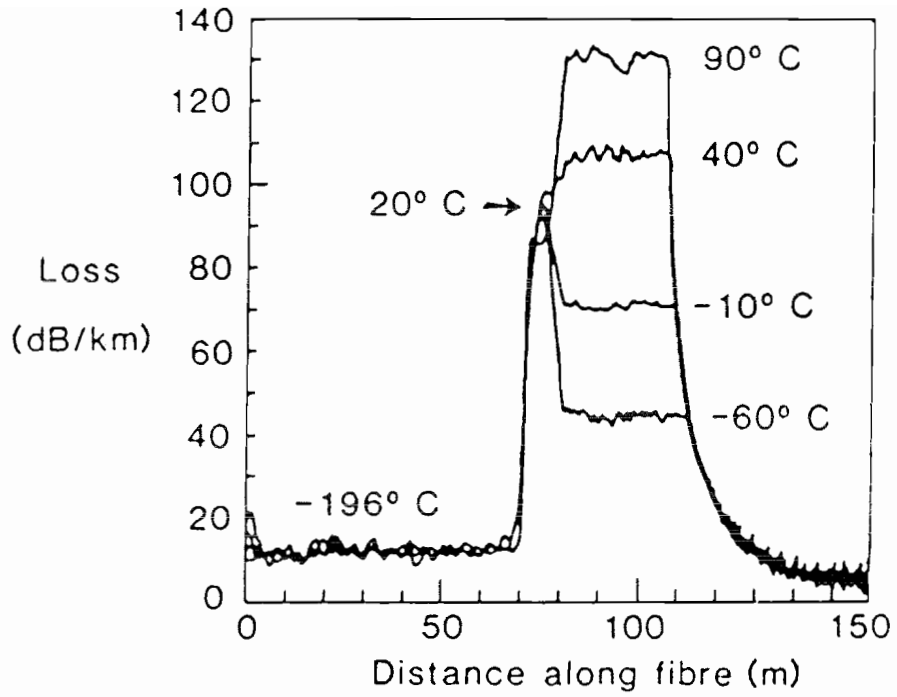

Figure 3.9 Temperature dependence of the absorption in a Ho^{3+}-doped fibre measured at 679nm.

CHAPTER 4: Energy-Transfer in Yb^{3+}/Er^{3+}-Doped Optical Fibres

4.1. Introduction

The development of rare-earth-doped fibres[1] has generated many differing applications including optical fibre lasers[2], amplifiers[3] and sensors[4]. Whilst in most of these applications ion/ion interactions were ignored due to the low doping levels used (<1%), improved fabrication techniques have led to fibres with ion doping levels as high as 3% and still higher doping levels appear to be possible[5]. At these higher levels ion/ion interactions may no longer be ignored, since they are the cause for easily observable effects including fluorescence quenching[6,7], excitation diffusion and energy-transfer[8,9]. Energy-transfer is of great interest, since it may further improve the versatility of rare-earth-doped fibres by extending the range of pump wavelengths available for fibre lasers and amplifiers. In particular, co-doping an Er^{3+}-doped glass with Yb^{3+} is well known as a sensitising technique in bulk glass lasers[9-13] and other combinations involving two or more ions have also been proposed[14].

The measurement techniques required to characterise energy transfer in fibres are therefore discussed. The emphasis here is put on the relevance of measurements using a pulsed excitation of the dopant ions to cw excitation as encountered when optically pumping fibre lasers and amplifiers. In particular, the fall-off of energy-transfer efficiencies with acceptor excitation is discussed under the conditions of slow and fast donor diffusion. Further, it is shown that back-transfer measurements may be used to account for donor diffusion in Yb^{3+}/Er^{3+} systems.

A set of Yb^{3+}/Er^{3+}-doped germano- and alumino-silicate fibres is manufactured and characterised according to the measurement criteria developed here. The potential of these fibres as optical amplifiers is investigated by measurements of gain as a function of wavelength.

Finally, YAG and semiconductor laser pumped Yb^{3+}/Er^{3+} fibre lasers are demonstrated and their performance discussed. It is concluded that for the relatively low doping levels used in fibres acceptor excitation is predominantly governed by slow donor diffusion, whereas in more heavily doped bulk Yb^{3+}/Er^{3+} phosphate glasses acceptor excitation is governed by fast donor diffusion. Both bulk and fibre laser systems, however, lead to the same energy-transfer efficiency at lasing threshold, namely 20%. Further, it is shown that co-doping with Yb^{3+} offers the opportunity to avoid excited state absorption in Er^{3+} and so results in very efficient Yb^{3+}/Er^{3+} lasers.

4.2. The Yb^{3+}/Er^{3+}-System

The major energy-levels of the Yb^{3+}/Er^{3+}-system are displayed in Fig. 4.1. Yb^{3+} efficiently absorbs pump light (800-1070nm) by excitation to the $^2F_{5/2}$-level, which is subsequently depopulated by spontaneous decay to the Yb^{3+} ground state along with energy-transfer to the $^4I_{11/2}$-level in Er^{3+}. The Yb^{3+} ground state consists of several Stark-splitted components, which are thermally populated. The $^4I_{11/2}$-level in Er^{3+} relaxes non-radiatively to the $^4I_{13/2}$-level from where fluorescence to the ground state, centred at 1536nm, is observed. Fluorescence from the $^4I_{11/2}$-level to the ground state is efficiently quenched by multi-phonon relaxations and therefore the $^4I_{13/2}$-level is the only meta-stable state in Er^{3+}-doped silica glasses. The decay-times from the $^4I_{13/2}$-level and the $^4I_{11/2}$-level typically differ by 4-5

orders of magnitude. Thus the population of the $^4I_{11/2}$-level may be neglected when considering the rate-equations for the Yb^{3+}/Er^{3+}-system. As in Yb^{3+} the Er^{3+}-ground state is Stark-splitted and consists of a total of 7 components[13]. The stimulated emission cross sections to the upper levels of the ground state are typically between 10 to 15 times smaller than to the bottom levels. Therefore, for bulk laser glasses lasing operation to the upper ground state levels (here referred to as quasi-four-level operation QFLO) has been generally considered to be too inefficient and not been attempted. However, it has been shown in erbium fibre lasers[15] that in high finesse cavities the lasing threshold for the QFLO is lower than for three-level operation (TLO) at 1536nm, since significantly less than 50% of the erbium atoms have to be excited to achieve population inversion for the QFLO of an erbium laser.

4.3. Theory of Energy-Transfer

4.3.1 Physical Mechanisms

Energy-transfer is caused by interactions between dopant ions in a host material. In this, the excitation of one ion is transferred non-radiatively to the other. The process is schematically represented in Fig. 4.2. The first ion, the donor ion, is excited from the ground state A to the excited state B, from where the ion decays radiatively or non-radiatively back to A. As a competing process transitions to the excited acceptor state 2 also occur. State 2 then decays down to 1 and in general there also is a probability for back-transitions to B. Commonly, one distinguishes two types of interaction causing energy-transfer. These are exchange and static

electromagnetic multipole interactions. Several authors[16-19] have written extensive review articles about a quantum-mechanical treatment of these interactions and this will not be discussed here. Exchange interactions are of very short range and are significant only at high dopant concentrations. At low dopant concentrations as encountered in optical fibres, the longer range electromagnetic multipole interactions are dominant. Magnetic and electric multipole interactions of the same order are indistinguishable, since they have the same radial dependence. As electric dipole interactions are stronger in general[13], only these will be considered here. The theory of electric dipole interactions was first treated by Foerster[20] and later by Dexter[21], who have given the probability of energy-transfer as a function of the overlap integral of the absorption spectrum of the acceptor and the fluorescence spectrum of the donor. The influence of phonons was first treated by Miyakawa and Dexter[22], who concluded that phonons lead to an increase in the fluorescence/absorption spectrum overlap integral, thus increasing the transfer efficiency.

The dependence of the energy-transfer rate on donor/acceptor separation R for electric multipole interactions may be written as

$$W_s(r) = \frac{a_6}{R^6} + \frac{a_8}{R^8} + \frac{a_{10}}{R^{10}} + \ldots \qquad (4.1)$$

where a_6, a_8, a_{10} are constants referring to the strength of the respective dipole/dipole, dipole/quadrupole and quadrupole/quadrupole interactions. When one of the interactions is dominant, it is convenient to write the energy-transfer rate as

$$W_s = \frac{1}{\tau_0}\left(\frac{r_0}{r}\right)^s \qquad (4.2)$$

where τ_0 is the intrinsic decay time of the donor, r_0 is the donor/acceptor separation at which the probability of intrinsic donor decay equals the probability of energy-transfer and s=6,8,10 depending on the order of the electric multipole interaction.

4.3.2 Measurement of Energy-Transfer Efficiencies and Rates

4.3.2.1 Fluorescence Decay Times

Fluorescence decay times and energy-transfer efficiencies are commonly measured using a pulsed excitation of the fluorescing medium, whereas fibre lasers operate predominantly cw. It is therefore necessary to elucidate the relevance of pulsed measurements to average cw-rates in the lasing system. At low rare-earth doping levels (<=1%) these discussions are simplified due to the absence of significant excitation diffusion between the dopant ions in the glass host[13,23]. Therefore we neglect diffusion in the following treatment.

Consider an ensemble of dopant ions excited by a flash of light to their respective metastable levels. The decaying population of that level as a function of time is then given by a measurement of the fluorescence $\Phi(t)$ as a function of time. Due to inhomogeneous broadening of the absorption bands in glass $\Phi(t)$ may be obtained from an average over the site-related decay rates

$$\Phi(t) = \int_0^\infty \rho(W)\exp(-Wt)dW, \qquad (4.3)$$

where $\rho(W)$ is the density of ions, normalised to one, with an intrinsic decay rate W. $\Phi(t)$ is thus the Laplace transform of $\rho(W)$. $\rho(W)$ may then be calculated from the inverse Laplace transform of $\Phi(t)$

$$\Phi(t) = L(\rho(W)) \qquad (4.4a)$$

$$\rho(W) = L^{-1}(\Phi(t)) \qquad (4.4b)$$

The proper average decay time under cw-pumping conditions may then be obtained from

$$<\tau> = \int_0^\infty \tau\rho(\tau)d\tau, \qquad (4.5)$$

where $\rho(\tau) = \rho(1/W)$. The average decay rate is given by the inverse of $<\tau>$

$$<W> = 1/<\tau>. \qquad (4.6)$$

It is generally difficult to directly calculate $\rho(\tau)$ for a given function $\Phi(t)$. Therefore, it is useful to approximate $\rho(\tau)$ by

$$\rho(\tau) = \sum_{i=1}^{N} a_i\delta(\tau-\tau_i), \qquad (4.7)$$

where $\delta(\tau-\tau_i)$ is the δ-function and N, a_i, τ_i are obtained by substituting (4.7) into (4.5) and optimising the fit of the resulting function $\Phi(t)$ to a real measurement of fluorescence as a function of time.

Substituting (4.7) into (4.3), and comparing the result to (4.5), we derive

$$\langle\tau\rangle = \int_0^\infty \Phi(t)dt, \qquad (4.8)$$

which is the sought after expression showing the connection between pulsed and cw measurements.

4.3.2.2 Energy-Transfer Efficiencies and Rates

When measuring energy-transfer efficiencies and rates between two different kinds of dopant ions, differences between cw rates and rates obtained from pulsed excitation must also be observed. Energy-transfer leads to a reduction of the donor decay time via the additional path of donor decay given by the acceptors. By comparing the donor fluorescence decay after pulsed excitation of a material doped with donors only and with both donors and acceptors, the transfer efficiency may be obtained from the integral over the fluorescence decay as[17]

$$\eta_T = 1 - \frac{\int_0^\infty \Phi(t)dt}{\int_0^\infty \Phi_0(t)dt}. \qquad (4.9)$$

Here $\Phi_0(t)$ is the fluorescence signal due to the intrinsic decay of the donor and $\Phi(t)$ is the fluorescence signal due to the donor decay in the presence of acceptors. The cw transfer efficiency is given by[16]

$$\eta_{cw} = \frac{\langle W_s \rangle}{\langle W_s \rangle + \langle W_D \rangle}, \qquad (4.10)$$

where $\langle W_s \rangle$, $\langle W_D \rangle$ are the ensemble averages of the energy-transfer rate and intrinsic donor decay rate. Since $\langle W_s \rangle$ and $\langle W_D \rangle$ may be written as

$$\langle W_{DA} \rangle = \langle W_s \rangle + \langle W_D \rangle, \qquad (4.11)$$

where $\langle W_{DA} \rangle$ is the ensemble average of the donor decay rate in the presence of both donor and acceptors. $\langle W_D \rangle$ and $\langle W_{DA} \rangle$ may be obtained from measurements of $\Phi(t)$ and $\Phi_0(t)$ and using (4.8). Grant[24] has shown that for linear systems, i.e. when the fluorescence intensity is a linear function of pump intensity, (4.9) and (4.10) are equivalent. However, for high pump powers and a resulting high excitation of the donor/acceptor system, a two-ion system behaves non-linearly due to excitation saturation and a generalisation of (4.9) and (4.10) is required.

Consider the rate equation of a two-level donor system at high excitation with energy-transfer

$$R_{ab}(N-2N_b) = N_b \langle W_{DA}(g) \rangle, \qquad (4.12)$$

where R_{ab} is the pump rate, N is the total number of donor ions, N_b is the number of excited donor ions and $\langle W_{DA}(g) \rangle$ is the ensemble average of the donor decay rate when a fraction g of all acceptors is in the ground state. $\langle W_{DA}(g) \rangle$ is an effective donor decay rate including deexcitation of the donor ions via effects like intrinsic donor decay, forward and back-transfer of energy. Assuming that $\langle W_{DA}(g) \rangle$ is a slow function of R_{ab}, we may linearise the response of N_b as a function of R_{ab} for pump powers $R_{ab} + dR_{ab}$, where $dR_{ab} \ll R_{ab}$. $\langle W_{DA}(g) \rangle$ is then obtained from equation (4.12) as

$$\langle W_{DA}(g)\rangle = (N-2N_b)(dR_{ab}/dN_b) - 2R_{ab}, \qquad (4.13)$$

dR_{ab}/dN_b may be obtained from a measurement of donor fluorescence $\Phi(t,g)$ as a function of time and acceptor excitation as follows. Consider a steady-state pump R_{ab} generating N_b excited donor ions. A small flash excitation on top of the steady-state pump then produces a time varying excitation of the donor ions as

$$N_b(t) = N_b + \Delta N_{b0}\Phi(t,g), \qquad (4.14)$$

where ΔN_{b0} is the initial excitation of the donor atoms due to the pump flash at t=0. ΔN_{b0} is proportional to the flash intensity for small flash powers. Therefore, following Grant[24], we may write for the change in population dN_b induced by a small change of cw pump power from R_{ab} to $R_{ab}+dR_{ab}$

$$dN_b = (N-2N_b)dR_{ab}\int_0^\infty \Phi(t,g)dt. \qquad (4.15)$$

By comparing equations (4.13) and (4.15), we obtain the ensemble averaged donor decay rate as a function of acceptor excitation as

$$\langle W_{DA}\rangle = \frac{1}{\int_0^\infty \Phi(t,g)dt} - 2R_{ab}, \qquad (4.16)$$

The energy-transfer rate and efficiency as a function of acceptor excitation may then be calculated by inserting (4.16) into equations (4.9)-(4.11). Thus $\langle W_{DA}(g)\rangle$ may be measured by a two laser technique. Here, a cw laser is required for the excitation of the acceptor atoms and a pulsed laser is required to read out the transfer

efficiency corresponding to the acceptor excitation. From a physical point of view (4.16) is almost obvious, since it is stated that the cw pump rate has to be subtracted from the measured donor decay rate in order to obtain the intrinsic donor decay rate. Nevertheless is (4.16) very important, since it allows us to make assumptions about the energy-transfer rate under strong pumping conditions using an essentially weak signal approximation.

4.3.3 The Donor Fluorescence Signal

In the limit that the dopant ions occupy a number of sites in the dopant host which is small compared to the total number of available dopant sites, we may assume that the ion sites are Poisson distributed. The probability of finding acceptor ions at a radius r around a donor ion in a shell of thickness dr is then given by

$$\rho(r) = n_A 4\pi r^2 dr, \qquad (4.17)$$

where n_A is the acceptor ion concentration. The probability of not finding any donor ions within a volume of radius R around an acceptor ion is similarly given by

$$P(r) = \exp\{-n_D(4\pi/3)r^3\}, \qquad (4.18)$$

where n_D is the donor concentration. When all acceptor ions are in the ground state, the donor fluorescence signal after pulsed excitation may be obtained from an average over all acceptor states available to each donor.

4.3.3.1 Slow Donor Diffusion

For glass hosts with a low doping level of Yb^{3+}/Er^{3+}, i.e. donor doping levels<1%, we may neglect the effect of back-transfer of energy from the donor to acceptor and donor diffusion[13]. Assuming that a multipole interaction of order s is the dominant energy-transfer causing mechanism, the donor fluorescence signal may then be written as[25]

$$\Phi(t) = \Phi_0(t) \lim_{\substack{R_V \to \infty \\ N \to \infty}} \left((4\pi/V) \int_0^{R_V} \exp[-tW_s(r)] r^2 dr \right)^N, \quad (4.19)$$

where r is the donor/acceptor separation, $W_s(r)$ is defined in equation (4.2), N is the number of acceptor ions in a volume of radius R_V and $\Phi_0(t)$ is the intrinsic fluorescence decay of the donor, which may be obtained from a measurement of donor fluorescence by doping the host material with donors only. For clarity we give the derivation of (4.19) in Appendix (4.I). When a fraction f=1-g of all acceptor ions is excited to a metastable state, the acceptor ions closest to the donor ions are excited first and quit the energy transfer process[11]. Thus instead of a uniform excitation of acceptor ions, we have a spatially ordered excitation of acceptor ions. Since the transfer rate is very strongly dependent on r, the spatially ordered excitation of acceptor ions may be approximated by assuming that all acceptor ions that see a donor ion within a radius r_{min} are excited. r_{min} may be obtained from equation (4.18) as

$$g = \exp\{-n_D(4\pi/3)r_{min}^3\}. \qquad (4.20)$$

Thus, when a fraction f of all acceptor ions are excited, the fluorescence signal due to pulsed excitation of the donor may be approximated by (see Appendix 4.II)

$$\Phi(t) = \Phi_0(t)\lim_{R_V,N\to\infty}\left(\frac{4\pi}{V^*}\int_{r_{min}}^{R_V}\exp[-t\rho(r)]r^2dr\right)^N, \qquad (4.21)$$

where

$$V^* = (4\pi/3)(R_V^3-r_{min}^3)$$

and N is now the number of acceptor ions in the ground state. As shown in Appendix 4.II, equation (4.21) may be evaluated as

$$\Phi(t)=\Phi_0(t)*\exp\left(\frac{-n_A}{n_{A0}}g\left([\Gamma(1-\tfrac{3}{s})-\Gamma(1-\tfrac{3}{s},z)]\frac{t^{3/s}}{\tau_0}-\ln(g)(1-e^{-z})\right)\right) \qquad (4.22)$$

where

$$z=\frac{t}{\tau_0}\left(\frac{-n_D}{n_{A0}\ln(g)}\right)^{s/3}$$

and $\Gamma(x)$, $\Gamma(x,z)$ are the complete and incomplete gamma functions, n_{A0} is the critical acceptor concentration at which the energy-transfer rate equals the intrinsic decay rate of the donor, n_D is the donor concentration and s=6,8,10 depending on the order of the dominant electric multipole interaction. For g=1, i.e. all acceptor ions are in the ground state, equation (4.22) reduces to

$$\Phi(t) = \Phi_0(t)*\exp\{-(n_A/n_{A0})\Gamma(1-3/s)(t/\tau_0)^{3/s}\}, \quad (4.23)$$

which is a result derived first by Inokuti and Hirayama[25]. By fitting equation (4.23) to an actual measurement of donor fluorescence decay (for an unexcited acceptor) we may determine the parameters s, and hence the electric multipole order of the dominant donor/acceptor interaction, and n_A/n_{A0}. Equation (4.22) is basically the donor fluorescence response to pulsed excitation for a given spatial configuration of acceptor excitation. Therefore, as explained in section 4.3.2, the cw-transfer efficiency and mean cw-transfer rate for this acceptor excitation may be obtained by inserting equation (4.22) into equations (4.9)-(4.11). Hence the transfer efficiency and rate may now be calculated as a function of acceptor excitation, which is necessary for the understanding of gain measurements as presented in section 4.6.6.

By using equations (4.9)-(4.11) and (4.22) we may analyse the effect of ion concentrations and dopant interactions on energy-transfer. The absolute value of the energy-transfer efficiency as a function of ion concentration does not come out of the previous model and may be deduced from more general theories[24,26] or from experiment. However, the relative dependence of energy-transfer on acceptor ion excitation may now be studied for different values of $\eta_T(g=1)$.

In Fig. 4.3 the dependence of η_T on the relative excitation of the acceptor ions is plotted for different ion/ion interactions. The results are displayed for a transfer efficiency $\eta_T(g=1)$ of 28%, which is typically obtained in silica fibres doped with 2000ppm Yb^{3+} and 500ppm Er^{3+}. It may be seen that the transfer efficiency rapidly decreases with acceptor ion excitation, where the

decrease is faster for the shorter range interactions. When plotting the transfer rate as a function of acceptor ion excitation as displayed in Fig. 4.4, a similar observation is made. For higher donor/acceptor doping level ratios and higher transfer efficiencies it may be evaluated from (4.22) that the transfer rate is linearly proportional to the number of acceptor ions in the ground state. However, donor excitation diffusion may then no longer be ignored and we have to use the approximation outlined in the next section.

4.3.3.2 Fast Donor Diffusion

At high donor doping levels and high donor/acceptor concentration ratios the rate of donor decay becomes dominated by donor excitation diffusion. Resonant energy transfer between the donor ions then leads to fast migration of the donor excitation between the donor ions until a donor in the vicinity of an acceptor is reached, to which the energy may be transferred directly. We then have a virtually spatially uniform donor excitation distribution, which means that all donors are equivalent in terms of their ability to transfer energy to an acceptor. Assuming that due to the high donor/acceptor concentration ratio acceptor diffusion is negligible, the rate of donor deexcitation is then limited by both the transfer rate between next neighbour donor/acceptor pairs and the acceptor decay rate. The decay of the donor fluorescence then assumes a simple exponential form (apart from a small deviation due to inhomogeneous broadening). The limit of fast donor diffusion usually applies for doping levels>3%[23].

Appreciable excitation of the acceptors then clearly implies that the acceptors closest to a donor get excited first. From (4.20) we obtain the minimum possible

donor/acceptor separation r_{min} at a given fraction of acceptor ions in the ground state as

$$g = \exp\left[-n_D \frac{4\pi}{3}(r_{min}^3 - d^3)\right], \qquad (4.24)$$

where we have included a minimum possible donor/acceptor distance in the host lattice, since at these high doping levels the finite volumes of the dopants may no longer be ignored. Assuming that for any amount of acceptor excitation, energy transfer is predominantly due to the unexcited acceptor ions closest to a donor, we obtain that at zero acceptor excitation the transfer rate is given by

$$W_{max} = \frac{1}{\tau_0}\left(\frac{r_0}{d}\right)^s \qquad (4.25)$$

and at appreciable acceptor excitation we have

$$W_s = \frac{1}{\tau_0}\left(\frac{r_0}{r_{min}}\right)^s. \qquad (4.26)$$

Inserting (4.24) into (4.26) and using (4.25) we finally obtain for the variation of the transfer rate as a function of acceptors in the ground state

$$W_s = W_{max}\left[1 - \frac{n_{cr}}{n_D}\ln(g)\right]^{-s/3}, \qquad (4.27)$$

where we have defined a critical donor concentration $n_{cr}=3/(4\pi d^3)$. Using the value of d=0.45nm for the minimum possible donor/acceptor separation in silicate glasses doped with Yb^{3+} and Er^{3+} as estimated by Alekseev et al[11,13], we obtain $n_{cr}= 2.6\times10^{21}$ions/cm^3, which

corresponds to an Yb^{3+} doping level of 12 mole%. Equation (4.27) explains why at very high doping levels the transfer rate decreases rapidly as soon as any acceptor ions get excited[11-13]. It may also be seen that in order to reduce the effect of acceptor saturation it is desirable to occupy all available dopant sites in the host lattice, such that the donor/acceptor separation becomes as small as possible, i.e. only limited by the dopant volume.

The decrease of the relative energy transfer efficiency and rate as a function of acceptor excitation is plotted in Figures (4.5) and (4.6), where a donor doping level of $10^{21}cm^{-3}$ (=4.5%) was assumed. We thus see that the effect of acceptor saturation is more severe than at low doping levels, where we neglected donor diffusion. At these high doping levels, further transfer-limiting mechanisms also exist. These were discussed by Gapontsev et al[11] and include back-transfer, excited state absorption, cumulative energy transfer and quenching in the acceptor.

At intermediate donor doping levels ($1\%<n_D<3\%$), donor diffusion and energy-transfer have comparable rates. The donor fluorescence signal due to pulsed excitation at zero acceptor excitation under these conditions has been given by Yokota and Tanimoto[27]. However, no estimate of acceptor saturation has been obtained yet. In general, we may expect a behaviour of the acceptors within the two limits discussed in this and the previous section.

4.3.3.3 Back-Transfer

The probability of back-transfer from Er^{3+} to Yb^{3+} is much smaller than forward transfer, since the life-time of the $^4I_{11/2}$-level in Er^{3+} ($\tau<3\mu$sec) is about three orders of magnitude smaller than for the corresponding $^2F_{5/2}$-level in Yb^{3+} ($\tau=750\mu$sec). Therefore Er^{3+} ions may only transfer energy to those Yb^{3+} ions in their ultimate vicinity. The transfer rate to Yb^{3+} ions further away from the Er^{3+} ions is so slow, such that all Er^{3+} ions relax down to the metastable state before any energy may be transferred to these distant Yb^{3+} ions. At low Yb^{3+} doping levels and slow Yb^{3+} excitation diffusion, back transfer may thus be used for selective excitation of Yb^{3+} ions in the glass host. This may be achieved by pumping the Er^{3+} ions up to the $^4I_{9/2}$ or higher levels. Back-transfer then leads to an excitation of the Yb^{3+} ions with next neighbour Er^{3+} ions. Once the Yb^{3+} ions are excited, forward energy transfer then leads to a fast transfer of energy back to the Er^{3+} ions. However, some Yb^{3+} ions also relax down to the ground state at a rate W_{DA}, which is given approximately by

$$W_{DA} = W_D + W_s(r\approx d),$$

where $W_s(r\approx d)$ stands for the energy transfer rate between next neighbour donor/acceptor pairs. A measurement of the decay rate of the Yb^{3+} ions by back transfer thus provides the opportunity to measure the maximum possible energy transfer rate that would be observable in a glass host saturated with dopant ions. In fact using this technique, the decay rate of Yb^{3+} ions excited by back transfer was measured as $W_s(r\approx d)=3.3\times10^4 s^{-1}$ in germanosilicate fibres with Yb^{3+} doping levels ranging from 0.03 to 2 mole% (see section 4.6.4). The magnitude of $W_s(r\approx d)$ is about twice as high as obtained by direct

excitation of very heavily doped Yb^{3+}/Er^{3+} bulk laser glasses (Yb^{3+} doping levels are typically about 6 mole%), indicating that even in bulk laser glasses a saturation of the glass host with dopant ions has not been achieved. The fact that $W_s(r \approx d)$ is constant over a large range of Yb^{3+} dopant concentrations, also indicates that at least for doping levels up to 1%, the assumption of slow donor excitation diffusion is approximately valid. If the donor doping levels are increased further, the onset of significant donor excitation diffusion eventually leads to the donor ions being indistinguishable, i.e. donor ions excited directly or by back-transfer then decay at the same rate. In the presence of donor excitation diffusion, the decay rate of donor ions excited by back-transfer is in fact slower than in the absence of donor diffusion, since the donor ions excited via energy-transfer from acceptor ions may then transfer energy to other donor ions without close acceptor ions leading to a longer equilibrium donor decay rate (see section 4.6.4).

4.3.4 Yb^{3+}/Er^{3+} Rate-Equations

For the Yb^{3+}/Er^{3+}-doped fibre, the potential for a low threshold cw erbium fibre laser is of primary interest. In order to obtain a value for the lasing threshold power, the rate equations describing the Yb^{3+}/Er^{3+} system may be solved. Assuming Er^{3+}-excitation only via energy-transfer we may write

$$dN_1/dt = N_2/\tau_{21} - R_F N_b + R_B N_3 + N_3/\tau_{31} + (N_2-N_1)W_{21}$$

$$dN_2/dt = N_3/\tau_{23} - N_2/\tau_{21} - R_{26}N_2 - (N_2-N_1)W_{21}$$

$$dN_3/dt = R_F N_b - R_B N_3 - N_3/\tau_{23} - N_3/\tau_{31} + R_{26}N_2$$

$$dN_b/dt = R_{aub}(N_{au}-N_b) + R_B N_3 - R_F N_b - N_b/\tau_{ba}$$

$$N_{au}/N_{ag} = \exp(-h\nu_a/kT) = \text{const.} = 1/a$$

$$N_{1u}/N_{1g} = \exp(-h\nu_b/kT) = \text{const.} = 1/b$$

$$N_1 = N_{1g} + N_{1u} \qquad (4.28a\text{-}4.28h)$$

$$N_a = N_{ag} + N_{au}$$

where

N_i, N_a, N_b	population density in levels i(i=1,2,3),a,b
N_{1g}, N_{1u}	population density in Stark-splitted level 1
N_{ag}, N_{au}	population density in Stark-splitted level a
$R_{aub}(N_a-N_b)$	pump rate from level au to b
$R_{26}N_2$	pump rate from level 2 to 6
$1/\tau_{ij}, 1/\tau_{ab}$	transition rates between levels
$(N_2-N_1)W_{21}$	stimulated emission rate
R_F, R_B	rate of forward and back energy-transfer

and the level notation refers to Fig.1. Due to the rapid non-radiative decay between levels 6,5,4 and 3, the population of levels higher than three has been neglected. Radiative and non-radiative losses in Er^{3+} from levels higher than 3 have been summarised by including the rate $1/\tau_{31}$. The Yb^{3+} split ground state is approximated by the two levels N_{au} and N_{ag} and the Er^{3+} ground state is approximated by the levels N_{1g} and N_{1u}, which are thermally populated. The transition rate

between the two Yb^{3+} and Er^{3+}-ground states has been assumed to be instantaneous. Energy-transfer rates between levels other than $^2F_{5/2}$ and $^4I_{11/2}$ have been neglected. Further, it is assumed that the laser is pumped from the upper level of the Yb^{3+} ground state. Pump excited state absorption from the metastable state in Er^{3+} has been accounted for by including the rate R_{26}. Pump excited state absorption also leads to a loss of pump power which has to be considered when the Er^{3+} excitation along the fibre length is calculated.

In steady state the equation involving the time derivative of N_3 may be written as

$$N_3(1/\tau_{23}+1/\tau_{31}) = R_F'N_b, \qquad (4.29)$$

where $R_F'=R_F/[1+R_B\tau_{23}\tau_{31}/(\tau_{23}+\tau_{31})]$ is the effective forward energy-transfer rate. For small doping levels (<1%), it holds $R_B\tau_{23}\tau_{31}/(\tau_{23}+\tau_{31})<<1$ and $R_F'\approx R_F$[11]. Since $\tau_{23}, \tau_{31}<<\tau_{21}$, one may write $N_E\approx N_1+N_2$, where N_E is the density of erbium ions. The previous rate equations then reduce to

$$\begin{aligned}
\eta R_F'N_b &= N_2(1/\tau_{21}+(1-\eta)R_{26}) + (N_2-N_1)W_{21} \\
R_{ab}(N_a-N_b) &= N_b/\tau_{ba} + \eta R_F'N_b \\
N_E &= N_{1g} + N_{1u} + N_2 \\
N_Y &= N_{ag} + N_{au} + N_b \\
N_{au}/N_{ag} &= 1/a \qquad (4.30a\text{-}4.30f) \\
N_{1u}/N_{1g} &= 1/b
\end{aligned}$$

where $\eta=\tau_{31}/(\tau_{31}+\tau_{32})$ is the Er^{3+} luminescence efficiency and N_Y is the density of ytterbium ions. For Er^{3+}-doped silicate glasses and in particular for the germanosilicate fibres used here, the luminescence efficiency is typically of the order of 90%[11,28]. In order to solve the equations, R_F' has to be known. As explained in section (4.3.3) R_F' may be calculated as a function of acceptor excitation by using equations (4.9)-(4.11) and (4.22) or (4.27). If we identify R_F' with $W_s(g)$ and employ the small signal approximation $W_{21}<<\tau_{21}$, the expressions for the population inversion on the two Er^{3+} ground states may be obtained by using equations (4.30) as

$$N_2-N_{1g} = \frac{(2b+1)k + 1}{2(b+1)} N_E \qquad (4.31a)$$

$$N_2-N_{1u} = \frac{(b+2)k + b}{2(b+1)} N_E, \qquad (4.31b)$$

where

$$k = \frac{\eta \frac{N_b}{N_E} \frac{W_s(g)}{g} - [\frac{1}{\tau_{21}} + (1-\eta)R_{26}]}{\eta \frac{N_b}{N_E} \frac{W_s(g)}{g} + [\frac{1}{\tau_{21}} + (1-\eta)R_{26}]}. \qquad (4.31c)$$

N_b is a function of intensity and therefore also of fibre length x. $N_b(x)$ may be obtained by solving equations (4.30) for N_b and using

$$R_{aub}(x) = I_p(x)\sigma_{au}/h\nu_p \qquad (4.32a)$$

$$R_{26}(x) = I_p(x)\sigma_{ea}/h\nu_p, \qquad (4.32b)$$

where

$I_p(x)$	pump intensity
σ_{au}	absorption cross section at pump wavelength
σ_{ea}	excited state absorption cross section from the metastable state in Er^{3+}.
h	Planck's constant
ν_p	pump frequency

and

$$I_p(x) = I_{p0}\exp\left((-1/x)\int_0^x \{\frac{\sigma_{au}}{1+a}[N_Y-(2+a)N_b(z)]+\sigma_{ea}N_2(z)\}\right)dz, \quad (4.33)$$

where I_{p0} is the launched pump intensity and we have assumed pumping from the upper ytterbium ground state.

The condition for lasing threshold in a fibre geometry is then obtained from the requirement that the gain G has to overcome the losses

$$G > 1/(R_1R_2), \quad (4.34)$$

where R_1, R_2 are the reflectivities of the end mirrors. The gain in a fibre geometry is given by

$$G = \exp\{2\int_0^1 [\phi\{N_2(x)-N_1(x)\}\sigma-N_2(x)\sigma_{ESA}-\alpha_c]dx, \quad (4.35)$$

where

$N_2(x)-N_1(x)$	population inversion as a function of length
σ	stimulated emission cross section
σ_{ESA}	excited state absorption cross section at the lasing wavelength
$\varnothing$	overlap integral of the pump and laser wavelength mode in the fibre
l	fibre length
α_c	intracavity loss coefficient.

The stimulated emission and absorption cross sections may be obtained from previously published data[11,12] or from measurements of fibre absorption provided the fibre doping levels are known. Note, if a>>1 then $\sigma_{au}/(1+a)\approx \sigma_{au}/a=\alpha/N_Y$, where α is the absorption constant at the pump wavelength. This means that σ_{au}/a may be directly obtained from measurements of the fibre absorption at the pump wavelength. The pump excited state absorption is particularly significant when a pump source emitting around 800nm and 850nm is used[29] (as in semiconductor-laser pumped Er^{3+}-doped erbium fibre lasers). Pumping at 800nm leads to an excitation of Er^{3+} ions from the $^4I_{13/2}$-level to the $^4S_{3/2}$-level. However, when pump wavelengths from 820nm-830nm and from 870-1050nm are used, no Er^{3+}-level is directly excitable from the $^4I_{13/2}$-level and thus pump excited state absorption only leads to small losses in this case and may be ignored in the presence of the dominant loss mechanism, i.e. acceptor saturation.

The lasing threshold of a weakly-doped Yb^{3+}/Er^{3+} fibre may now be estimated using equations (4.22) and (4.9)-(4.11) to calculate the energy-transfer rate as a function of acceptor excitation and inserting these results into (4.30)-(4.35). Due to the absence of

significant back-transfer and donor excitation diffusion at low doping levels (<1% donor ions)[13], the theoretical predictions may be expected to agree well with the performance of real fibres. However, as the donor doping levels are increased to values as high as 12% (currently not achievable in MCVD fibres), donor excitation diffusion becomes dominant and we have to use (4.27) to obtain an estimate of the transfer-rate as a function of acceptor excitation. Further, back-transfer and additional Er^{3+} fluorescence quenching at high excitation levels become more significant as energy-transfer limiting mechanisms[12].

4.4 Fibre Fabrication

The fibres employed in this study were fabricated by a modified MCVD method which allows the addition of rare-earth dopant ions from solution[30]. A conventional cladding layer is first deposited and then the core layers are formed at a reduced temperature to produce an unsintered, porous soot. The soot is immersed in a dilute aqueous solution (typically 0.1M) containing the dopant ions in the required ratio. For experimental convenience the solutes chosen are the rare-earth halides, although any soluble form of the dopant ions may be employed.

Due to the aqueous nature of the fabrication technique an effective dehydration process is essential to produce low-loss fibres and so, after the tube has been rinsed with acetone to remove the excess water, the preform is dried at 600°C whilst chlorine flows in the tube. The core layers are then sintered and the preform collapsed in the usual manner. Fibre drawing is conventional.

Fibres with a germanosilicate core and also with a P_2O_5-doped aluminosilicate core were produced. The germanosilicate fibres had a GeO_2 concentration of 13 mole% and the aluminosilicate fibres had a concentration of 5 mole% Al_2O_3 and 2 mole% P_2O_5. It was found that a maximum concentration of about 0.5 mole% Yb^{3+} could be incorporated into the germanosilicate fibres without the occurrence of scatter centres, whereas the aluminosilicate fibres allowed the incorporation of up to 3 mole% Yb^{3+} without scatter centres.

4.5 Experimental Techniques

Absorption, fluorescence and gain spectra, and fluorescence decay times were measured in this study. Further, the lasing performance of Er^{3+}/Yb^{3+} co-doped fibres was characterised.

The absorption spectra were obtained by employing a multiple cut-back technique[1] requiring fibre lengths between 2cm and 200m. Fibre lengths shorter than 20cm were spliced between two lengths of matched undoped fibres in order to minimise the effects due to cladding modes. The most absorbing part of the spectrum was measured directly in the fibre preforms. To this end a disc of about 5mm width was cut from the preform, then polished and the absorption measured with a photometer. Dopant concentrations were estimated from the absorption spectra using the data from Smith and Cohen[31]. Fibres doped with only Yb^{3+} or Er^{3+} were produced in addition to Yb^{3+}/Er^{3+}-doped fibres in order to obtain the relative strength of the absorption bands. All fibres were examined for scatter centres by launching light from a He-Ne laser emitting at 633nm. Scatter centres are then easily detectable by irregularly distributed scattering along the fibre.

The fluorescence spectra were recorded by pumping with a cw-GaAs laser emitting at 825nm and with a GaInAsP diode as a light detector. The fluorescence decay times were measured by using a Raman-shifted dye-laser emitting at 880nm with a 6nsec pulse width to excite the $^2F_{5/2}$ atomic level in Yb^{3+}. The Yb^{3+} fluorescence decay was measured at 1079nm, where a monochromator was used to filter out the exact wavelength. The peak optical input power was typically 1W. The fluorescence signal was recorded as a function of time and averaged 2000 times in a digitising oscilloscope in order to improve the signal/noise ratio. The recorded fluorescence signals were subsequently analysed in a computer and the mean fluorescence decay rates were estimated.

Wavelength-dependent gain was measured by a two-source technique as displayed schematically in Fig. (4.7). A cw YAG laser operating at 1.064μm or a cw Styryl-9 dye laser were used as the pump sources. The pump light was launched into an optical fibre from one end, to pump the Er^{3+} via absorption in Yb^{3+} and energy-transfer, and a white light source was launched from the other. The white light source signal emerging from the fibre was passed through a monochromator to give a wavelength dependent read-out of signal strength. The pump laser and the white light source power were monitored via two Ge-detectors. The gain spectrum in the fibre may then be obtained by comparing the signal strength of the white light source with the pump laser pump switched on and off. If the fibre length is short enough so that the laser pump power may be assumed to be constant along the fibre and wavelength-independent losses may be neglected, the population inversion in the fibre may be simply obtained from equation (4.35) and by a measurement of fibre loss. Fibre loss may be measured by a standard cut-back technique using the same set-up.

4.6 Results

4.6.1 Dopant Concentrations and Absorption Spectra

The doping concentrations of the fibres employed in this study are shown in Table 4.1. Two fibres doped with different amounts of Yb^{3+} and no Er^{3+} were manufactured to determine whether concentration quenching leads to a reduction in Yb^{3+} fluorescence decay time at high doping levels and to allow the estimate of energy-transfer efficiencies in the co-doped fibres following equation (4.9). A range of co-doped aluminosilicate-core fibres with a constant amount of Er^{3+} and varying amounts of Yb^{3+} were fabricated to measure the energy-transfer rate as a function of Yb^{3+} concentration.

The absorption spectrum obtained with fibre ND536, doped with Yb^{3+}/Er^{3+} is shown in Fig.4.8. Since Yb^{3+} is a two-level system, no absorption due to Yb^{3+} outside the 700-1100nm Yb^{3+}- absorption band is introduced. Although losses of up to 1000dB/m are obtained at 980nm, in the low-loss window a minimum loss of 100dB/km at 1150nm is recorded in the fibre. Factors contributing to the loss include residual absorption from the tail of the absorption bands and increased scatter in the fibre due to the high dopant ion concentration. The minimum loss is high compared with losses obtained in telecommunications fibres but is not unacceptable in view of the short lengths of fibre, around 50cm required in this study. The absorption spectrum of Er^{3+} in the range from 1500nm to 1650nm is shown in more detail in Fig. 4.9. Neglecting the Stark-splitting of the metastable $^4I_{13/2}$-level in Er^{3+} and assuming that the absorption at 1536nm and 1600nm is due to two thermally populated atomic levels separated by 260 cm^{-1}, this corresponds to a ratio of the relative populations of these two levels of 3.6.

4.6.2 Fluorescence Spectra

The fluorescence spectrum obtained in fibre ND385 with broad band excitation at 825nm is shown in Fig. 4.10. As expected the erbium fluorescence spectra obtained in an Yb^{3+}/Er^{3+}- and an Er^{3+}-doped fibre do not differ. The broad erbium fluorescence band in silica is providing the opportunity for widely tunable fibre lasers[2]. The peak Yb^{3+} fluorescence occurs at 1050nm, which corresponds to the tail of the Yb^{3+} absorption band. Due to the crystal-field splitting of the Yb^{3+} ground state, QFLO of an purely Yb^{3+}-doped fibre should in principle be possible. Since the stimulated emission cross sections of Yb^{3+} and Er^{3+} have a comparable magnitude, and due to the short decay time of Yb^{3+} (<1msec), the lasing threshold of such a laser should be about one order of magnitude higher than in Er^{3+}. Recently, such a fibre laser has been demonstrated by Hanna et al[32].

4.6.3 Fluorescence Decay Measurements

The intrinsic Er^{3+} fluorescence decay from the metastable level $^4I_{13/2}$ was measured in the co-doped fibres and compared to fibres doped with only Er^{3+}. No difference in decay time (τ_{21}=14msec) could be observed for the two sets of fibre, which verifies that back-transfer from Er^{3+} to Yb^{3+} is negligibly small in the co-doped fibres.

The intrinsic Yb^{3+} fluorescence decay time was measured in fibres ND426 and ND548, doped with only Yb^{3+}. Both fibres had a decay time of 750μsec, which shows that for Yb^{3+}-doping levels up to 3 mole% no concentration quenching of Yb^{3+} occurs in the dopant glass hosts, i.e. germanosilicate and P_2O_5-doped aluminosilicate, used in the experiments. Further, since the core-glass composition consists of about 90% silica no difference in

Yb^{3+} decay time could be detected due to the different oxide dopants, i.e. GeO_2 or Al_2O_3.

The fluorescence signal measured as a function of time in fibre ND426, doped only with Yb^{3+}, and ND414, doped with both Er^{3+} and Yb^{3+}, is shown in Fig. 4.11. The effect of energy-transfer in fibre ND414 is clearly visible by the initial fast decay of the Yb^{3+}-fluorescence. At larger times energy transfer becomes less significant and the instantaneous fluorescence-decay rate asymptotically reaches a value equal to the one measured in fibre ND426.

Best fits of the Yb^{3+} fluorescence signal in the germanosilicate fibres ND385 and ND414 to a function as given in equation(4.23) with s=6,8,10 were calculated. The best fit was obtained with s=8. A best fit curve for fibre ND414 is also displayed in Fig. 4.11. This indicates that dipole/quadrupole interactions are the dominant energy-transfer mechanisms in the germanosilicate fibres at these relatively low doping levels. The ratios n_A/n_{A0} obtained for the best fit curve with s=8 and the mean energy-transfer rates and transfer efficiencies are given in table 4.2. Fibre ND414 has a slightly higher ratio n_A/n_{A0} than fibre ND385, which corresponds to a better transfer efficiency and transfer rate. The mean transfer rate is very slow at 500 sec^{-1}, which is about 3 times smaller than the intrinsic decay rate of Yb^{3+}.

Best fits of the Yb^{3+} fluorescence signal in the more heavily doped aluminosilicate fibre ND536 to equation (4.23) were obtained with s=6, which indicates that in this fibre dipole/dipole interactions are the dominant energy-transfer mechanisms. As shown below in the even more heavily doped aluminosilicate fibres donor diffusion

may no longer be ignored and therefore equation (4.23) is no longer valid exactly and functions as given by Yokota and Tanimoto[27] now correctly describe the Yb^{3+} fluorescence decay.

4.6.4 Forward and Back-Transfer as a Function of Yb^{3+}-Concentration

The back-transfer rate obtained by measuring the Yb^{3+} fluorescence decay after excitation into the $^4S_{3/2}$-level in Er^{3+} (see section 4.3.3.3) is shown in Fig. 4.12 as a function of Yb^{3+} concentration. It may be seen that the back-transfer rate stays constant up to Yb^{3+} doping levels of 2 mole%, which may be explained by the fact that donor diffusion is slow compared to the energy-transfer rate up to these doping levels (see section 4.3.3.3). At the higher donor doping levels the back-transfer rate decreases due to the onset of donor diffusion and approaches the forward-transfer rate, also displayed in Fig. 4.12. This verifies that as the donor doping levels increase the donor ions become more and more indistinguishable.

The forward transfer rate for the two germanosilicate fibres is almost the same despite their difference in Yb^{3+} concentration. This may indicate that there is a non-uniform distribution of dopant ions, i.e. clustering[7], in the dopant host. Fibre ND414 exhibited easily detectable scatter centres, which indicates that microcrystalisation and possibly also clustering is indeed occurring. However, no direct experimental evidence for clustering, i.e. a short fluorescence decay component as observed in germanosilicate Nd^{3+}-doped germanosilica glasses[7], could be found.

The solubility of the dopant ions was increased in the aluminosilicate fibres and only fibre ND547 exhibited scatter centres. The transfer rates for the aluminosilicate fibres show a strong dependence of energy-transfer rate on Yb^{3+} concentration. Following data obtained by Gapontsev[11], we would expect a linear dependence (on a log/log scale) of energy-transfer rates on donor concentration for a constant acceptor concentration. However, when analysing the combined data for the aluminosilicate and germanosilicate fibres, we see that this is clearly not the case here. The transfer rate increases only slowly up to Yb^{3+}-doping levels of about 2 mole%, whereas at higher doping levels the increase is much more rapid. This is another indication that clustering is indeed significant in these fibres and leads to relatively high transfer rates at low donor doping levels.

4.6.5 Yb^{3+} Absorption Saturation

As explained in section 4.3.4, one has to account for the thermal population of the Yb^{3+} levels when pumping an Yb^{3+}/Er^{3+} system from the upper Stark levels of the Yb^{3+} ground state. This is particularly important when pumping with a YAG-laser emitting at 1.064μm. Assuming the 1.064μm absorption band is due to an upper Stark level of the 980nm absorption band, we obtain a frequency difference between these levels of 800cm^{-1} and a thermal population of this upper Stark level of 2%. It is straight forward to estimate the thermal population of the upper Stark level by a measurement of Yb^{3+} absorption saturation at high pump intensities. In this, the thermal population of the upper Stark level is given by

$$(1/a) = \frac{I_{sat}\tau_{ab}\sigma_a}{h\nu_p}, \qquad (4.36)$$

where I_{sat} is the absorption saturation intensity, where bleaching of the Yb^{3+} absorption occurs. A measurement of Yb^{3+} absorption saturation at 1.064μm was made in fibre ND545, where pump light delivered from a YAG-laser was launched into the fibre and the output power measured as a function of input power. The fibre had a core diameter of 5μm and a cut-off wavelength of 1.5μm. The absorption cross section at the pump wavelength was estimated from measurements of the absorption at 1.064μm and the Yb^{3+} concentration as $\sigma_a = 1\times10^{-23}cm^2$. The results are shown in Fig. (4.13), from which we obtain $I_{sat}\approx6\times10^5$ W/cm^2. This corresponds to a launched power of about 120mW. Inserting the value for I_{sat} into (4.36), we obtain for the thermal population of the upper Stark level $(1/a)\approx2.5\%$, which is in good agreement with the value 2% obtained from the frequency separation of the Stark level from the ground state.

4.6.6 Gain in Yb^{3+}/Er^{3+}-Doped Fibres

By applying the measurement technique described in section 4.5 to fibre ND385, erbium excitation levels achievable by pumping with a Nd YAG laser operating at 1064nm were determined as a function of pump power. Fibre ND385 was used for these measurements rather than fibre ND414 because it did not exhibit scatter centres. The results are shown in Fig. 4.14 along with a theoretical curve obtained from the measured energy-transfer efficiency at zero erbium excitation and a calculation of the quitting effect for dominant dipole/quadrupole interactions following equation (4.22) and (4.30). In this, a thermal population of the upper Yb^{3+} Stark level

of 2.5% as estimated in section 4.6.5 has been used. A good agreement between experiment and theory is observed indicating that indeed the quitting effect is the dominant energy-transfer-limiting mechanism at these doping levels. It may also be seen that it is impossible to obtain more than 30% excitation of the erbium ions, even at infinite pump powers. This is due to Yb^{3+} absorption saturation at high pump intensities, which occurs since the absorption at 1.0641m is due to Yb^{3+} thermally excited into the upper Stark levels of the ground state. Yb^{3+} absorption saturation may be avoided by pumping at wavelengths shorter than 980nm, which enables much higher Yb^{3+} excitation levels. Measurements of gain were also carried out in fibre ND545 using pump-wavelengths between 810 and 850nm[33]. In this, the fibre length was kept constant at 47cm and a pump power of 25mW was used. Similar gain spectra were obtained for all pump wavelengths. The highest gain of about 5dB/m was measured between 1550 and 1570nm.

4.6.7 Lasing Performance

The lasing performance of Yb^{3+}/Er^{3+}-doped fibres was characterised in fibre ND545 using a YAG laser emitting at 1.0641m as the pump source[34]. Initial results have also been obtained for semiconductor laser pump sources emitting at 810 and 826nm[35].

As seen in section 4.6.6 YAG-laser pumping of an Yb^{3+}/Er^{3+}-doped fibre is impossible due to acceptor and Yb^{3+}-absorption saturation. In this, the saturation mechanisms limit the maximum possible excitation of the Er^{3+} ions to only 30%. Since the transfer efficiencies of the aluminosilicate fibres are higher, the onset of Yb^{3+} absorption saturation starts at much higher Er^{3+} excitation levels (>50%). Thus threshold may be reached

with relatively low pump powers. Fibre ND545 was chosen rather than any other of the aluminosilicate fibres, since it exhibited the highest transfer efficiency without the presence of scattering centres in the fibre. The fibre had a core diameter of 5μm and a cut-off wavelength of 1.5μm, hence giving rise to a high launch efficiency (≈60%) at the pump wavelength and single-mode operation of the Er^{3+} laser.

A standard low-loss cavity with two dielectric mirrors butted to the cleaved fibre ends was used[28]. Both the YAG laser and the Yb^{3+}/Er^{3+}-fibre laser operated cw. The input mirror had a reflectivity of 98% at the lasing wavelength and was highly transmitting at the pump. Output couplers with 1.57μm transmission of 7% and 27% were used. These had reflectivities of 10% at the pump wavelength. The optimum fibre length was found by cutting back a long length of fibre while monitoring the laser performance in terms of threshold, pump power, slope efficiency and lasing wavelength. The lasing characteristics proved to be optimum and relatively insensitive to fibre length for lengths of 0.8-1.5m. However, a shift in lasing wavelength from 1.568μm for a 2.8m fibre length to 1.549μm for a 0.25m fibre length was observed. This results from preferential QFLO of the Er^{3+} laser at the longer fibre lengths[15].

A fibre length of 88cm produced laser emission at a wavelength of 1.56μm and this length ± 3cm was subsequently used to evaluate the lasing performance. The launched (absorbed) power at threshold was found to be 16mW (8.0mW) for 27% output coupling and 12mW (6.6mW) for 7% output coupling. The slope efficiencies for the two cases with respect to launched (absorbed) power were found to be 2.0% (4.2%) and 1.5% (2.8%), respectively. Fig. (4.15) is a plot of the output power versus

launched power for the two output couplers. It is evident that the amount of output coupling is not very critical. The output power saturation seen at pump powers > 100mW is due to Yb^{3+} absorption saturation, as characterised in section (4.6.6). A maximum output power of 1.6mW was obtained with a launched power of 160mW. Higher output powers than those shown can be achieved with higher Yb^{3+} concentrations or simply by using longer fibre lengths.

Subsequently, the same fibre was also pumped with a mini-YAG or YLF laser operating at 1.064μm and 1.053μm[36]. Using a 27% output coupler and an optimum fibre length ($\approx$1m and 0.5m for the two wavelengths) threshold was obtained with 13.5mW of launched power at 1.064μm and 8.5mW at 1.053μm. The slope efficiencies with respect to launched power were stated as 3.1% and 5% for the two cases. It is interesting to note that the slope efficiencies are higher than obtained by Snitzer et al[37]. He used slightly higher Yb^{3+} concentrations of 4.2 mole% and a dopant ratio of 63. Pumping with a 1.064μm source his reported slope efficiency was only 0.7% with a maximum output power of 100μW and a lasing threshold of 9mW with a 2% output coupler.

Using fibre ND536 Barnes et al[34] demonstrated a lasing threshold with respect to launched (absorbed) pump power of 6mW (2.2mW or 4mW) employing semiconductor lasers emitting at either 810nm or 826nm. A maximum output power of 0.9mW was obtained with 11mW absorbed pump light and slope efficiencies up to 10% were demonstrated with an 18% output coupler. Further, Q-switched operation was also shown to be feasible and maximum peak powers of 5W were obtained in 60nsec pulses.

4.7 The Yb^{3+}/Er^{3+} Fibre Laser-Discussion

It is instructive to compare the lasing thresholds obtained in fibre ND545 to the theory of energy-transfer as outlined in section 4.3. To simplify the discussion we discuss the results obtained with YAG-laser pumping first, since Er^{3+} excitation is then only achieved via energy-transfer. Further, we neglect the Stark splitting of the Yb^{3+} and Er^{3+} ground states, since Yb^{3+} absorption saturation did not occur at lasing threshold in fibre ND545 and the erbium laser was emitting at $1.56\mu m$. This is close to laser emission down to the Er^{3+} ground state, which would correspond to emission at $1.536\mu m$[28]. In order to obtain an approximate expression for the lasing thresholds we may solve equations (4.30). Assuming the effective forward energy-transfer rate at lasing threshold is $W_s(g=0.5)$, an erbium luminescence efficiency η, ignoring the finite length of the fibre and excited state absorption, we may (as a rule of thumb) compare the expressions for the lasing threshold for an Er^{3+} (equation 4.37a) and Yb^{3+}/Er^{3+}-doped fibre (equation 4.37b)

$$\eta R_{13} > 1/\tau_{21} \qquad (4.37a)$$

$$\eta R_{ab} \frac{N_Y}{N_E} \frac{2W_s(g=0.5)}{2R_{ab}+W_s(g=0.5)+1/\tau_{ba}} > 1/\tau_{21}, \qquad (4.37b)$$

where R_{13} is the pump rate of an Er^{3+}-only doped fibre; $R_{ab}=I\sigma_a/h\nu_p$ and σ_a is the absorption cross section at the pump wavelength. In the absence of Yb^{3+} absorption saturation and for large dopant ratios N_Y/N_E it holds $2R_{ab} << W_s(g=0.5)+1/\tau_{ba}$ and therefore (4.37b) reduces to

$$\eta R_{ab} \frac{N_Y}{N_E} 2\eta_T(g=0.5) > 1/\tau_{21}, \qquad (4.37c)$$

where $\eta_T(g=0.5)$ is the transfer efficiency at lasing threshold. We see that even very low values for $\eta_T(g=0.5)$ may be compensated by large dopant ratios in the fibres, thus giving rise to low lasing thresholds. Further, we may interpret the effect of a large dopant ratio as producing a large effective absorption cross section given by $(\sigma_a)_{eff}=(N_Y/N_E)\sigma_a$ which also compensates for a low absorption cross section at the pump wavelength.

As seen in section 4.6.7 pumping with a YAG laser at 1.064μm gave rise to a lasing threshold of about 12mW with a 7% output coupler; this is equivalent to a pump rate $R_{ab}\approx 3.3$ sec^{-1}. Using the value for τ_{21}=14msec, η=90%[28] and N_Y/N_E=54, we derive from (4.37c) that a pump rate R_{ab} of 3.3 sec^{-1} is equivalent to a transfer efficiency at lasing threshold of about 22%.

This simple result is significant in a number of ways. The energy-transfer efficiency at lasing threshold obtained in fibre ND545 is the same as reported by Gapontsev et al[12] in high-quality phosphate laser glasses, which had a 9 times faster transfer rate at zero acceptor excitation corresponding to a transfer efficiency $\eta_T(g=1)$=95%. Thus very high dopant concentrations do not necessarily lead to better energy-transfer lasers. Qualitatively, this may be explained by the fact that back-transfer becomes more significant at high dopant concentrations as shown in sections (4.3.3.3) and (4.6.4). Further, as discussed in section (4.6.3.2) acceptor saturation at high dopant concentrations is governed by fast donor diffusion, which leads to a very rapid fall-off of transfer rate with acceptor excitation. At lower donor doping levels we have the conditions of slow donor diffusion, where the fall-off of transfer rate with acceptor excitation is comparatively slow.

We may calculate the transfer efficiency of fibre ND545 as a function of acceptor excitation under the conditions of slow donor diffusion, i.e. using equations (4.22) and (4.9). In this, we assume dipole/dipole interactions, i.e. s=6, and the ratio $n_A/n_{A0}=0.63$, which gives rise to a transfer efficiency at zero acceptor excitation of 58%. Further parameters used here are listed in table 4.3. At 50% acceptor excitation we readily show that the transfer efficiency is $\eta_T(g=0.5)= 36\%$. This value is 14% higher than the value of $\eta_T(g=0.5)$ as estimated from (4.67c). However, (4.67c) does not account for a fractional overlap between the laser and pump modes of 80%. A more accurate estimate for $\eta_T(g=0.5)$ may be obtained from the measurement of lasing thresholds by solving the rate equation (4.30) and using (4.34) and (4.35). Assuming, for simplicity, that $\eta_T(g=0.5)$ is constant along the fibre length we obtain that $\eta_T(g=0.5)$ needs to have a value of 28% to give the observed lasing thresholds with the two output couplers. This value for $\eta_T(g=0.5)$ is only 8% lower than estimated from (4.22). As expected the assumption of slow donor diffusion produces a value for the energy-transfer efficiency at lasing threshold which is too high. The small discrepancy may be explained by the onset of donor diffusion in fibre ND545, which leads to a more rapid decrease in transfer efficiency with acceptor excitation.

The observed increase in slope efficiency when pumping at 1.053μm as compared to 1.064μm[36] may be explained by the onset of Er^{3+} excited state absorption at 1.064μm, which leads to excitation from the metastable state $^4I_{13/2}$ to the $^4F_{9/2}$ level. At shorter pump-wavelengths this is avoided and therefore when pumping at 1.047μm, which is a wavelength available from mini Nd:YLF lasers, even higher slope efficiencies than reported in ref. 36 should be possible.

The results obtained with 810 and 826nm pump sources[34] are the most difficult to analyse, since pumping at these wavelengths also leads to direct excitation into the $^4I_{9/2}$-level in Er^{3+}. However, from (4.37c) we can derive an approximate estimate of the proportion of direct Er^{3+} excitation versus Er^{3+} excitation via energy-transfer for the two cases. From measurements of fibre absorption presented in section 4.6.1 we see that the Yb^{3+} absorption cross section at 810nm is about the same as at 1.064μm, namely $1\times10^{-23}cm^2$. Since the diameter of fibre ND536 was 5μm, a launched power of 6mW thus corresponds to a pump rate $R_{ab}\approx1.2$ sec^{-1}. Ignoring the direct absorption into Er^{3+}, we obtain from (4.37c) that a transfer efficiency at lasing threshold of about 100% is required to achieve threshold, whereas at 826nm the required transfer efficiency is about 40% due to the higher Yb^{3+} absorption cross section. The measured transfer efficiency in fibre ND536 was only 37% at zero acceptor excitation. The minimum reduction in transfer efficiency at lasing threshold is now easily estimated, if we neglect the quitting effect. This is justified, since a large proportion of the Er^{3+} ions get excited directly. In this case the transfer rate is proportional to the number of acceptor ions in the ground state[17], i.e.

$$W_s(g) = gW_s(g=1). \qquad (4.38)$$

Thus the transfer rate reduces from $780sec^{-1}$ at g=1 to $390sec^{-1}$ at g=0.5 at lasing threshold. Therefore the maximum possible transfer efficiency in this fibre at threshold is about $\eta_T(g=0.5)=22\%$ (Note that under the conditions of slow donor diffusion we derive almost the same value, namely $\eta_T(g=0.5)=20\%$). We may conclude that pumping at 810nm is predominantly due to direct Er^{3+}

excitation (by a factor of 5:1), whereas at 826nm energy-transfer contributes not more than 50% to the excitation of Er^{3+}. Higher contributions of energy-transfer versus direct excitation may be achieved by increasing the dopant ratio.

4.8 Conclusions

Optical fibres co-doped with Yb^{3+} and Er^{3+} were fabricated with the aim to achieve energy-transfer between them. Both germanosilicate and P_2O_5-doped aluminosilicate glasses were used as the dopant hosts. Yb^{3+}-dopant concentrations up to 0.5 mole% could be incorporated into the germanosilicate and up to 3 mole% into the aluminosilicate fibres without the occurrence of scatter centres and concentration quenching. The measurement techniques required for the characterisation of energy-transfer in rare-earth-doped fibres were then analysed. In particular, the relevance of pulsed measurements to cw laser applications have been outlined. The energy-transfer properties of the co-doped fibres were characterised according to these measurement techniques. Energy-transfer efficiencies of up to 73% were measured. Energy-transfer was found to be caused predominantly by static dipole/quadrupole interactions in the germanosilicate fibres and by dipole/dipole interactions in the aluminosilicate fibres. Forward and back-transfer rates were measured as a function of Yb^{3+} concentration and the difference in these two rates was used to evaluate the effect of donor diffusion in the fibres. This result was subsequently incorporated along with a treatment of the random orientation of the dopant ions in the glass host to account for the rapid fall-off of transfer efficiency with acceptor excitation in these fibres. Gain (or reduction in loss) measurements were

used to demonstrate this significant reduction in energy-transfer efficiency. A maximum gain of 5dB/m could be obtained in an aluminosilicate fibre using a launched power of 25mW at 820nm.

Finally, the efficient operation of an Yb^{3+}/Er^{3+} laser was demonstrated in a fibre exhibiting a transfer efficiency at zero acceptor excitation of 58%. Using a 1.064μm pump source lasing threshold was obtained with 7mW absorbed power. Slope efficiencies up to 4.2% could also be obtained. Higher slope efficiencies could be achieved by avoiding pump excited state absorption in Er^{3+} by using appropriate pump-wavelengths within the broad Yb^{3+} absorption band. It was further shown that at lasing threshold the transfer efficiency was about 28%. The reduction in transfer efficiency from 58% at zero acceptor excitation to 28% at lasing threshold was shown to be predominantly governed by slow donor diffusion.

Appendix 4.I

Equation (4.19) may be derived as follows: The fluorescence decay signal of a donor ion with a total number of N neighbouring acceptor ions at positions r_i is given by

$$\Phi(t) = \Phi_0(t) \prod_{i=1}^{N} \exp(-tW_i(r_i)), \qquad (A.1)$$

where $\Phi_0(t)$ is the intrinsic decay signal and $W_i(r_i)$ is the transfer rate to the i'th acceptor ion. (A.1) may be written as

$$\Phi(t) = \Phi_0(t)\exp(-\bar{W}(\xi))^N, \qquad (A.2)$$

where $\bar{W}(\xi)$ is the mean transfer rate to all N acceptor ions within the volume around a donor. Using the mean value theorem we may then write

$$\Phi(t) = \Phi_0(t)\left[\frac{1}{V} \int_0^{R_V} \rho(r)\exp(-W(r))dr \right]^N, \qquad (A.3)$$

where $\rho(r)=4\pi r^2 dr$ is the probability of finding an acceptor at a radius r. Taking the limit $V\to\infty$, we finally obtain (4.19).

Appendix 4-II

It was shown in section 4.3.3 that the donor fluorescence response to δ-pulse excitation in the presence of a fraction f=1-g excited acceptors is given by (4.21). Substituting

$$Z = (t/\tau_0)(r_0/r)^s \tag{A.4}$$

we obtain

$$\Phi(t)=\Phi_0(t)\lim_{Z,R_V,N_V\to\infty}\left\{\frac{3}{s}\frac{1}{1-(r_{min}/R_V)^3}Z_V^{3/s}\left[\int_{Z_V}^{\infty}Z^{-1-3/s}e^{-Z}dZ-\int_{Z_{min}}^{\infty}Z^{-1-3/s}e^{-Z}dZ\right]\right\}^N \tag{A.5}$$

where

$$Z_{V;min} = \left(\frac{t}{\tau_0}\right)\left(\frac{r_0}{R_{V;min}}\right)^s. \tag{A.6}$$

Equation (A.6) may be written to first order as

$$\Phi(t)=\Phi_0(t)\lim\left\{\frac{1}{1-(r_{min}/R_V)^3}\left[1-Z_V^{3/s}[\Gamma(1-\tfrac{3}{s})-\Gamma(1-\tfrac{3}{s},Z_{min})]+Z_{min}^{-3/s}\exp(-Z_{min})\right]\right\}^N. \tag{A.7}$$

Since $N = gn_A(4\pi/3)R_V^3$, where n_A is the acceptor concentration, (A.7) reduces to

$$\Phi(t) = \Phi_0(t)\exp\{-(n_A/n_D)g\ln(g) -$$

$$(t/\tau_0)^{3/s}g(n_A/n_{A0})[\Gamma(1-3/s)-\Gamma(1-3/s,Z_{min})] + \quad (A.8)$$

$$(n_A/n_D)g\ln(g)\exp(-Z_{min})\},$$

where n_{A0} is the so assumed uniform critical acceptor concentration at which the energy transfer rate would equal the intrinsic donor decay rate. Rewriting Z_{min} in terms of the critical acceptor concentration we finally obtain (4.22).

References

1) S.B. Poole, D.N. Payne and M.E. Fermann: "Fabrication of Low-Loss Optical Fibres Containing Rare-Earth Ions", Electron. Lett., **21**, 1985, pp.737-738

2) L. Reekie, R.J. Mears, S.B. Poole and D.N. Payne: "Tunable Single-Mode Fibre Lasers", J. Light. Tech., **LT-4**, 1986, pp.956-961

3) R.J. Mears, L. Reekie, I.M. Jauncey and D.N. Payne: "High Gain Rare-Earth-Doped Fibre Amplifier at 1.54μm", Optical Fibre Communication Conference, OFC/IOOC, Reno, 1987, paper WI2

4) M.C. Farries and M.E. Fermann: "Temperature Sensing by Thermally Induced Absorption in Neodymium Optical Fibre", 4th International Symposium on Optical and Optoelectronic Applied Science and Engineering, The Hague, 1987

5) S.B. Poole, unpublished data

6) J. Chrysochoos: "Nature of the Interaction Forces Associated with the Concentration Quenching of Nd^{3+} in Silicate Glasses", J. Chem. Phys., **61**, 1974, pp. 4596-459

7) K. Arai, H. Namikawa, K. Kumota and T. Honda: "Aluminium or Phosphorus Co-Doping Effects on the Fluorescence and Structural Properties of Neodymium-Doped Silica Glasses", J. Appl. Phys., **59**, 1986, pp. 3430-3436

8) S.A. Brawer and M.J. Weber: "Observation of Fluorescence Line Narrowing, Hole Burning and Ion-Ion Energy-Transfer in Neodymium Laser Glass", Appl. Phys. Lett., **35**, 1979, pp.31-33

9) M.J. Weber: "Luminescence Decay by Energy-Migration and Transfer: Observation of Diffusion Limited Relaxation", Phys. Rev. B, **4**, 1971, pp. 2932-2939

10) E. Snitzer and R. Woodcock: "Yb^{3+}-Er^{3+} Glass Laser", Appl. Phys. Lett., **6**, 1966, pp. 45-46

11) V.P. Gapontsev, S.M. Matitsin, A.A. Isineev and V.B. Kravchenko: "Erbium Glass Lasers and their Applications", Optics and Laser Technology, 1982, pp.189-196

12) V.P. Gapontsev, S.M. Matitsin and A.A. Isineev: "Channels of Energy Losses in Erbium Laser Glasses in the Stimulated Emission Process", Opt. Comm., **46**, 1983, pp.226-230

13) N.E. Alekseev, V.P. Gapontsev, M.E. Zhabotinski, V.B. Kravchenko and Y.P. Radnitski: "Lasernie Fosfatnie Stekla (Phosphate Laser Glasses)", Nauka Press, Moscow, 1980

14) J.G. Edwards and J.N. Sandoe: "A Theoretical Study of the Nd:Yb:Er Glass Laser", J. Phys. D: Appl. Phys., **7**, 1974, pp.1078-1095

15) L. Reekie, I.M. Jauncey, S.B. Poole and D.N. Payne: "Diode-Laser-Pumped Operation of an Er^{3+}-Doped Single-Mode Fibre Laser", Electron. Lett., **23**, 1987, pp.1076-1078

16) R. Reisfeld and C.K. Joergensen: "Lasers and Excited States of Rare-Earths", Springer Verlag, 1977, pp.157-198

17) J.C. Wright: "Up-Conversion and Excited State Energy Transfer in Rare-Earth-Doped Materials" in Topics in Applied Physics, Vol. 15, 1976, ed. F.K. Fong

18) R.K. Watts: "Energy Transfer Phenomena" in Optical Properties of Solids, Plenum Press, 1975, ed. B. DiBartolo, pp. 307-336

19) R. Orbach: "Relaxation and Energy Transfer" in Optical Properties of Solids, Plenum Press, 1975, ed. B. DiBartolo, pp. 355-400

20) T. Foerster: Naturwissenschaften, 33, 1946, pp.166-; "Zwischenmolekulare Energiewanderung und Fluoreszenz", Ann. Phys., 2, 1948, pp.55-75

21) D.L. Dexter: "A Theory of Sensitised Luminescence in Solids", J. Chem. Phys., 21, 1953, pp. 836-850

22) T. Miyakawa and D.L. Dexter: "Phonon Sidebands, Multiphoton Relaxation of Excited States, and Phonon-Assisted Energy Transfer between Ions in Solids", Phys. Rev., B1, 1970, pp. 2961-2969

23) D.C. Brown: "High-Peak-Power Nd:Glass Laser Systems", Springer Verlag, 1981

24) W.J.C. Grant: "Role of Rate Equations in the Theory of Luminescent Energy Transfer", Phys. Rev. B, 1971, pp. 648-663

25) M. Inokuti and F. Hirayama: "Influence of Energy Transfer by the Exchange Mechanism on Donor Luminescence", J. Chem. Phys., **43**, 1965, pp. 1978-1989

26) F.K. Fong and D.J. Diestler: "Many-Body Processes in Nonradiative Energy-Transfer Between Ions in Crystals", J. Chem. Phys., **56**, 1972, pp. 2875-2880

27) M. Yokata and O. Tanimoto: "Effects of Diffusion on Energy-Transfer by Resonance", J. Phys. Soc. Japan, **22**, 1967, pp.779-784

28) R.J. Mears: "Optical Fibre Lasers and Amplifiers", PhD-Thesis, Southampton, 1987

29) R.I. Laming et al.: "Pump Excited-State Absorption in Erbium-Doped Fibres", subm. to Opt. Lett.

30) J.E. Townsend, S.B. Poole and D.N. Payne: "Solution Doping Technique for the Fabrication of Rare-Earth-Doped Optical Fibres", **23**, 1987, pp. 329-331

31) H.L. Smith and A.J. Cohen: "Absorption Spectra of Cations in Alkali Silicate Glasses of High Ultra-Violet Transmission", **4**, 1983, pp. 173-187

32) D.C. Hanna, R.M. Rercival, I.R. Perry, R.G. Smart, P.J. Suni, J.E. Townsend: "Continuous-Wave Oscillation of Monomode Ytterbium-Doped Fibres", Electron. Lett., **24**, 1988, pp. 1111-1112

33) R.I. Laming: unpublished data

34) M.E. Fermann, D.C. Hanna, D.P Shepherd, P.J. Suni and J.E. Townsend: "Efficient Operation of an Yb Sensitised Er Fibre Laser at 1.56μm", Electron. Lett., **24**, 1988, pp. 1135-1136

35) W.L. Barnes, D.J. Taylor, M.E. Fermann, J.E. Townsend, L. Reekie and D.N. Payne: "A Diode-Laser-Pumped Er^{3+}/Yb^{3+}-Doped Fibre Laser Operating at 1.57μm", to be presented at Optical Fibre Conference, OFC, New Orleans, 1988

36) G.T. Maker and A.I. Ferguson: "A 1.56μm Yb Sensitised Er Fibre Laser Pumped by a Diode Pumped Nd:YAG and Nd:YLF Laser", Electron. Lett., **24**, 1988, pp. 1160-1161

37) E. Snitzer, H .Po, F. Hakimi, R. Tumminelli, B.C. McCollum, "Erbium Fibre Laser Amplifier at 1.55μm with Pump at 1.49μm and Yb Sensitised Er Oscillator", Optical Fibre Communications Conference, OFC, 1988, paper PD2-1

Fibre	$[Yb^{3+}]$	$[Er^{3+}]$	$[GeO_2]$	$[Al_2O_3]$	$[P_2O_5]$
	mole%	mole%	mole%	mole%	mole%
ND426	0.4	-	13	-	-
ND548	3.5	-	-	5	2
ND385	0.2	0.05	13	-	-
ND414	0.6	0.15	13	-	-
ND536	1.7	0.055	-	5	2
ND545	3.0	0.055	-	5	2
ND547	3.7	0.05	-	5	2

Table 4.1)

Dopant concentrations of fibres used in the experiments.

Fibre	n_A/n_{A0}	s	W_s / sec^{-1}	η_t
ND385	0.25	8	470	0.26
ND414	0.27	8	520	0.28
ND536	0.32	6	780	0.37
ND545			1840	0.58
ND547			3600	0.73

Table 4.2)

Energy transfer rate $W_s(g=1)$ and energy-transfer efficiency $\eta_T(g=1)$ of the Yb^{3+}/Er^{3+}-doped fibres. n_A/n_{A0} is the ratio of the acceptor concentration over the critical acceptor concentration at zero acceptor excitation. s=6 stands for dominant dipole/dipole interactions and s=8 stands for dominant dipole/ quadrupole interactions.

Parameters	values	units
τ_{21}	14	msec
τ_{ba}	0.75	msec
$\eta_T(g=1)$	58	%
$W_s(g=1)$	1800	sec^{-1}
$[N_E]$	0.12	10^{20} cm^{-3}
$[N_Y]$	6.7	10^{20} cm^{-3}
s	6	
n_A/n_{A0}	0.63	
$\eta_{FT}(g=0.5)$	37	%
$W_s(g=0.5)$	670	sec^{-1}
$\sigma(1.56\mu m)$	1.5	10^{-21} cm^2
λ_{pump}	1.064	μm
$\sigma_a(1.064\mu m)$	1.0	10^{-23} cm^2
η	0.9	
r	2.5	μm
ø	0.8	

Table 4.3)

Relevant parameters describing the properties of fibre ND545 used in section (4.7) for discussions of its lasing performance.

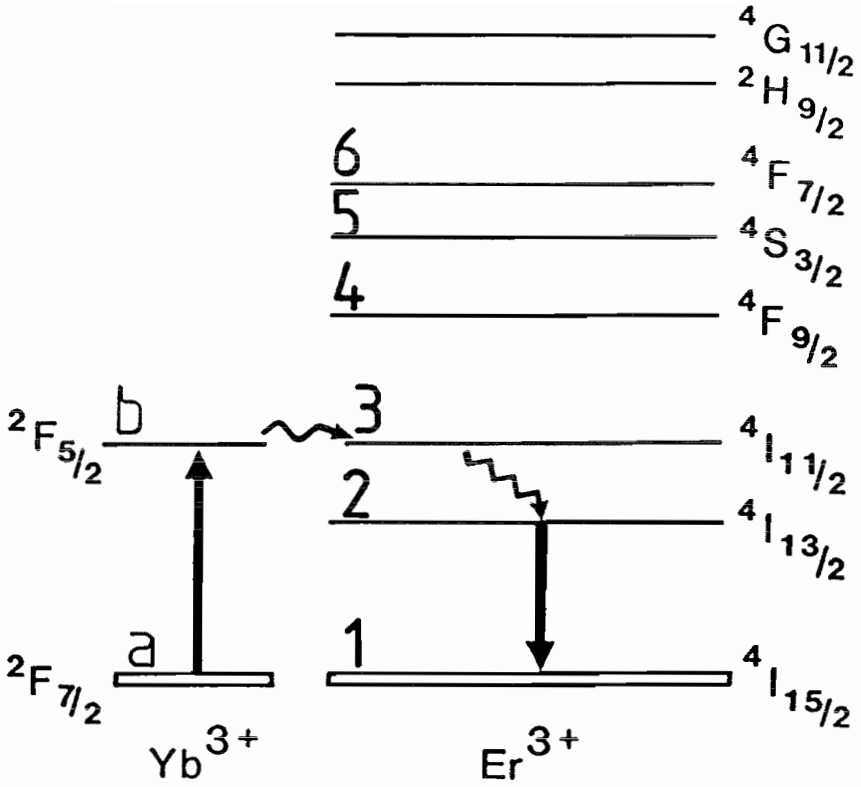

Figure 4.1 Energy-level diagram of the Yb^{3+}/Er^{3+} system.

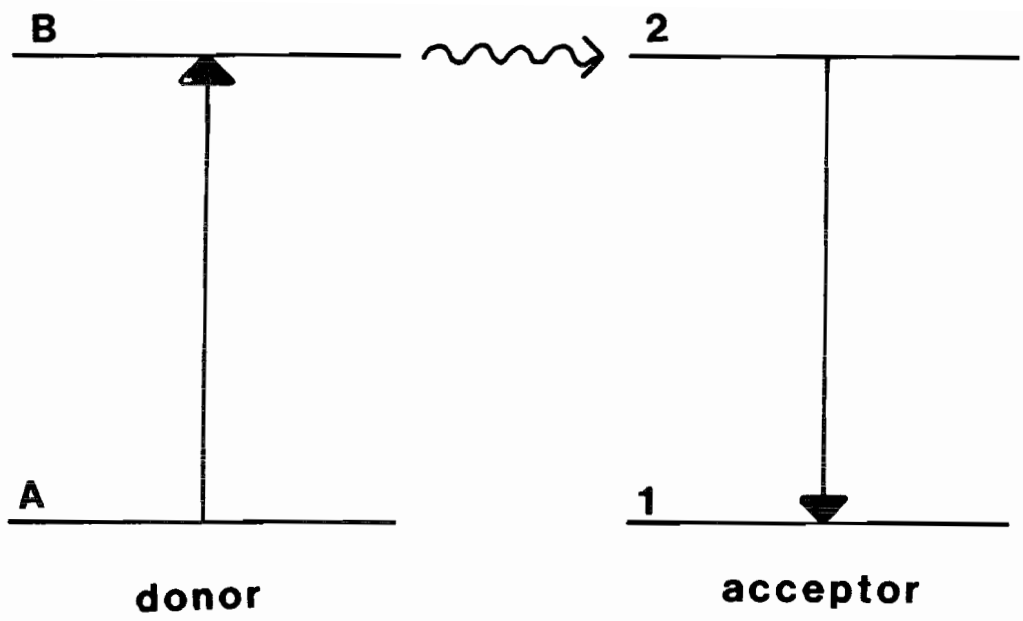

Figure 4.2 The principal processes involved in energy-transfer. The donor absorbs pump energy, which is then transferred to the acceptor, from where fluorescence to the acceptor ground state occurs.

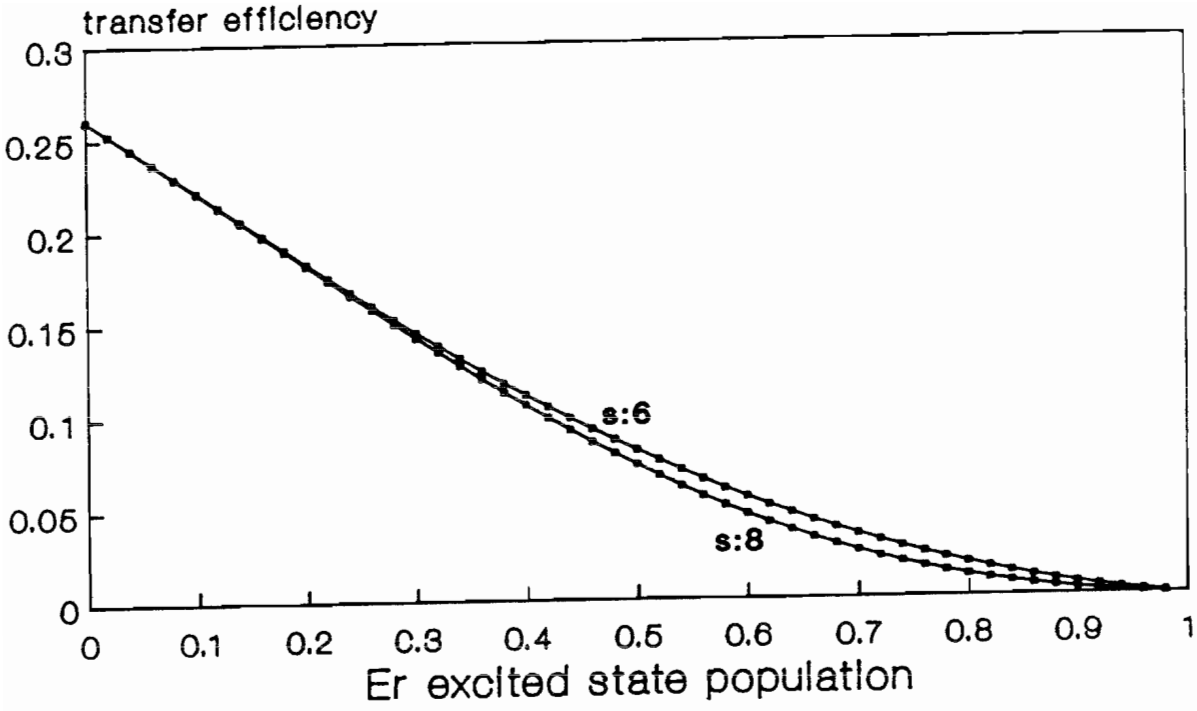

Figure 4.3 Transfer efficiency as a function of acceptor excitation for dipole/dipole (s=6) and dipole/quadrupole (s=8) interactions assuming slow donor diffusion.

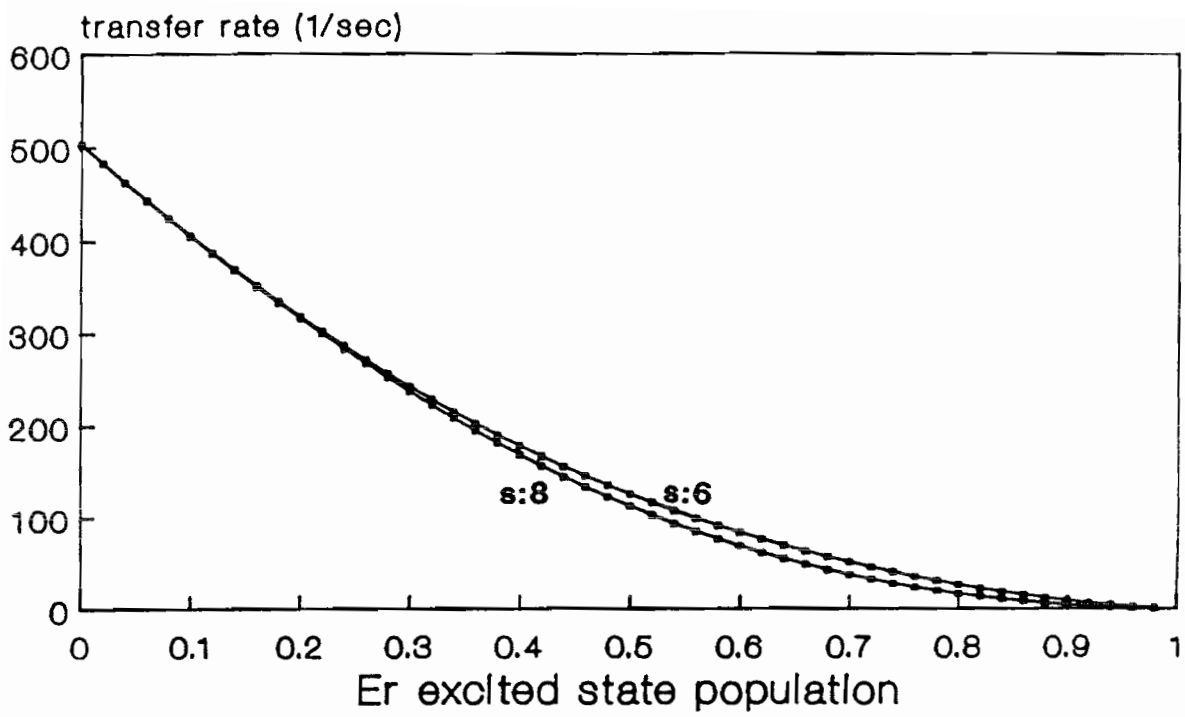

Figure 4.4 Same as Fig. (4.3), except that transfer rate is displayed.

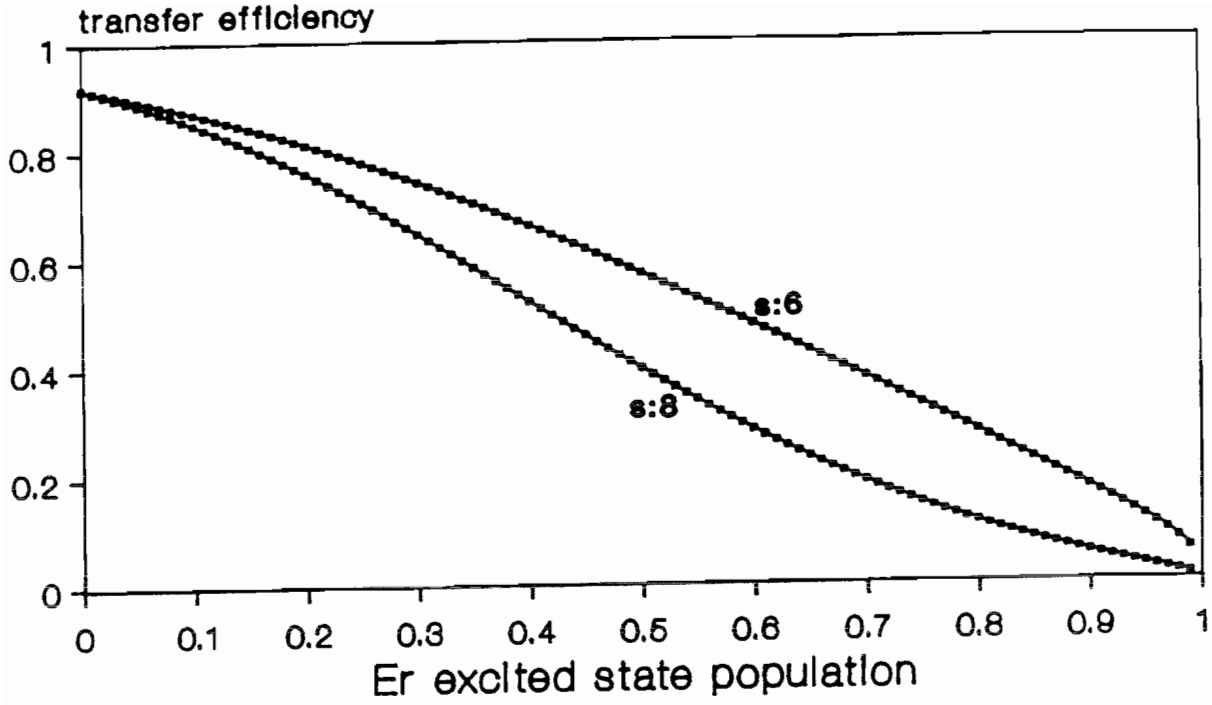

Figure 4.5 Transfer efficiency as a function of acceptor excitation for dipole/dipole (s=6) and dipole/quadrupole interactions assuming fast donor diffusion.

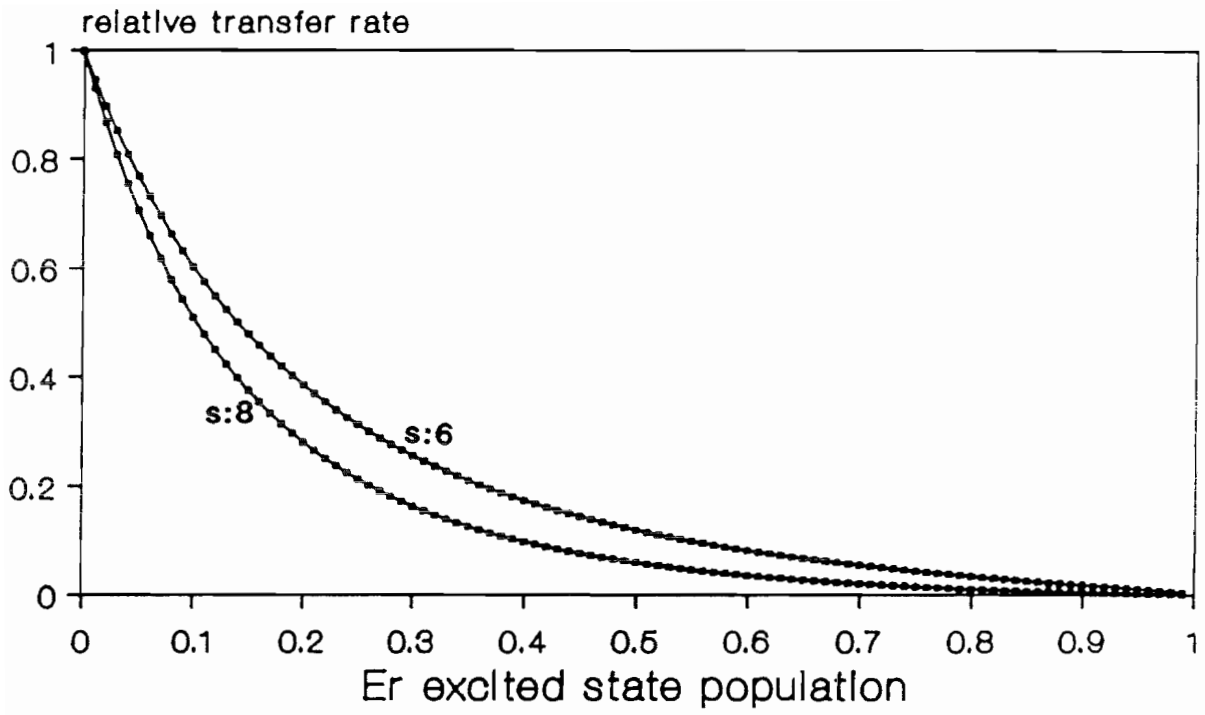

Figure 4.6 Same as Fig. (4.5), except that transfer rate is displayed.

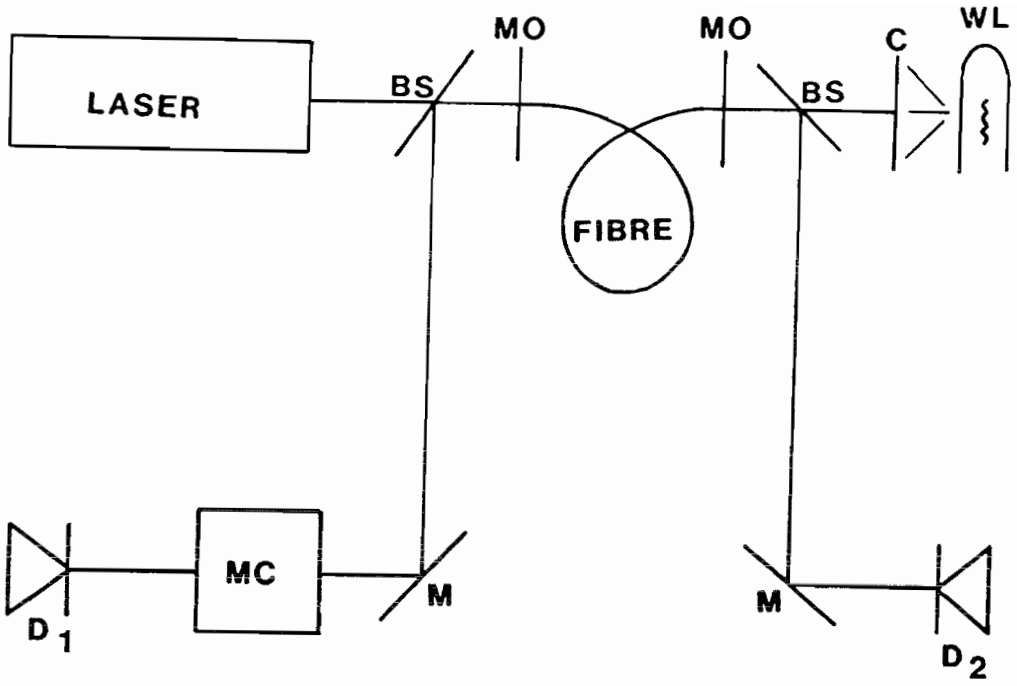

Figure 4.7 Set-up for the measurement of gain in rare-earth-doped optical fibres. D_1, D_2=detectors; MC=monochromator; BS=beamsplitters; MO=microscope objectives; C=condensor; M=mirrors.

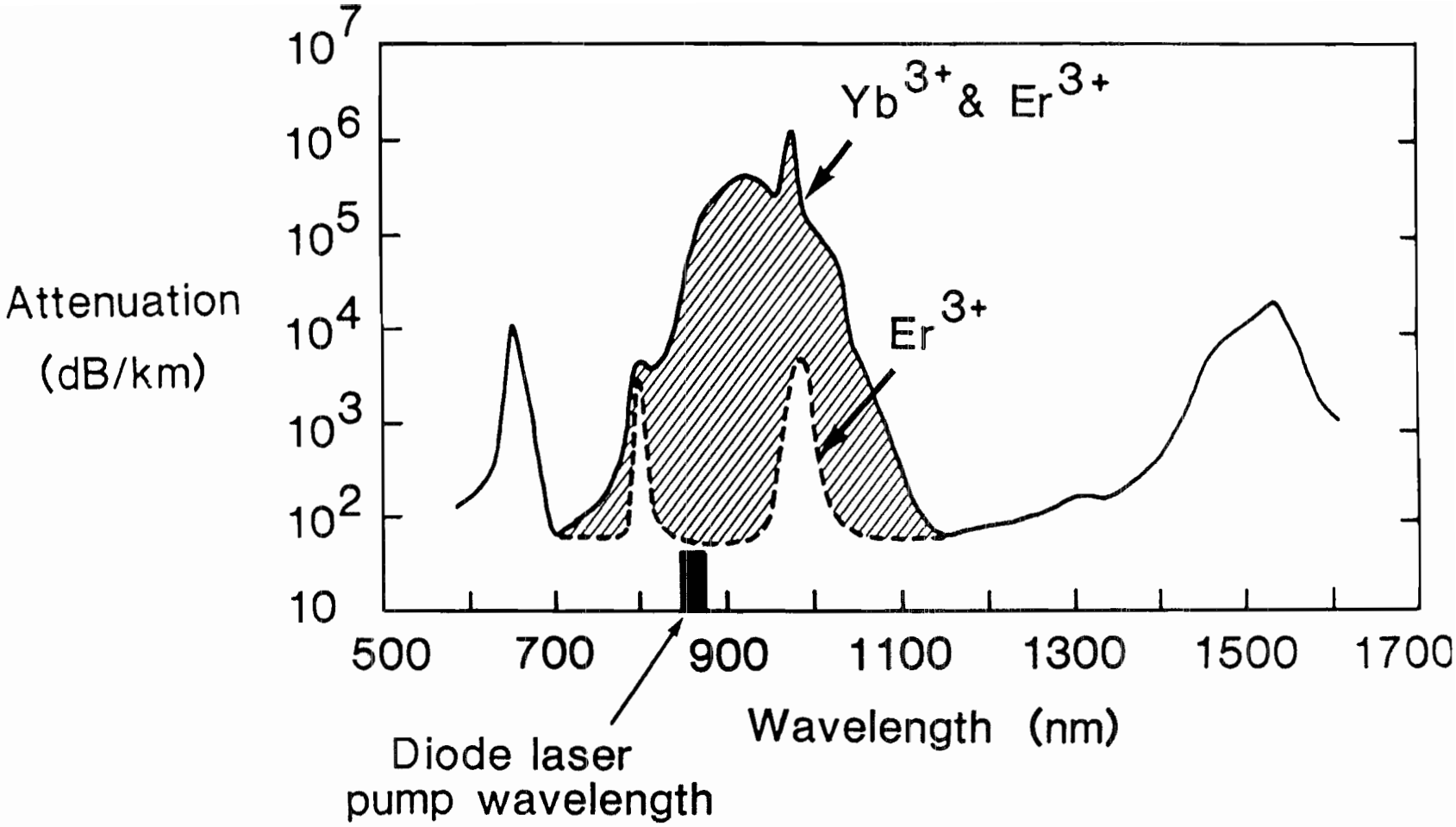

Figure 4.8 Absorption spectrum of fibre doped with 1.7 mole% Yb^{3+} and 0.055 mole% Er^{3+}.

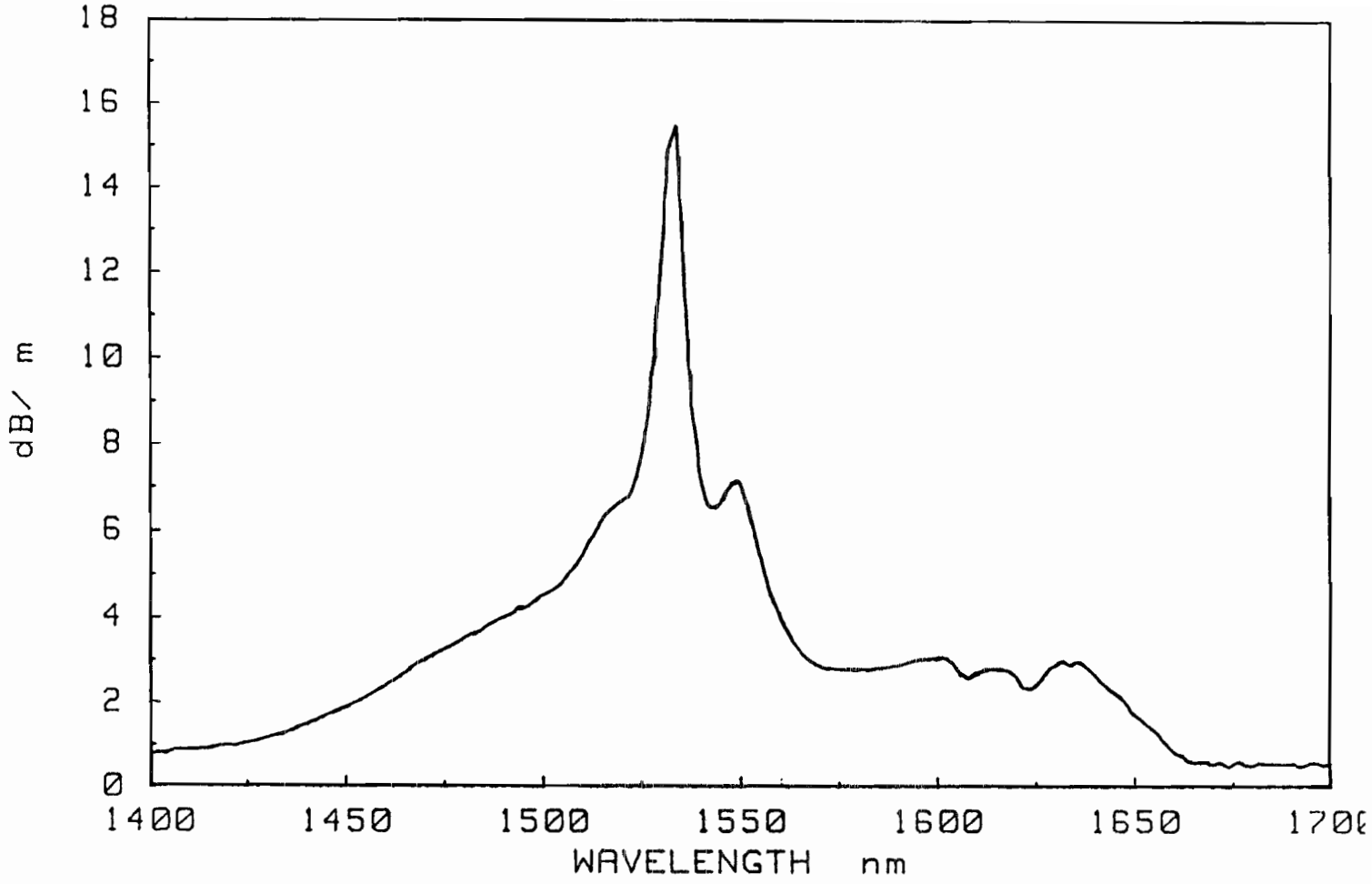

Figure 4.9 Detailed absorption spectrum of fibre doped with 300ppm Er^{3+} for wavelengths from 1400-1700 nm.

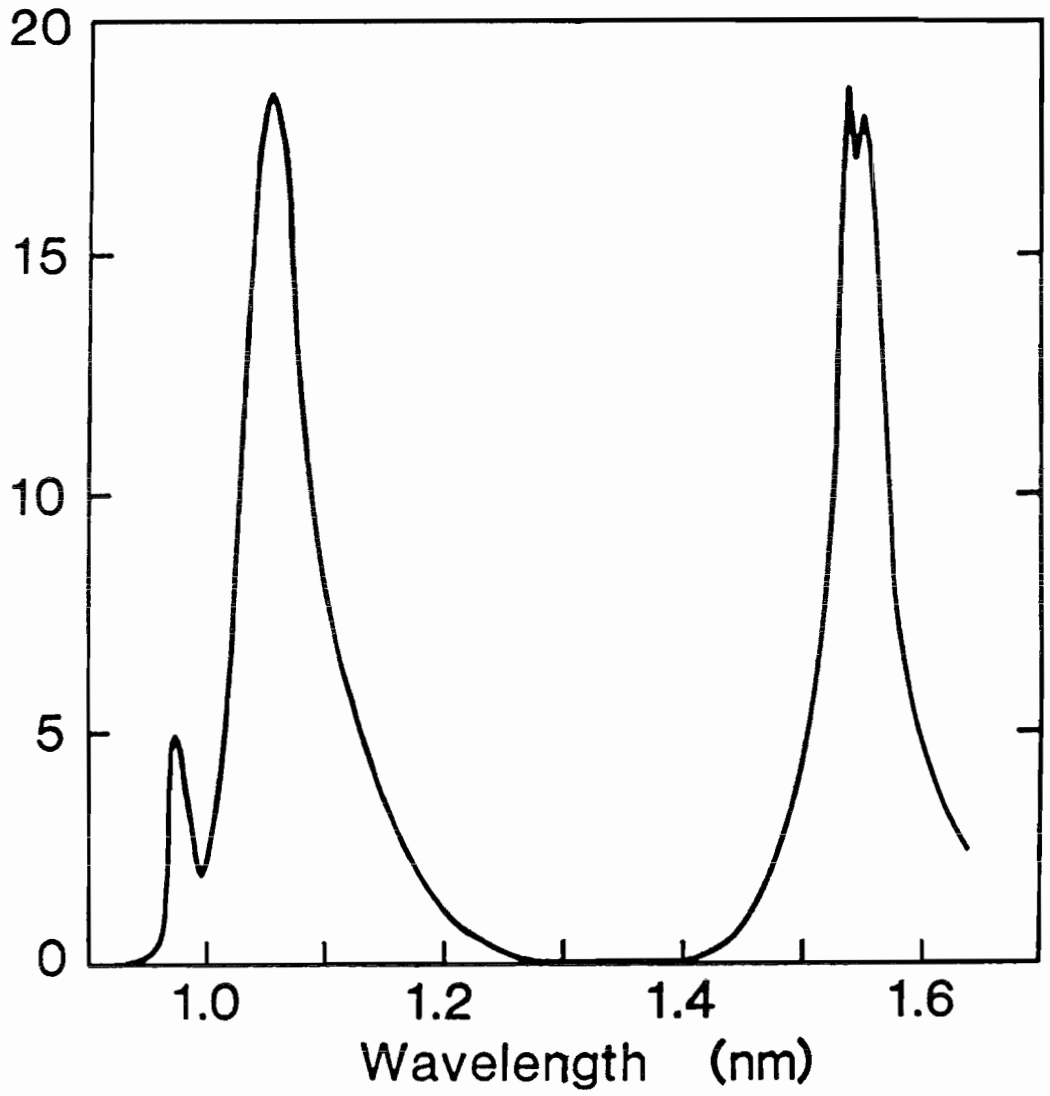

Figure 4.10 Fluorescence spectrum of Yb^{3+}/Er^{3+}-doped fibre excited at 825nm.

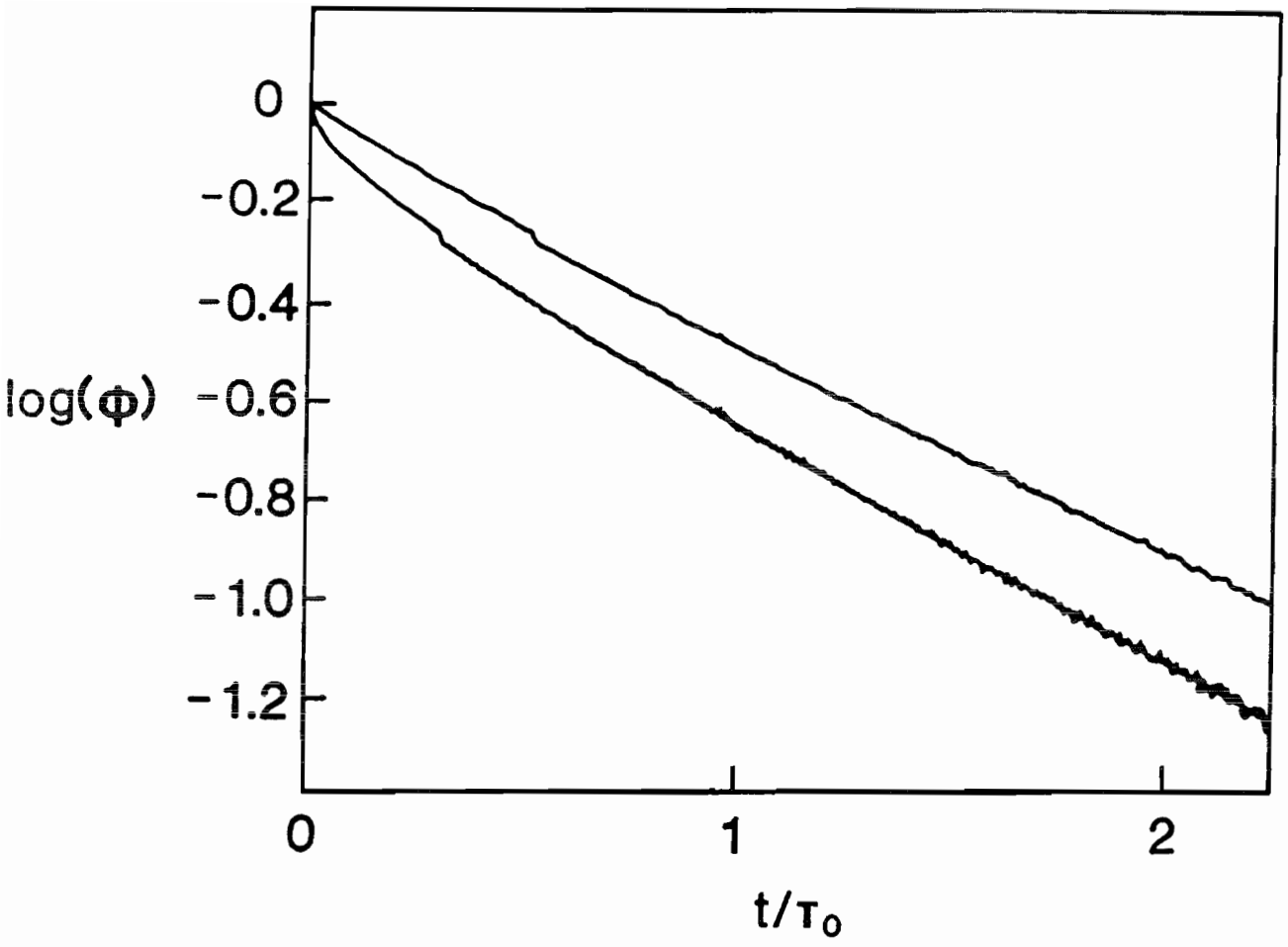

Figure 4.11 Yb^{3+} fluorescence as a function of time in Yb^{3+}-doped fibre (ND426, upper trace) and Yb^{3+}/Er^{3+}-doped fibre (ND414, lower trace). A theoretical curve following equation (4.23) has been fitted to the fluorescence decay curve of fibre ND414, which is not distinguishable from the measured curve.

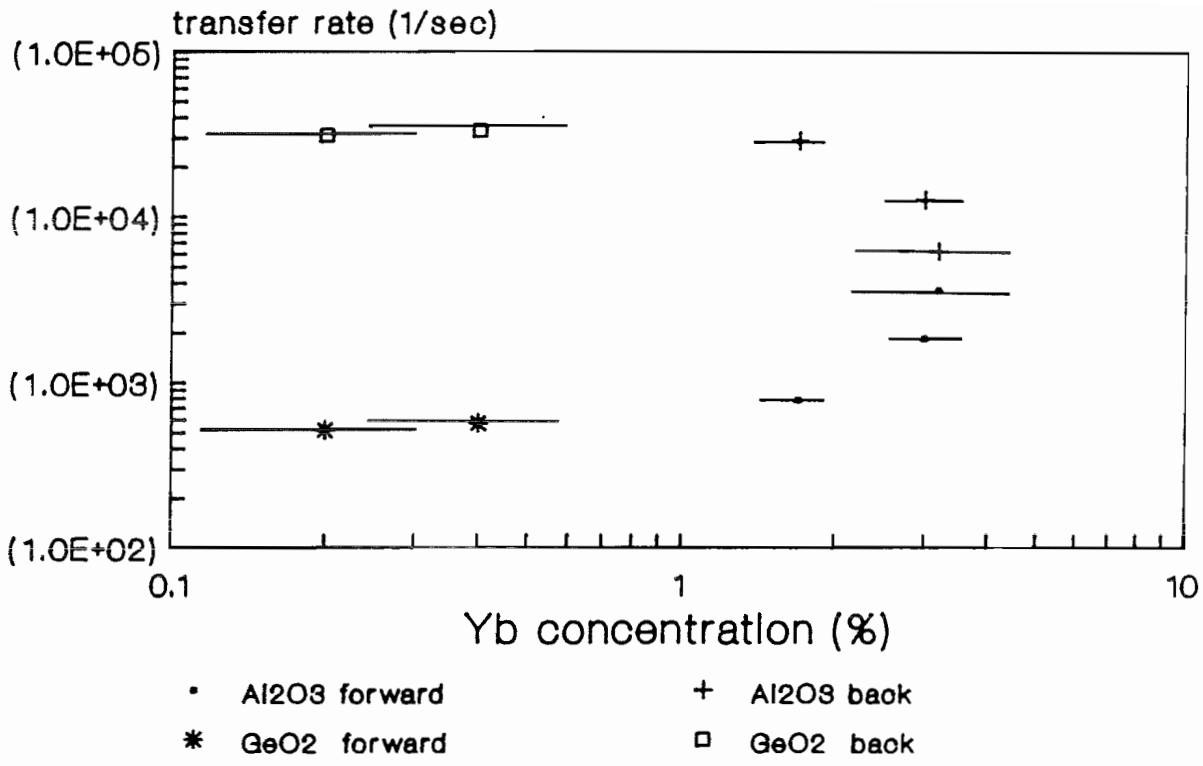

Figure 4.12 Forward and back-transfer rates for the Yb^{3+}/Er^{3+}-doped fibres.

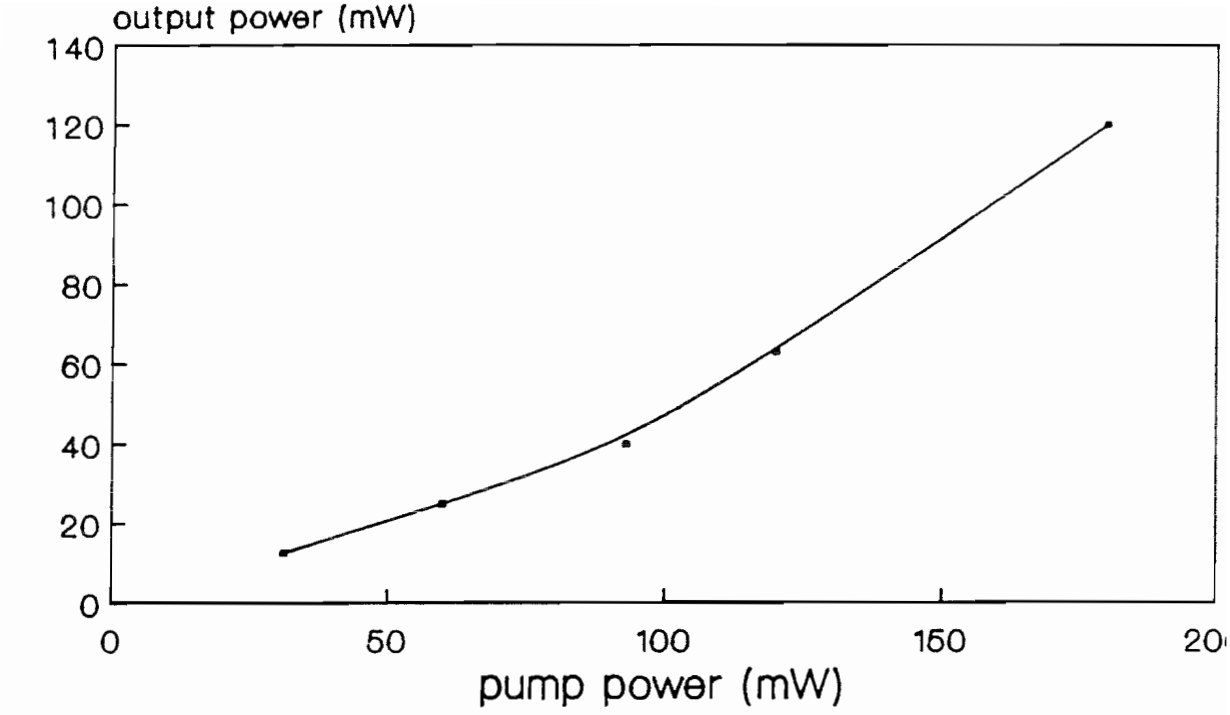

Figure 4.13 Output power versus pump power in fibre ND545 using a pump laser at 1064 nm. At a pump power of about 120 mW the Yb^{3+} absorption is totally bleached.

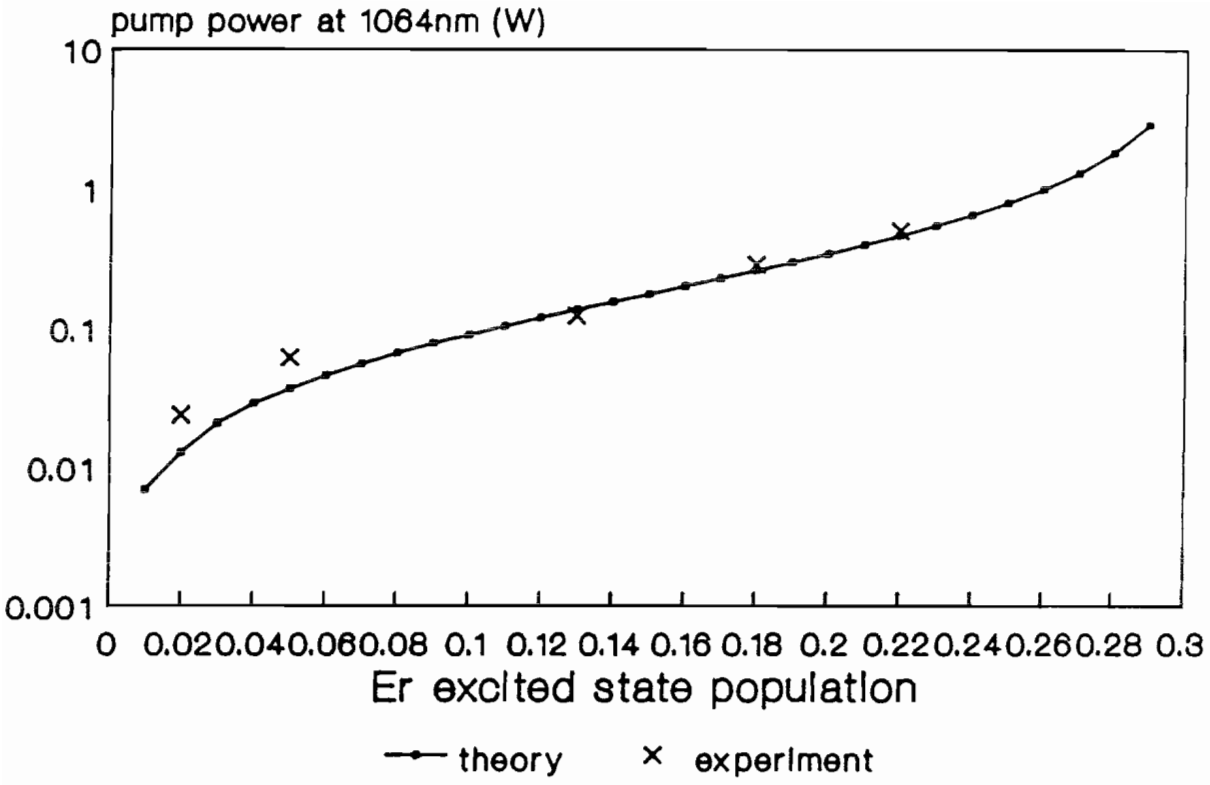

Figure 4.14 Fraction of excited Er^{3+} ions as a function of pump power at 1064nm in fibre ND385. A maximum excitation of only about 30% of the Er^{3+} ions is possible due to acceptor and Yb^{3+} absorption saturation.

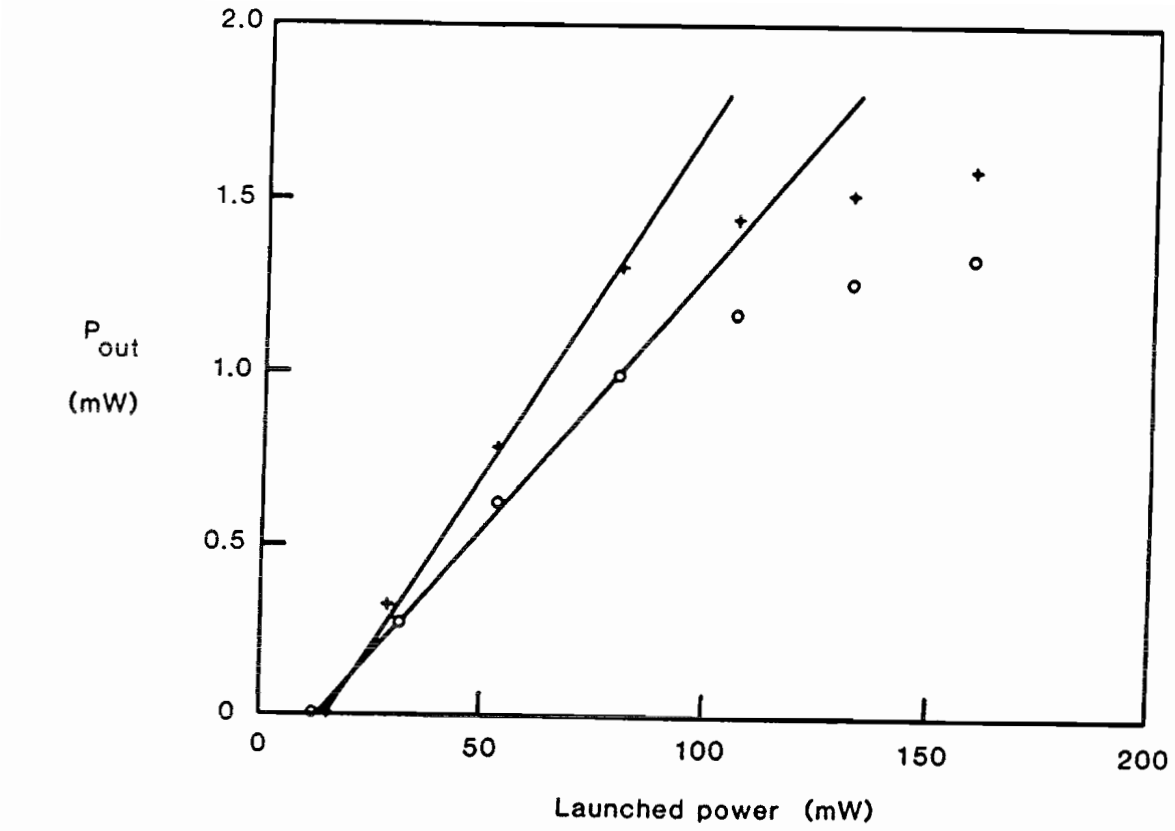

Figure 4.15 Laser output power versus pump power at 1064nm for fibre ND545 using a 27% (+) and 7% (o) output coupler.

Chapter 5: Second-Harmonic Generation in Optical Fibres

5.1 Introduction

Optical Fibres are an ideal material for the observation of nonlinear effects due to the high optical powers and interaction lengths that are possible inside a fibre core. This stimulated early workers to study nonlinear interactions in fibres and has led to the establishment of nonlinear optics as a major research area in fibre optics. The continuing interest in nonlinear optics has stemmed mainly from i) the limitations in power transmission in optical fibres resulting from nonlinear interactions, ii) the possibility of all-optical devices for signal processing and transmission and iii) optical frequency conversion. Here we are mainly concerned with optical frequency conversion. Extensive reviews of i) and ii) may be found elsewhere[1]. Frequency conversion is of particular interest for extending the wavelength regions that may be generated with semiconductor-laser pumped wavelength-tunable fibre lasers, which at present are limited to operation around 920nm, 1080nm and 1540nm[2]. The extension of operation to longer wavelengths via stimulated Raman scattering is easily achievable. Using a Nd-Yag laser emitting at 1.064μm, wavelengths from 1.064μm to 2.1μm have been so obtained[3]. The extension of operation to shorter wavelengths may be achieved via four-wave mixing, which, however, is difficult to accomplish in fibres, since phasematching of the fundamental with the Stokes and anti-Stokes lines is required[4,5]. The maximum frequency-shift obtainable for the efficient generation of frequency-upconverted light is about 1000cm^{-1} to 4000cm^{-1} in standard fibres[6]. The frequency-shift is limited by the requirement that material and waveguide dispersion have to be compensated in order to satisfy the phasematching condition. Frequency-upconversion by second-harmonic generation (SHG), on the other hand, provides a frequency-shift of 9390cm^{-1} (pump at 1.064μm), where phasematching is easily achieved by

optically writing nonlinear second-order susceptibility gratings into the fibre or by externally modulating an induced nonlinearity.

5.2 Review of Second-Harmonic and Sum-Frequency Generation in Optical Fibres

The first observation of sum-frequency generation in an optical fibre was made in 1979[7]. The efficiency achieved with optical powers of ≈ 70kW in the fibre core was very low ($<10^{-7}$%) due to the lack of efficient phasematching. The observation may now be attributed to quadrupole second-harmonic generation. In 1981, phasematched sum-frequency generation was claimed in slightly multi-moded optical fibres[8,9]. Phasematching by compensating material with waveguide dispersion in a germanosilicate fibre with 5.9% germania concentration was quoted. However, a simple analysis shows that at least 11% germania concentration is necessary to achieve the required refractive-index difference between core and cladding in order to compensate for material dispersion. It seems probable, rather, that phasematching between cladding modes was accomplished. In 1985 sum-frequency generation was reported in polarisation-preserving fibres, with a total conversion efficiency of about 0.5-1% with an input power of 22kW[10]. The sum-frequency output was broad band. Thus four-wave mixing appears to be responsible for the effect.

In 1986 the first observation of true efficient SHG was made by Österberg and Margulis[11]. In this, high intensity light (20-70kW peak optical power) delivered from a mode-locked and Q-switched YAG laser was launched into an ordinary telecommunications fibre doped with <1% phosphorus and during hours of continuous irradiation a slow build-up of SH light was observed until the SH conversion efficiency eventually saturated at about 0.5%. Optimisation of fibre parameters and optical input coupling led to SH conversion efficiencies of 5% with a peak optical input power of 50kW[12,13]. These results

were remarkable, since SHG in glass is forbidden due to its inversion symmetry. Thus only very weak SHG due to electric quadrupole or magnetic dipole moments[14,15] is normally observable.

The results of Österberg and Margulis were explained at Southampton by the postulation of an optically written $\chi^{(2)}$ grating in the fibre that provides phasematching of the fundamental and SH wave and the required non-inversion symmetry, thus giving rise to high conversion efficiencies[16]. This suggestion was triggered by work the author was involved in, namely electric-field-induced SHG (ESHG) which was carried out at the same time. In ESHG, phasematching may also be achieved by the spatial modulation of the effective second-order nonlinearity induced by the dc electric field applied alongside the fibre.

This similarity was taken even further by Stolen and Tom[17] who realised that in a fibre, nonlinear mixing of two mutually coherent seed waves, i.e. a fundamental (at 1.064μm) and its SH wave (at 532nm), gives rise to a spatially periodic dc electric field. The periodicity of the dc-field is then exactly the same as the $\chi^{(2)}$ grating period required to provide phasematching. Stolen and Tom suggested that this induced electric field is the origin for an alignment mechanism for defect centres in the fibre, breaking the non-inversion symmetry and providing the required spatial modulation of the so-generated second-order nonlinearity.

In summer 1987 wavelength tunable SHG was demonstrated at Southampton[18]. In this, it was shown that fibre birefringence may be used to modify the phasematching conditions giving efficient SHG at wavelengths other than the seeding wavelength. Conversion efficiencies of 5% were in fact achieved for pump wavelength varying from 1.036 to 1.090μm with optical pump powers of about 1kW. In November 1987 Farries demonstrated the so far highest SH conversion efficiency of 13% in a highly birefringent

phosphorus-doped fibre with a launched optical peak power of 950W[19].

In January 1988 the workers at Southampton university succeeded in aligning defect centres in optical fibres by exciting them with high intensity light and simultaneously applying a strong dc electric field[20]. In this a large second-order nonlinearity was created by using a cw Argon laser emitting at 488nm as the defect excitation source. Further, it was shown that high intensity pulsed light may also be used for the excitation and orientation of defect centres, where blue wavelengths were more efficient in creating second-order nonlinearities than red wavelengths. Subsequently, the author developed a technique by which the defect-centre-induced second-order nonlinearity could be accurately measured and verified that saturation mechanisms limit the achievable $\chi^{(2)}$ in fibres. The results showed that the nonlinear susceptibilities generated by an internal orientation field are about hundred times smaller than created by an external alignment field.

In February 1988 Li[21] demonstrated the Pockels effect in poled optical fibres and later that month the author demonstrated efficient SHG in poled fibres by modal phasematching[22,23]. In June 1988 the author was able to measure the excitation spectrum of $\chi^{(2)}$ in the blue/green part of the spectrum and showed that poling of germanosilicate fibres is strongly related to Ge E' centres.

These results indicate that the full potential for efficient SHG in fibres has not yet been approached. It is hoped that by optimising fibre design and fibre materials, a further increase in conversion efficiency may be possible at even lower pump powers. SHG in optical fibres looks to have a considerable potential for applications such as in-line or intracavity frequency-doubling of fibre lasers. Further, the study of second-order nonlinear phenomena in fibres may lead to a better

understanding of colour centres and photochromic effects in fibres.

5.3 Nonlinear Polarisation

In linear optics the transmission of electromagnetic waves is assumed to be governed by an induced electric dipole moment leading to a polarisation in the transmission medium, which reacts linearly to the electric field strength. Most processes in nonlinear optics may be accounted for by introducing a nonlinear induced polarisation, which is proportional to the square or the cube of the electric field. In this, the polarisation due to induced dipole moments may be expanded in powers of the electric field[24,25]

$$P_i = \chi^{(1)}_{ij} E_j + \chi^{(2)}_{ijk} E_j E_k + \chi^{(3)}_{ijkl} E_j E_k E_l, \qquad (5.1)$$

where $\chi^{(1)}$, $\chi^{(2)}$, $\chi^{(3)}$ are the components of the first, second and third-order susceptibility tensor and $E_{j,k,l}$ are the components of the total electric field and Einstein's notation is used, i.e. duplicated indices are summed over. For spatially varying electric fields, a nonlinear polarisation second-order in E is also created by induced magnetic dipole and electric quadrupole moments (see section 5.9), which is small compared to the induced dipole polarisation and was neglected here. The electric field and the polarisation are conveniently written as

$$E_j = E'_j \exp(ik_j r - i\omega t)$$

and a similar form for the polarisation.

In general, a propagating electromagnetic field consists of a number (finite or infinite) of Fourier components oscillating at fixed frequencies $\omega_{i1}....\omega_{in}$. The second order susceptibility tensor then leads to the mixing of any pair of frequency components forming a wave at the mixed frequency. Similarly, the third-order

susceptibility tensor leads to the mixing of three waves. In particular, if two waves of frequency ω_1 and ω_2 propagate inside the medium along the i-axis, the $\chi_{ijk}^{(2)}$ component of $\chi^{(2)}$ is responsible for the generation of the sum-frequency wave propagating along the i-axis with a frequency $\omega=\omega_1+\omega_2$. The i-component of the polarisation at ω is then specifically written as

$$P_i^{\omega} = \chi_{ijk}^{(2)} \ (\omega=\omega_1+\omega_2) E_j^{\omega 1} E_k^{\omega 2},$$

where the frequencies involved in the mixing process have been included in the symbol for $\chi^{(2)}$.

5.3.1 Symmetries of Nonlinear Susceptibilities

In most applications of nonlinear optics, optical wavelengths are used, which are far from electronic or phonon-resonances. In this case, the effect of absorption may be neglected in the form of the nonlinear susceptibility tensor and the following permutation symmetries are valid

$$\begin{aligned} & \chi_{ijk}^{*}(\omega=\omega_1+\omega_2) \\ &= \chi_{jki}(\omega_1=-\omega_2+\omega) \\ &= \chi_{kij}(\omega_2=\omega-\omega_1) \end{aligned} \qquad (5.2)$$

Similar symmetries also hold for higher-order nonlinear susceptibility tensors.

The number of independent elements of $\chi^{(2)}$ and $\chi^{(3)}$ are 27 and 81 respectively. If dispersion of the nonlinear susceptibility tensors may be neglected, the permutation symmetries become independent of frequency. The number of independent elements of $\chi^{(2)}$ and $\chi^{(3)}$ then reduces to 10 and 15 respectively[26].

The number of independent susceptibility tensor components are further reduced by structural symmetries, which in crystals may be deduced from transformations,

such as rotations (about certain axes) and mirror operations that map the crystal structure into itself. Under these transformations the length of a space vector remains invariant. The independent elements of $\chi^{(2)}$ and $\chi^{(3)}$ for different crystal symmetries are listed elsewhere[24,25]. In particular, for isotropic materials such as glass it follows that $\chi^{(2)}$ is zero, since an inversion operation transforms a uniform structure into itself and it holds with I being the inversion operation

$$I:\chi_{ijk} = -\chi_{ijk} = \chi_{ijk}, \tag{5.3}$$

which is valid only when all elements of χ_{ijk} are zero.

The lowest order nonlinear susceptibility tensor for isotropic materials is therefore $\chi^{(3)}$ with, as is easily shown, 3 independent tensor elements, i.e.

$$\chi_{1122} \qquad \chi_{1221} \qquad \chi_{1212},$$

where $\chi_{1111} = \chi_{1122} + \chi_{1221} + \chi_{1212}$.

However, for isotropic materials an effective $\chi^{(2)}$ may still be defined due to induced nonlinear magnetic dipole and electric quadrupole moments. Since they are too small for any practical exploitation, they are only briefly discussed in section 5.9.

5.4 Electromagnetic-Wave Propagation in Nonlinear Media

The wave equation governing optical wave propagation in a medium may be obtained from Maxwell's equations. Using cgs-units the wave-equation is written as[24]

$$\left[\mathrm{rot}(\mathrm{rot}(\,)) + \frac{1}{c^2}\frac{\partial^2}{\partial t^2}\right]\mathbf{E}(\mathbf{r},t) = -\frac{4\pi}{c^2}\frac{\partial^2}{\partial t^2}\mathbf{P}(\mathbf{r},t), \tag{5.4}$$

where the polarisation is given by 5.1. If an infinite plane wave approximation is valid (infinite in time and space), the electric field and the polarisation may be

decomposed into Fourier components in ω and with (5.1) we obtain

$$E(r,t) = \sum_i E_i(k_i,\omega_i) \qquad (5.5a)$$

$$P(r,t) = \sum_i \chi^{(1)} E_i(k_i,\omega_i) + \sum_j P^{NL}(k_j,\omega_j), \qquad (5.5b)$$

where P^{NL} corresponds to the nonlinear polarisation arising from second and higher-order terms in (5.1). The nonlinear polarisation in equation (5.5b) leads to a coupling of all Fourier components of the optical wave with each other. In particular, the wave equation governing the nonlinear generation of a wave propagating at a frequency ω may be written as

$$\left[\mathrm{rot}(\mathrm{rot}(\,)) + \frac{\omega^2}{c^2}\varepsilon\cdot\right] E(k,\omega) = \frac{4\pi\omega^2}{c^2} P^{NL}(k_j,\omega_j=\omega), \qquad (5.6)$$

where ε is the linear dielectric tensor. Similar equations also hold for the propagation of the fundamental waves at the frequencies ω_i, which together with (5.6) give a system of coupled-wave equations describing the propagation of optical waves under the influence of a nonlinear polarisation. Due to energy conservation a set of N frequency components ω_i must add up to ω, where N is the order of the nonlinear interaction. In order to obtain a strong coupling of the waves at ω_i to a wave at ω, the wavevectors k_i must also add up to k, i.e. the interaction must be phasematched.

The electric field propagating at a frequency ω may be expressed as

$$E^{\omega}(k,z) = E^{\omega}(z)\exp\{i(k^{\omega}z-\omega t)\}. \qquad (5.7)$$

Neglecting longitudinal field components of $E^{\omega}(k,z)$, the spatial derivative of $E^{\omega}(k,z)$ in (5.6) may be written as

$$\text{rot}(\text{rot}(\mathbf{E})) = -\Delta\mathbf{E} = -(\partial^2\mathbf{E}/\partial z^2) = -\exp(i(kz-\omega t)[\partial^2/\partial z^2 + i2k\partial/\partial z - k^2]E^{\omega}(z) \tag{5.8a}$$

and

$$-k^2\mathbf{E} + (\omega^2/c^2)(\varepsilon\cdot\mathbf{E}) = 0. \tag{5.8b}$$

Using the slowly varying amplitude approximation

$$\left| \frac{\partial^2 E(z)}{\partial z^2} \right| << \left| k \frac{\partial E}{\partial z} \right| \tag{5.9}$$

and writing the nonlinear polarisation in terms of its amplitude $P^{NL}{}_{\omega}(z)$ and wavevector $k_p{}^{\omega}$

$$P^{NL}(k,\omega) = P^{NL}_{\omega}(z)\exp\{i(k^{\omega}_p z-\omega t)\} \tag{5.10}$$

(5.6) reduces to

$$\frac{\partial E^{\omega}(z)}{\partial z} = \frac{i2\pi\omega}{n(\omega)c} P^{NL}_{\omega}(z)\exp[i(k^{\omega}_p-k^{\omega})z], \tag{5.11}$$

where $n(\omega)$ is the refractive index at frequency ω. An expression for the complex conjugate $E^{\omega}(z)^*$ may be obtained similarly.

Assuming a constant polarisation along the fibre we may integrate (5.11) directly and obtain

$$E^{\omega}(z) = \frac{2\pi\omega}{n(\omega)c} P^{NL}_{\omega} \frac{\exp[i(k_p-k^{\omega})z-1]}{(k_p-k^{\omega})}. \tag{5.12}$$

The intensity of the generated wave is then given by

$$I^{\omega}(z) = \frac{cn}{8\pi} E^2$$

$$= \gamma P_{\omega}^{NL}(P_{\omega}^{NL})^{*}\mathrm{sinc}^{2}(\tfrac{1}{2}\Delta kz), \qquad (5.13)$$

where

$$\gamma = \frac{\pi z^{2}\omega^{2}}{2n(\omega)c}.$$

5.5 Nonlinear Propagation in Optical Fibres-Overlap Integrals

Owing to the tight confinement of the optical modes in fibres, an infinite plane-wave approximation is no longer valid when nonlinear wave propagation is analysed. In particular, optical waves may propagate in different order fibre modes and in this case (5.11) needs some modification.

The electric field of a propagating fibre mode m may be written as[27]

$$E_{m}(\omega) = a_{m}(\omega)e_{m}(\omega,x,y)\exp[i\beta_{m}(\omega)z]\exp(-i\omega t), \qquad (5.14)$$

where $\beta_{m}(z)$ is the propagation constant. By integrating the Poynting vector over the mode cross section, the modes may be normalised such that the power in mode m is given by

$$P_{m} = \frac{cn}{8\pi} a_{m}a_{m}^{*}. \qquad (5.15)$$

The correct form for the normalised fibre modes may hence be calculated from an arbitrary mode notation Ψ_{m} as

$$e(\omega_{m},x,y) = \frac{\Psi_{m}}{\left(\iint \Psi_{m}\Psi_{m}^{*}dA\right)^{1/2}}. \qquad (5.16)$$

Assuming the nonlinear polarisation at the frequency ω is due to the mixing of n pump waves, the i-component of $P^{NL}(\omega=\omega_{1}+\ldots+\omega n)$ may be written as

$$(P_{\omega}^{NL})_i = \alpha\chi^{(n)}_{iil\ldots in}(E^{\omega 1}_{m1})_{i1}\times\ldots\times(E^{\omega n}_{mn})_{in}, \qquad (5.17)$$

where $(E^{\omega n}{}_{mn})_{in}$ is the electric field along the in direction in mode mn and of frequency ωn, α is a constant and the nonlinear susceptibility is assumed to be non-uniform across the fibre cross section. Assuming $\Delta k=0$, equation (5.13) is then correctly written as[14]

$$(P_m^{\omega}(z))_i = \gamma \iint_{-\infty}^{\infty} (e_m)_i^{*}(P_{\omega}^{NL})_i dxdy, \qquad (5.18)$$

where $(P_m{}^{\omega}(z))_i$ is the total power in the m'th fibre mode along the direction i and γ has been defined in (5.13). (5.18) may be written in the form

$$(P_m^{\omega}(z))_i = \gamma\left(\frac{8\pi}{c}\right)^n \frac{1}{A^{n-1}} \frac{\left[\bar{\chi}^{(n)} O_m^{(n)}\right]^2}{n(\omega_1)\times\ldots\times n(\omega_n)} P^{\omega 1}_{m1}\times\ldots\times P^{\omega n}_{mn}, \qquad (5.19)$$

where $\bar{\chi}^{(n)}$ is the n-th order nonlinear susceptibility averaged over the equivalent core area A and we have defined an overlap integral as

$$O_m^{(n)} = \frac{(A^{n-1})^{1/2}}{\bar{\chi}^{(n)}} \iint_{-\infty}^{\infty} \chi^{(n)}_{iil\ldots in}(e_m^{\omega})_i^{*}(e^{\omega 1}_{m1})_{i1}\cdots(e^{\omega n}_{mn})_{in} dxdy. \qquad (5.20)$$

5.6 Phasematching Techniques for SHG in Optical Fibres

In order to obtain efficient SHG in a medium, two conditions have to be satisfied. These are

i) An effective $\chi^{(2)}$ must be present in the fibre and

ii) Phasematching between the fundamental and the SH wave must be possible

The various methods available for inducing large values for $\chi^{(2)}$ are described in sections (5.8)-(5.10). For the discussion of phasematching techniques for SHG it is necessary only to assume that a $\chi^{(2)}$ is present in the fibre. In this case a pump wave at frequency ω is converted into a wave at frequency 2ω. Since the conversion efficiency is small in optical fibres (<10%) it is sufficient to make the no pump-depletion approximation, i.e. to assume that the intensity of the pump wave remains constant in this process.

The wavevector of the nonlinear polarisation at 2ω is then given by twice the wavevector of the pump wave, i.e.

$$k_p^{2\omega} = 2k^{\omega}. \qquad (5.21)$$

Phasematching may be achieved by arranging the wavevector of the nonlinear polarisation at 2ω of a free wave propagating at 2ω to equal the wavevector at ω, i.e.

$$2k^{\omega} = k^{2\omega}. \qquad (5.22)$$

This may be achieved by appropriate mode selection for the pump and SH wave. Fibre birefringence could theoretically also be used for adjusting the phase velocity of these waves. However, at present the available birefringence in fibres is not high enough to make this technique practicable.

Phasematching may also be obtained by introducing a periodic structure into the fibre to compensate for the difference in phase velocities. The phasematch condition is then written as

$$G = k^{2\omega} - 2k^{\omega}, \qquad (5.23)$$

where $G=2\pi/\Lambda$ is the grating vector and Λ its period. Most effective for phasematching are gratings in $\chi^{(2)}$. In this the magnitude of $\chi^{(2)}$ is modulated or the

direction of $\chi^{(2)}$ periodically reversed. Refractive index gratings are inferior compared to $\chi^{(2)}$ gratings due to the small modulations in refractive index that are possible in fibres. In addition, internal index gratings produced by standing wave patterns in fibres as described by Hill et al.[28] cannot be used since the grating period for phasematching is too small, thus only relatively inefficient gratings accessing the evanescent field as described by Russell et al.[29] are viable, which also couple light out of the fibre.

All these phasematching techniques suffer from fibre imperfections that limit coherent in-phase propagation of the fundamental and SH-wave to only a few centimetres. Coherence lengths of a few tens of centimetres are possible via an internally written $\chi^{(2)}$-grating as demonstrated in section (5.7.2.2).

5.6.1 Modal Phasematching

Unlike in four-wave mixing experiments, modal phasematching for SHG is difficult to achieve in fibres due to the much larger difference in optical frequencies of the propagating waves. From (5.22) it follows that the condition for phasematching is

$$n(\lambda/2) = n(\lambda), \qquad (5.24)$$

where $n(\lambda)$ is the effective index of a propagating fibre mode at vacuum wavelength λ. It is therefore necessary to ensure that the effective index $n(\lambda)$ of the pump wavelength and the effective index $n(\lambda/2)$ of the SH are the same. This may be achieved by a special fibre design, such that the pump wavelength propagates in the fundamental mode and the SH in a higher-order mode. In this case waveguide dispersion may compensate chromatic dispersion between the two wavelengths. The effective index of a fibre mode may be calculated from the normalised propagation constant b[30], i.e.

$$b = \frac{n^2(\lambda) - n_{cl}^2(\lambda)}{n_{co}^2(\lambda) - n_{cl}^2(\lambda)} \qquad (5.25a)$$

where $n_{co}(\lambda)$, $n_{cl}(\lambda)$ are the refractive indices of the fibre core and cladding glass, which may be obtained from a standard Sellmeier expansion. b is given by the V-value of the propagating fibre mode

$$b = 1 - \frac{[u(V)]^2}{V^2} \qquad (5.25b)$$

where u(V) may be calculated by solving the eigenvalue equation[27] or using an approximate expression as given by Gloge[30]. The number of modes that may be phasematched to each other is limited by symmetry. In particular, it follows directly from (5.20) that for a uniform $\chi^{(2)}_{111}$ phasematching is only possible from either a symmetric or asymmetric fundamental mode to only a symmetric SH mode. The reason for this is that the overlap integral is zero unless phasematching between modes of the correct symmetry is obtained. A fundamental wave in the LP_{01} mode may thus couple only to higher order LP_{0n} modes. Fig. (5.1) shows the variation of the effective index as a function of V-value for the lower-order fibre modes for a pump wavelength of 1.064μm and its SH. A typical fibre with the high numerical aperture NA=0.32 was chosen. In this particular fibre the lowest-order phasematch is obtained for the LP_{01} as the pump and the LP_{02} mode as the SH for a V-value at the fundamental wavelength of V=2.0. The required core radius to give this V-value is then calculated from

$$a = \frac{\lambda V}{2\pi NA} \qquad (5.26)$$

as a=1.1μm. In general it is necessary to produce fibres with a NA>0.25 in order to ensure that waveguide dispersion may compensate chromatic dispersion.

An example of modal phasematching is shown in Fig. (5.2). In this a fibre with a NA=0.25 was manufactured

and pulled to the required core radius specification (a=2.3μm) to phasematch the fundamental LP_{01}-mode with the SH LP_{02} mode. A $\chi^{(2)}$-nonlinearity was induced in the fibre via a defect poling technique (see section 5.10) and the SH conversion efficiency measured as a function of infrared pump wavelength. The fundamental wave phasematches to its SH at a pump wavelength of 1.208μm. The large half-width of the phasematch peak of about 1nm is due to fibre imperfections and may be used to estimate the length of coherent propagation of the fundamental and SH wave as explained in section (5.7.1.1).

The overlap integral for phasematched LP_{01} and LP_{0n} modes is always small ($\approx$10%), since the two modes are almost orthogonal. The reason may be seen immediately if we consider the following. In order to obtain phasematching, the fundamental wave must propagate in the fundamental mode and the SH-wave must propagate in the higher-order mode. Therefore, the V-value of the higher order mode is twice that of the fundamental mode. In expression (5.20) for the overlap integral the fundamental wave has to be squared, which is approximately equivalent to doubling the V-value. Hence (5.20) results in the field overlap integral of two almost orthogonal waves, which is a small number. The overlap integral may be increased, if a nonlinearity is present only in the fibre core, which is achieved by using different materials for fibre core and cladding. In Fig. 5.3 the overlap integral is plotted for phasematching between the LP_{01}, LP_{02} and LP_{03} modes for a range of V-values, assuming both a uniform nonlinearity, i.e. ($\chi^{(2)}= \chi^{(2)}_{111}$), and a nonlinearity present only in the fibre core. Here the eigenvalue equation was solved in the weak-guidance approximation[30] and the effect of dispersion was neglected, since it was found to lead to relative errors of less than 5%. It may be seen that far from cut-off of the higher-order modes, the overlap integrals for the two $\chi^{(2)}$'s tend to have the same value, where if the higher-order modes are close to cut-off, the overlap integral for the uniform $\chi^{(2)}$ approaches zero

and the ratio of the two overlap integrals becomes large. This behaviour is expected since for large V-values all optical power is propagating in the fibre core and therefore the two overlap integrals are the same. Close to cut-off the higher-order modes spread out, causing the difference in overlap integrals.

5.6.2 Phasematching by Externally Induced Modulation of $\chi^{(2)}$

Phasematching may be achieved by an external periodic modulation of $\chi^{(2)}$. It is a well known technique in integrated optic wave-guides[31] and gases[32], but has, however, not yet been demonstrated in fibres due to technical difficulties. In principle, phasematching by modulation of $\chi^{(2)}$ should be better than modal phasematching, since the modulation of $\chi^{(2)}$ enables phasematching between the same-order modes and thus ensures overlap integrals between the fundamental and SH-wave of the order of unity.

The amplitude of the nonlinear polarisation due to a modulation of $\chi^{(2)}$ may be written as

$$P_{2\omega}^{NL} = \chi^{(2)} E^{\omega} E^{\omega} \ (C + M\cos Gz), \qquad (5.27)$$

where M ($0 \leq M \leq 1$) is the modulation depth and C ($0 \leq C \leq 1$) is the dc-offset of $\chi^{(2)}$. The phase of the nonlinear polarisation is given by (5.21). For negligible pump depletion the expression for $E^{2\omega}$ as a function of z is obtained by inserting (5.27) and (5.21) into (5.11)

$$\frac{\partial E^{2\omega}}{\partial z} = i\zeta M\left[\frac{2C}{M} e^{i(2k^{\omega}-k^{2\omega})z} + e^{i(G+2k^{\omega}-k^{2\omega})z} + e^{i(2k^{\omega}-k^{2\omega}-G)z}\right] \qquad (5.28)$$

where

$$\zeta = \frac{4\pi\omega}{n(2\omega)c} \chi^{(2)} E^{\omega} E^{\omega}.$$

The first and third term on the right hand side of (5.28) may now be neglected, since they are highly dephased and

do not contribute to the build-up of $E^{2\omega}$. The solution for $E^{2\omega}$ is obtained from (5.28) as

$$E^{2\omega}(z) = \frac{\zeta M}{\Delta k}\,[\exp(i\Delta kz)-1] \qquad (5.29)$$

where $\Delta k=G-(k^{2\omega}-2k^{\omega})$. The power in the SH-wave is then given by

$$P^{2\omega}(z) = 4\xi M^2\ P^{\omega}_{m1}P^{\omega}_{m2}\,\mathrm{sinc}^2\left[\frac{1}{2}\Delta kz\right], \qquad (5.30)$$

where

$$\xi = \frac{32\pi^3\omega^2z^2}{n(2\omega)\varepsilon(\omega)c^3A}\left[\bar{\chi}^{(2)}O_m\right]^2.$$

Note that if the fundamental wave propagates in only one mode, $P^{\omega}_{m1}=P^{\omega}_{m2}=(1/2)P^{\omega}$, where P^{ω} is the total power in the fundamental mode. Again, as explained in section (5.7.1.1) fibre imperfections limit coherent propagation of the fundamental and SH wave in optical fibres. It may also be argued that phasematching by modulation of $\chi^{(2)}$ is not a real phasematching process since the phase velocity of the fundamental and SH wave are still different. The important feature of the process is that the nonlinearity is strong when the fundamental and SH-wave are in phase and weak in the opposite case, thus acting as a net source for the SH-wave.

5.6.3 Phasematching via an Internally-Written $\chi^{(2)}$-Grating

The method for producing the longest coherence lengths between a fundamental wave and its SH in optical fibres is by internally writing a $\chi^{(2)}$ grating structure into the fibre via a four-wave mixing process (involving $\chi^{(3)}$)[17]. In this, two mutually coherent optical waves, i.e. a fundamental and its SH, are launched into the fibre. Following Stolen and Tom[17] we call these waves seed waves. We denote the seed SH with $E_0{}^{2\omega}$, where the

subscript is added to indicate that it is a free wave. Four-wave mixing of the fields at ω and 2ω via $\chi^{(3)}$ now generates a dc polarisation in the optical fibre. Assuming, for simplicity, that both waves are plane polarised and parallel to each other the amplitude of the dc polarisation is obtained as

$$P_{dc}=\frac{1}{2}\chi^{(3)}_{1111}(0=-2\omega+\omega+\omega)[E_0^{2\omega}(z)]^{*}E^{\omega}(z)E^{\omega}(z)e^{-i\Delta kz}+c.c.. \tag{5.31}$$

As may be seen from (5.31) this dc polarisation produces a transverse dc electric field E_{dc} along the fibre, whose direction is periodically reversing. E_{dc} is obtained from the polarisation via

$$E_{dc} = -\frac{4\pi}{\varepsilon}P_{dc}, \tag{5.32}$$

where ε is the dielectric constant at zero frequency. Assuming typical optical input powers of 2kW and 100W respectively for the fundamental and SH wave into a 4μm diameter fibre, the electric field strength is obtained as E_{dc}=46V/cm. As explained in section (5.10), a second-order nonlinearity is then created in the fibre over a period of several minutes. Central to the process is the assumption that defect centres are excited by high intensity light, which may then align in the presence of a dc-field. This creates a dipole nonlinearity and hence a second-order nonlinear susceptibility. Since the dc-field is periodically reversing its direction, the $\chi^{(2)}$ nonlinearity is also periodically reversing its orientation and a $\chi^{(2)}$ grating structure is created. The amplitude of this $\chi^{(2)}$-grating is assumed to be proportional to first order to E_{dc}, i.e.

$$\chi^{(2)} = \kappa E_{dc}, \tag{5.33}$$

where κ is a constant. Since the induced $\chi^{(2)}$ has the correct periodicity for phasematching the fundamental wave at ω to a SH wave generated by the induced $\chi^{(2)}$ internally in the fibre, two SH waves are then

propagating in the fibre: the free (or seed) SH wave launched into the fibre and the driven SH wave generated by the induced $\chi^{(2)}$. The driven SH wave also interacts with the pump wave to produce another dc polarisation generating its own $\chi^{(2)}$. However, the $\chi^{(2)}$ induced by the driven SH-wave lags in phase compared to the $\chi^{(2)}$ induced by the free wave leading to an equilibrium condition, at which the visibility of the $\chi^{(2)}$ grating varies sinusoidally along the fibre, thus limiting the achievable SH conversion efficiency. The amplitude of the nonlinear polarisation at 2ω generating the driven SH wave is given by

$$P^{NL}_{2\omega}(z) = \chi^{(2)}E^{\omega}(z)E^{\omega}(z) \qquad (5.34)$$

and the wavevector is given by (5.21). Inserting (5.31) and (5.33) into (5.34), the full expression for $P^{NL}{}_{2\omega}$ may now be obtained. By inserting (5.34) into (5.11) we get the following two coupled wave equations for the evolution of the driven wave $E^{2\omega}$ in the fibre

$$\frac{\partial E^{2\omega}}{\partial z} = i\alpha[E^{2\omega} + (E^{2\omega})^{*}e^{-2i\Delta kz}] \qquad (5.35a)$$

$$\frac{\partial (E^{2\omega})^{*}}{\partial z} = -i\alpha[(E^{2\omega})^{*} + E^{2\omega}e^{2i\Delta kz}], \qquad (5.35b)$$

where

$$\alpha = \beta E^{4}(\omega)$$

and

$$\beta = \frac{4\pi\omega}{n(2\omega)c}\,\kappa\chi^{(3)}_{1111}.$$

The solution for $2\alpha<\Delta k$ is given by

$$E^{2\omega}(z) = E_0^{2\omega} e^{i\Delta kz}\left[\cos(gz) - i\left(\frac{\Delta k - 2\alpha}{g}\right)\sin(gz)\right], \quad (5.36)$$

where $g=(\Delta k^2 - 2\alpha\Delta k)^{1/2}$. It is instructive to evaluate the dc-field that is generated by the total SH-field given by (5.36). Inserting (5.36) into (5.31) we obtain at equilibrium

$$P_{dc} \approx \cos(gz)\cos(2\Delta kz) + (1-2\alpha/\Delta k)^{1/2}\sin(gz)\sin(2\Delta kz).$$

For $\alpha << \Delta k$ this is conveniently written as

$$P_{dc} \approx \cos[(\Delta k-\alpha)z] - (\alpha/\Delta k)\sin[(\Delta k-\alpha)z]\sin(2\Delta kz). \quad (5.37)$$

The second term of the left hand side of (5.37) is small and may be neglected. However, the first term shows that the coefficient α leads to a phase delay of the $\chi^{(2)}$ grating, which reduces the effective coherence length for SHG to π/α. The SH conversion efficiency generated once the seed SH is switched off may be obtained by subtracting $E^{2\omega 0}$ from (5.36) and is given by (for $\alpha << \Delta k$)

$$I^{2\omega} = 4I_0^{2\omega}\,\frac{I^2(\omega)}{I_0^2(\omega)}\,\sin^2(\alpha z/2). \quad (5.38)$$

It may be seen that provided the fundamental wave has the same intensity in both the seeding and reading process, the induced SH may then not be larger than the seed SH.

The theory of internally-written $\chi^{(2)}$ gratings as proposed by Stolen and Tom[17] and summarised here is still central to the understanding of SHG by alignment of defect centres (see section (5.10)). However, the requirement that defect centres have to be excited in order to make their alignment possible was not discussed by these authors and is included here. Several aspects of the physical process behind the mechanism are not yet understood. In particular, this theory does not give a convincing explanation as to why $\chi^{(2)}$ gratings may be formed over a long period of time, when only a

fundamental wave is launched. The only SH light present in this case is due to quadrupole and magnetic dipole nonlinearities. The intensity of the so generated SH-wave amounts to only 100pW for a pump power of 2kW (fibre radius=4μm). The mixing of these waves then gives rise to a dc electric field of only 33μV/cm. As seen in section (5.10.3.2), the magnitude of the induced field is much too small for the alignment of defect centres. In addition, the effects of linear and nonlinear limiting mechanisms have not been taken into account. A detailed description of coherence and competing nonlinear effects is given in section (5.7).

5.7 Limiting Mechanisms

Several mechanisms limit coherent propagation of the fundamental and the SH wave in optical fibres. Due to the high optical powers used in the fibres not only linear, but also nonlinear processes are important. The linear limiting mechanisms are temporal coherence due to the finite spectral width of the waves, spatial coherence due to fibre non-uniformities and fibre absorption arising from colour centres in the fibre. The nonlinear mechanisms are the intensity-dependent refractive index, self-phase modulation, stimulated Brillouin and Raman scattering, optical breakdown and damage.

5.7.1 Linear Limiting Mechanisms

5.7.1.1 Temporal Coherence

Finite temporal coherence is the main factor limiting the lengths of internally-written $\chi^{(2)}$-gratings. Spatial non-uniformities are automatically compensated by the optical writing process and have to be considered only when $\chi^{(2)}$-gratings are externally written or in modal phasematching. Therefore we restrict the discussion of temporal coherence to self-written $\chi^{(2)}$-gratings.

From section (5.3.3) we may write for the induced dc-polarisation in a fibre

$$P_{dc}(z) = \chi^{(3)}_{1111} E^{\omega 0} E^{\omega 0} (E^{2\omega 0})^{*} \mathrm{Re}\{J_{21}\}, \qquad (5.39)$$

where

$$J_{21} = \frac{1}{N} \int_0^{\infty}\int E(\omega_1)E(\omega_2)E(\omega_1+\omega_2) e^{i[k(\omega_1+\omega_2)-k(\omega_1)-k(\omega_2)]z} d\omega_1 d\omega_2 \qquad (5.40)$$

where $E^{\omega 0}$ is the integral over the spectral distributions $E(\omega)$ and ω_0 is the centre frequency. The normalisation factor N is obtained from

$$N = \int_0^{\infty}\int E(\omega_1)E(\omega_2)E(\omega_1+\omega_2) d\omega_1 d\omega_2. \qquad (5.41)$$

We assume now that the wavevector varies linearly as a function of frequency around the centre frequency and may therefore write

$$k(\omega_{1;2}) = k(\omega_0) + a(\omega_{1;2}-\omega_0), \qquad (5.42a)$$

$$k(\omega_1+\omega_2) = k(2\omega_0) + b(\omega_1+\omega_2-2\omega_0). \qquad (5.42b)$$

For symmetric spectral distributions we may then write for the real part of J_{21}

$$\mathrm{Re}\{J_{21}\} = \cos(\Delta k z) K_{21}, \qquad (5.43)$$

where K_{21} is the temporal coherence factor

$$K_{21} = \frac{1}{N} \int_0^{\infty}\int E(\omega_1)E(\omega_2)E(\omega_1+\omega_2) \cos\{(b-a)(\omega_1+\omega_2-2\omega_0)z\} d\omega_1 d\omega_2. \qquad (5.44)$$

It may be seen that for symmetric spectral distributions the temporal coherence factor is a real number; only in the case of non-symmetric spectral distributions K_{21} would be complex.

It is useful to introduce factors $s_1=\omega_1-\omega_0$ and $s_2=\omega_2-\omega_0$; the spectral distributions are then written as

$$E(s_{1;2}) = \exp\left[-\left(\frac{s_{1;2}}{\delta s}\right)^2\right] \tag{5.45a}$$

$$E(s_1+s_2) = \exp\left[-\left(\frac{s_1+s_2}{\delta s/\sqrt{2}}\right)^2\right]. \tag{5.45b}$$

We then obtain for K_{21}

$$K_{21} = \frac{1}{N}\int_{-\infty}^{+\infty}\int E(s_1)E(s_2)E(s_1+s_2)\cos\{\gamma(s_1+s_2)\}ds_1ds_2, \tag{5.46}$$

where $\gamma=(b-a)z$. This integral may be evaluated as

$$K_{21} = \exp\left[-\left(\frac{\gamma\delta s}{2}\right)^2\right], \tag{5.47}$$

which is conveniently written as

$$K_{21} = \exp\left[-\left(\frac{z}{L_{coh}}\right)^2\right], \tag{5.48}$$

where $(L_{coh})^{-1}=(1/2)(b-a)\delta\omega$ and $\delta\omega$ is the spectrum half width of the pump source. This result may also be obtained by integrating over the total number of available Δk's as demonstrated by Tom et al.[33].

Assuming a fundamental wavelength of $\lambda=1.064\mu m$, neglecting waveguide dispersion and using standard Sellmeier expansions for the wavelength dependence of the refractive index, it may be found b-a=0.023/c. A typical laser linewidth of $\delta\omega$=190GHz (=1cm^{-1}) thus gives a temporal coherence length of 14cm. By using intra-cavity etalons, the line-width of a YAG laser may be easily reduced by a factor of 10, giving rise to coherence lengths as long as 140cm. However, as discussed in

section 5.7.2, non-linear effects prevent such long coherence lengths.

An estimate of the temporal coherence length may be obtained by measuring the bandwidth $\delta\omega_g$ of the $\chi^{(2)}$-grating, i.e. by scanning the pump-wavelength around the phasematch peak (in terms of the SH-conversion efficiency) and measuring the width of the phasematch peak at half maximum. Tom[33] has shown that when the coherence length is small compared to the fibre length, the coherence length may be calculated from the spectrum half-width in the following way

$$L_{coh} = \frac{1}{(b-a)\delta\omega_g} \approx 7\,\frac{\lambda^2}{\delta\lambda} \qquad (5.49)$$

at a pump-wavelength of 1.064μm, where $\delta\lambda$ is the spectrum half-width in terms of wavelength.

5.7.1.2 Spatial Coherence

Spatial non-uniformities in fibres severely limit the efficiency of i) modal phasematching and ii) phasematching via an externally-induced periodic $\chi^{(2)}$ modulation. If the spatial non-uniformities of the fibre were known, the amplitude of the SH wave could be directly calculated from (5.11). In practice, however, one has insufficient knowledge of fibre irregularities. It is then useful to resort to a simple model. In this, we assume that a fibre length L consists of a number of uniform sections of length δL with a distribution of values for Δk. The total SH intensity may then be assumed to be given by incoherent addition of the SH waves generated in each uniform section[14]. The total SH output intensity from a fibre is then given by the convolution of the Δk distribution function f(Δk) with the spread function corresponding to the lengths of a segment

$$I(\Delta k) = \int_{-\infty}^{\infty} f(\Delta k - \Delta k_0)\,\mathrm{sinc}^2\left(\tfrac{1}{2}\Delta k_0 \delta L\right) d\Delta k_0 \qquad (5.50)$$

A lower limit for the SH-output intensity is then obtained if we assume that only one fibre section has $\Delta k=0$ and we neglect the contributions from all other fibre sections. The SH intensity is then given by (5.30). The half-width $\delta\omega$ of the resulting sinc-function may be obtained by scanning the pump-wavelength and measuring the SH conversion efficiency as shown in Fig. 5.3. A lower limit for the coherence length is then estimated from

$$L_{coh} \approx \frac{1.39}{(b-a)\delta\omega} \approx 10\frac{\lambda^2}{\delta\lambda} \qquad (5.51)$$

for pump-wavelengths around 1.064μm, where b and a were defined in section (5.7.1.1). From (5.51) and using the value of 1nm for $\delta\lambda$ from Fig. (5.2), it may be calculated that the fibre described in section (5.6.1) has a lower limit for the spatial coherence length of 1.5cm. Tighter diameter control gave a half-width of 0.5nm and a coherence length of 3cm. This is considerably shorter compared to coherence lengths, $L_{coh}\approx$30cm, obtained in fibres having an internally written $\chi^{(2)}$-grating. Spatial coherence may be further increased if external gratings are used for phasematching, since both the fundamental and SH may then propagate in the same-order mode, which reduces the negative effect of wave-guide imperfections on phasematching.

Apart from the total spatial coherence length in a fibre, the repeatability of the centre frequency λ_0 of the phasematch peak is also important. λ_0 is a function of the glass refractive index and core diameter. However, it may be shown that variations in refractive index are negligible compared to core diameter fluctuations in determining ω_0[14]. Thus to a good approximation it is only necessary to consider variations of ω_0 as a

function of core diameter variations δa, and we may therefore write

$$\delta\omega_0 = \frac{\partial\Delta k}{\partial a_c}\bigg|_{a_{c0}} \frac{\partial\omega}{\partial\Delta k}\bigg|_{\omega_0} \delta a \qquad (5.52)$$

where a_{c0} is the core diameter at a given frequency ω_0, which corresponds to perfect phasematching. For a fibre design with a NA=0.30 phasematching between the LP_{01} and LP_{02} modes is obtained for a V-value V=2.0 and a core radius of 1.2μm. Assuming a total fibre diameter of 92μm, an increase in fibre diameter of 1μm leads to an increase of the centre wavelength, λ_0, of 7nm. Since fibre diameters may only be controlled to within 0.5μm, we may expect a repeatability of λ_0 of about ±2nm. Tapers in the preform lead to a further deterioration of repeatability, which, however, are expected to show up only if fibre samples are taken that are at least several tens of meters apart. Thus, it may be seen that the fibre is very uniform over at least very short sections, since a 0.5nm bandwidth of the phasematch peak corresponds to diameter variations of less than 0.05μm or core diameter variations of only about 1nm in a 3cm length of fibre.

5.7.1.3 Group-Velocity Walk-Off

Temporal walk-off between the fundamental and SH wave due to group-velocity dispersion leads to a further reduction in interaction length. For diffraction limited pulses we may approximate temporal walk-off in a fibre length L by

$$\delta t = \frac{L}{c}\,[n_{co}(2\omega) - n_{co}(\omega)], \qquad (5.53)$$

where $n_{co}(\omega)$ is the group refractive index at the frequency ω. Thus for a fibre of length L=1m and $n_{co}(2\omega)-n_{co}(\omega)=0.012$ we obtain a temporal walk-off of δt=40psec, which for a pulse length of 100psec leads to a reduction in coupling between the two waves of about 40%.

5.7.1.4 Absorption

The creation of permanent second-order nonlinearities leads to high losses in the fibre (see section 6.10). In fact losses of up to 20dB/m at 532nm have been measured. Therefore it is useful to briefly discuss the effect of absorption on SH conversion efficiency. In general the fibre loss is several orders of magnitude higher at blue/green wavelengths than at infrared wavelengths. Hence we only assume a loss coefficient α for the SH. Equation (5.11) is then modified to

$$\left[\frac{d}{dz} - \alpha\right] E^{2\omega}(z) = i\varsigma \exp(i\Delta kz), \tag{5.54}$$

where ς has been defined in (5.28). Solving this equation in terms of intensity we obtain

$$P^{2\omega}(z) = \xi e^{-\alpha z} \frac{\sinh^2\left(\frac{\alpha z}{2}\right) + \sin^2\left(\frac{\Delta kz - \alpha z}{2}\right)}{\left(\frac{\Delta kz}{2}\right)^2 + \left(\frac{\alpha z}{2}\right)^2}, \tag{5.55}$$

where ξ has been defined in (5.30). For $\Delta k=0$ the maximum is obtained for $z=2.2/\alpha$, which may be interpreted as an effective interaction length of $z\approx 1/\alpha$. The conversion efficiency in a lossy fibre is then simply calculated by using the effective interaction length and setting $\alpha=0$ in the above expression. A loss of 20dB/m corresponds to an effective interaction length of 22cm.

5.7.2 Limitations due to Competing Nonlinear Effects

5.7.2.1 Intensity-Dependent Refractive Index

The intensity dependence of the refractive index for plane parallel light of frequency ω may be written as[34,35]

$$\delta n = \frac{16\pi^2}{c\varepsilon(\omega)} \chi^{(3)}_{1111}(\omega=\omega+\omega-\omega) I(\omega), \qquad (5.56)$$

where I is the intensity of the optical wave at frequency ω. For an optical power of 1kW in a 4μm diameter fibre at 1.064μm and using the value $\chi^{(3)}_{1111}= 2.0\times10^{-14}$esu (see Appendix 6.II), we obtain $\delta n\approx 4\times10^{-6}$. Thus a phase-shift of π is generated in 12cm of fibre. It is clear then that when optical wave-trains consisting of pulses of different intensities (as generated via simultaneous mode-locking and Q-switching) are launched into a fibre, each pulse sees a different refractive index, which leads to a loss of the fixed phase-relations between the fundamental and SH-wave. This is not important when coherence lengths are already short. However, for internally written $\chi^{(2)}$-gratings, the coherence length at this intensity is then reduced to less than 12cm and it is thus useful to write $\chi^{(2)}$-gratings at lower intensities.

5.7.2.2 Self-Phase Modulation

Self-phase modulation in fibres leads to a frequency broadening of the optical input wave, which is proportional to the derivative of the phase perturbation given by the intensity-dependent refractive index. The frequency broadening is written as[36,37]

$$\delta\omega(t) = \frac{\partial\delta\Phi}{\partial t}\bigg|_{max} = \frac{\partial}{\partial t}\frac{2\pi\delta nL}{\lambda} = \frac{32\pi^3}{cn^2}\frac{L}{\lambda}\chi^{(3)}_{1111}\frac{\partial I}{\partial t}\bigg|_{max}, \qquad (5.57)$$

where L is the fibre length. Self-phase modulation is thus only important when very short pulses are used. Assuming a Gaussian pulse shape

$$I(t) = I_0 \exp[-2(t/t_p)^2] \qquad (5.58)$$

with an 1/e width of t_p=100psec and a power of 1kW in a 4μm diameter fibre we obtain

$$\delta\omega \approx 2.6\text{GHz/cm}. \qquad (5.59)$$

This gives a limit for the temporal coherence length in internally written $\chi^{(2)}$-gratings of $L_{coh}\approx$23cm. The intensity dependent refractive index is therefore dominant in reducing the effective grating length at this pulse width.

The intensity-dependent refractive index and self-phase modulation may be used for varying the width of the phasematch peak in internally-written $\chi^{(2)}$-gratings and provide the opportunity for limited tuning of the pump-wavelength for SHG at the expense of a reduced coherence length. Fig. (5.4) is a measurement of the bandwidth of an internally-written $\chi^{(2)}$ grating obtained by using a YAG laser operating Q-switched only (pulse-width=200nsec) and also Q-switched and mode-locked (pulse-width=100psec) in the writing process. Optical input powers delivered from mode-locked and Q-switched pulses were about 5 times more intense than delivered from Q-switched pulses. The bandwidth in the latter case is 0.04nm and in the former case it is about 0.2nm, showing the broadening of the $\chi^{(2)}$-grating due to self-phase modulation and the intensity-dependent refractive index. From (5.49) the coherence lengths for the two cases are calculated as 20cm and 4cm.

5.7.2.3 Stimulated Light Scattering

Stimulated light scattering in optical fibres is caused by the interaction of high intensity light with material excitational waves. These may be high energy optical phonons arising from molecular vibrations as observed in Raman scattering or lower energy acoustic phonons arising from vibrations of the crystal lattice as seen in Brillouin scattering. Several other stimulated light scattering mechanisms also exist[24], which however are of less importance in glass optical fibres and are therefore not discussed here. The frequency conversion of light by stimulated light scattering processes leads necessarily to a loss of pump power for SHG. We outline here the power levels and fibre lengths at which stimulated light scattering becomes significant in order to establish the importance of these effects in frequency-doubling.

5.7.2.3.1 Stimulated Raman Scattering

Stimulated Brillouin scattering has been theoretically described by Bloembergen[38]. He showed that it is a third-order nonlinear effect, which may be treated by a set of coupled-wave equations similar to (5.6). In this a pump wave of amplitude E_p and frequency ω_p couples to a Stokes wave (E_s and ω_s) via a molecular vibration ω_v, such that $\omega_p-\omega_s=\omega_v$. In the slowly varying amplitude approximation the coupled-wave equations for plane polarised light are written as

$$\left(\frac{d}{dz}+\frac{\alpha_p}{2}\right)E_p=\frac{-i2\pi\omega_p^2}{k^pc^2}\chi_R^{(3)}(\omega_p=\omega_p+\omega_s-\omega_s)|E_s|^2E_p \qquad (5.60a)$$

$$\left(\frac{d}{dz}+\frac{\alpha_p}{2}\right)E_s=\frac{i2\pi\omega_s^2}{k^sc^2}\chi_R^{(3)}(\omega_s=\omega_s+\omega_p-\omega_p)|E_p|^2E_s, \qquad (5.60b)$$

where $\chi^{(3)}_R$ is the Raman nonlinear susceptibility, which is the negative imaginary part of the third-order nonlinear susceptibility. It may be seen that phasematching is automatically achieved due to the mixing of the photons like $\omega_p=\omega_p+\omega_s-\omega_s$. Assuming zero pump-depletion due to the nonlinear process, the solution for the intensity of the Stokes wave is obtained as

$$I_s(z) = I_s(0)\exp\left[g_R I_p \frac{[1-\exp(-\alpha_p z)]}{\alpha_p} - \alpha_s z\right], \qquad (5.61)$$

where g_R is the Raman gain coefficient

$$g_R = \frac{64\pi^3}{c\varepsilon\lambda}\chi_R^{(3)}. \qquad (5.62)$$

The critical pump power P_{cr} required to give rise to a pump and Stokes wave of equal intensity in a fibre length L was derived by Smith[39] by integrating the amplified spontaneous Raman emission over the whole fibre length. For typical silica fibre parameters P_{cr} is given by

$$P_{cr} \approx 16\left[\frac{A}{g_R}\frac{\alpha}{1-\exp(-\alpha L)}\right], \qquad (5.63)$$

where α is the fibre attenuation and A is the fibre core area. At SH-pump powers of P_{cr}, the SH-conversion efficiency is reduced by a factor of two. Assuming a pump power of 1000W, a core diameter of 4μm, neglecting absorption and using the value of $g_R=9.2*10^{-14}$ m/W at 1.064μm[40], we obtain that the pump and the Stokes wave have equal intensity after L=2m. The significance of stimulated Raman scattering in limiting useful fibre lengths for SHG is therefore one order of magnitude smaller than the intensity-dependent refractive index and may be neglected as long as fibre lengths shorter than 1m are used.

5.7.2.3.2 Stimulated Brillouin Scattering

Stimulated Brillouin scattering only occurs in the backward direction, since no frequency shift is obtained in the forward direction. The analysis of the effect is similar to the treatment of stimulated Raman scattering. Critical powers for optical fibres were derived by Smith[39]. Assuming an optical input in form of pulses, the interaction length for backward amplification is reduced to the pulse length L. Neglecting pump absorption during the pulse length the critical power for typical silica fibres is obtained as

$$P_{cr} = 21 \frac{\Delta\nu_B}{\Delta\nu_p} \frac{A}{g_B L}, \qquad (5.64)$$

where g_B is the Brillouin gain coefficient and $\Delta\nu_B/\Delta\nu_p$ is the ratio of the linewidth of the Brillouin gain spectrum and the pump-laser. This ratio has to be included in equation (5.64), since the Brillouin gain spectrum has a linewidth of only 30MHz at 1.064μm[40], which is small compared to a typical laser linewidth of several GHz. On the other hand the Raman gain linewidth is several THz and thus it is large compared to a typical laser linewidth. The Brillouin gain scales as $1/\lambda^2$ and was measured at 1.064μm as $g_B=4\times10^{-11}$(m/W)[40]. Assuming an interaction length of 20cm (pulse or fibre length), a core diameter of 4μm and a laser linewidth of 30GHz (=1cm^{-1}), we obtain for the critical power P_{cr}=30kW. A reduction in linewidth by a factor of 30 in order to increase the temporal coherence length reduces the critical power to 1kW. However, as seen in section (5.7.2.2), when pulses of this intensity and 20cm length are launched, self-phase modulation leads to a frequency broadening of 2.6GHz/cm and thus prevents the build-up of stimulated Brillouin scattering. Hence stimulated Brillouin scattering becomes the dominant stimulated light scattering mechanism only at narrow laser line

width and long pulse-lengths. The critical power of 1kW in an interaction length of 20cm may be compared to the nonlinear refractive index. In section (5.7.2.1) it was shown that 1kW of pump power leads to a phase-shift of π in 12cm of fibre. Thus both effects are then similarly effective in reducing the SH conversion efficiency provided the pulse length is long enough to prevent self-phase modulation, i.e. longer than about 1 nsec. In the experiments performed here, laser line width of about 30GHz or pulse width of less than 500psec have always been used and thus the effect of stimulated Brillouin scattering may then be neglected.

5.7.2.4 Electrical and Optical Dielectric Breakdown

Dielectric breakdown limits both the creation of second-order nonlinearities and their exploitation. Here we are concerned with both dc-electric breakdown and breakdown at optical frequencies. Dc-electric breakdown limits the electric field that may be used for externally aligning defect centres (see section 5.10) and also the strength of the dc-field in electric-field-induced harmonic generation (see section 5.8). Optical breakdown limits the optical power that may be launched into fibres both for the excitation of defect centres (see section 5.10) and harmonic generation.

Dielectric breakdown in solids may occur because of several mechanisms. The most common is due to electron avalanche ionisation. The requirement for this is that free electrons exist in the conduction band of the solid, which may occur due to thermal excitation or due to ionisation via a multi-photon absorption process. The free electrons may then absorb energy from the optical field in collisions with lattice atoms or be accelerated by the electric field until they have enough energy to ionise surrounding atoms. This eventually leads to an electron avalanche process and results in catastrophic local heating of the solid and visible damage[24].

Dc-electric breakdown was investigated by Moon and Norcross[41]. They measured that a silica film of 20μm width could withstand fields of up to 200V/μm at room temperature. This is in fact less than obtained in germanosilicate fibres. For a fibre design as described in section (5.10) with an electrode spacing of 20μm fields of up to 400V/μm could be applied. This corresponds to an optical intensity of 31GW/cm^2 and demonstrates that no edge effects lower the breakdown threshold.

Recently it has also been shown[42] that when very large dc-electric fields (>100V/μm) are applied to silica glass over several hours, colour centres are introduced into the material. Losses up to 10dB/m have been measured at 532nm after the application of a large field. This indicates that the electrons may be accelerated such that they break bonds in the glass without causing electric breakdown.

Optical breakdown in solids was investigated by Smith et al[43] using picosecond pulses and in silicate glasses by Glebov et al[44] using pulses of 25nsec width. Glebov found that for photon energies smaller than half the band-gap energy breakdown occurs for optical intensities of the order of 500GW/cm^2, where the optical breakdown intensity is defined as the intensity at which there is a 50% probability of optical breakdown to occur. For higher photon energies two-photon absorption leads to a reduction in threshold by a factor of 50.

In the experiments performed with germanosilicate fibres it was found that when using 6nsec pulses delivered from a dye laser breakdown occurred at intensities of only 5GW/cm^2 for blue light of wavelength λ=480nm. For wavelengths around 1μm breakdown thresholds of about 10GW/cm^2 were obtained. These much lower breakdown thresholds may be explained by fibre end-face imperfections, which give rise to strong local fields at sharp edges and a reduction in threshold power. Further,

the laser light was slightly multi-moded (especially around 1μm) leading to hot spots outside the fibre core area and optical damage. Using ultra-polished fibre end-faces and spatial filters to clean-up the laser mode, it should be possible to raise the breakdown thresholds to the levels published by Glebov.

Using a YAG laser emitting 100psec pulses at 1.064μm threshold intensities of the order of 100GW/cm^2 were obtained. The improvement is due to the better spatial profile of the YAG laser beam and also the approximately inverse dependence of optical breakdown threshold on optical pulse length.

5.7.3 Summary of Limiting Mechanisms

In conclusion we have found that spatial coherence limits the coherence lengths achievable when modal phasematching or phasematching via externally-written $\chi^{(2)}$-gratings is considered. Maximum coherence lengths of about 3cm have been experimentally verified for modal phasematching between the LP_{01} and LP_{02} mode.

Temporal coherence and the intensity-dependent refractive index are the dominant mechanisms limiting coherence lengths when internally-written $\chi^{(2)}$-gratings under the following typical writing conditions are considered: mode-locked and Q-switched pulses of 1kW peak intensity, 100psec pulse width and 1cm^{-1} bandwidth delivered into a 4μm diameter fibre core. Coherence lengths of up to 4cm have been so demonstrated. By operating the writing laser only in the Q-switched mode, coherence lengths up to 20cm have been measured.

5.8 Second-Harmonic Generation Induced by an Electric Field

Electric-field induced second-harmonic generation (ESHG) was first observed by Terhune[45,46] in calcite. The generation of SH light in ESHG is governed by the third-order nonlinear susceptibility $\chi^{(3)}(2\omega=\omega+\omega+0)$, which produces an effective second-order nonlinearity in the material. The amplitude of the nonlinearity in a fibre is given by

$$P_{2\omega}^{NL} = \frac{1}{3}\chi^{(3)}_{1111}(2\omega=\omega+\omega+0)[E_{dc}(E^{\omega}\cdot E^{\omega})O_1+2E^{\omega}(E_{dc}\cdot E^{\omega})O_2]. \tag{5.65}$$

The overlap integrals may be calculated from (5.20). For plane polarised light the effective nonlinearity reduces to

$$P_{2\omega}^{NL} = \chi^{(3)}_{1111}(2\omega=\omega+\omega+0)E_{dc}E^{\omega}E^{\omega}O_0, \tag{5.66}$$

where the overlap integral O_0 is again obtained from (5.20). By defining the effective second-order nonlinearity $\chi^{(2)}{}_{dc}=(\chi^{(2)}{}_{111})_{eff}=\chi^{(3)}{}_{1111}E_{dc}$, the SH power generated may be calculated by using (5.30). For a field strength at the dielectric breakdown limit of silica, i.e. $E_{dc}=400V/\mu m$ and using the value for $\chi^{(3)}{}_{1111}=2.0\times10^{-14}$ esu ($=2.7\times10^{-22}$ m^2/V^2) as converted into our notation from measurements of the nonlinear refractive index at $1.06\mu m$ (see Appendix 6.II), we obtain $\chi^{(2)}{}_{dc}=2.7\times10^{-10}$ esu ($=5.5\times10^{-14}$ m/V). This is only about 9 times smaller than the value of $\chi^{(2)}$ of KDP ($\chi^{(2)}(KDP)=2.3\times10^{-9}$ esu)[24] at this wavelength.

Since $\chi^{(2)}{}_{dc}$ is symmetric, phasematching of a fundamental wave in the fundamental mode is only possible to symmetric higher order modes. The overlap integral for modal phasematching between the LP_{01} and the LP_{02} or LP_{03} modes as a function of V-value is plotted in Fig. (5.3). Independent of pump polarisation, the SH is always polarised parallel to the dc-field. The intensity of the

SH-wave is proportional to the square of the dc-field strength.

Measurements of modally phasematched ESHG were made in a germanosilicate fibre doped with 0.5 mole% P_2O_5. The fibre had a NA=0.25, a core radius of 2.3μm and a length of 20cm. The fibre had a specially designed D-form with internal electrodes (see section 5.10) which allowed the application of fields up to 400V/μm. The fibre core was elliptical with an aspect ratio of 1/2; the major axis of the ellipse was aligned with the dc-field to within 10%. The fibre phasematched the LP_{01} to the LP_{02} mode at a wavelength of λ=1.208μm. The SH conversion efficiency as a function of wavelength is plotted in Fig. 5.3. The phasematch peak has a half-width of 1nm corresponding to a coherence length of 1.5cm as discussed in section (5.7.1.1). The SH conversion efficiency as a function of dc-field strength is shown in Fig. (5.5). It may be seen that indeed the SH output power is proportional to the square of the dc-field strength.

The SH signal as a function of time after the dc-field was switched on or off is shown in Fig. (5.6). The measurement was obtained by launching pulses from a Raman-shifted dye laser (30Hz repetition rate) and averaging the SH output signal in a digitising oscilloscope. The peak pulse power was limited to 40W in order to avoid writing any $\chi^{(2)}$ gratings into the fibre and the applied electric field was 125V/μm. Each measurement point in Fig. (5.6) is an average of 100 pulses, which thus corresponds to an acquisition rate of measurement points of 0.3 per second. Each data point was transferred to a computer and stored.

We see that the SH-signal almost simultaneously appears/disappears (within the sampling rate) with the switching on/off of the dc-field. Even when the dc-field was left on for 15 minutes and high-intensity infrared light (λ=1.208μm) was launched into the fibre, no measurable increase of the SH signal was noticed. Also,

once the dc-field was switched off the SH signal dropped to the same base value measured prior to the 'treatment'. This is in contrast to results published by Mizrahi et al.[47] who used external electrodes for a similar measurement and claimed that a long response time, of the order of several 10's of seconds, of the ESHG signal in fibres to a dc-field exists. Similar effects were noticed in my work only when external electrodes were used to create a dc-field, which indicates that external electrodes tend to collect surface charges over a period of time, which counteract the applied electric field.

The maximum SH conversion efficiency obtained with an applied field of 125V/μm and an optical input power of 40W was 0.002%. The overlap integral was calculated as O_0=11%, which indicates that much higher conversion efficiencies are possible when external gratings are used for phasematching. However, the dc-fields will then have to be smaller, since edge effects will reduce the breakdown field strength. Another way of increasing the SH-conversion efficiency is to use lead based glasses, which have a up to 5 times higher third-order nonlinear susceptibility than silica, which would thus give rise to an increase in the SH signal of 25 times.

The observed SH-conversion efficiency may be compared to equation (5.30). For the fibre parameters given above and assuming an effective fibre length L equal to the coherence length of 1.5cm, where perfect phasematching is obtained, equation (5.30) predicts a conversion efficiency of 0.001%. This is in good agreement with the experiment. The discrepancy is due to the fact that the influence of coherence lengths shorter than the actual fibre length was not accounted for and therefore the assumption of perfect phasematching in a fibre length equal to the coherence length is only a crude approximation to the real situation. Further, the value used for $\chi^{(3)}$ is only approximate. $\chi^{(3)}(\omega=\omega+\omega-\omega)$ for the intensity-dependent refractive index and

$\chi^{(3)}(2\omega=\omega+\omega+0)$ for ESHG are the same only in dispersion and absorption free materials.

5.9 Effective Second-Order Nonlinearities due to Quadrupole and Magnetic Dipole Moments

SHG induced by electric quadrupole and magnetic dipole moments is assumed to be relevant to the formation of $\chi^{(2)}$ gratings generated from noise, i.e. over a period of several hours when only light at the fundamental wavelength is launched into a fibre. The nonlinearities induced by electric quadrupole and magnetic dipole moments may be treated as an effective second-order nonlinearity which then allows the application of equation (5.30) to calculate the power of the generated SH-wave once the magnitude of the second-order nonlinearity is known.

Quadrupole-induced SHG was first observed by Terhune in Calcite[45] and subsequently treated theoretically by Pershan[48], Adler[49] and Bloembergen[50] and more recently by Payne[15] and Terhune and Weinberger[14] for the specific case of harmonic generation in optical fibres. The nonlinear polarisation for isotropic materials may be written to second order in **E** as[15]

$$\mathbf{P} = \chi\mathbf{E}+\alpha_1\mathbf{E}(\mathrm{div}\mathbf{E})+\alpha_2(\mathbf{E}\cdot\mathbf{grad})\mathbf{E}+\alpha_3\mathbf{E}\times(\mathrm{curl}\mathbf{E}), \qquad (5.65)$$

where χ is the linear susceptibility and α_1 and α_2 arise from electric quadrupole interactions and α_3 arises from magnetic dipole interactions.

When the SH-wave is not phasematched to the fundamental wave, as is usually the case at the start of the $\chi^{(2)}$ writing process, the term with α_1 is small compared to the terms with α_2 and α_3. Further, it may be shown that $\alpha_2=\alpha_3$. The terms with α_2 and α_3 lead to a coupling of the fundamental wave in the LP_{01} mode to the SH in the LP_{11} mode. In optically induced $\chi^{(2)}$ gratings generated from noise the SH wave is indeed seen to be propagating in the

LP_{11} mode, which indicates that quadrupole interactions contribute to the formation of $\chi^{(2)}$ gratings. Payne[15] has calculated the overlap integral between the LP_{01} and LP_{11} mode using a Gaussian approximation for the modal field distribution and has defined an effective second-order nonlinearity as the product of the quadrupole and magnetic dipole nonlinearity with the overlap integral. His result in SI units is

$$\chi^{(2)}_{eff} = \sqrt{2}\,\frac{(n_{co}-n_{cl})^{1/2}}{n_{co}\varepsilon_0}\,(\Delta k)\alpha_2, \qquad (5.66)$$

where α_2 was calculated using a classical dispersion analysis and was obtained as $\alpha_2=1.8\times10^{-33}$ in SI units for silica glass. For a typical non-phasematched fibre $\chi^{(2)}{}_{eff}$ is then calculated as $\chi^{(2)}{}_{eff}\approx10^{-17}$m/V ($=2.4\times10^{-14}$ esu). It is interesting to compare the effective $\chi^{(2)}$ due to quadrupole interactions with the effective $\chi^{(2)}{}_{dc}$ due to ESHG. Assuming again non-phasematched harmonic generation and conversion from the LP_{01} mode to the LP_{02} mode, we find that a field of only ≈0.4V/μm is necessary to generate the same SH signal as that due to quadrupole interactions.

5.10 Second-Order Nonlinear Phenomena by Alignment of Defect centres

5.10.1 Physical Processes

As pointed out in section 5.3.1 the presence of second-order nonlinearities is due to a material being non-centrosymmetric. Since glass is an isotropic material, it is also centrosymmetric and therefore the lowest-order nonlinearities are of third order.

However, it may be envisaged that the centrosymmetry may be broken by defect centres. Is is well known that electrons or holes may be trapped at defect sites[51]. A defect site with a trapped electron breaks the centrosymmetry and leads to a local dipole moment. If

electrons or holes are trapped at defect centres in an ordered way, the sum of the local dipole moments may eventually give rise to a second-order nonlinearity. The ordering of electrons or holes could be accomplished by applying a dc electric field across the glass, which could favour trapping electrons facing the anode or holes facing the cathode.

Free electrons and holes may be created in a number of ways. In germanosilicate glass the following process is known. In oxygen deficient germanosilicate glass as encountered in as drawn optical fibres GeO exists in addition to GeO_2[52]. A basic model (taken from ref. 53) for the coordination of GeO in the glass matrix is shown in Fig. 5.7. In this covalent Ge=Ge bonds with a characteristic absorption band at 240nm exist[52]. These bonds may be broken by ionising radiation (UV or nuclear radiation) leading to the formation of Ge E' defect centres with a trapped hole and free electrons[53]. As shown in section 5.10.3.2.1 two-photon absorption of intense light of wavelength 480nm may also lead to excitation into the 240nm absorption band and breaking of Ge=Ge bonds. Generalising this discussion, multi-photon absorption or third-harmonic generation in fibres may also lead to the breakage of bonds and the creation of free electrons. In addition, as discussed in section 5.7.2.4, in the presence of very strong external dc electric fields (>100V/μm) applied to the glass, thermally excited electrons in the conduction band may be accelerated to high energies and also break bonds giving rise to colour centres. This effect is in fact a precursor to dielectric breakdown.

Once the free electrons are created, electron trapping sites are provided by four-coordinated Ge[53] as shown in Fig. 5.8. The resulting defect sites are known as Ge(1) and Ge(2) centres[53]. In what way the application of a dc-electric field leads to an alignment of Ge(1), Ge(2) or Ge E' centres and whether these defect centres lie at the root of second-order nonlinearities is not yet known.

Information about the underlying exact physical mechanisms could be obtained by relating ESR measurements of the concentration of Ge E', Ge(1) and Ge(2) centres to measurements of the magnitude of the defect centre induced second-order nonlinearity. In section 5.10.3.2 experimental evidence is presented, which indicates that the breaking of Ge=Ge bonds and the formation of Ge E' colour centres indeed plays a significant role in the creation of second-order nonlinearities.

From a practical point of view, the following technique has to be applied to generate second-order nonlinearities: defect centres have to be excited and simultaneously a poling field must be applied to enable a defect alignment mechanism to take place.

As shown in section 5.6.3 simultaneous launching of a fundamental wave and its SH into an optical fibre leads to the generation of a spatially varying dc-electric field in the fibre along which defect centres excited by a multi-photon process may align. The magnitude of the induced $\chi^{(2)}$ is very small and may only be used for SHG or possibly three-wave mixing. This technique is discussed in section 5.10.2.

Another technique for the creation of second-order nonlinearities is to excite defect centres by intense blue radiation or strong dc-electric fields and to simultaneously apply a poling field along which defect centres may align. The $\chi^{(2)}$ induced by this technique (i.e. externally induced second-order nonlinearities) is up to 26 times larger than achievable by internally writing a $\chi^{(2)}$-grating. The technique may potentially be used for the demonstration of all second-order nonlinear effects, which are already known in crystals. So far, only SHG and the Pockels effect have been demonstrated in poled optical fibres and a detailed discussion of these effects is given in section 5.10.3.

5.10.2 Second-Harmonic Generation in Internally-Written $\chi^{(2)}$-Gratings

5.10.2.1 Formation of $\chi^{(2)}$-Gratings from Noise and by Seeding

Second-order nonlinear susceptibility gratings may be written into fibres using either only a pump wave (from noise) or a pump-wave with its SH (by seeding). In the latter case the formation of a grating takes several hours, where in the former case the time is reduced to a few minutes. $\chi^{(2)}$-gratings may be written into pure germanosilicate fibres and germanosilicate fibres doped with phosphorus[54]. However, it was found that silica fibres doped with both GeO_2 and P_2O_5 produce the highest second-order nonlinearities[19]. No $\chi^{(2)}$-gratings may be written into pure silica-core fibres and only very weak gratings may be written into fibres doped with only phosphorus[54].

In order for the formation of a $\chi^{(2)}$-grating from noise to occur, peak intensities of typically more than 10GW/cm^2 have to be launched into fibres for wavelengths around 1μm. When $\chi^{(2)}$-gratings are formed by seeding, the threshold intensities are reduced and $\chi^{(2)}$-gratings have been written using peak intensities of only 1GW/cm^2. $\chi^{(2)}$-gratings have also been written from noise using a fundamental wave of wavelength λ=647nm and peak powers of only 5GW/cm^2[55], where the time for the preparation process was reduced to only a few minutes. Further, it has also been shown that $\chi^{(2)}$-gratings may be written by launching a fundamental wavelength of 1.32μm using a seeding technique and peak intensities of 2GW/cm^2[56]. In all cases lasers of a high repetition rate, i.e.>1kHz have been used in the writing process and it has not been established yet whether gratings may be written by using lasers of lower repetition rate.

A standard experimental set-up used for the writing of a $\chi^{(2)}$-grating is shown in Fig. 5.9. A $LiIO_3$ crystal may be

inserted into the fundamental laser beam to generate the coherent seed SH. The intensity of the launched fundamental and seed SH wave is measured by the calibrated detector D_1 and after given time intervals, the seed SH is blocked and the SH conversion efficiency measured by detector D_2. A monochromator is used in order to filter out the SH signal and to reject signals due to third-harmonic generation and four-wave mixing.

A typical measurement of the formation of a $\chi^{(2)}$-grating as a function of time is shown in Fig. 5.10. The growth of both a $\chi^{(2)}$-grating generated from noise and by seeding was monitored. In this, a fibre doped with 7% GeO_2 and < 1% P_2O_5 with a core diameter of 5μm was used. Pulses of wavelength λ=1.064μm, 10kW peak power, 100psec width and 1kHz repetition rate delivered from a mode-locked and Q-switched YAG laser were launched over a period of time. For the fibre prepared by seeding, the seed SH had an intensity of 4% of the fundamental wave. The formation of a $\chi^{(2)}$ grating from noise takes about 10 hours and the formation of a $\chi^{(2)}$-grating by seeding is accomplished after about 15 minutes.

The growth of the SH-signal along the fibre length was measured by side-scatter. The experimental set-up is shown in Fig. 5.11. For ease of measurement the fundamental wave was launched from the back of the $\chi^{(2)}$-grating. The bandwidth of the $\chi^{(2)}$-grating could also be obtained along the fibre length by scanning the pump wavelength and measuring the SH conversion efficiency. In this, a wavelength-tunable Raman-shifted dye laser (6 nsec pulse width and 30Hz repetition rate) was employed to provide the pump wave. The result of the measurement of the evolution of the SH signal along the fibre due to a $\chi^{(2)}$-grating written from noise is shown in Fig. 5.12. It may be seen that in this fibre the main contribution to the SH signal is generated in the last 5cm of the fibre, which is in good agreement with the temporal coherence length of this grating, which was

calculated from (5.49) and the FWHM spectral width ($\Delta\lambda$=0.24nm) of the grating as L_{coh}=3cm.

The polarisation dependence of the SH conversion efficiency was established in $\chi^{(2)}$-gratings written from noise and by seeding. Here all waves used in the writing process were linearly polarised and parallel to each other. It was found that the highest conversion efficiency was obtained for a pump polarisation parallel to the polarisation of the writing wave, where the polarisation of the SH was also parallel to the direction of the writing wave. The conversion efficiency was proportional to $\cos^4(\alpha)$, where α is the angle between the direction of the polarisation of the writing waves and the read-out waves. This confirms that the induced second-order nonlinear susceptibility tensor consists of only one dominant component $\chi^{(2)}_{111}$, which is oriented parallel to the internally-generated dc-field.

The reciprocity of a $\chi^{(2)}$ grating written by seeding was also confirmed. The results were that independent of whether a $\chi^{(2)}$-grating was read-out from the front or back end, the phasematch wavelength and the polarisation direction giving the highest SH conversion efficiency were the same. However, when gratings were written and read out at very high optical intensities, the SH conversion efficiency was found to be higher when launching from the front end owing to nonlinear limiting mechanisms not being reciprocal.

The launching of high intensity light into the fibre and the creation of a $\chi^{(2)}$-grating led to large increases in fibre loss. Typically, induced losses up to 10dB/m have been measured at 532nm, which confirms that indeed colour centres are being created by the writing process. So far, however, it has not been established whether the formation of colour centres is due to third or second-harmonic generation or multi-photon absorption. It appears that colour centres may be written into fibres at

any wavelength as long as the launched peak intensity is high enough.

The highest SH conversion efficiency obtained with an internally-written $\chi^{(2)}$-grating to date was 13% with a pump intensity of 10GW/cm^2 as demonstrated by Farries[19]. In this, the same highly-birefringent fibre as discussed in section (5.10.2.4) was used. The coherence length of this fibre was 20cm, from which (5.30) allows the calculation of the magnitude of the induced second-order nonlinearity. Assuming an overlap integral of unity between the fundamental and SH-wave, we obtain $\chi^{(2)}=2\times10^{-11}$ esu, which is in good agreement with the value of $\chi^{(2)}$ measured by other workers. The induced $\chi^{(2)}$ is about 230 times smaller than the second-order nonlinear susceptibility for KDP at this wavelength. Higher values for the induced nonlinearity may be obtained by using strong external dc-fields in the writing process.

In order to verify that a $\chi^{(2)}$-grating is formed by high intensity light a series of experiments have been carried out and these are discussed in sections (5.10.2.2-5.10.2.4).

5.10.2.2 Temperature Effects

The dependence of the refractive index on temperature and thermal expansion may be used for limited wavelength-tuning of a $\chi^{(2)}$ grating. In order to measure the dependence of the SH conversion efficiency and the phasematch wavelength on temperature a prepared P_2O_5 and GeO_2 doped fibre with a $\chi^{(2)}$-grating was spliced into two pieces of untreated fibre and then totally enclosed inside a furnace with the two end pieces of untreated fibre kept outside. Laser light could then easily be launched into one fibre end and the SH signal measured at the other end. The fibre was then kept at given temperatures for periods of 15 minutes each and after the

end of each period, the position of the phasematch peak and the SH conversion efficiency were measured. No attempts were made to compensate for a non-uniform temperature distribution inside the furnace, which led to a broadening of the FWHM width of the phasematch peak at elevated temperatures.

The temperature-dependence of the phasematch wavelength and the SH conversion efficiency are shown in Fig. 5.13. From this we obtain that the phasematch wavelength shifts by 0.04nm/°C towards the infrared. The SH conversion efficiency stays constant up to about 100°C and then detiorates rapidly with a further increase in temperature. At 400°C the SH conversion efficiency is only about 10% of the initial value at room temperature. However, it was found that over a period of months the strength of a $\chi^{(2)}$-grating deteriorated even at room temperature. Therefore, it is useful to cool $\chi^{(2)}$-gratings in order to keep high conversion efficiencies over long periods of time and for wavelength tuning. By cooling a fibre to liquid nitrogen temperatures, the phasematch wavelength would be shifted by about 8nm towards the blue end of the spectrum.

It is interesting to note that the induced loss in P_2O_5-doped germanosilicate fibres could not be bleached by heating up to temperatures of 300°C. This indicates that the aligned defect centres created by high intensity light redistribute themselves without disappearing once the temperature is raised. Another possibility is also that the aligned defect centres transform into other defect centres with a similar absorption cross section. In order to obtain an improved knowledge of how defect centres are transformed and affected by temperature ESR measurement would have to be carried out.

5.10.2.3 Fibre Stretching

A fibre-stretching experiment was performed in order to confirm the presence of a $\chi^{(2)}$-grating in an optical fibre and to demonstrate fine-tuning of the phasematch wavelength. Here a uniform uniaxial stress is applied to the fibre, which changes the unstretched $\chi^{(2)}$-grating period, Λ_0, to

$$\Lambda' = \Lambda_0(1+\Delta l/l), \tag{5.67}$$

where $\Delta l/l$ is the relative longitudinal elongation of the fibre, which may be calculated from Young's modulus and the applied stress. In addition, the applied stress leads to a decrease in refractive index by Δn, which may be written for $\Delta l/l<<1$ as[57]

$$n = Cn^3(\lambda)(\Delta l/l), \tag{5.68}$$

where $C\approx 0.102$ is a constant derived from Poisson's ratio and the relevant components of the elasto-optic strain tensor, and $n(\lambda)$ is the refractive index at the wavelength λ of interest at zero stress. The wavelength λ_p at which phasematching occurs for a given applied stress may be thus calculated from

$$\frac{1}{\Lambda'} = \frac{2}{\Lambda_p}[n'(\lambda_p/2)-n'(\lambda_p)], \tag{5.69}$$

where Λ' is given by (5.67) and $n'(\lambda_p)$ and $n'(\lambda_p/2)$ are the effective phase refractive indices at the pump and SH wavelength given by

$$n'(\lambda) = \left[b[(n_{co}+\Delta n_{co})^2-(n_{cl}+\Delta n_{cl})]/[(n_{co}+\Delta n_{co})^2-(n_{cl}+\Delta n_{cl})^2]\right]^{1/2} \tag{5.70}$$

where b is the normalised propagation constant and Δn_{co}, Δn_{cl} may be calculated using (5.68).

The stretching experiment was performed on a fibre with a numerical aperture NA=0.183 and an outer diameter of 100μm. The cut-off wavelength for the LP_{11} mode was λ_c=703nm. However, both the pump and the SH were propagating in the LP_{01} mode. The experimental arrangement is shown in Fig. 5.14. Here the grating end of the test fibre was glued into a disk containing weights in the range from 0-150g. The grating end was then spliced onto a dummy fibre which directed the output onto a detector. Wavelength-tuning was achieved by using the usual Raman-shifted dye laser.

The results of the tuning experiment are shown in Fig. 5.15 along with the theoretically predicted curve calculated from (5.67)-(5.70). An excellent agreement between theory and experiment is obtained, confirming the presence of a $\chi^{(2)}$-grating which provides phasematching between the LP_{01} modes at the fundamental and SH wavelengths. The maximum obtainable wavelength shift before fibre breakage occurred was 0.78nm corresponding to an elongation of 0.26% of the fibre. Thus stretching a fibre may be a useful tool for fine-tuning the phasematch wavelength of a $\chi^{(2)}$-grating and it may also be used as a crude stress sensor. Theoretically, a fibre elongation of 1% should be possible in a good fibre. But it was found that the stress resistance in the fibre used here was unusually low.

5.10.2.4 Birefringence Effects

Highly-birefringent fibres may be used for obtaining frequency-doubled radiation at wavelengths, which are shifted from the writing wavelength. In order to calculate the effect of fibre birefringence, we must consider the general expression for the dc-field induced by a pump wave and its coherent seed SH. Employing a procedure similar to the one used in obtaining (5.31), the general form for the induced dc-field is obtained as

$$\mathbf{E}_{dc} = \frac{1}{6}\chi^{(3)}_{1111}\Big[2\mathbf{E}_0(\omega_0)[\mathbf{E}_0(\omega_0)\cdot\mathbf{E}_0^*(2\omega_0)]+ \mathbf{E}_0^*(2\omega_0)[\mathbf{E}_0(\omega_0)\cdot\mathbf{E}_0(\omega_0)]+c.c.\Big]. \quad (5.71)$$

It may be seen that the unit vector $\mathbf{u}_{dc}$ along the direction of the induced dc-field is always parallel to the polarisation of the seed SH. The following analysis is simplified if we assume in addition that the seed waves are launched along the minor or major axes of the fibre. Since highly-birefringent fibres are polarisation preserving, the polarisation state of the seed waves is maintained and depending on which axis the seed SH is launched, $\mathbf{u}_{dc}$ also aligns with that axis. As verified in section (5.10.2.1), the $\chi^{(2)}_{111}$-tensor element also aligns with $\mathbf{u}_{dc}$. This may then be exploited for shifting the phasematch wavelength from the fundamental wavelength used in the seeding process, if the two seed waves are launched orthogonally into the fibre.

This may be seen as follows: The two optical seed waves launched into the HiBi fibre generate $\chi^{(2)}$-gratings oriented along $\mathbf{u}_{dc}$ whose grating vectors are given by

$$G_{ijk}(\omega_0) = \frac{2\pi}{\lambda_0}\Big[2n_i(2\omega_0)-n_j(\omega_0)-n_k(\omega_0)\Big], \quad (4.72)$$

where i,j and k can equal s or f depending on whether the relevant seed-wave is launched along the slow ar fast axis. $n_i(2\omega_0)$, $n_j(\omega_0)$ and $n_k(\omega_0)$ are the phase indices of the seed waves. We can reduce the further discussion to three simple cases, where we consider

a) seed fundamental and SH || slow axis
   resulting grating vector $G_{sss}(\omega_0)$, $\mathbf{u}_{dc}$ ||slow axis

b) seed fundamental||slow axis, seed SH||fast axis
   grating vector $G_{fss}(\omega_0)$, $\mathbf{u}_{dc}$ ||fast axis

c) seed fundamental||fast axis, seed SH||slow axis
   grating vector $G_{sff}(\omega_0)$, $\mathbf{u}_{dc}$ ||slow axis

Since $\chi^{(2)}_{111}$ is aligned along $\mathbf{u}_{dc}$, the SH is always generated along $\mathbf{u}_{dc}$, where the SH conversion efficiency is proportional to $(\mathbf{u}_{dc}\cdot\mathbf{E}(\omega))^4$. Thus the highest SH conversion efficiency is obtained when the read-out fundamental and generated SH are aligned with $\mathbf{u}_{dc}$. Phasematching then occurs for a read-out wavelength λ, for which the $\chi^{(2)}$-grating vector equals the wavevector mismatch of the fundamental and generated SH wave, i.e. when

$$\begin{aligned} &\text{a)}\ G_{sss}(\omega_0) = K_{sss}(\omega) \\ &\text{b)}\ G_{fss}(\omega_0) = K_{fff}(\omega) \\ &\text{c)}\ G_{sff}(\omega_0) = K_{sss}(\omega) \end{aligned} \qquad (5.73)$$

where ω is the optical frequency at wavelength λ and we define the wavevector mismatch K_{ijk} in the same way as the grating vector, i.e.

$$K_{ijk}(\omega) = \frac{2\pi}{\lambda}\Big(2n_i(\omega)-n_j(\omega)-n_k(\omega)\Big). \qquad (5.74)$$

In case a) phasematching occurs for a wavelength equal to the seed fundamental. In case b), phasematching occurs at a wavelength shorter than λ_0 and in case c), phasematching occurs at a wavelength longer than λ_0. This may also be seen from Fig. (5.16), where the grating vector was calculated for the fibre used in the experiments (to be described) for different choices of fibre axes for the seed waves at 1.064μm. The shift in optical frequency $\Delta\nu$ (from the fundamental wavelength) was then estimated as a function of grating vector frequency. Phasematching is then obtained when the grating vector G_{ijk} at $\Delta\nu$=0 equals the wavevector mismatch K_{ijk}.

To test the predictions obtained from theory a P_2O_5 and GeO_2-doped highly birefringent fibre was manufactured. The fibre had a numerical aperture NA=0.24 and the core

was elliptical with an aspect ratio of 1/3 (see Fig.5.17) and an equivalent core radius of 1μm.. Only the LP_{01} mode was guided at 1.064μm. At 532nm both the LP_{01} and the LP_{11} mode were guided. The main contribution to the fibre birefringence arose from stress birefringence. The fibre birefringence $B(\lambda)$ was measured as a function of wavelength using a white-light source technique. $B(1.064\mu m)$ was 4.8×10^{-4} and B(532nm) was 2.2×10^{-4}. The birefringence dispersion $\partial B/\partial\lambda$ was 1.38×10^{-3} μm^{-1} in the vicinity of 1.064μm and effectively zero at 532nm. Over the 1m fibre length used in the experiments, cross-coupling between the two polarisation states amounted to 1% of the total output power.

The phase index of the propagating waves was calculated using the approximation

$$n_{s;f} = n(\lambda) \pm 0.5[B(\lambda_0)+(\lambda-\lambda_0)\partial B(\lambda_0)/\partial\lambda] \qquad (5.75)$$

where $n(\lambda)$ is the phase index as calculated for a non-birefringent fibre by using equations (5.25) and the approximate form for the solution of the eigenvalue equation as given by Gloge[30]. λ_0 is chosen according to whether the phase indices are required in the vicinity of 1.064μm or 532nm.

The $\chi^{(2)}$-gratings were produced by the seeding technique described in section (5.10.2.1). The two seed waves were linearly polarised. The $LiIO_3$ crystal produced the SH orthogonally polarised to the pump wave. A half-wave plate (at 1064nm) was inserted after the $LiIO_3$ crystal to change the relative polarisation directions of the seed pump and SH. Dispersion in the plate introduced a maximum 10% ellipticity into the writing SH when its polarisation was aligned at 45° to the plate's major axis. The wavelength and polarisation dependence were probed using the Raman-shifted dye-laser. The probe pulse peak power was about 10W and the polarisation of the probe pulses could be adjusted with a compensator.

The measured conversion efficiency as a function of frequency deviation $\Delta\nu$ from 1.064μm is shown in Fig. 5.18 for the three cases mentioned above. The SH was generated predominantly in the LP_{01} mode. Conversion to the LP_{11} mode, which occurs through inevitable minor radial asymmetries in the input coupling of the SH writing light, was only observed in case b). Numerical solutions of equations (5.73) for conversion to the SH LP_{01} mode predict conversion peaks at b) of 1.078μm and c) of 1.051μm, which agrees very well with the measurement. The simple theory does not predict the minor peaks visible in Fig. 5.18, which have not been explained satisfactorily yet. However, they are thought to be due to inaccuracies in alignment, the relatively poor polarisation preserving properties of the fibre (1% cross-coupled intensity represents 10% in dc-field terms), and axial nonuniformities in birefringence. These alignment inaccuracies also lead to substantial conversion efficiencies when the orthogonal read-out pump polarisation state is chosen (see Fig. 5.19). The elliptically polarised conversion peaks suggest that phasematching is achieved simultaneously at the same wavelength for both fast and slow pump-waves. This odd result is an artefact of the inability to resolve several very closely spaced peaks, some of which are slow and others fast-polarised.

Finally, it may be noted that it is well known that the fibre-birefringence may be increased by thermal annealing. In this, the fibre is heated at a temperature of about 600°C for several hours. After annealing of the HiBi fibre described here, the orthogonal seeding technique produced phasematch peaks shifted by up to 225cm^{-1} ($\approx\pm$26nm) from 1.064μm. This corresponds to an increase in fibre birefringence to about 10^{-3} at 1.064μm. It was found, however, that thermal annealing did not produce the same birefringence consistently, i.e. typically the obtainable frequency-shift varied between 200 and 225cm^{-1}.

By pulling the HiBi fibre to a larger diameter, so that it also guided the LP_{02} mode and using the orthogonal seeding technique, frequency-shifts up to $330cm^{-1}$ were obtained for the LP_{02} mode.

In conclusion, orthogonal seeding may be used to produce phasematching at wavelength other than the writing wavelength. Frequency-shifts up to $330cm^{-1}$ ($\approx \pm 40nm$) were indeed demonstrated. This technique may also be used to measure the fibre birefringence and it was confirmed that a birefringence up to 10^{-3} may be obtained in a HiBi fibre. Further, the orthogonal seeding technique does not lead to a decrease in SH conversion efficiency. In fact conversion efficiencies up to 5% have been demonstrated using an input intensity of $10GW/cm^2$ in an orthogonally seeded HiBi fibre described here. Parallel seeding produced conversion efficiencies up to 13% in this fibre, which is the highest conversion efficiency reported so far. The higher conversion efficiency for parallel seeding indicates that the $\chi^{(2)}$ induced by the internally-generated dc-field may not be saturated, since the dc-field is by a factor of three stronger for parallel seeding, which produced an almost three times stronger conversion efficiency.

5.10.3 Second-Order Nonlinear Phenomena Using Externally-Induced Second-Order Nonlinearities

The application of large external dc-electric fields to GeO_2 and GeO_2/P_2O_5-doped fibres over a period of time leads to the formation of large second-order nonlinearities. By simultaneously irradiating the fibre with high-intensity light the time constant of the process may be significantly shortened and poling may be achieved at much smaller external dc-fields. The process is thought to be due to the alignment of defect centres.

5.10.3.1 Fibre Design and Fabrication

External dc-electric fields equivalent to the dc-electric breakdown limit may be conveniently applied to specifically designed optical fibres. The fibre structure was developed by L. Li. A typical fibre cross section is shown in Fig. 5.20. In order to produce this fibre shape a standard MCVD preform is treated in the following way: Initially, a hole is drilled into the preform on one side of the fibre core. Then the part of the preform on the opposite side of the core is removed by grinding. Fibre pulling is conventional, however, it is necessary to use relatively low pulling temperatures in order to avoid a deformation of the fibre. The flat side of the fibre does not have to be polished to give a sufficiently smooth surface, since it was found that the pulling process smoothes out the unavoidable surface irregularities introduced by grinding.

An electrode consisting of an In Ga alloy with a melting temperature of about 20^0C is pumped into the fibre hole at a temperature of about 40^0C. The flat side is then pressed onto a smooth metal plate, which provides the second electrode. Electrical contact is established to the liquid metal by inserting a gold wire into the fibre hole and soldering it onto a circuit board.

5.10.3.2 Creation of Nonlinearities

5.10.3.2.1 Defect Excitation by Pulsed Blue Light

As discussed in section 5.10.1 in germanosilicate glass Ge=Ge bonds may be broken by two-photon absorption of 480nm light, which is resonant with the 240nm absorption band of these bonds. Broken Ge=Ge bonds transfer into Ge E′ centres with a trapped hole plus a free electron, which is then trapped by four-bonded Ge to form Ge(1) and Ge(2) centres. Ge E′ centres have no corresponding absorption bands, however, Ge(1) and Ge(2) centres have absorption bands centred at 282nm and 214nm[53]. The

214nm absorption band is narrow and the 282nm absorption band is very broad with an absorption tail that extends well into the visible.

Several experiments were performed to qualitatively show that the defect formation process as discussed above indeed occurs in germanosilicate fibres[58]. Initially a range of fibres doped with 1.5 to 6.5 mole percent GeO_2 were fabricated. Pulsed blue light of a fixed pulse intensity of $1GW/cm^2$ and wavelength of 470nm was then launched into the fibres. The pulses were delivered from a frequency-tripled YAG laser pumping a dye laser and had a 6nsec pulse width and 30Hz repetition rate. The high intensity light induces a strong absorption into the fibre with an absorption tail in the visible similar to a Ge(1) centre. The induced absorption took typically several minutes to saturate at a steady-state level. The induced absorption saturation was measured by launching very low-intensity monochromatic light delivered from a white light source into the fibres and monitoring the fibre transmission as a function of time.

Once the induced absorption saturated, the irradiation was stopped and the absorption spectrum of the treated fibres was measured. It was found that the induced absorption scaled linearly with Ge concentration. At 460nm an absorption of 170dB/km per mole percent GeO_2 was measured. This confirms that the defects excited by blue/green light are germania related. A typical absorption spectrum of a treated fibre is shown in Fig. 5.22, where the results of thermally annealing a treated fibre at 250°C and 750°C are also displayed. The induced absorption at a wavelength of 470nm as a function of peak blue light intensity was also measured. In this, a series of 5m lengths of fibre were used and irradiated with a constant light intensity until the absorption saturated. The fibre had a GeO_2 concentration of 6.5 mole percent and the excitation wavelength was 470nm. The results are shown in Fig. 5.23, where the induced loss is shown directly after the irradiation with blue light was

stopped and the induced loss measured one day later is also displayed.

Further, the excitation spectrum of the induced absorption was measured. In this, pulses of wavelengths ranging from 420 to 540nm were launched into a series of 5m lengths of fibre (2.7 mole percent GeO_2) for a period of 15 minutes each. The peak intensity was $1GW/cm^2$ at each wavelength. The results are shown in Fig. 5.24, where the loss induced at 450nm is plotted against excitation wavelength. A resonance is observed for wavelengths around 480nm, which corresponds to the Ge=Ge or Ge=Si absorption band of 240nm. Since there is no absorption band in an untreated fibre at 480nm, two-step absorption may be excluded and it is thus assumed that two-photon absorption leads to excitation into the 240nm absorption band and the breakage of Ge=Ge and Ge=Si bonds. These broken bonds then lead to the formation of Ge E′ centres with a trapped hole and the formation of Ge(1) or Ge(2) centres with a trapped electron. The Ge E′ centres form deep traps, where the Ge(1) and Ge(2) centres form relatively shallow traps and are easily bleachable[59]. When blue light is launched into a fibre for a period of time a dynamic equilibrium between populations of Ge(1), Ge(2) and Ge E′ centres is present[58]. The equilibrium is governed by two-photon absorption creation of Ge E′ centres and the formation of free electrons, which may recombine with a hole at another Ge E′ centre to form Ge(1) and Ge(2) centres, which may in turn be bleached by single-photon absorption. In addition thermal excitation of electrons also plays a role as shown in Fig. 5.22.

5.10.3.2.2 Excitation of Defect Centres by Pulsed Blue Light and Simultaneous Poling

As discussed in section 5.10.1, it is assumed that when defect centres are excited, the simultaneous application of a dc-electric field should lead to an ordered trapping of electrons and holes and the formation of second-order nonlinearities.

To verify these assumptions, the formation of second-order nonlinearities in germanosilicate fibres was investigated. A multi-mode fibre doped with 28 mole% GeO_2 and a single-mode fibre doped with 18 mole% GeO_2 were used in this study. The multi-mode fibre had internal electrodes and the cross section is shown in Fig. 5.24. The core diameter was 10μm. The single-mode fibre had no internal electrodes. Its core was elliptical with an aspect ratio of 2:1 and the effective core area was $5.9*10^{-8}cm^2$. Due to the core ellipticity the fibre had two cut-off wavelengths of 0.9 and 1.0μm respectively. When the experiments were performed the fibre was kept straight, which meant that it was polarisation preserving. The fibre was designed to allow for modally phasematched SHG of a fundamental wave at about 1.065μm propagating in the LP_{01} mode and the SH propagating in the LP_{02} mode.

To measure the effect of poling on the formation of a second-order nonlinearity, the experimental set-up shown in Fig. 5.25 was used. The pulsed blue dye-laser (wavelength=485nm) and the fundamental of the YAG laser were launched into the front end of a fibre. The optical power launched was measured with calibrated photodetectors and the SH light signal generated by the fundamental of the YAG laser in the fibre was measured by a photomultiplier. A monochromator was used to filter out the exact wavelength of 532nm. A dc-field was then applied across the multi-mode fibre and blue light launched into it. At regular time intervals the blue light was blocked, the dc-field was switched off and the

infrared light unblocked to probe the magnitude of the induced $\chi^{(2)}$ by measuring the generated SH signal.

Prior to any treatment of the fibres, a very weak SH signal caused by nonlinear quadrupole and magnetic dipole moments was detected. A minimum in-core peak intensity I_{th} of 100MW/cm^2 was necessary before any increase in SH signal was detectable. However, this was verified for a dc-field strength of less than 30V/μm only. At intensities above this threshold the SH conversion efficiency typically took several minutes to reach a saturation value $P_{sat}{}^{2\omega}$ that depended on E_{dc}. The maximum observed SH power in the multi-mode fibre at an applied field of 4V/μm is plotted in Fig. 5.26 as a function of peak blue light intensity. Just above I_{th} this function is strongly nonlinear, and for higher intensities it saturates. The saturated SH power $P_{sat}{}^{2\omega}$ in the multi-mode fibre as a function of dc-field strength is shown in Fig. 5.27. For small fields $P_{sat}{}^{2\omega}$ grows quadratically with electric field and above 4V/μm it saturates. This suggests that almost perfect alignment of all orientable defect centres is achieved for E_{dc}>4V/μm.

Once created, the induced $\chi^{(2)}$ nonlinearity could not be erased by pulsed blue light alone. Even at intensities twice as high as used in the alignment process. However, a $\chi^{(2)}$ created in the single-mode fibre could be bleached by using intense cw Argon laser light at 488nm. This was confirmed in the following way. The SH conversion efficiency in the single-mode fibre was measured after poling it and the fibre then taken to an Argon laser, where an optical power of 550mW (intensity of 1MW/cm^2) was launched for 10min. A subsequent measurement of the SH conversion efficiency showed a reduction in SH signal of 90%. Further bleaching experiments were performed by Oulette et al[60], who used a mode-locked and Q-switched frequency-doubled YAG-laser for optical bleaching of internally-written $\chi^{(2)}$-gratings in germanosilicate fibres. They showed that peak optical intensities in excess of 1kW and average powers higher than 1mW had to

be used to bleach the $\chi^{(2)}$-grating in a time of several minutes. It is therefore not surprising that optical bleaching of a second-order nonlinearity could not be achieved by using blue light peak pulse powers of only 100W and average powers of only 20μW. However, Oulette et al showed that for the same average power, optical bleaching by light pulses is more effective than bleaching by cw light, which indicates that optical bleaching is governed by a multi-photon process.

The pump polarisation dependence of the SH conversion efficiency was also verified. It was found that the highest conversion efficiency is obtained for an infrared pump polarisation parallel to the direction of the dc-field or poling axis. The SH signal varied as $\cos^4\alpha$ with α being the angle of the pump polarisation with the poling axis. Therefore it may be concluded that as in the case of internally-written $\chi^{(2)}$-gratings only a $\chi^{(2)}_{111}$ tensor component is formed by the poling process.

5.10.3.2.3 **Measurement of $\chi^{(2)}(2\omega=\omega+\omega)$ Induced by Poling**

The magnitude of the induced $\chi^{(2)}$ could be estimated in two ways. The first method is to compare the SH signal due to ESHG in an unpoled fibre with the SH signal in a poled fibre. The second method is by measuring the SH conversion efficiency directly in a modally phasematched fibre. $\chi^{(2)}$ may also be be measured by using the Pockels effect and optical rectification. These techniques will be discussed in section 5.10.3.3 and 5.10.3.5.

When comparing the ESHG signal ($P^{2\omega}{}_{dc}$) with the SH signal induced by poling ($P^{2\omega}{}_{pol}$) the following expression for the ratio of the two signals is obtained (assuming plane polarised light with the polarisation axis parallel to the poling axis)

$$\frac{P^{2\omega}_{pol}}{P^{2\omega}_{dc}} = \frac{\left[\chi^{(2)}_{pol}(2\omega=\omega+\omega)O_{pol}\right]^2}{\left[\chi^{(2)}_{1111}(2\omega=\omega+\omega+0)E_{dc}O_{dc}\right]^2}, \qquad (5.76)$$

where E_{dc} is the field strength used for the ESHG measurements and O_{pol} and O_{dc} are the respective overlap integrals for the two processes. The magnitude of $\chi^{(2)}_{pol}$ is then obtained from

$$\chi^{(2)}_{pol} = \chi^{(3)}_{1111}\frac{O_{dc}E_{dc}}{O_{pol}}\left(\frac{P^{2\omega}_{pol}}{P^{2\omega}_{dc}}\right)^{1/2} . \qquad (5.77)$$

For a multi-mode fibre a comparison using this technique is only approximately valid, since the polarisation of the fundamental wave is scrambled and the two overlap integrals may not be accurately calculated. However, an approximate value for $\chi^{(2)}_{pol}$ may so be estimated. Using the value for $\chi^{(3)}_{1111}=2.0\times10^{-14}$ esu, the maximum value for $\chi^{(2)}_{pol}=2\times10^{-11}$ esu was so estimated. This is about 120 times smaller than $\chi^{(2)}(2\omega=\omega+\omega)$ for KDP.

A comparison as described above could not be made for the single-mode fibre since the overlap integral for ESHG was almost zero. This may be seen if we consider that this fibre was designed for modally phasematching the LP_{01} with the LP_{02}-mode. ESHG is essentially governed by an effective $(\chi^{(2)}_{111})_{eff}=\chi^{(3)}_{1111}E_{dc}$, which is uniform across the fibre. Since in this fibre the V-value at a pump wavelength of around 1.065μm is 2.0, according to Fig. 5.3, the overlap integral is indeed almost zero. Therefore the direct measurement of the SH conversion efficiency was used to estimate the magnitude of $\chi^{(2)}_{pol}$.

When measuring $\chi^{(2)}_{pol}$ it is important to induce a $\chi^{(2)}$ along a length of fibre, which is shorter than the spatial coherence length. This may be easily achieved by using very short electrodes in the poling process. As shown in section 5.7.1.2, a spatial coherence length of typically 1.5 to 3cm can be obtained by modal phasematching. Therefore, the electrode length was reduced to only 3.25mm in the following experiments. The electrodes consisted simply of two polished metal plates

separated by 1mm with index matching oil inserted between them to increase the breakdown field strength.

In general the poling field was applied to the fibre at an unknown angle α with respect to the major axis. However, α could be obtained by measuring the SH conversion efficiencies η_1, η_2 along the two fibre axes. Neglecting the difference in phasematch wavelength for wave propagation along the two fibre axes and assuming the pump-wavelengths are simultaneously phasematched to the SH-wave, i.e. they are in the centre of the phasematch peak, η_1 and η_2 are then given by

$$\eta_1 = \xi \, P^{\omega} \cos^4\alpha \qquad (5.78)$$

$$\eta_2 = \xi \, P^{\omega} \sin^4\alpha, \qquad (5.79)$$

where ξ has been defined in (5.30). By comparing η_1 and η_2 the magnitude of the induced $\chi^{(2)}$ may then be calculated. If the SH-wave is not simultaneously phasematched to the fundamental wave propagating along the two fibre axes, as may be the case in fibres with a strongly elliptical core or when longer poling electrodes are used, the width of the phasematch peak is narrower than the separation of the two phasematch peaks corresponding to phasematching along the two fibre axes. Assuming the conversion efficiencies are measured for wave propagation along the two fibre axes, η_1 and η_2 are then proportional to $\cos^6\alpha$ and $\sin^6\alpha$ respectively.

5.10.3.2.4 The Excitation Spectrum of $\chi^{(2)}(2\omega=\omega+\omega)$ in Germanosilicate Fibres

The single-mode fibre described in section 5.10.3.2.2 was used in this experiment. The direct measurement technique described in the previous section was applied to measure $\chi^{(2)}(2\omega=\omega+\omega)$. Defects were excited by launching pulsed blue light (as described earlier) of wavelengths ranging from 430-540nm into different fibre samples of length 22cm. The peak blue pulse intensity was kept constant at

1.7GW/cm^2 and an external dc-field of 2.5V/μm was applied by using the 3.25mm long electrodes. Each fibre sample was irradiated with blue light and simultaneously poled for a time of 5 minutes. The blue light was then blocked and the dc-field left on for another minute. The fibre samples were then stored at room temperature for six weeks and afterwards SHG measurements were made. In this the Raman-shifted dye laser was used. The polarisation of the infrared light could be adjusted by a compensator in order to measure the SH conversion efficiency along the two fibre axes. In order to find the modal phasematch peak infrared light of 1.2GW/cm^2 peak intensity was launched into a fibre sample and the SH signal monitored while the infrared wavelength was scanned until a resonance was found. The phasematch wavelength varied from 1.050 to 1.080μm between fibre samples, which is due to unavoidable small fibre inhomogeneities as explained in section 5.7.1.2. Due to the ellipticity of the fibre the phasematch peak along the major and minor axis of the fibre was split by 0.8nm.

The results are shown in Fig. 5.28. A strong resonance at an excitation wavelength of about 480-490nm is observed. In terms of the measured SH-signal for a given infrared intensity, the resonance is even stronger, since the SH signal is proportional to the square of $\chi^{(2)}$. The maximum induced $\chi^{(2)}$ is about 7.5×10^{-13} esu, which is about 30 times smaller than the magnitude of $\chi^{(2)}$ estimated for the multi-mode fibre as calculated in the previous section.

5.10.3.2.5 Formation of Second-Order Nonlinearities in Germanosilicate Fibres—Discussion

By comparing Figs. 5.28 and 5.23 we see that there is a close correlation between the creation of second-order nonlinearities by poling and the excitation of defect centres by high-intensity pulsed blue light, at least for germanosilicate fibres. An excitation wavelength of 480nm, corresponding to the 240nm absorption peak of

oxygen deficient germanosilicate glass produces the highest induced absorption and the highest induced second-order nonlinearity. This indicates that both processes are governed by two-photon absorption induced breaking of Ge=Ge or Ge=Si bonds and the formation of Ge E' centres with the trapping of holes and the generation of free electrons. As explained in section 5.10.3.2.1 it is assumed that the blue light induced absorption is due to the subsequent trapping of free electrons at four-coordinated Ge and the formation of Ge(1) and Ge(2) centres.

It has been shown that Ge(1) and Ge(2) centres are easily bleachable by cw Argon laser light[59]. This was verified when the loss in germanosilicate fibres was measured while high-intensity cw light (λ=488nm) was launched into it. While the high-intensity light was on, the induced loss in the fibre was small, due to continuous reexcitation of free electrons that got trapped at Ge(1) and Ge(2) centres. However, as soon as the blue light was switched off, the loss increased very rapidly due to permanent trapping of these free electrons and the formation of Ge(1) and Ge(2) centres.

On the other hand bleaching of second-order nonlinearities is a slow process. Therefore, unless there is a mechanism that causes the colour centres to fall into the same traps after a short exposure to high-intensity cw blue light, it is unlikely that the relatively unstable Ge(1) and Ge(2) centres contribute dominantly to $\chi^{(2)}$. A possible explanation could be that aligned colour centres form domains, which cause bleached Ge(1) and Ge(2) centres to fall into the same traps when the bleaching process is stopped. A possible experiment to show that this is not the case may be to launch high-intensity cw blue light into a fibre and to measure the SH conversion efficiency at the same time. If the SH conversion would drop during the presence of the blue light and increase after the blue light had been switched off, it would indeed indicate that Ge(1) and Ge(2) play a

significant role in the formation of second-order nonlinearities.

A more plausible explanation is, however, that the more stable Ge E' centres lie at the root of second-order nonlinearities. In this case an ordering mechanism could arise by preferential trapping of a hole at broken Ge=Ge bonds. The inducable second-order nonlinearity should then be proportional to the square of the GeO_2 concentration. If, on the other hand, preferential breaking of Ge=Si bonds under the influence of an applied dc-electric field is dominant, the inducable second-order nonlinearity should be linearly proportional to GeO_2 concentration.

All three models discussed here do not explain the saturation mechanisms observed in section 5.10.3.2.2 satisfactorily. However, the initial strongly nonlinear dependence of the inducable $\chi^{(2)}$ for a given applied dc-field strength on blue light intensity as shown in Fig. 5.26 indicates that a multi-photon process is responsible for the initial creation of second-order nonlinearities.

Summarising, the physical processes behind the formation of second-order nonlinearities that have been elucidated so far and backed up with experimental evidence are:

1) High intensity blue light (λ=480nm) is resonantly absorbed via two-photon absorption

2) Ge=Ge or Ge=Si bonds are broken

3) Free electrons are created that get trapped to form Ge(1) and Ge(2) centres and holes get trapped to form Ge E' centres

In order to determine which defect centres are dominant in the formation of second-order nonlinearities under the influence of an applied dc-field, further experiments as described above and ESR measurements are necessary.

However, the initial stages of the process have been revealed by the experiments described in sections 5.10.3.2.1-5.10.3.2.4.

5.10.3.2.6 Other Poling Techniques

In addition to optical fibre poling by using pulsed blue light, other techniques have also been employed successfully for the creation of second-order nonlinearities. These are i) defect excitation by cw blue light and simultaneous application of strong dc-electric fields, ii) the application of strong dc-electric fields only and iii) γ-irradiation and the application of dc-electric fields.

However, the experimental data for these three poling techniques are still very limited and therefore they are only briefly described here. Technique ii) was discovered by Li[61] and is described in section 5.10.3.3, where results obtained with technique iii) are also discussed.

Defect excitation by cw blue light and simultaneous fibre poling has so far produced the highest magnitude for $\chi^{(2)}(2\omega=\omega+\omega)$ in optical fibres. In this, the fibre already described in section 5.8 was used. As described in section 5.8, applying a dc-field of 125V/μm to the fibre for a period of 15 minutes did not lead to a measurable creation of a $\chi^{(2)}(2\omega=\omega+\omega)$ in the fibre. A large $\chi^{(2)}$ was generated in the fibre in the following way. 400mW of cw Argon laser light of wavelength 488nm was launched into the fibre for 10 minutes and simultaneously a field of 100V/μm was applied. The blue light was then switched off and the dc-field left on for another minute. The magnitude of the induced $\chi^{(2)}$ was estimated by comparing the SH signal created in the poled fibre with the ESHG signal before poling. The measurements were made at a fundamental wavelength of 1.208μm, where the fibre was modally phasematched. The two overlap integrals in equation (5.77) were calculated as O_{dc}=11% and O_{pol}=15% in this fibre. Using equation

(5.77) $\chi^{(2)}(2\omega=\omega+\omega)$ was calculated as $(2.7\pm1)\times10^{-10}$ esu, which is only about 9 times smaller than the value of $\chi^{(2)}(2\omega=\omega+\omega)$ for KDP. Launching a pump power of 40W at 1.208μm, a SH conversion efficiency of 0.05% was measured. Using the estimated spatial coherence length for modal phasematching of 1.5cm (see section 5.8), equation (5.30) predicts a conversion efficiency of 0.02% for the above pump power, which is in good agreement with the measurement considering the measurement uncertainties outlined in section 5.8.

No exact comparison of $\chi^{(2)}(2\omega=\omega+\omega)$ created by the same poling technique in phosphogermanosilicate and germanosilicate fibres has yet been made. However, a comparison of $\chi^{(2)}(\omega=\omega+0)$ (see section 5.10.3.3) between these two fibre shows that P_2O_5-doping leads to higher nonlinearities.

5.10.3.3 The Pockels Effect

The long interaction lengths available in poled optical fibres allow the measurement of even a very weak Pockels effect and the demonstration of electrooptic modulation via the Kerr effect. When a dc electric field is applied to a poled fibre and a fundamental wave launched into it, the Pockels effect creates a nonlinear polarisation at the frequency of the fundamental wave. Assuming the second-order nonlinearity consists of only the $\chi^{(2)}{}_{111}(\omega=\omega+0)$ component, the nonlinear polarisation at frequency ω is obtained as

$$P_{NL}^{\omega} = \chi_{111}^{(2)}(\omega=\omega+0)(E^{\omega})_1(E_{dc})_1. \qquad (5.80)$$

The nonlinear polarisation is proportional to E_{dc} and gives rise to a phase retardation $\Delta\phi_p$ of the pump wave. $\Delta\phi_p$ is commonly expressed in terms of the Pockels coefficient r_{11}, where $\Delta\phi_p$ is given by

$$\Delta\phi_p = \frac{\pi n^3 r_{11} E_{dc} L}{\lambda}, \qquad (5.81)$$

where L is the interaction length and λ is the wavelength of the pump wave. Using (5.80) it may be verified using a standard procedure[62] that r_{11} may be expressed in terms of $\chi^{(2)}_{111}(\omega=\omega+0)$ like

$$r_{11} = \frac{4\pi}{n^4} \chi^{(2)}_{111}(\omega=\omega+0) \qquad (5.82)$$

Similarly, a phase retardation proportional to the square of the electric field is observable in glass fibres, which is governed by the Kerr coefficient s_{11}

$$\Delta\phi_k = \frac{\pi n^3 s_{11} E_{dc}^2 L}{\lambda}. \qquad (5.83)$$

The amplitude of the nonlinear polarisation giving rise to the Kerr effect is of third order and may be obtained as

$$P^{\omega}_{NL} = \chi^{(3)}_{1111}(\omega=\omega+0+0)(E^{\omega})_1(E_{dc})_1(E_{dc})_1. \qquad (5.84)$$

Applying a similar procedure as employed in obtaining (5.82) and using (5.84), the relation between the Kerr coefficient and the third-order nonlinear susceptibility is found as

$$s_{11} = \frac{4\pi}{n^4} \chi^{(3)}_{1111} (\omega=\omega+0+0). \qquad (5.85)$$

In the case of a poled fibre with a pure silica cladding, a $\chi^{(2)}$ is only induced in the fibre core. It may then be shown that the phase retardation is proportional to the intensity overlap integral O_{pock} between $\chi^{(2)}(r)$ and the fibre mode. It is important to have single-mode operation of the fibre at the pump wavelength. Further, if the fibre is elliptical, as often encountered in as drawn D-shaped fibres, the poling axis has to be aligned with one of the fibre axes to obtain the highest possible phase

retardation with an applied electric field. The general expression for the phase difference of two waves propagating along the two fibre axes with a poling axis at an angle α with respect to the major axis and an applied dc-field at an angle ß with respect to the major axis (see Fig. 5.29) is

$$\Delta\phi_p = \frac{\pi n^3 r_{11} E_{dc} L}{\lambda} \cos(\alpha+\beta) O_{pock}. \qquad (5.86)$$

Since the third-order nonlinear susceptibility has an orthogonal component, which is about one third of the parallel component, the Kerr effect induced phase difference for two pump waves propagating along the two fibre axes is given by

$$\Delta\phi_k = \frac{\pi n^3 s_{11} E_{dc}^2 L}{\lambda} \frac{2}{3} (\cos^2\beta - \sin^2\beta). \qquad (5.87)$$

The techniques for measuring the Pockels and Kerr effect have been discussed in detail by Li[63] and are summarised here. The Pockels or Kerr effect induced phase retardation may be measured by launching linearly polarised light at 45° with respect to the fibre axes and applying a modulating dc-electric field along one fibre axis, i.e. the poling axis in the case of the Pockels effect. A Soleil-Babinet compensator is used at the output end to adjust the phase difference of the two waves propagating along the fibre axes to a multiple of $\pi/2$ at the fibre output end. A polariser is then inserted between the output end of the fibre and a detector, where the polarisation axis is at 45° to the fibre axes. If the compensator is adjusted to give a phase-difference of $n\pi$ (n=integer), then an applied small modulating electric field gives rise to a modulated detector signal with a modulation depth of $(\Delta\phi)^2$ with respect to the maximum transmitted signal. If the compensator is adjusted to give a phase difference of $(2n-1)(\pi/2)$, then a small modulating electric field gives rise to a modulated detector signal with a modulation depth of $2\Delta\phi$. The

Pockels effect modulates the signal with a frequency equal to the frequency of the modulating electric field and the Kerr effect modulates the detector signal at twice that frequency. This difference in frequency may therefore be exploited to distinguish between these two effects in a poled fibre.

Detailed experimental results for the characterisation of the Pockels effect in fibres are not yet available. However, a number of important observations have already been made, which show that the Pockels effect and SHG are governed by different second-order nonlinearities, which are also created in different ways. These observations are summarised here.

Unlike observed in the creation of $\chi^{(2)}(2\omega=\omega+\omega)$, $\chi^{(2)}(\omega=\omega+0)$ is induced in a phosphogermanosilicate fibre (described in sections 5.8 and 5.10.3.2.6) when a dc-field (E_{dc}=125V/μm) is applied to the fibre for a time of less than 5 minutes[61] and no defect excitation light is used. No difference in the maximum $\chi^{(2)}(\omega=\omega+0)$ created by using a poling field only or by using a poling field and simultaneously launching cw blue light, pulsed blue light or quasi-cw mode-locked blue light into the fibre was observed. Further, a minimum poling field of 60V/μm had to be applied to the fibres in order to create a Pockels effect in fibres without using any blue light. These results indicate that no defect excitation light is needed for the creation of $\chi^{(2)}(\omega=\omega+0)$ and that therefore the mechanisms behind the creation of $\chi^{(2)}(\omega=\omega+0)$ and $\chi^{(2)}(2\omega=\omega+\omega)$ are different.

Further, the effect of high-energy γ-rays on the poling process was investigated. In this, a germanosilicate fibre with a numerical aperture NA=0.15 and a cut-off wavelength of 600nm was used. The fibre was exposed to γ radiation ($\approx$1.5 MeV energy) from a Co^{60} source while a poling field of 150V/μm was applied. Four different total radiation doses of 1×10^3, 1×10^4, 5×10^4, 2×10^5 rads were used. After the γ radiation exposure was stopped, the

poling field was left on for another minute. $\chi^{(2)}(\omega=\omega+0)$ was then measured using the Pockels effect and a pump wavelength of 633nm. The results are displayed as a function of total radiation dose in Fig. 5.30. It may be seen that γ radiation is detrimental to the creation of $\chi^{(2)}(\omega=\omega+0)$. It was then verified whether $\chi^{(2)}(\omega=\omega+0)$ could recover in the fibre exposed to the highest amount of radiation when this fibres was exposed to a poling field of 200V/μm for a time of up to 5 hours. No recovery of $\chi^{(2)}(\omega=\omega+0)$ could be observed. This shows that whatever defect is responsible for the creation of $\chi^{(2)}(\omega=\omega+0)$, it is gradually eliminated by high energy irradiation.

The highest value for an induced $\chi^{(2)}(\omega=\omega+0)$ was obtained in the phosphogermanosilicate fibre described in section 5.8. In this a poling field of 400V/μm and no defect excitation light was used. It was observed[61] that total amplitude modulation at a wavelength of 633nm could be obtained for an applied field of 65V/μm in an interaction length of 50cm. Using these results and assuming an intensity overlap integral O_{pock} of 80%, the magnitude of $\chi^{(2)}(\omega=\omega+0)$ is calculated from (5.82) and (5.86) as 8.6×10^{-11} esu. This is about 3 times less than the maximum $\chi^{(2)}(2\omega=\omega+\omega)$ observed in a phosphogermanosilicate fibre. The maximum value of $\chi^{(2)}(\omega=\omega+0)$ observed in germanosilicate fibres was typically between three and five times less than measured in phosphogermanosilicate fibres.[61]

5.10.3.4 Comparison of SHG and the Pockels Effect- Discussion

The results described in sections 5.10.3.2 and 5.10.3.3 indicate that $\chi^{(2)}(2\omega=\omega+\omega)$ and $\chi^{(2)}(\omega=\omega+0)$ are induced into the two types of oxide glasses studied by different mechanisms. $\chi^{(2)}(2\omega=\omega+\omega)$ measures the purely electronic contribution[35] to the second-order nonlinear susceptibility and was shown to be only 10 times smaller than in KDP in the best fibres. $\chi^{(2)}(\omega=\omega+0)$ measures a

mixture of electronic and ionic contributions and was shown to be about 3 times smaller than $\chi^{(2)}(2\omega=\omega+\omega)$ in the best fibres. Further, phosphogermanosilicate fibres were found to lead to higher nonlinearities than germanosilicate fibres. $\chi^{(2)}(2\omega=\omega+\omega)$ was shown to be closely related to the formation of Ge E', Ge(2) and Ge(1) centres by high-intensity light in germanosilicate glass and an ordered trapping of holes or electrons has been proposed to lead to the creation of $\chi^{(2)}(2\omega=\omega+\omega)$.

However, though it was shown that the formation of $\chi^{(2)}(\omega=\omega+0)$ is also related to the excitation of defect centres (see section 5.7.2.4), it is not yet known what defect centres are involved in the process and what mechanisms are responsible for the creation of the Pockels effect. Further studies of the Pockels effect are clearly necessary to elucidate these processes. In particular, a fibre design is needed that allows the simultaneous measurement of $\chi^{(2)}(2\omega=\omega+\omega)$ and $\chi^{(2)}(\omega=\omega+0)$ to a high accuracy and under similar poling conditions. A modally phasematched fibre with internal electrodes or a fibre with an externally-induced $\chi^{(2)}$-grating would enable these important measurements.

5.10.3.5 Optical Rectification

Optical rectification has so far not been observed in poled optical fibres. However, we include a brief discussion of this effect, since it may potentially serve as a very useful measurement technique. In an optical rectification experiment, the total electromagnetic field inside the fibre is given by the fundamental wave and may be expressed as in equation (5.7). Inserting (5.7) into (5.1), we obtain for the nonlinearity governing optical rectification

$$P_{NL}^{\omega=0} = \chi_{111}^{(2)} (E^{\omega})_1 (E^{\omega})_1^{*}. \qquad (5.88)$$

High intensity light thus induces a dc-polarisation inside a poled optical fibre. The dc-polarisation induces a voltage across electrodes applied to the fibre (see Fig. 5.31). If, for simplicity, we assume the core cross section to be rectangular with axes of length a and b, the induced dc voltage across the electrodes may be calculated following an analysis given by Shen[24] and is obtained as

$$V \approx -\frac{4\pi ab}{\varepsilon w} \chi_{111}^{(2)} E^2, \qquad (5.89)$$

where E is the electric field of the pump wave, ε is the dielectric constant at zero frequency and w is the width of the internal electrode. Since $\varepsilon \approx 4$ and using (5.13), we may express V as

$$V \approx -\frac{32\pi}{cn(\omega)w} \chi_{111}^{(2)} P, \qquad (5.90)$$

where P is the launched power. V should in principle be measurable by using a cw pump source and a phase-sensitive detection technique. Assuming plane polarised light aligned parallel to the poling axis, a launched cw power of 500mW, an electrode width of 40μm and a $\chi^{(2)}(0=\omega-\omega)=\chi^{(2)}(\omega=\omega+0)=8.6\times10^{-11}$ esu, V is calculated as 76nV. In a multi-mode fibre, the polarisation is scrambled and thus V would be a factor of two smaller, i.e. V$\approx$38nV. These are very small voltages, which however could be increased by using smaller electrodes and larger core areas, which would allow the launching of more light power. Further, pulsed measurements are also possible, since the launched power could then be increased by a factor of 100 to 1000.

5.10.6 Summary

The results presented in section 5.10 show that poling of oxide glass fibres is a viable method for the creation of second-order nonlinearities. It has been shown that poling may be obtained by using at least three different techniques. In the first technique (poling by using only light) a poling field (<100V/cm) is created via four-wave mixing of a fundamental wave and its SH; defect excitation is accomplished via a multi-photon process. In the second technique (poling by using both light and a dc-field) a poling field (>1000V/cm) is applied externally to the fibre and defect excitation is accomplished via high-intensity blue light. In the third technique (poling by using only a dc-field) a poling field (>$6*10^5$V/cm) is applied to the fibre and defect excitation is accomplished via electrons accelerated by the large dc-field.

The common feature to all three poling techniques is that whenever a second-order nonlinearity is induced, colour centres are formed and the fibre loss increases. The maximum magnitude of the induced second-order nonlinearity by the three poling techniques is summarised in table 5.1. It may be seen that P_2O_5-GeO_2-doped silica fibres exhibit the highest nonlinearities. Further, poling by cw-blue light is about 10 times more effective than poling by pulsed blue light in a P_2O_5-GeO_2-doped fibre. It has not been established whether this is also true for GeO_2-doped silica fibres. The creation of the Pockels effect is dominated by a strong poling field, i.e. it does not make a difference to the final magnitude of $\chi^{(2)}(\omega=\omega+0)$ whether defect excitation light has been used in the poling process or not.

There still remain several discrepancies when linking these poling techniques to each other. In particular, the question why an external poling field has to be two to three orders of magnitude larger than an internal poling field to create a second-order nonlinearity of the same

magnitude remains unsolved. It may be that the involved defects exhibit strong excitation resonances similar to the one revealed in section 5.10.3.2.4. Further measurements of $\chi^{(2)}$-excitation spectra in phosphogermanosilicate glass and for different wavelength regions should resolve the question of defect resonances.

Another open question is the discrepancy between $\chi^{(2)}(2\omega=\omega+\omega)$ and $\chi^{(2)}(\omega=\omega+0)$ measured in externally poled fibres. However in order to make a good comparison between these nonlinear coefficients, measurements have to be carried out on fibres poled by using exactly the same technique. In addition, a comparison of nonlinear coefficients is only valid in dispersion-free and loss-free materials, which is clearly not the case here, since the second-order nonlinearity is related to colour centres.

The physical origin of the second-order nonlinearities is still not known. Though it has been shown in section 5.10.3.2 that the creation of second-order nonlinearities is closely related to known defect centres in germanosilicate glass, is was not possible to establish which defect centres and in what form are responsible for the poling of the glass. A significant improvement in the amount of data available on defect centres should be possible by ESR measurements on poled bulk optical glass samples. Poling bulk germanosilicate samples should be rather straight-forward, since a poling field of only several V/μm and UV-light is necessary in the process.

5.11 Second-Order Nonlinear Phenomena in Glasses: Conclusions and Future

The understanding of second-order nonlinear phenomena in optical fibres has clearly improved since they were first reported by Österberg and Margulis in 1986[11]. The work described in this chapter has proved that a defect poling mechanism lies behind the creation of second-order

nonlinearities in glass. A variety of poling techniques have been discovered, which have been readily characterised and classified into: i) poling by light, ii) poling by light and an external dc-field and iii) poling by an external dc-field. The detailed characterisation of technique ii) described here has shown that there is a close correlation between defect centre induced nonlinear transmission and the creation of defect centres. It may well be that future work will also reveal a strong link of this work to the observation of light-induced refractive index changes as described by Hill et al[28].

Future work in the area of second-order nonlinear phenomena will provide an opportunity for improving our knowledge of defect centres in glasses. It will involve:

1) Improvements in the understanding of the physical processes behind the formation of second-order nonlinearities. Further characterisation of the poling techniques described here is therefore required – several experiments to achieve this have been proposed in this chapter.

2) Continuation of the search for optical glasses with very high inducable second-order nonlinearities; the poling and measurement techniques described here should serve as a guide-line for the accurate characterisation of the quality of these glasses.

3) Characterisation of other second-order nonlinear phenomena apart from SHG and the Pockels effect; in particular, optical rectification and three-wave mixing needs to be studied.

4) Development of improved phasematching techniques; in particular, externally induced $\chi^{(2)}$-gratings appear to be potentially very useful and could be employed as practical frequency-doublers.

Appendix 5.I

Table for conversion of SI to cgs-si units:

	SI	cgs-si
length	meter	10^2 centimetres
mass	kilogram	10^3 grams
time	second	1 second
force	newton	10^5 dynes
energy	joule	10^7 ergs
power	watt	10^7 ergs/second
charge	coulomb	$3*10^9$
electric potential	volt	1/300
electric field intensity	volt/meter	$1/(3*10^4)$
electric current	ampere	$3*10^9$
conductivity	mho/meter	$9*10^9$
resistance	ohm	$1/(9*10^{11})$
capacitance	farad	$9*10^{11}$
magnetic flux	weber	1/300
magnetic induction	tesla	$1/(3*10^6)$
magnetic field intensity	ampere/meter	$12\pi*10^7$
poynting vector S	joule/second/ meter^2	10^3
$\chi^{(2)}$	meter/volt	$(3*10^4)/4\pi$
$\chi^{(3)}$	(meter/volt)^2	$(3*10^4)^2/4\pi$

For silica glasses it holds

$S_{mks} \approx 1.93*10^{-3}\ E^2_{mks}$

$S_{esu} \approx 1.74*10^{9}\ E^2_{esu}$

Appendix 5.II

Definition of Nonlinear Coefficients

Unfortunately, no standard definition of nonlinear coefficients has yet been accepted. Even in the area of SHG in optical fibres three different definitions have been used. Throughout this chapter we have adopted the definition of nonlinear coefficients as proposed by Shen[24], since it is the only definition that remains consistent when mixing of degenerate waves and waves of zero frequency is considered[24]. This definition has also been used by the author[18,20,22,23] in the original fibre poling work. Stolen and Tom have used a different definition in their important papers on SHG[17,33]. This definition has subsequently also been used by Mizrahi et al[47]. The early theoretical work by Terhune and Weinberger[14] employed the definition according to Maker and Terhune[34]. In the following we list the expression for the amplitude of the nonlinear polarisation as encountered in this chapter assuming both Shen's and Stolen and Tom's definition. For simplicity we assume plane polarised light throughout and consider mixing only via $\chi^{(2)}_{111}$ and $\chi^{(3)}_{1111}$.

Nonlinear process	Shen	Stolen and Tom
SHG	$\chi^{(2)}E^{\omega}E^{\omega}$	$(1/2)X^{(2)}E^{\omega}E^{\omega}$
TWM	$\chi^{(2)}E^{\omega 1}E^{\omega 2}$	$X^{(2)}E^{\omega 1}E^{\omega 2}$
SOR	$\chi^{(2)}E^{\omega}(E^{\omega})^{*}$	$(1/2)X^{(2)}E^{\omega}(E^{\omega})^{*}$
PE	$\chi^{(2)}E^{\omega}E_{dc}$	$2\ X^{(2)}E^{\omega}E_{dc}$
ESHG	$\chi^{(3)}E^{\omega}E^{\omega}E_{dc}$	$(3/2)X^{(3)}E^{\omega}E^{\omega}E_{dc}$
NDFWM	$\chi^{(3)}E^{\omega}E^{\omega 1}(E^{\omega 1})^{*}$	$(3/2)X^{(3)}E^{\omega}E^{\omega 1}(E^{\omega 1})^{*}$
TOR	$\chi^{(3)}(E^{2\omega})^{*}E^{\omega}E^{\omega}$	$(3/4)X^{(3)}(E^{2\omega})^{*}E^{\omega}E^{\omega}$
IDRI	$\chi^{(3)}E^{\omega}E^{\omega}(E^{\omega})^{*}$	$(3/4)X^{(3)}E^{\omega}E^{\omega}(E^{\omega})^{*}$
KE	$\chi^{(3)}E^{\omega}E_{dc}E_{dc}$	$3\ X^{(3)}E^{\omega}E_{dc}E_{dc}$

In this, SHG=second-harmonic generation; TWM=three-wave mixing; SOR=second-order optical rectification;

PE=Pockels effect; ESHG=electric-field-induced-second-harmonic generation; NDFWM=near-degenerate four-wave mixing; TOR=third-order optical rectification; IDRI=intensity-dependent refractive index; KE=Kerr effect.

The disadvantage of using Stolen and Tom's definition is now apparent, since it may be seen that for example in second-order nonlinear mixing there is a sudden change of $X^{(2)}(\omega_3=\omega_1+\omega_2)$ to $2X^{(2)}(2\omega=\omega+\omega)$ when ω_1 and ω_2 become degenerate or a change from $X^{(2)}(\omega+\delta=\omega+\delta)$ to $(1/2)X^{(2)}(\omega=\omega+0)$ when δ goes to zero. On the other hand Shen's definition provides smoothly varying coefficients even in the case of degeneracy.

However, a problem is encountered when Shen's definition is applied to third-order optical rectification. Strictly following that definition we obtain for the created dc-polarisation

$$P_{dc} = \chi^{(3)}(E^{2\omega})^* E^{\omega} E^{\omega} e^{-i\Delta kz}.$$

The physically relevant dc-field is given by the real part of the polarisation, which however is not obvious from the above definition. We may rectify this problem by writing

$$P_{dc} = (1/2)\chi^{(3)}[(E^{2\omega})^* E^{\omega} E^{\omega} + E^{2\omega}(E^{\omega})^*(E^{\omega})^*],$$

which then results in a real expression for the dc-polarisation.

The magnitude of $\chi^{(3)}_{1111}$ may be obtained from measurements of the intensity-dependent refractive index n_2. Adair[64] measured the value $n_2=8.5\times10^{-14}$ esu at a wavelength around 1.060μm. In Shen's definition n_2 is given by

$$n_2 = (2\pi/n)\chi^{(3)}_{1111}(\omega=\omega+\omega-\omega),$$

which results in the value of $\chi^{(3)}_{1111}(\omega=\omega+\omega-\omega)=2.0\times10^{-14}$ esu. This value of $\chi^{(3)}$ is subsequently also used in other third-order nonlinear effects described in this chapter.

References

1) C. Lin: "Nonlinear Optics in Fibres for Fibre Measurements", J. Light. Tech., **LT-4**, 1986, pp. 1103-1115

2) L. Reekie, R.J. Mears, S.B. Poole, D.N. Payne: "Tunable Single-Mode Fibre Lasers", J. Light. Tech., **LT-4**, 1986, pp. 956-960

3) C. Lin and V.T. Nguy: "Wideband Near I.R. Continuum (0.7-2.1)μm Generation in Low-Loss Optical Fibres", Electron. Lett., **14**, 1978, pp. 822-823

4) R.H. Stolen: "Phase-Matched-Stimulated Four-Photon Mixing in Silica-Fibre Waveguides", IEEE J. Quantum Electronics, **QE-11**, 1974, pp. 100-109

5) R.H. Stolen and J.E. Bjorkholm: "Parametric Amplification and Frequency Conversion in Optical Fibres", IEEE J. Quantum Electronics, **QE-18**, 1982, pp. 1062-1072

6) C. Lin and M.A. Boesch: "Large-Stokes-Shift Stimulated Four-Photon Mixing in Optical Fibres", Appl. Phys. Lett., **38**, 1981, pp. 479-481

7) Y. Fujii, B.S. Kawasaki, K.O. Hill and D.C. Johnson: "Sum-Frequency Light Generation in Optical Fibres", Opt. Lett., **5**, 1980, pp. 48-50

8) Y. Sasaki and Y. Ohmori: "Phase-Matched Sum-Frequency Light Generation in Optical Fibres", Appl. Phys. Lett., **39**, 1981, pp. 466-468

9) Y. Ohmori and Y. Sasaki: "Two-Wave Sum-Frequency Light Generation in Optical Fibres", IEEE J. Quantum Electronics, **QE-18**, 1982, pp. 758-762

10) T. Nakashima, M. Nakazawa and Y. Nagishi: "Sum-Frequency Generation in a Polarisation-Preserving Optical Fibre", Japanese J. Appl. Phys., **24**, 1985, pp. L308-L310

11) U. Österberg and W. Margulis: "Efficient Second Harmonic Generation in an Optical Fibre", 14th Int. Quantum Electronic Conference IQEC, San Fransisco, 1986, paper WBB2

12) U. Österberg and W. Margulis: "Dye Laser Pumped by Nd:YAG Laser Pulses and Frequency Doubled in a Glass Optical Fibre", Opt. Lett., **11**, 1986, pp. 516-518

13) W. Margulis and U. Österberg: "Second-Harmonic Generation in Optical Glass Fibres", J. Opt. Soc. Am. B, **5**, 1988, pp. 312-315

14) R.W. Terhune and D.A. Weinberger: "Second-Harmonic Generation in Fibres", J. Opt. Soc. Am. B, **4**, 1987, pp. 661-674

15) F.P. Payne: "Second-Harmonic Generation in Single-Mode Optical Fibres", Electron. Lett., **23**, 1987, pp. 1215-1216

16) M.C. Farries, P.St.J. Russell, M.E. Fermann and D.N. Payne: "Second-Harmonic Generation in an Optical Fibre by Self-Written $\chi^{(2)}$ Grating", Electron. Lett., **23**, 1987, pp. 322-324

17) R.H. Stolen and H.W.K. Tom: "Self-Organised Phase-Matched Harmonic Generation in Optical Fibres", Opt. Lett., **12**, 1987, pp. 585-587

18) M.E. Fermann, M.C. Farries, P.St.J. Russell and L.J. Poyntz-Wright: "Tunable-Holographic Second-Harmonic Generators in High-Birefringence Optical Fibres", Opt. Lett., **13**, 1988, pp. 282-284

19) M.C. Farries: "Efficient Second Harmonic Generation in an Optical Fibre", IEE Colloquium on Non-Linear Optical Waveguides, London, 1988, paper 20

20) M.V. Bergot, M.C. Farries, M.E. Fermann, L. Li, L.J. Poyntz-Wright, P.St.J. Russell and A. Smithson: "Generation of Permanent Optically-Induced Second Order Nonlinearities in Optical Fibres by Poling", Opt. Lett., **13**, 1988, pp. 592-594

21) L. Li: unpublished results

22) M.E. Fermann, L. Li, M.C. Farries and D.N. Payne: "Phase-Matched Second-Harmonic Generation in Permanently-Poled Optical Fibres", to be presented at European Conf. on Optical Communications, ECOC, 1988,

23) M.E. Fermann, L. Li, M.C. Farries and D.N. Payne: "Frequency-Doubling by Modal Phase-Matching in Poled Optical Fibres", Electron. Lett., **24**, 1988, pp. 894-895

24) Y.R. Shen: "The Principles of Nonlinear Optics", 1984, John Wiley and Sons

25) A. Yariv and P. Yeh: "Optical Waves in Crystals", 1984, John Wiley and Sons

26) D.A. Kleinman: "Theory of Second-Harmonic Generation of Light", Phys. Rev., **128**, 1962, pp. 1761-1767

27) A.W. Snyder and J.D. Love: "Optical Waveguide Theory", 1983, Chapman and Hall

28) K.O. Hill, Y. Fujii, D.C. Johnson and B.S. Kawasaki: "Photosensitivity in Optical Fibre Waveguides: Application to Reflection Filter Fabrication", Appl. Phys. Lett., **32**, 1978, pp. 647-650

29) P.St.J. Russell and R. Ulrich: "Grating-Fibre Coupler as a High-Resolution Spectrometer", Opt. Lett., **10**, 1985, pp. 291-293

30) D. Gloge: "Weakly Guiding Fibres", Appl. Opt., **10**, pp. 2252-2258

31) R. Kashap: "Nonlinear Optical Interactions in Devices with Cylindrical Geometry", SPIE Vol. 682, Molecular and Polymeric Optoelectronic Materials: Fundamentals and Applications", 1986, pp. 170-178

32) D.P. Shelton and A.D. Buckingham: "Optical Second-Harmonic Generation in Gases with a Low-Power Laser", Phys. Rev. A, **26**, 1982, pp. 2787-2798

33) H.W.K. Tom, R.H. Stolen, G.D. Aumiller and W. Pleibel: "Preparation of Long-Coherence-Length Second-Harmonic Generating Optical Fibres Using Modelocked Pulses", Opt. Lett., **13**, 1988, pp. 512-514

34) P.D. Maker and R.W. Terhune: "Study of Optical Effects Due to an Induced Polarisation Third Order in the Electric Field Strength", Phys. Rev., **3A**, 1965, pp. A801-A818

35) A. Owyoung: "The Origins of Nonlinear Refractive Indices of Liquids and Glasses", PhD Thesis, California Institute of Technology, 1971

36) E.P. Ippen, C.V. Shank and T.K. Gustafson: "Self-Phase-Modulation of Picosecond Pulses in Optical Fibres", Appl. Phys. Lett., **24**, 1974, pp. 190-192

37) R.H. Stolen and C. Lin: "Self-Phase Modulation in Silica Optical Fibres", Phys. Rev. A, **17**, pp. 1448-1453

38) N. Bloembergen and Y.R. Shen: "Coupling Between Vibrations and Light Waves in Raman Laser Media", Phys. Rev. Lett., 12, 1964, pp. 504-507

39) R.G. Smith: "Optical Power Handling Capacity of Low Loss Optical Fibres as Determined by Stimulated Raman and Brillouin Scattering", Appl. Opt., 11, 1972, pp. 2489-2494

40) M. Dnariez and G. Bret: "Investigation of Rayleigh Wings and Brillouin-Stimulated Scattering in Liquids", Phys. Rev., 171, 1968, pp. 160-171

41) P.H. Moon and A.S. Norcross: "Three Regions of Dielectric Breakdown", Electrical Engineering, 49, 1930, pp. 125-129

42) L. Li unpublished results

43) W.L. Smith, J.H. Bechtel and N. Bloembergen: "Dielectric-Breakdown Threshold and Nonlinear-Refractive-Index Measurements with Picosecond Laser Pulses", Phys. Rev. B, 12, 1975, pp. 706-714

44) L.B. Glebov, D.M. Efimov, G.T. Petrovskii and P.N. Rogortsev: "Optical Breakdown of Silicate Glasses under Conditions of Two-Photon Absorption of Laser Radiation", Sov. J. Quantum Electronics, 13, 1983, pp. 972-974

45) R.W. Terhune, P.D. Maker and C.M. Savage: "Optical Harmonic Generation in Calcite", Phys. Rev. Lett., 8, 1962, pp. 404-406

46) R.W. Terhune: "Non-Linear Optics", Solid State Design, 1963, pp. 38-46

47) V. Mizrahi, U. Österberg, J.E. Sipe and G.I. Stegeman: "Test of a Model of Efficient Second-Harmonic Generation in Glass Optical Fibres", Opt. Lett., **13**, 1988, pp. 279-281

48) P.S. Pershan: "Nonlinear Optical Properties of Solids: Energy Considerations", Phys. Rev., **130**, 1963, pp. 919-929

49) E. Adler: "Nonlinear Optical Frequency Polarisation in a Dielectric", Phys. Rev., **134**, 1964, pp. A728-A733

50) N. Bloembergen, R.K. Chang, S.S. Jhan and C.H. Lee: "Optical Second-Harmonic Generation in Reflection from Media with Inversion Symmetry", Phys. Rev., **174**, 1968, pp. 813-822

51) H. Kawazoe: "Effect of Modes of Glass Formation on Structure of Intrinsic or Photoinduced Defects Centred on III, IV or V Cations in Oxide Glasses", J. Non Cryst. Sol., **71**, 1985, pp. 231-243

52) M.J. Yuen: "Ultraviolet Absorption Studies of Germanium Silicate Glasses", Appl. Opt., **21**, 1982, pp. 136-140

53) E.J. Friebele and D.L. Griscom: "Colour Centres in Glass Optical Waveguides", Mat. Res. Soc. Symp. Proc., **61**, 1986, pp. 319-331

54) M.A. Saifi and M.J. Andrenjco: "Second-Harmonic Generation in Single-Mode and Multi-Mode Fibres", Optical Fibre Conf., OFC, New Orleans, 1988, paper THD5

55) B. Valk, E.M. Kim and M.M. Salour: "Second-Harmonic Generation in Ge-Doped Fibres with a Mode-Locked Kr^+ Laser", Appl. Phys. Lett., 1987, pp. 722-724

56) M.C. Farries and M.E. Fermann: "Frequency-Doubling of 1.319μm Radiation in an Optical Fibre by Optically Written $\chi^{(2)}$ Grating", Electron. Lett., **24**, 1988, pp. 294-295

57) S.C. Rashleigh: "Polarimetric Sensors Exploiting the Axial Stress in High Birefringence Fibres", Optical Fibre Sensors, OFS, London, 1983, pp. 210-213

58) L.J. Poyntz-Wright, M.E. Fermann and P.St.J. Russell: "Nonlinear Transmission and Colour Centre Dynamics in Germanosilicate Fibres at 420-540nm", subm. to Opt. Lett.

59) L.J. Poyntz-Wright and P.St.J. Russell, "Photochromic Dynamics and Non-Linear Transmission at Modulated cw Blue/Green Wavelengths in Germanosilicate Optical Fibres", subm. to Electron. Lett.

60) F. Oulette, K.O. Hill and D.C. Johnson: "Light-Induced Erasure of Self-Organised $\chi^{(2)}$-Gratings in Optical Fibres", Opt. Lett., **13**, pp. 515-517

61) L. Li: in preparation

62) F. Zernike and J.E. Midwinter: "Applied Nonlinear Optics", John Wiley&Sons

63) L.Li PhD-thesis: in preparation

64) R. Adair, L.L. Chase and S.A. Payne: "Nonlinear Refractive-Index Measurements of Glasses Using Three-Wave Frequency-Mixing", J. Opt. Soc. Am. B, **4**, 1987, pp. 875-881

rel $\chi^{(2)}$	dopants	i	iia	iib	iii
$\chi^{(2)}(2\omega=\omega+\omega)$ in 10^{-11}esu	GeO_2-P_2O_5	1	2	27	-
	GeO_2	0.4	2	-	-
$\chi^{(2)}(\omega=\omega+0)$ in 10^{-11}esu	GeO_2-P_2O_5	-	-	-	8.6
	GeO_2	-	-	-	2.8

Table 5.1)

Measured values of second-order nonlinear coefficients in oxide glass silica optical fibres. The results under i refer to poling by using only light. ii corresponds to poling by light and a dc-field, where a refers to pulsed blue light excitation and b refers to cw blue light excitation. iii stands for poling by using only a dc-field.

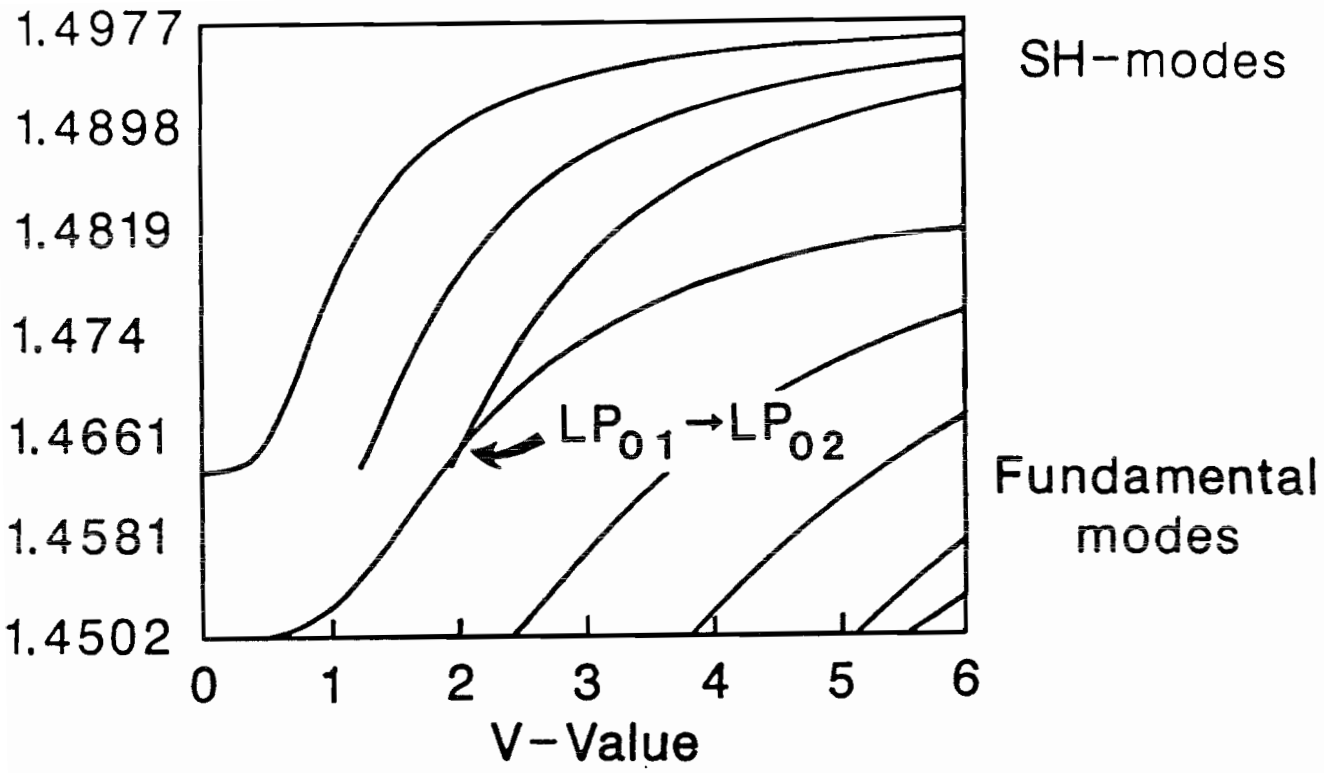

Figure 5.1 Variation of phase-index of fundamental wave at 1064nm (lower traces) and its SH (upper traces) as a function of V-value (at 1064nm) for the lower-order fibre modes. A GeO_2 concentration of 23% is assumed. Phase-matching occurs where the upper and lower traces intersect. For a V-value of 2.0 phasematching between the fundamental in the LP_{01} and the SH in the LP_{02} mode is possible.

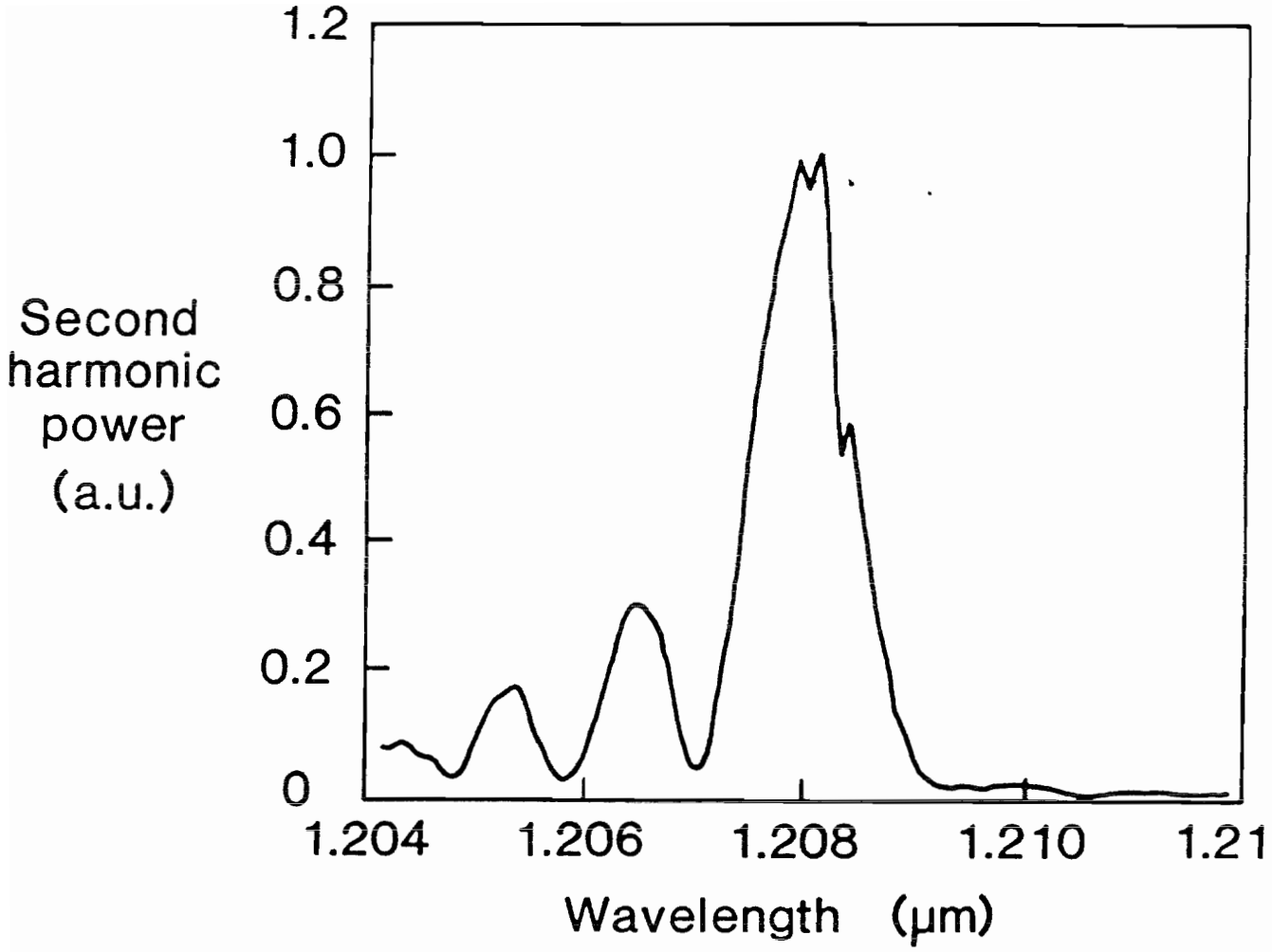

Figure 5.2 SH-power as a function of wavelength in a modally phasematched fibre.

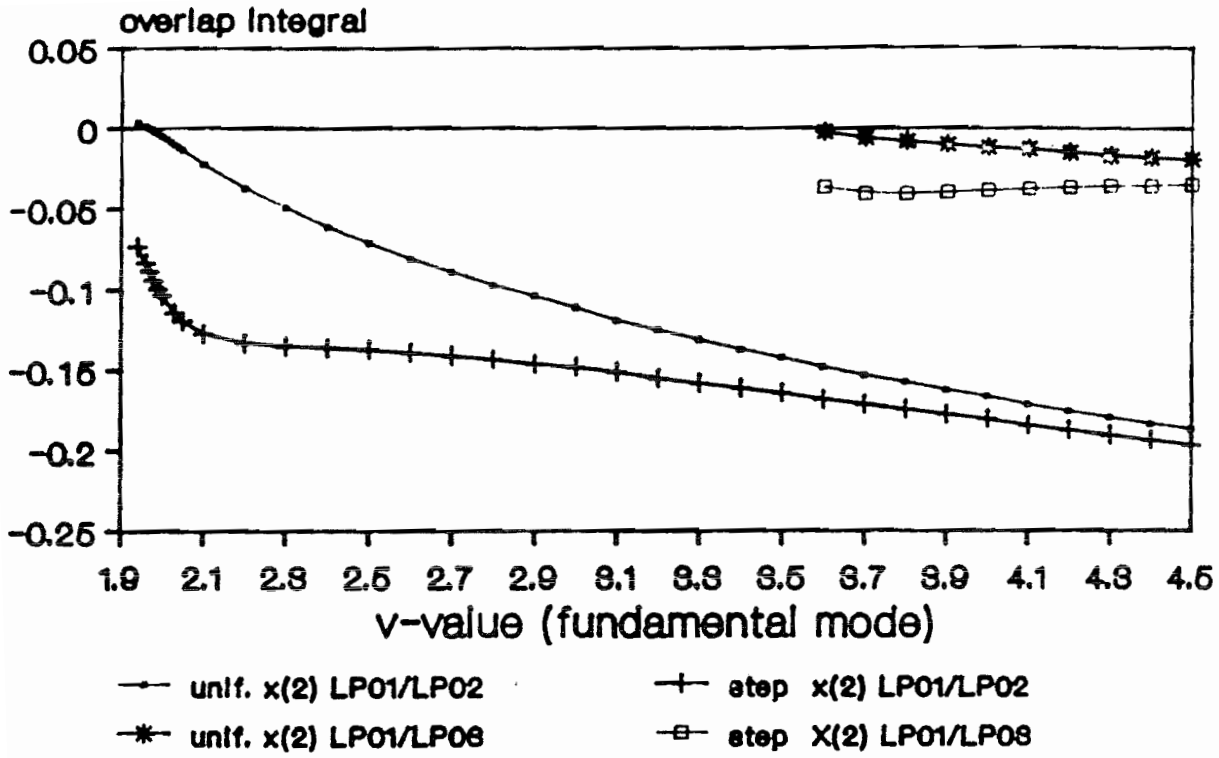

Figure 5.3 Amplitude overlap integral between a fundamental wave in the LP_{01}-mode and a SH-wave in the LP_{02} or LP_{03} mode. The overlap integrals for both a uniform $\chi^{(2)}$ and a step-profile $\chi^{(2)}$ present only in the fibre core are displayed. A second-order nonlinearity $\chi^{(2)}_{111}$ and linearly polarised light are assumed.

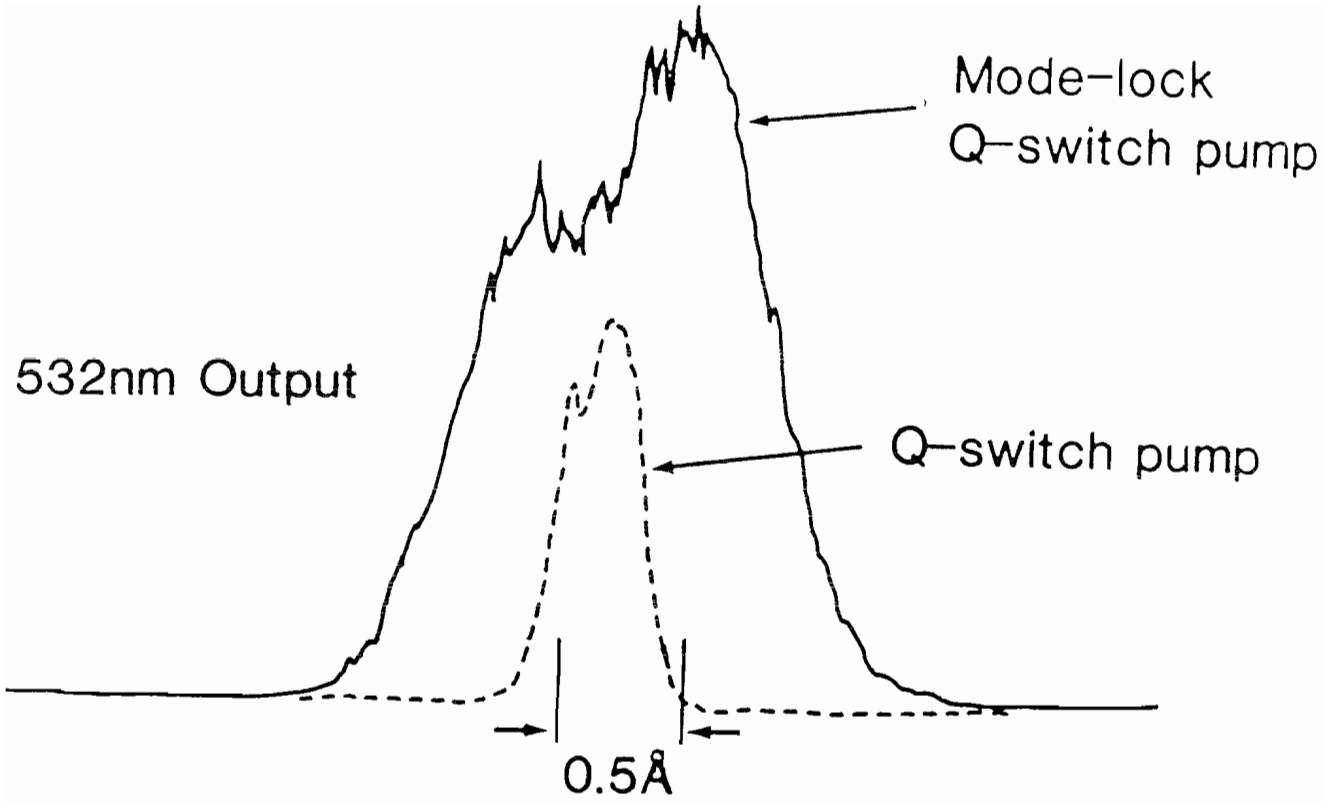

Figure 5.4 Effect of using a Q-switched or a Q-switched and mode-locked pump on the bandwidth of an internally-written $\chi^{(2)}$-grating.

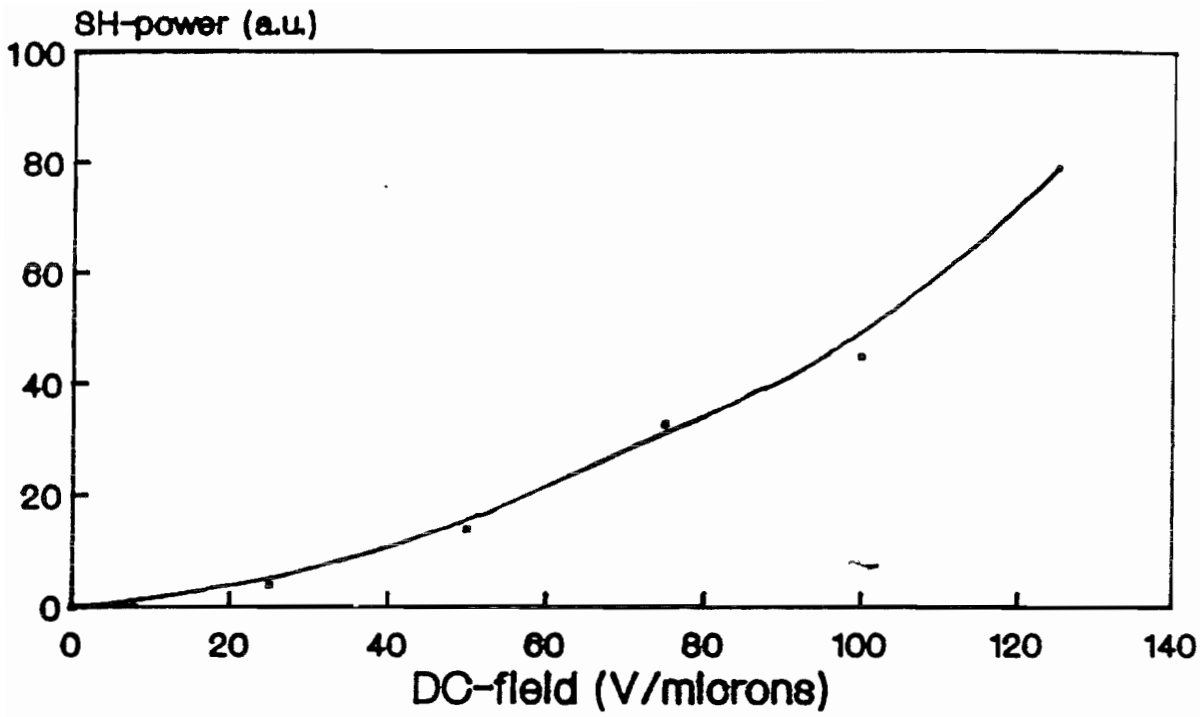

Figure 5.5 SH-power as a function of applied dc-electric field strength.

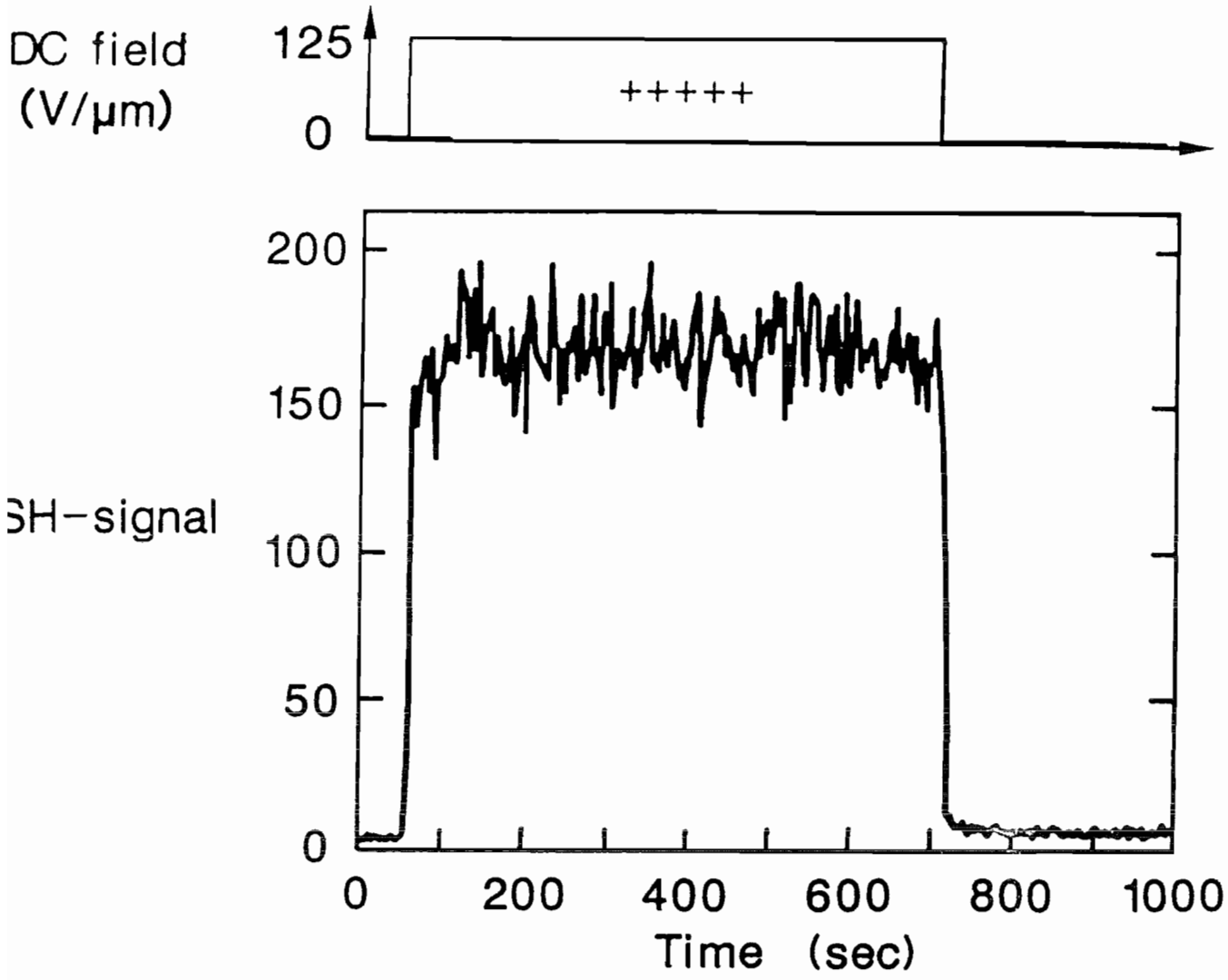

Figure 5.6 Long-time and short-time response of SH-signal to an applied dc-electric field in a P_2O_5-doped germano-silicate fibre. The SH-signal is only present when the dc-field is on and disappears almost immediately once the dc-field is switched-off. A negligibly small permanent increase in the SH-signal may be observed after switching-off the dc-field.

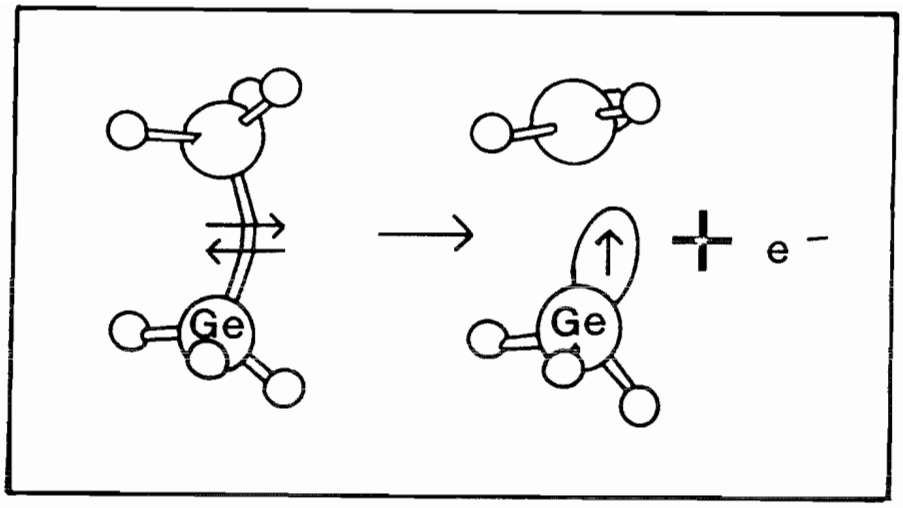

Figure 5.7 Model for the formation of a Ge E' centre. Large spheres represent Ge or Si ions and small spheres represent oxygen cations. Ge-Ge or Ge-Si bonds get broken by high-energy radiation and form Ge E' centres with a trapped hole and a free electron, which subsequently gets trapped to form a Ge(1) or Ge(2) centre. (see Fig. 5.8).

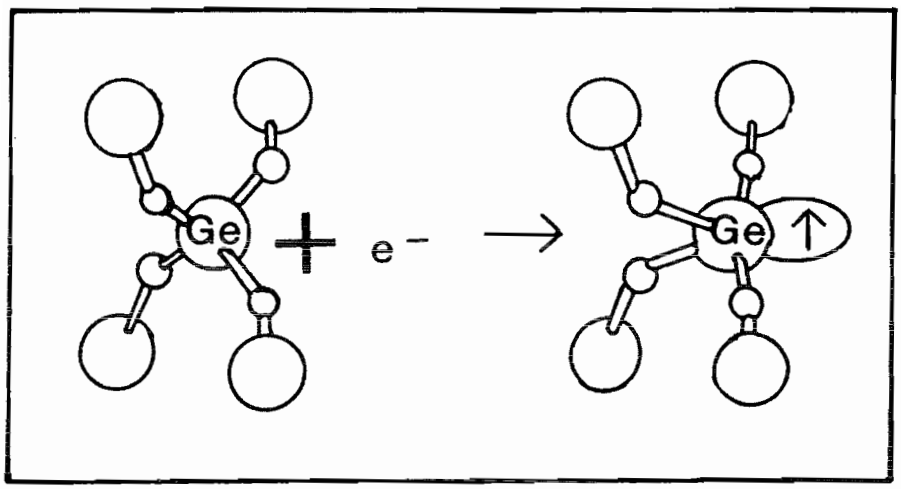

Fig. 5.8 Model for the formation of a Ge(1) or Ge(2) centre.

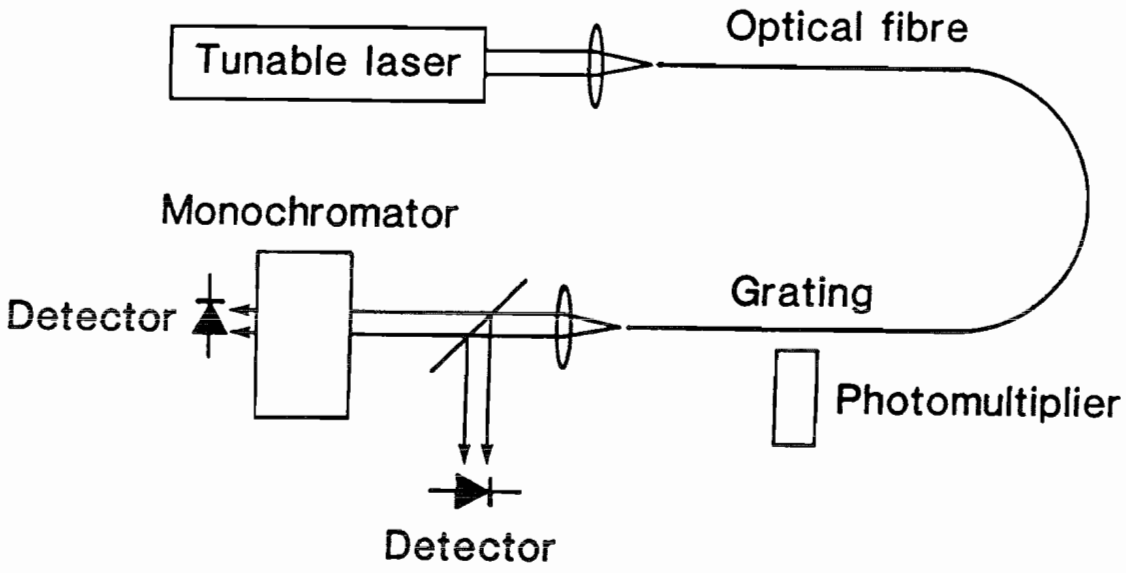

Figure 5.9 Set-up for writing a $\chi^{(2)}$-grating into an optical fibre.

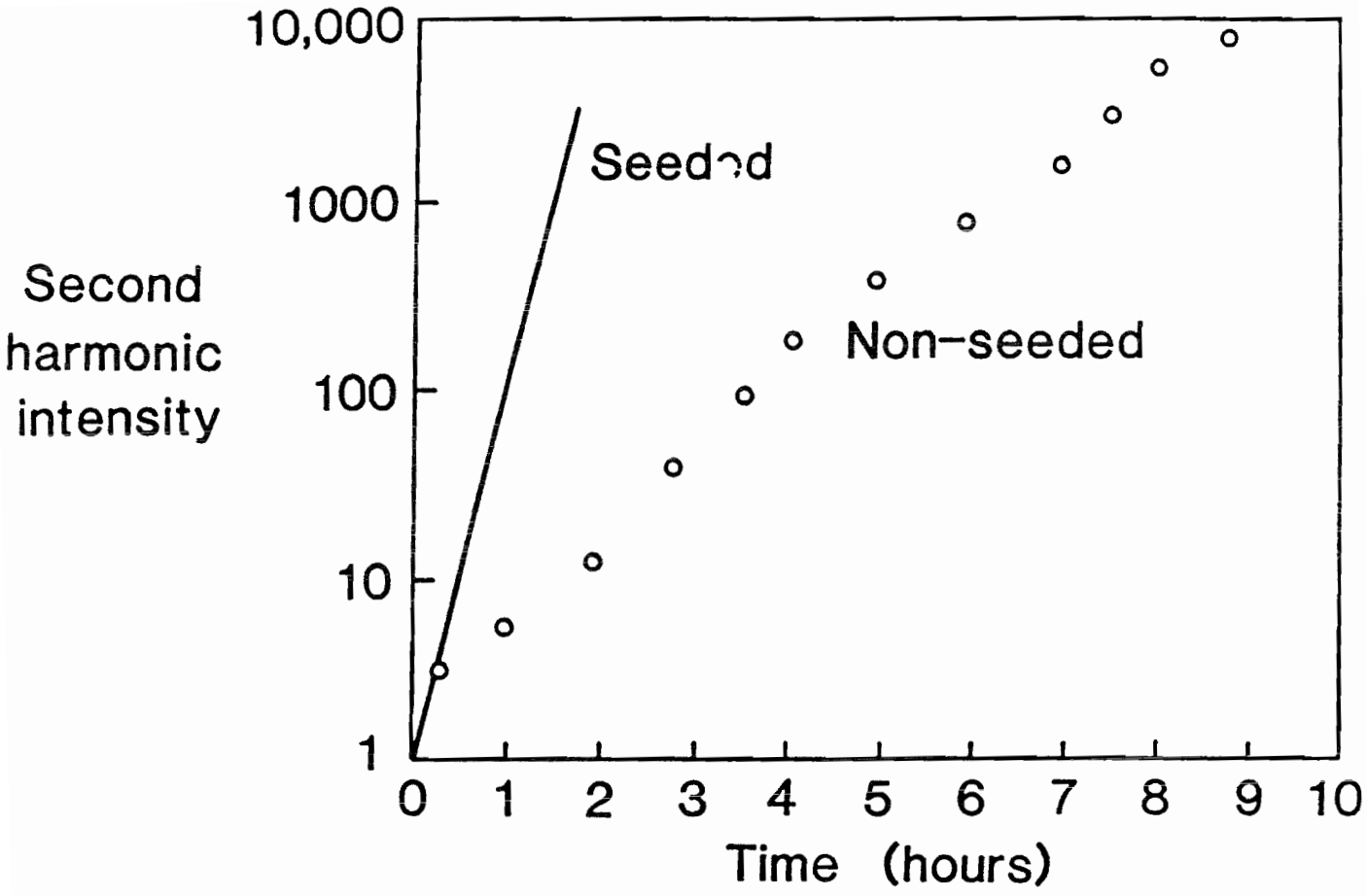

Figure 5.10 Sh-signal as a function of writing time for a seeded $\chi^{(2)}$-grating and a $\chi^{(2)}$-grating generated from noise (non-seeded).

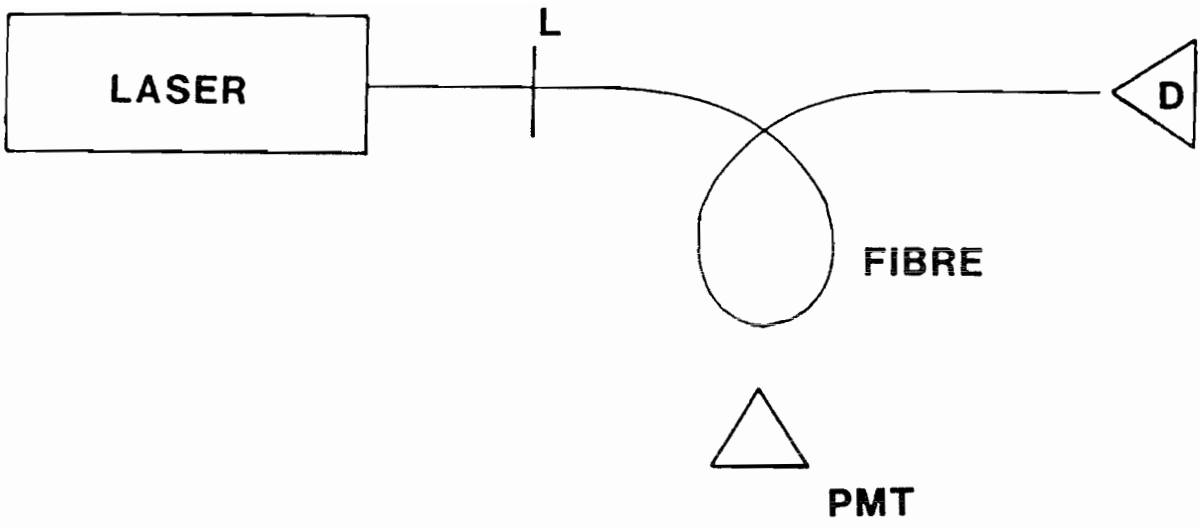

Figure 5.11 Set-up for the measurement of the evolution of the SH-signal along a $\chi^{(2)}$-grating by side-scatter. D=detector; PMT=photomultiplier.

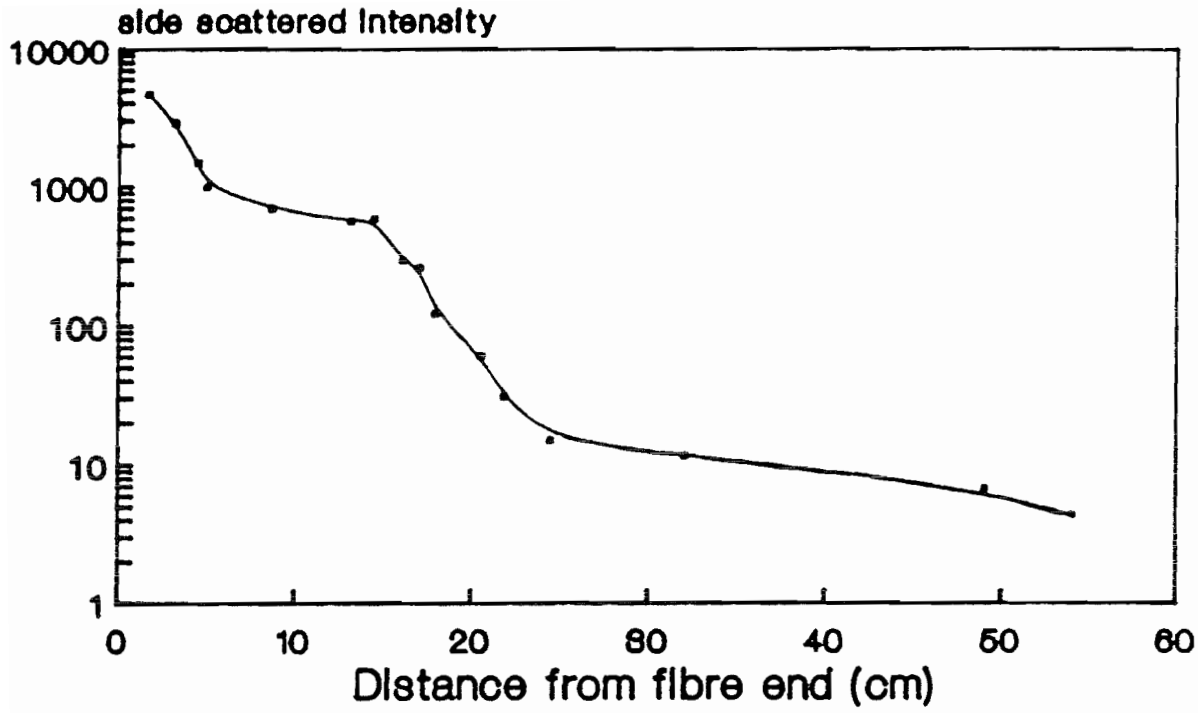

Figure 5.12 Measured side-scattered SH-intensity as a function of distance from fibre end.

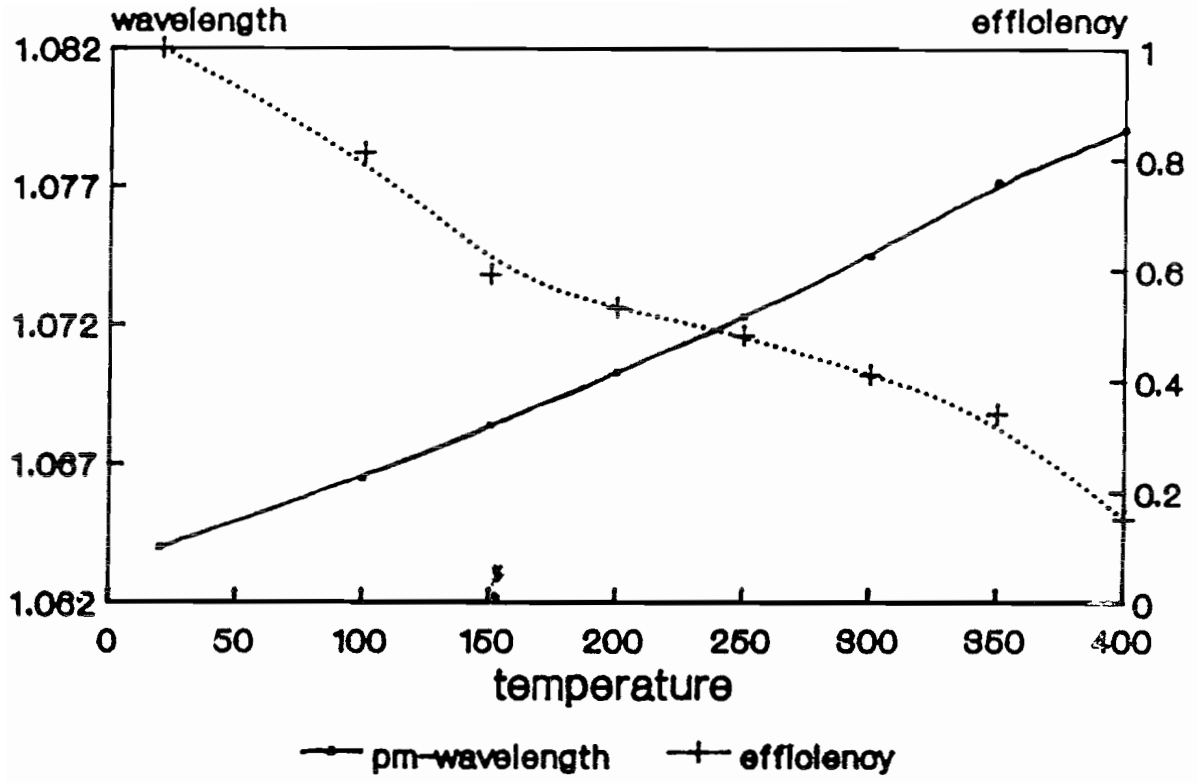

Figure 5.13 Phasematched fundamental wavelength for SHG using a $\chi^{(2)}$-grating as a function of temperature. Note the reduction in SH-conversion efficiency at elevated temperatures.

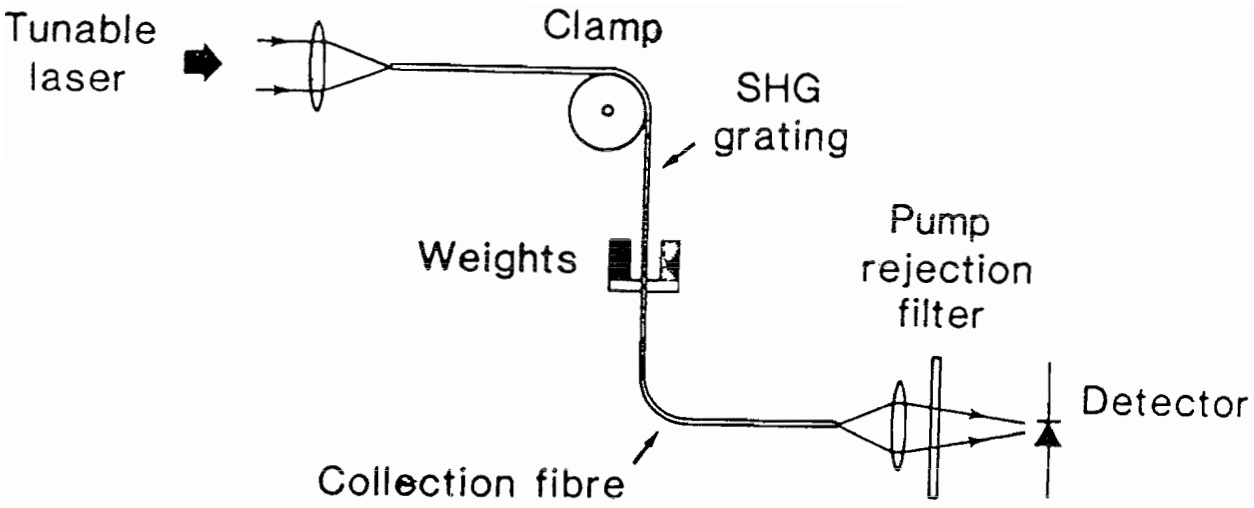

Figure 5.14 Set-up for the stretching of a $\chi^{(2)}$-grating.

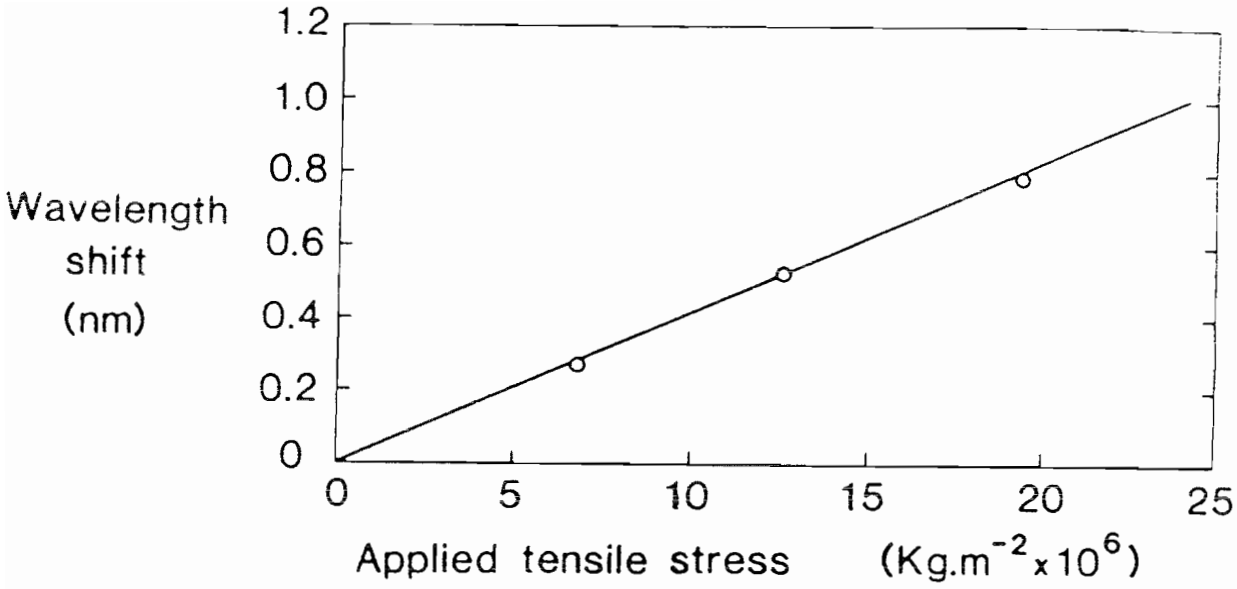

Figure 5.15 Comparison of results obtained by stretching a $\chi^{(2)}$-grating with theory. The theory predicts a straight line for the wavelength-shift of the phasematch wavelength as a function of applied stress, which is in good agreement with the experimental points (o).

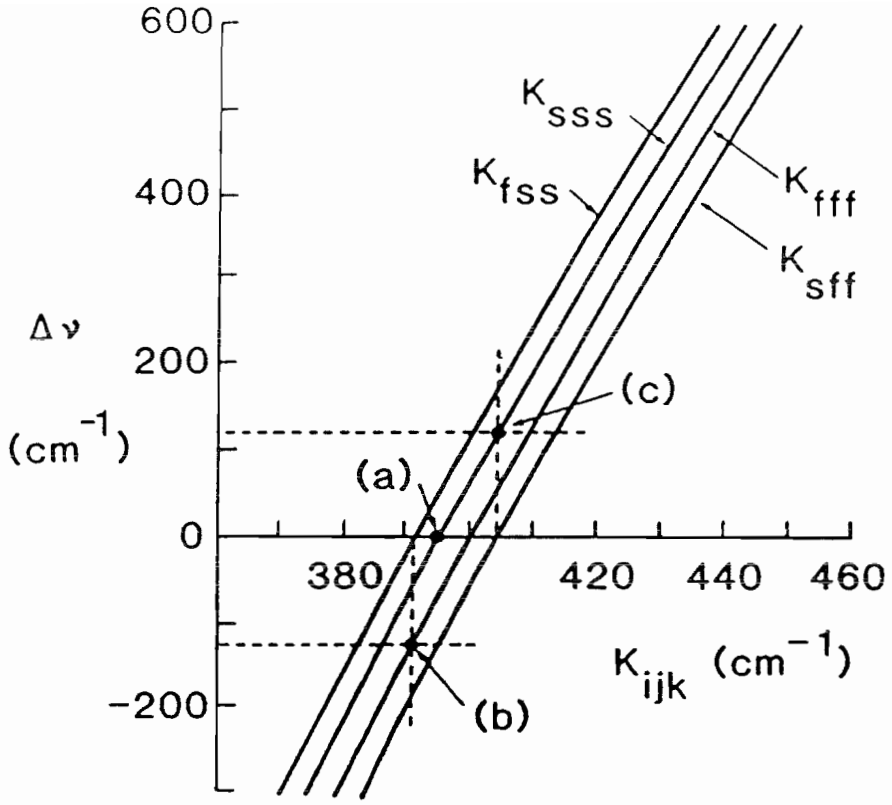

Figure 5.16 The dispersion of the grating vectors K_{ijk} relevant to the three cases treated in section 5.10.2.4. In case b) phasematching is achieved at $\Delta\nu$=-123 cm^{-1} from 1064nm and in case c) at $\Delta\nu$=+123cm^{-1}.

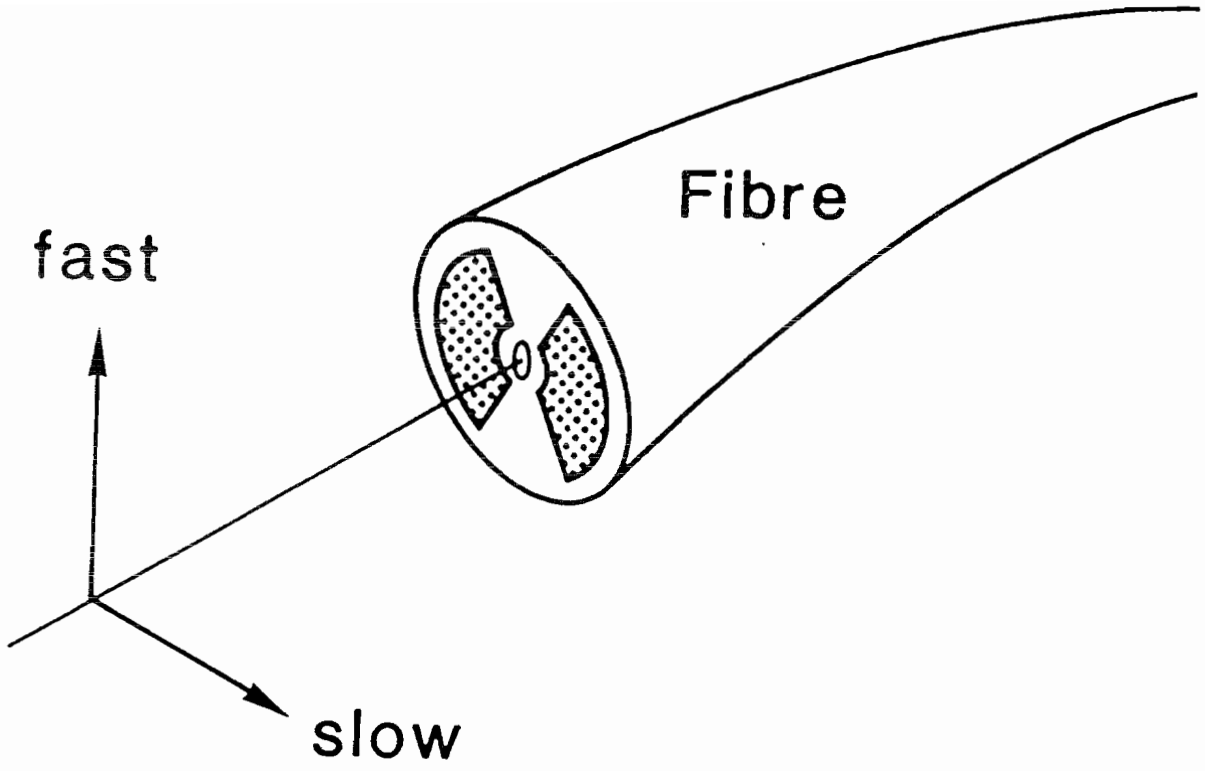

Figure 5.17 Cross-section of a P_2O_5-doped high-birefringence germanosilicate fibre.

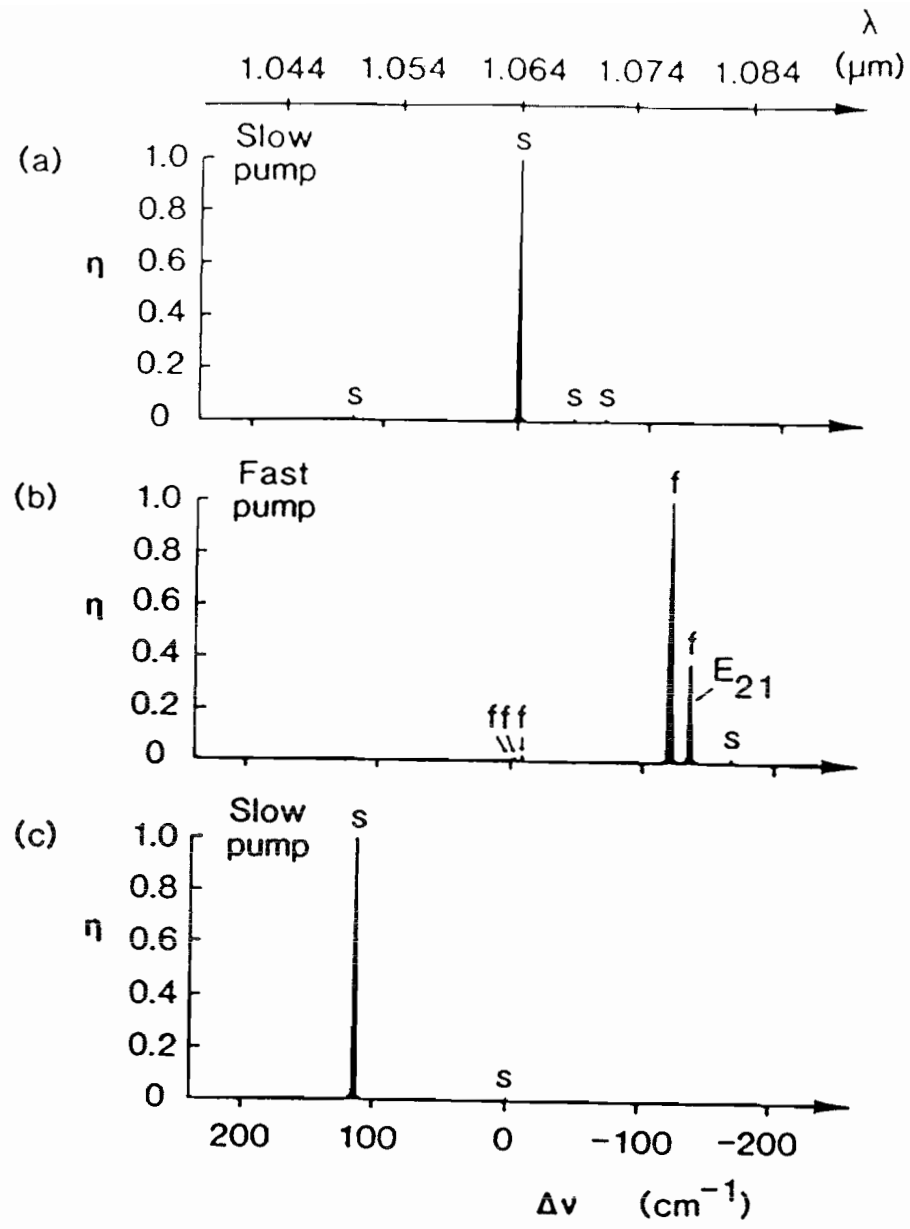

Figure 5.18 The measured SH-conversion efficiency η as a function of wavenumber deviation $\Delta\nu$ from the writing pump wavelength, 1064nm, for the three cases discussed in section 5.10.2.4. In this Figure (and Figure 5.19) η is normalised to its maximum measured value in each case. Notice that phasematched conversion to the SH LP_{11} mode occurs at 135 cm^{-1} in case b). The presence of slow or fast-polarised SH light is denoted by the letters "f" and and "s". The peaks marked"fs" are mixed. The additional minor conversion peaks are caused by inevitable small misalignments of the polarisation during writing and read-out and poor polarisation properties in the fibre used.

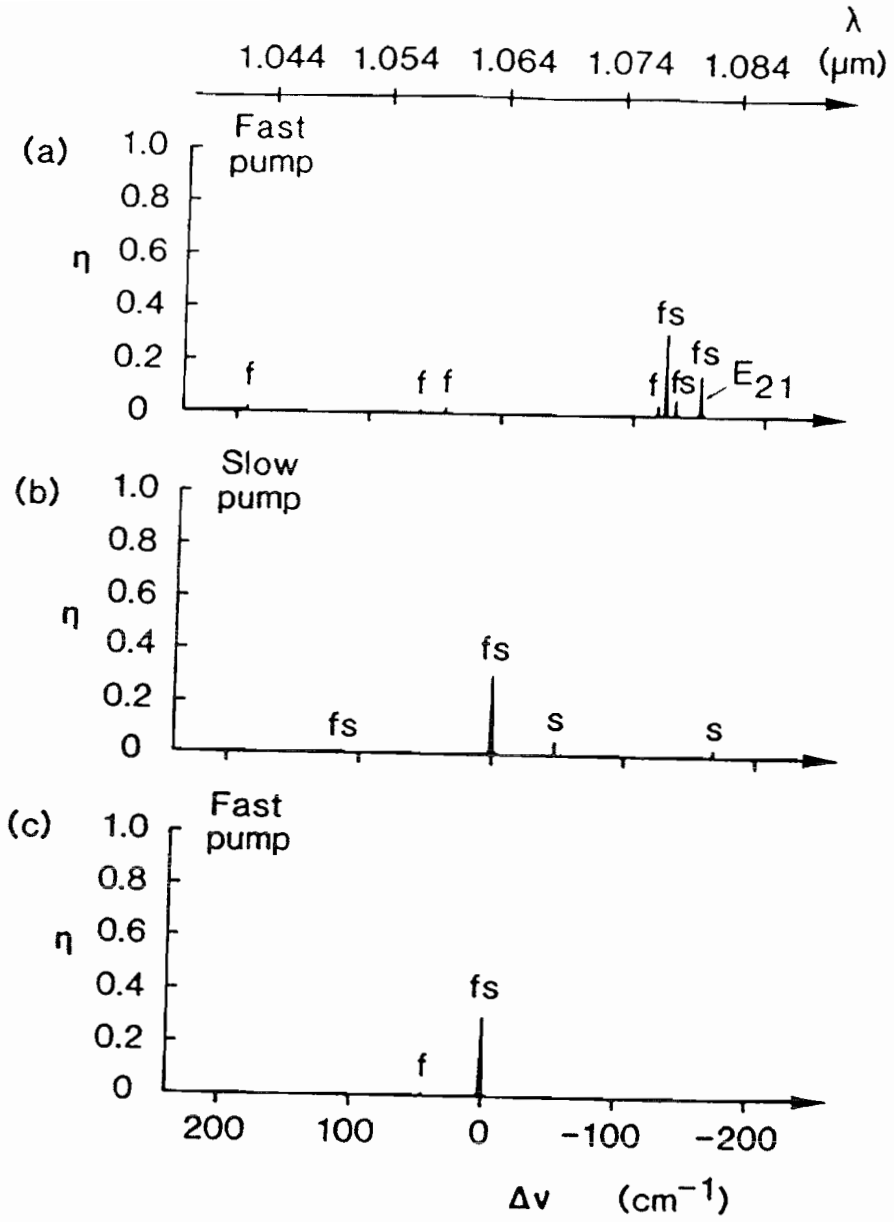

Figure 5.19 As in Fig. 5.18, except that the read-out pump polarisation is orthogonal to the expected alignment direction of $\chi^{(2)}$. The conversion efficiencies are normalised to the maximum measured values in Fig.5.18.

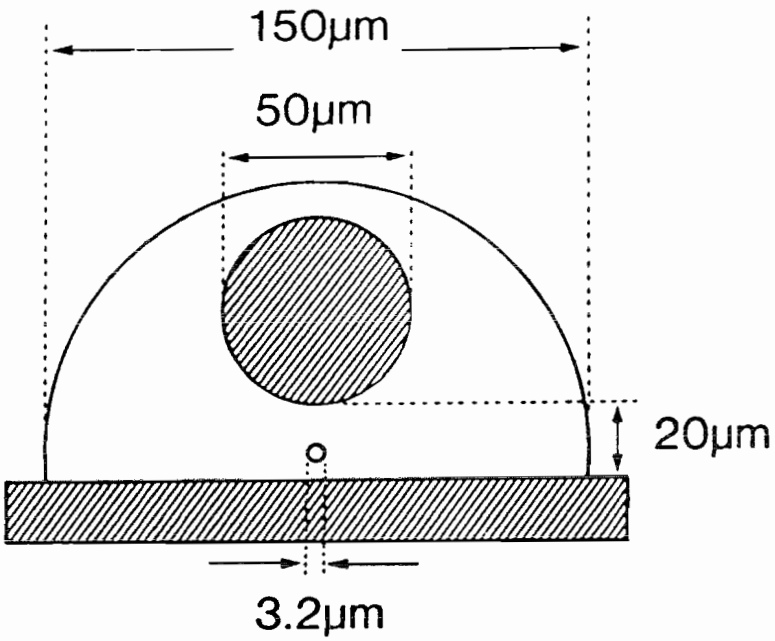

Figure 5.20 Cross-section of a D-shaped fibre with internal electrodes.

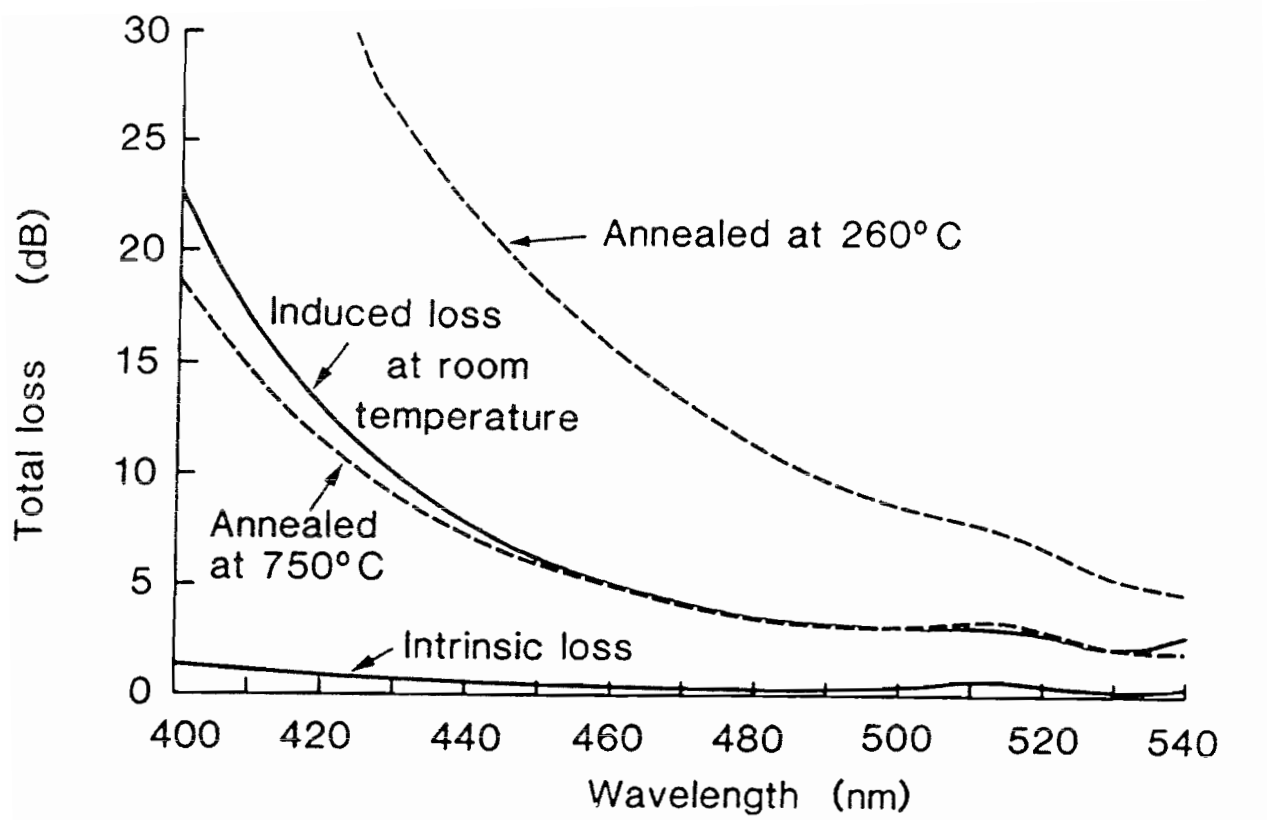

Figure 5.21 Absorption spectrum and effects of thermal annealing for 5m of fibre exposed to 300MW/cm^2 peak power pulses at 463nm.

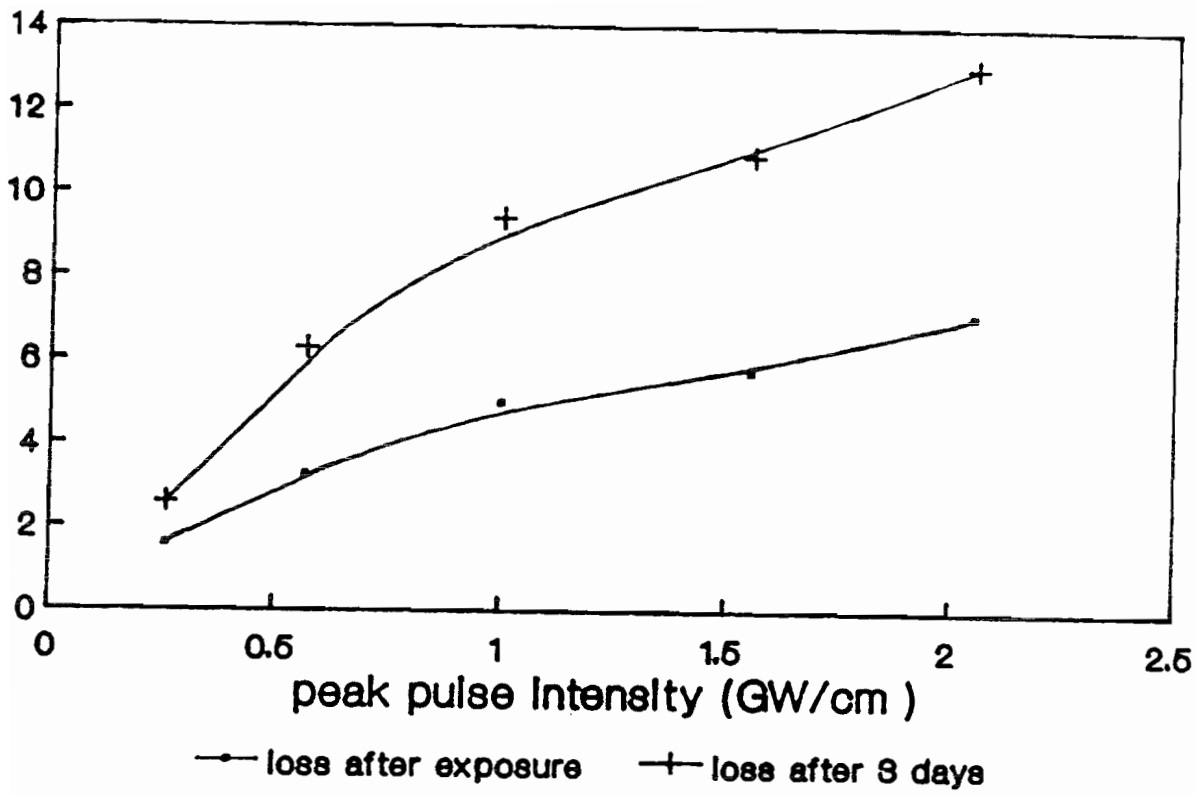

Figure 5.22 Saturated absorption levels for various launched intensities in 5m lengths of fibre. The lower points represent the loss immediately after exposure, the upper ones the loss measured one day later.

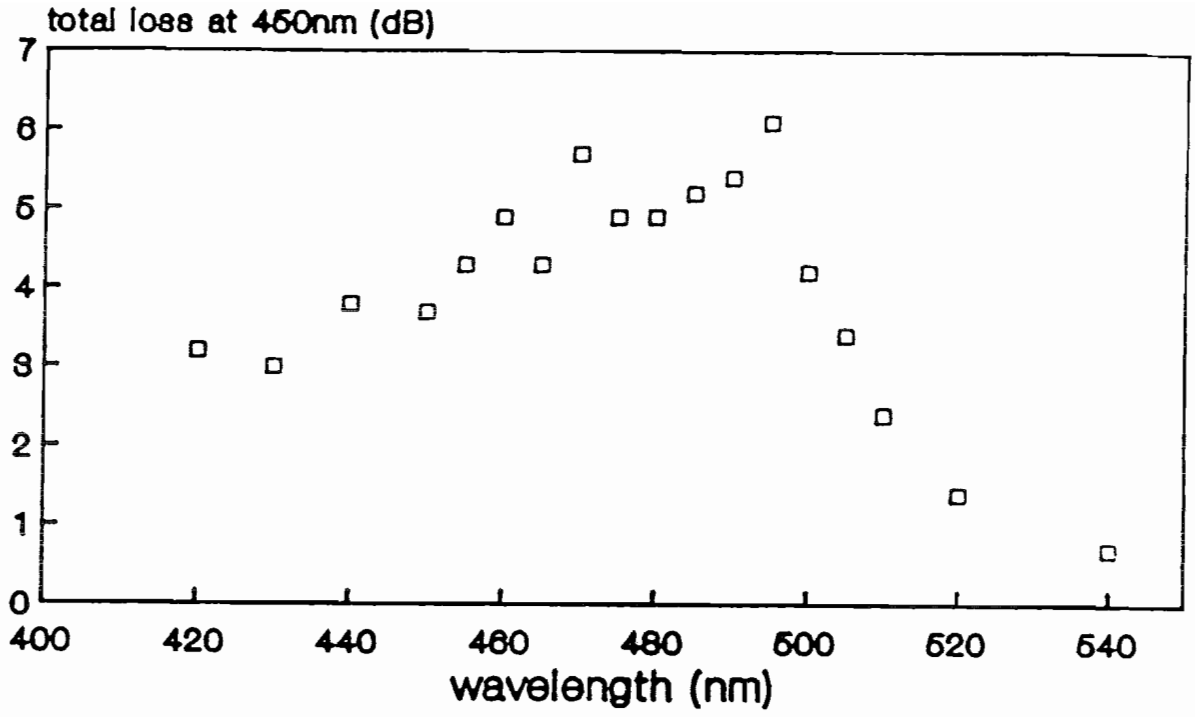

Figure 5.23 Attenuation at 450nm in 5m lengths of fibre after 10min exposure to pulses of 1 GW/cm^2 peak power at various pump wavelengths.

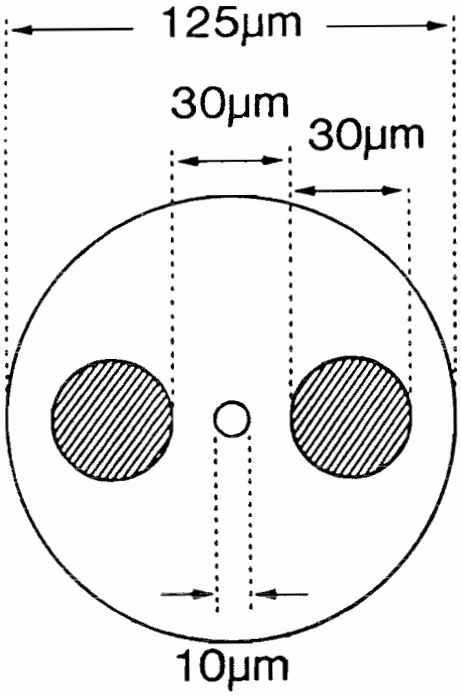

Figure 5.24 Cross section of a circular fibre with internal electrodes.

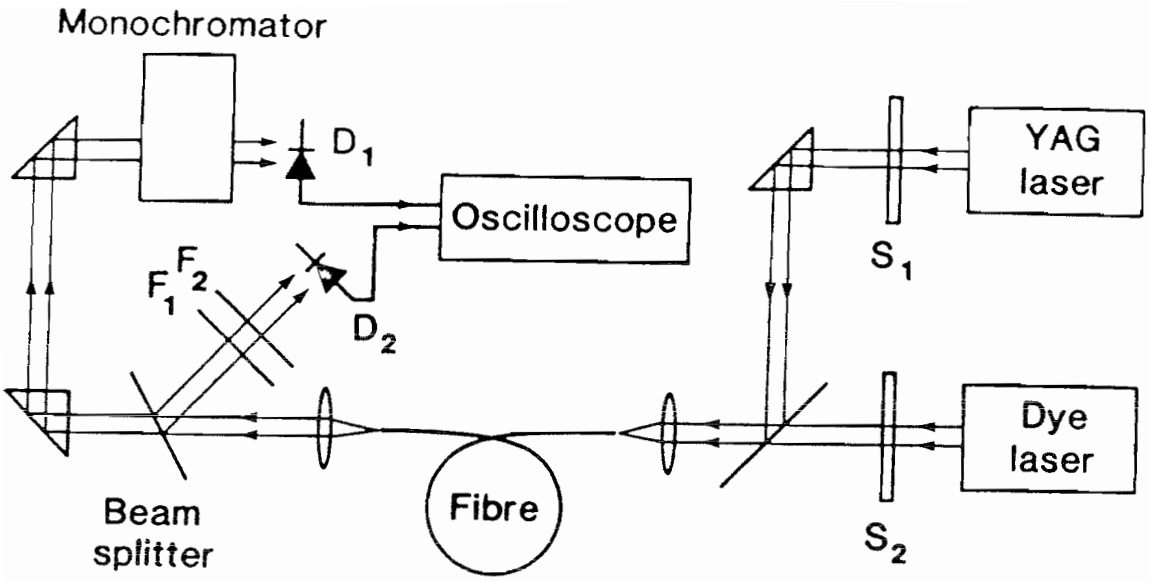

Figure 5.25 Set-up used to measure the response of optical fibres to defect excitation and poling fields.

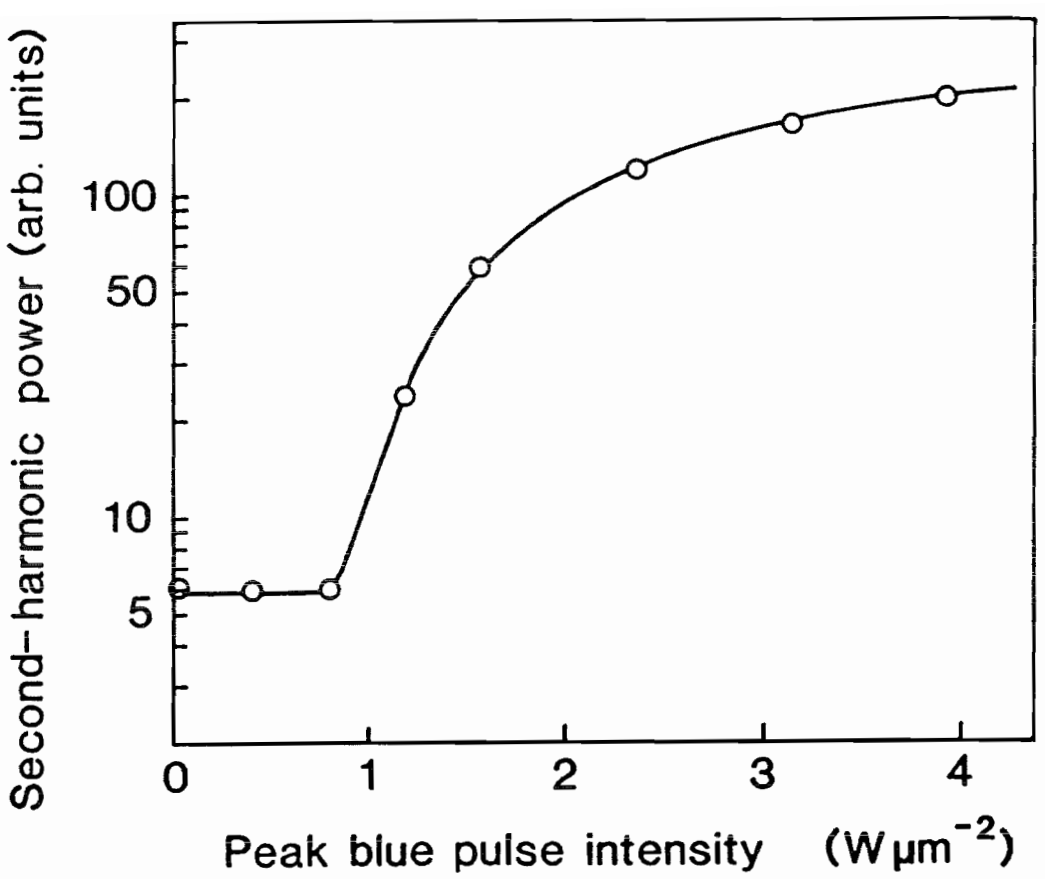

Figure 5.26 Saturated SH-power at a constant poling field of 4 V/μm as a function of peak blue pulse intensity in a germanosilicate fibre.

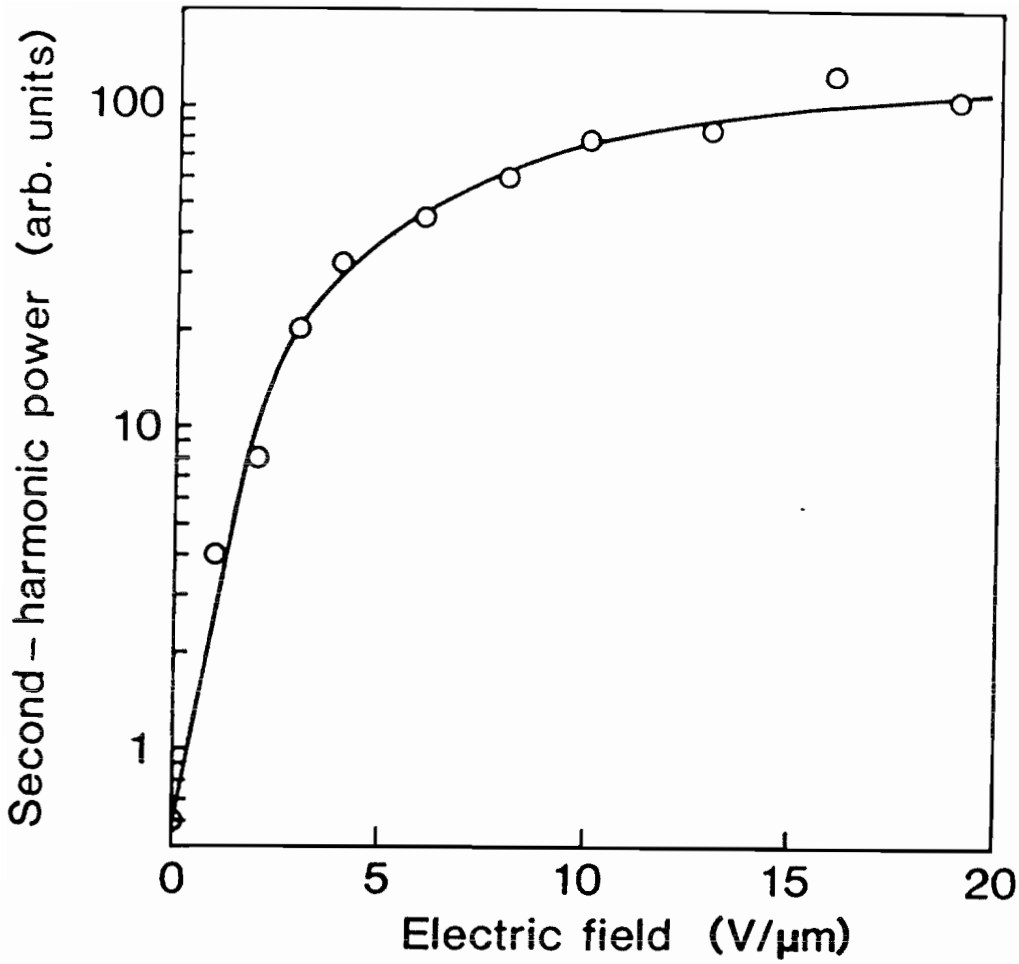

Figure 5.27 Saturated SH-power at a constant launched peak blue light intensity as a function of applied poling field in a germanosilicate fibre.

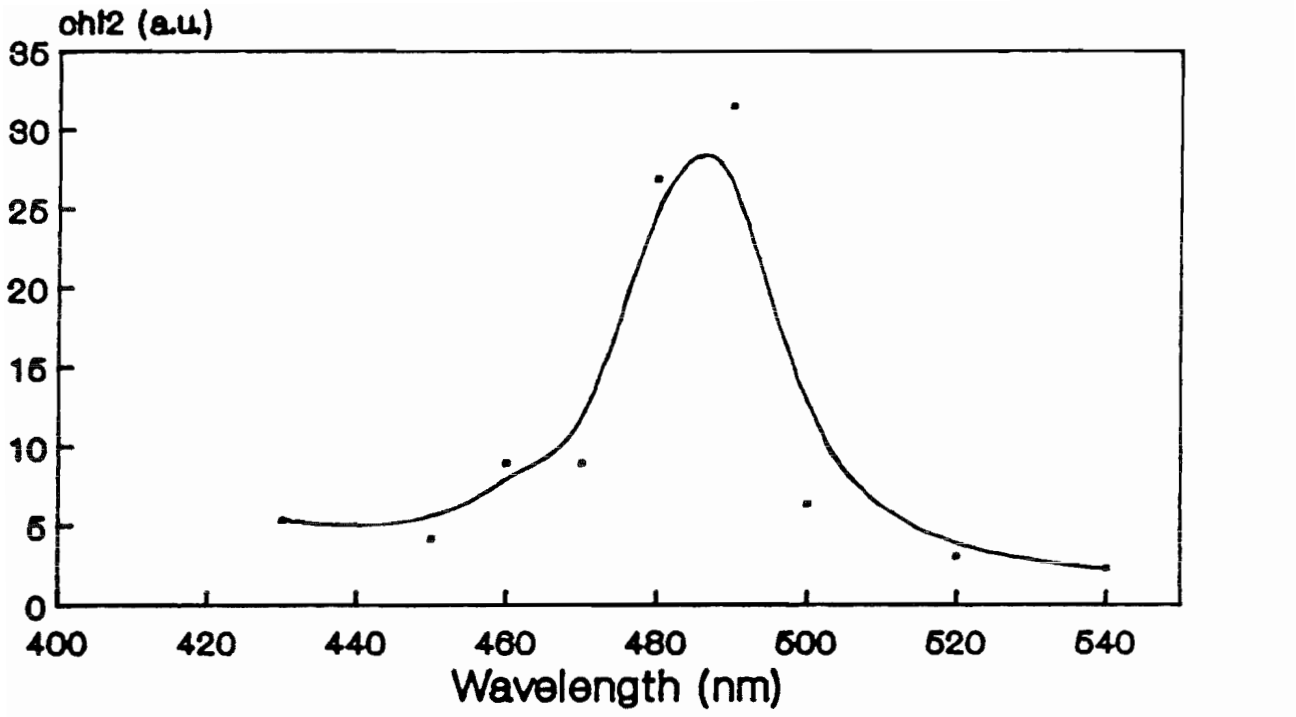

Figure 5.28 Induced $\chi^{(2)}$ as a function of pump-wavelength in a germanosilicate fibre. A poling field of 2.5 V/μm and a peak blue pulse intensity of 1.7 GW/cm^2 were used.

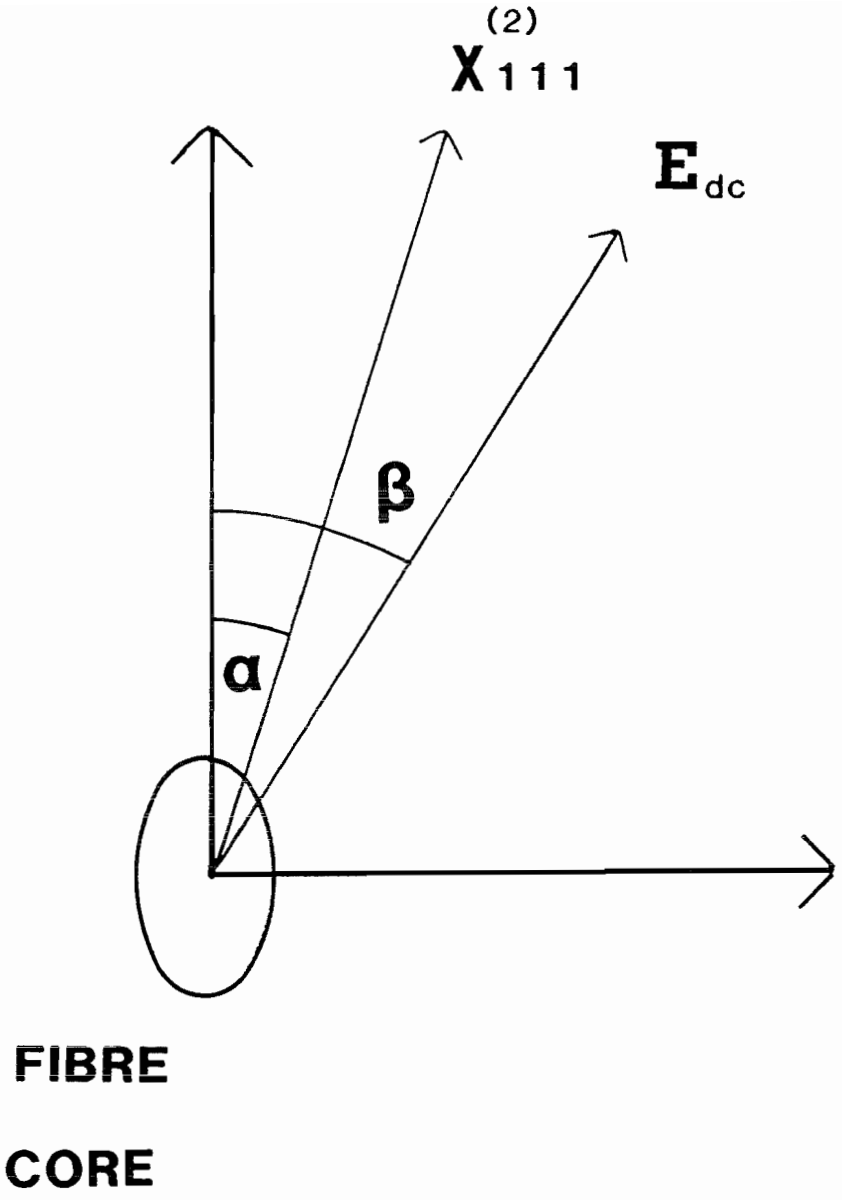

Figure 5.29 Geometry of an externally-poled optical fibre. It is assumed that a $\chi^{(2)}$ has been induced at an angle α with respect to the major axis and that a small modulating dc-electric field is applied at an angle β with respect to the major axis.

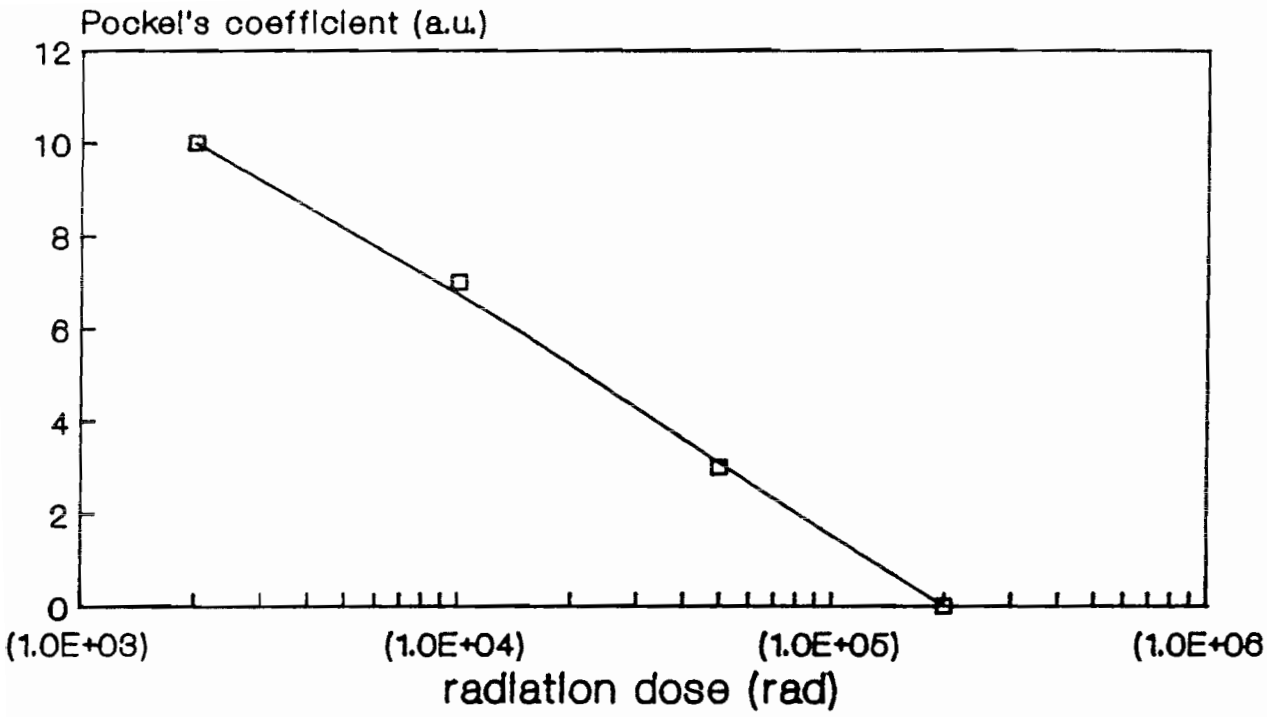

Figure 5.30 Effect of γ-irradiation on induced Pockels coefficient in a germanosilicate fibre.

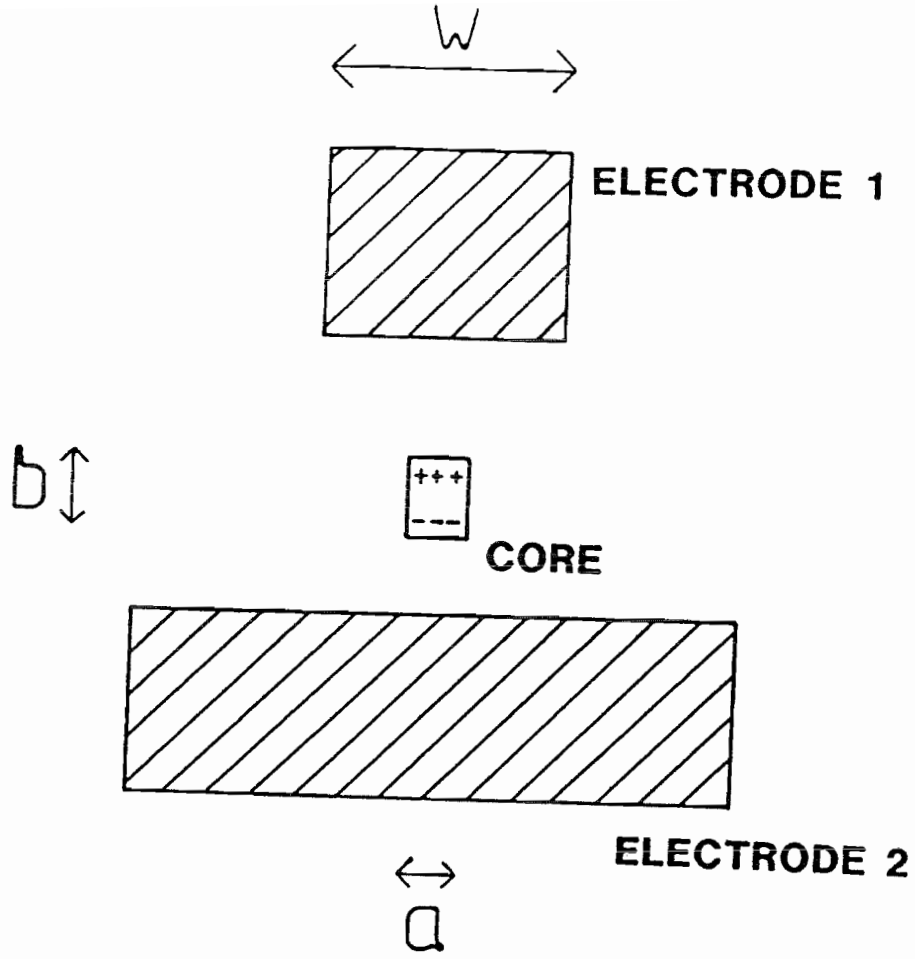

Figure 5.31 Simplified arrangement for the measurement of optical rectification in optical fibres.

Chapter 6: Conclusions

A series of achievements related to two novel types of special optical fibre, i.e. rare-earth-doped fibres and fibres with crystal-like properties, have been described in this thesis.

Rare-earth-doped fibres have been shown to be applicable to distributed temperature sensing with a performance that is comparable or better than the Raman-type distributed temperature sensor for low-temperature applications. Basic requirements for a sensitive rare-earth temperature sensor in other temperature regions have also been outlined. Further applications of rare-earth-doped fibres as point sensors may also be envisaged. In particular, fluorescence properties of rare-earths could be exploited. At high doping levels the magneto-optic properties of the composite material improve[1] and thus magnetic field sensing could also be possible. Resonances of the Verdet constant of rare-earth-doped glasses near their absorption bands[2] may also be investigated with respect to their sensitivity to environmental conditions, i.e. magnetic and electric fields.

Co-doping of optical fibres with two rare-earths aimed at causing energy-transfer between them has also been carried out. It has been shown that energy-transfer occurs in rare-earth-doped silica glass even at moderate ion doping levels of only 1-2% thus leading to more efficient pumping of fibre lasers. In particular, the energy-transfer mechanisms in an ytterbium/erbium system have been analysed. Energy-transfer from ytterbium to erbium has been used to demonstrate an efficient erbium laser operating in the important third window of telecommunications. It has been shown that both YAG and diode-laser pumping of such a system is possible. Further research may lead to a further improvement of the laser performance by optimising both the dopant host and dopant concentrations. Similar energy-transfer pumping schemes may also improve the versatility of other fibre lasers. Efficient frequency-upconversion[3] should also

be possible via energy-transfer between rare-earth ions through the use of dopant hosts with low phonon energies.

Finally, optical fibres with crystal-like properties have been investigated. Several techniques (optical fibre poling) have been developed for inducing second-order nonlinearities into glass (germanosilicate and phosphogermanosilicate) optical fibres. These poling techniques have led to the creation of the highest reported second-order nonlinear susceptibilities in optical glass. With the fibre designs described in this thesis the most efficient fibre frequency-doubler[4] yet reported has been produced and electrooptic modulation demonstrated via the Pockels effect[5]. Further, some of the physical processes behind the poling of optical fibres have been elucidated, where it has been proved that poling is due to the excitation and orientation of defect centres. It may be that different oxide glasses other than investigated here could produce even higher nonlinearities. Further systematic research on glass compositions is therefore required. In addition, the poling techniques developed in this thesis could be further refined by investigating the defect centres behind the formation of second-order nonlinearities. The efficiency of frequency-doubling could also be improved by the optimisation of phase-matching techniques. Summarising, the fibre poling work described in this thesis has greatly increased the interest in defect centres in optical glasses and will hopefully be subject to much more research in the years to come.

References

1) N.F. Borelli: "Faraday Rotation in Glasses", The J. of Chemical Physics, **41**, 1961, pp. 3289-3298

2) S.J. Collocott and K.N.R Taylor: "Magneto-Optical Properties of Praesodymium- and Holmium-Doped Soda Glass", J. Phys. C: Solid State Phys., **12**, 1979, pp. 1767-1775

3) J.C. Wright: "Up-Conversion and Excited State Energy Transfer in Rare-Earth-Doped Materials", in Topics in Applied Physics, Vol. 15, 1976, ed. F.K. Fong

4) M.C. Farries: "Efficient Second Harmonic Generation in an Optical Fibre", IEE Colloquium on Non-Linear Optical Waveguides, London, 1988, paper 20

5) L. Li: in preparation

Publications

1) S.B. Poole, D.N. Payne and M.E. Fermann: "Fabrication of Low-Loss Optical Fibres Containing Rare-Earth Ions", Electron. Lett., **21**, 1985, pp. 737-738

2) M.C. Farries, M.E. Fermann, S.B. Poole, R.I. Laming, D.N. Payne and A. Leach: "Distributed Temperature Sensor Using Nd^{3+}-Doped Optical Fibre", Electron. Lett., **22**, 1986, pp. 418-419

3) S.B. Poole, D.N. Payne, R.J. Mears, M.E. Fermann and R.I. Laming: "Fabrication and Characterisation of Low-Loss-Optical Fibres Containing Rare-Earth Ions", J. Light. Tech., **LT-4**, 1986, pp. 870-876

4) M.C. Farries, P.St.J. Russell, M.E. Fermann and D.N. Payne: "Second Harmonic Generation in an Optical Fibre by Self Written $\chi^{(2)}$ Grating", Electron. Lett., **23**, 1987, pp. 322-324

5) M.E. Fermann, S.B. Poole, D.N. Payne and F. Martinez: "Comparative Measurement of Rayleigh Scattering in Single-Mode Optical Fibres Based on an OTDR Technique", J. Light. Tech., **LT-6**, 1988, pp. 545-551

6) M.C. Farries and M.E. Fermann: "Frequency-Doubling of 1.319μm Radiation in an Optical Fibre by Optically Written $\chi^{(2)}$ Grating", Electron. Lett., **24**, 1988, pp. 294-295

7) M.E. Fermann, M.C. Farries, P.St.J. Russell and L.J. Poyntz-Wright: "Tunable-Holographic Second-Harmonic Generators in High-Birefringence Optical Fibres", Opt. Lett., **13**, 1988, pp. 282-284

8) M.V. Bergot, M.C. Farries, M.E. Fermann, L. Li, L.J. Poyntz-Wright, P.St.J. Russell and A. Smithson: "Generation of Permanent Optically-Induced Second Order Nonlinearities in Optical Fibres by Poling", Opt. Lett., **13**, 1988, pp. 592-594

9) M.E. Fermann, L. Li, M.C. Farries and D.N. Payne: "Frequency-Doubling by Modal Phase-Matching in Poled Optical Fibres", Electron. Lett., **24**, 1988, pp. 894-895

10) L.J. Poyntz-Wright, M.E. Fermann, P.St.J. Russell: "Two-Photon Absorption Limited Blue/Green Light Transmission in Germanosilicate Fibres", Opt. Lett., **13**, 1988, pp. 1023-1025

11) M.E. Fermann, D.C. Hanna, D.P. Shepherd, P.J. Suni and J.E. Townsend: "Efficient Operation of an Yb Sensitised Er Fibre Laser at 1.56μm", Electron. Lett., **24**, 1988, pp. 1135-1136

12) M.E.Fermann, L. Li and M.C. Farries: "Second-Harmonic Generation Using Gratings Optically Written by Mode Interference in Poled Optical Fibres", subm. to Opt. Lett.

13) M.E. Fermann, L. Li, L.J. Poyntz-Wright and L. Dong: "Dynamics of CW-Excitation Poling for Second-Harmonic Generation in Germanosilicate Optical Fibres", subm. to Opt. Lett.

Conference Presentations

1) S.B. Poole, D.N. Payne, M.E. Fermann:, R.I. Laming and R.J. Mears: "Fabrication of Fibres Containing Rare-Earth Ions", JOERS Advanced Fibre Measurement Symposium, London, 1985

2) M.E. Fermann, S.B. Poole, D.N. Payne and F. Martinez: "A New Technique for the Relative Measurement of Scatter Levels in Single-Mode Optical Fibres", IEE Colloquium on Test Equipment for Optical Communication Systems, London, 1986

3) M.E. Fermann, S.B. Poole, D.N. Payne and F. Martinez: "A New Technique for the Measurement of Scatter Levels in Single-Mode Optical Fibres", Tech. Dig. Symp. on Opt. Fibre Measurements, Boulder, 1986, pp. 77-80

4) M.C. Farries, M.E. Fermann, S.B. Poole and J.E. Townsend: "Distributed Temperature Sensor Using Holmium-Doped Fibre", 6th International Conference on Integrated Optics and Optical Communication, OFC/IOOC, Reno, 1987, pp. 170

5) M.C. Farries and M.E. Fermann: "Temperature Sensing by Thermally Induced Absorption in a Neodymium Doped Optical Fibre", 4th International Symposium on Optical and Optoelectronic Applied Science and Engineering, Proc. SPIE, The Hague, 1987

6) M.E. Fermann, J.E. Townsend, M.C. Farries, S.B. Poole and D.N. Payne: "Multi-Photon Effects in Rare-Earth Doped Fibres", IEE Colloquium on Advanced Fibre Measurements, London, 1987

7) M.C. Farries, P.St. J. Russell, M.E. Fermann and D.N. Payne: "Second Harmonic Generation in an Optical Fibre by Self-Written $\chi^{(2)}$-Grating", IEE Colloquium on Advanced Fibre Measurements, London, 1987

8) M.C. Farries, M.E. Fermann, P.St.J. Russell and D.N. Payne "Tunable Second-Order Susceptibility Gratings for Harmonic Generation in Optical Fibres", Conference on Optical Fibre Communications, OFC, New Orleans, 1988, paper THE2

9) M.C. Farries and M.E. Fermann: "Frequency-Doubling of 1.319μm Radiation in an Optical Fibre by Optically-Written $\chi^{(2)}$-Grating", International Conference on Nonlinear Phenomena, Ireland, 1988

10) P.St.J. Russell, M.C. Farries, M.E. Fermann and D.N. Payne: "Efficient Frequency-Doubling in Silica Optical Fibres", Gordon Conference on Non-Linear Optics, 1987

11) L.J. Poyntz-Wright, M.E. Fermann and P.St.J. Russell: "Dynamics of Colour-Centre-Induced Nonlinear Transmission in GeO_2-SiO_2 Fibres", Conference on Lasers and Electrooptics, CLEO, Anaheim, 1988

12) L.J. Poyntz-Wright, M.E. Fermann and P.St.J. Russell: "Non-Linear Transmisssion in Germanosilicate Fibres at Blue/Green Wavelengths", IEE Colloquium on Nonlinear Optical Waveguides, London, 1988

13) M.E. Fermann, L. Li, M.C. Farries and D.N. Payne: "Phase-Matched Second-Harmonic Generation in Permanently-Poled Optical Fibres", European Conference on Optical Communications, ECOC, Brighton, 1988

14) W.L. Barnes, D.J. Taylor, M.E. Fermann, J.E. Townsend, L. Reekie and D.N. Payne: "A Diode-Laser-Pumped Er^{3+}/Yb^{3+}-Doped Fibre Laser Operating at 1.57μm", to be presented at Optical Fibre Conference, OFC, Houston, 1989

15) L. Li and M.E. Fermann: "Poling Techniques for Optical Fibres", to be presented at Quantum Electronics and Laser Science, QELS, Baltimore, 1989

16) M.C. Farries, M.E. Fermann and P.St.J. Russell: "Second Harmonic Generation in Optical Fibres", to be presented at Topical Meeting on Nonlinear Guided Wave Phenomena, Houston, 1989